

DISSERTATION

SYNTHESIS AND CHARACTERIZATION OF MULTIDENTATE IMINOPYRIDINE AND
POLYPYRIDINE TRANSITION METAL COMPLEXES

Submitted by

Ashley M. McDaniel

Department of Chemistry

In partial fulfillment of the requirements

For the Degree of Doctor of Philosophy

Colorado State University

Fort Collins, Colorado

Spring 2013

Doctoral Committee:

Advisor: Matthew Shores

Oren Anderson
Thomas Borch
Richard Finke
Dawn Rickey

Copyright by Ashley Marie McDaniel 2012

All Rights Reserved

ABSTRACT

SYNTHESIS AND CHARACTERIZATION OF MULTIDENTATE IMINOPYRIDINE AND POLYPYRIDINE TRANSITION METAL COMPLEXES

The work described in this dissertation details the syntheses and characterization of transition metal complexes featuring polypyridyl and iminopyridine ligands. The primary focus has been the synthesis of 3d metal complexes of multidentate iminopyridine ligands bearing functionalizations relevant to spin crossover and photochemistry. These seemingly disparate areas of research are linked by the facts that subtle metal-ligand interactions play enormous roles in determining complex properties and that understanding these types of interactions is crucial for eventual property control.

In Chapter 1, the underpinnings of spin crossover in transition metals with d^4 - d^7 configurations are discussed along with progress toward linking spin-switching events with host-guest interactions in solution. My research on Fe(II) hexadentate iminopyridine complexes is placed into context with extending anion sensing to biologically and environmentally relevant media. Also in Chapter 1, my work on hexadentate iminopyridine and polypyridine Cr complexes is related to the current understanding of the excited state behavior of 3d iminopyridine complexes, specifically, and 3d aromatic diimines in general. Additionally, the redox non-innocence of iminopyridine and polypyridine ligands is discussed.

In Chapter 2, the preparation and characterization of a series of divalent 3d transition metal complexes (Cr to Zn), featuring an ester functionalized multidentate, tripodal iminopyridine Schiff-base L^{5-OOMe} is reported. X-ray structural studies reveal complex geometries ranging from local octahedral coordination to significant distortion towards trigonal prismatic geometry to heptacoordinate environments. Regardless of coordination mode, magnetic and spectroscopic studies show the ligand to provide moderately strong ligand fields: the Fe complex is low-spin, while the Co and Mn complexes are high-spin at all temperatures probed. Cyclic voltammograms exhibit multiple reversible ligand-based

reductions, which are relatively consistent throughout the series; however, the electrochemical behavior of the Cr complex is fundamentally different from those of the other complexes. Time-dependent (TD) DFT and natural transition orbital (NTO) computational analyses for the ligand, its anion, and complexes were provided by Prof. Anthony Rappé: the computed spectra reproduce the major differential features of the observed visible absorption spectra, and NTOs provide viable interpretations for the observed features. The combined studies indicate that for Mn-Zn complexes, neutral ligands are bound to M(II) ions, but Cr is best described as a Cr(III) species bound to a radical anionic ligand.

In Chapter 3, the syntheses and characterizations of Fe(II) complexes of hexadentate ligands poised for anion-triggered spin-state switching in polar solution media are reported. The tripodal iminopyridine ligands L^{5-OH} , L^{6-OH} and $L^{5-ONHtBu}$, $L^{6-ONHtBu}$ contain methanolic or *t*-butylamide functional groups, respectively. Solid-state evidence for anion-cation hydrogen bonding interactions are observed for halide complexes of $[Fe(L^{6-OH})]^{2+}$ and $[Fe(L^{5-ONHtBu})]^{2+}$; $[Fe(L^{5-ONHtBu})]^{2+}$ forms a preorganized pocket which strongly binds Cl^- . Strong anion binding events in the 5-position complexes are also observed in solution via 1H NMR monitored chloride titrations in acetonitrile. And while no temperature dependence or anion dependence on spin-state is apparent for 6-position complexes in solution, a small but significant increase in magnetic susceptibility is observed for $[Fe(L^{5-ONHtBu})]^{2+}$ as up to one equivalent of tetrabutylammonium chloride is added; suggesting that spin-state control by anion-cation interactions may be accessible for this class of compounds.

In Chapter 4, the preparation and characterization of homo- and heteroleptic Cr(III) coordination complexes featuring the dimethyl 2,2'-bipyridine-4,4'-dicarboxylate (4-dmcbpy) ligand are discussed. Static and nanosecond time-resolved absorption and emission properties of these complexes dissolved in acidic aqueous (1 M $HCl_{(aq)}$) solutions were investigated by Huan-Wei Tseng and Prof. Niels Damrauer. The photophysical data suggest that in these acidic aqueous environments these complexes store ~ 1.7 eV for multiple microseconds at room temperature. The electrochemical properties of these polypyridyl complexes were investigated by cyclic voltammetry. It is found that inclusion of 4-dmcbpy shifts the $Cr^{III/II}$ $E_{1/2}$ by +0.22 V compared to those of homoleptic parent complexes. The electrochemical and

photophysical data allow for excited state potentials to be determined: for $[\text{Cr}(4\text{-dmcby})_3]^{3+}$, $\text{Cr}^{\text{III}/\text{II}}$ lies at +1.44 V versus $\text{Fc}^{+/0}$ ($\sim +2$ V vs NHE), suggesting it would act as one of the most powerful photooxidants reported.

In Chapter 5, the preparation, photophysical characterization, and computed excited state energies for Cr(III) complexes of a family of tripodal hexadentate and tris(bidentate) iminopyridine ligands are reported. Cyclic voltammograms reveal that the hexadentate and tris(bidentate) analogues have almost identical reduction potentials, and overall electrochemical behavior similar to the polypyridyl complexes described in Chapter 3. The absorption spectra of the hexadentate complexes show improved absorption of visible light compared to the tris(bidentate) analogues. Photophysical characterization provided by Huan-Wei Tesng and Prof. Niels Damrauer show a doublet excited state with 17 to 19 μs lifetime at room temperature for the ester functionalized tris(bidentate) complex, while no doublet states are observed for the ester functionalized hexadentate analogue under the same conditions. The electronic structure contributions to the differences in observed photophysical properties are compared by extensive computational analyses provided by Prof. Anthony Rappé. These studies indicate that the presence of non-ligated bridgehead nitrogen atoms in the complexes of tripodal hexadentate iminopyridines significantly reduce excited state doublet, quartet, and sextet energies and change the character of the low lying doublet states in compared to species that show population of doublet excited states.

In Chapter 6 the syntheses and characterization of reduced forms of Cr complexes of 4-dmcby (described in Chapter 4), $[\text{Cr}(4\text{-dmcby})_3]^{n+}$ ($n = 2, 1$), and $\text{tren}(\text{py})_3$ (L1, described in Chapter 5) $[\text{Cr}(\text{tren}(\text{py})_3)]^{n+}$ ($n = 2$) are reported. Comparison of electrochemical data for the series ($n = 3, 2, 1$) and solid state structures of the divalent complexes are consistent with consecutive reducing equivalents added to Cr polypyridine or iminopyridine complexes not residing on the metal, and that these complexes are best described as Cr(III) ions ligated to anionic radical ligands.

Final remarks about the work in Chapters 2-6 and suggested directions for future work are presented in Chapter 7.

ACKNOWLEDGMENTS

The work presented in this dissertation and the time I have spent at Colorado State University certainly did not occur in a vacuum; I have been supported and encouraged by a great many people who have helped make the accomplishments described in this document possible. I am very grateful for the many opportunities I have been able to enjoy though CSU, the Department of Chemistry and specifically through work in the Shores Group.

I would like to specifically thank the collaborators I have worked with, including Huan-Wei Tseng and Prof. Niels Damrauer at the University of Colorado, Boulder. I will never forget our afternoons on Skype discussing data and hashing out explanations for our observations. I feel very lucky to have had the chance to work with them both, and sincerely thank them for teaching me so much about excited-state complex behavior. Additionally, I am thankful to Prof. Tony Rappé for his critical work which finally made everything make sense. It was a pleasure working with him and every time I ran into him in the hallway outside my office, I appreciated being able to chat about the complexes I made and his calculations on them, and his consistent encouragement as I was writing up.

There were several people at CSU who, although we did not work together directly, helped me tremendously. Prof. Mike Elliott has taught me everything I know about electrochemistry, for which I am eternally grateful. On top of that, he was always available to talk about some crazy CV I had collected and generously allowed me access to his lab for equipment use and for reagents. I was lucky to have Prof. Oren Anderson on my committee and to be able to learn about X-ray crystallography from him, including structure solution and the theory behind it. I am also grateful to Susie Miller for teaching me how to be competent in an X-ray lab.

I owe special appreciation to my labmates, Dr. Zhaoping Ni, Dr. Wes Hoffert, Dr. Brian Newell, Stephanie Fiedler and Christina Klug, and the undergraduate students I worked with, especially Ethan Hill. Graduate school is a difficult endeavor—being able to learn from, bounce ideas off of, commiserate

with and celebrate with all of them was vital to my success at CSU as well as to my overall well-being as a graduate student. Thanks guys.

The person who has had the single greatest impact on me while at CSU has been my advisor, Prof. Matt Shores. I have learned so much during my time in his lab that it would be impossible to summarize it all. I thank him for making me a better scientist, for pushing me to keep improving and for caring about his students and his work.

My family has been incredibly supportive throughout my many years of schooling. I am grateful for their support for my pursuit of science and their pride in me and my work. Lastly, I would have never pursued a Ph.D. if not for the initial encouragement of my husband, JP Moon. I could not have completed the work described in this dissertation without his love of chemistry, his love of me and his unending support, so I dedicate this work to him. Thanks for everything, Panda.

AUTOBIOGRAPHY

Ashley Marie McDaniel was born January 18, 1980 in Fremont, CA to parents Gerry and Carol McDaniel. She attended Mission San Jose High School in Fremont, CA and graduated in 1998. She attended the University of California, Berkeley on a National Merit Scholarship and graduated with a B.S. in Chemistry in 2002. While at Berkeley, she worked in T. Don Tilley's group under the direction of Ben Mork, on the synthesis of ruthenium organometallics. After graduation, Ashley moved to Seattle, WA, where she worked for Neah Power Systems electrochemically testing direct methanol fuel cells, fuel cell stacks, and components. In 2006, Ashley began her Ph.D. work at Colorado State University, where she studied Inorganic Chemistry with Prof. Matthew P. Shores. Ashley earned her doctorate in 2012 and will be doing Postdoctoral research with Prof. Jake Soper at the Georgia Institute of Technology in Atlanta, GA.

Ashley is an outdoor enthusiast who enjoys backpacking, hiking, snowshoeing, and surfing when she has the chance. She is also an experienced martial artist who practices Aikido.

TABLE OF CONTENTS

Chapter 1. Iminopyridine Complexes of First Row Transition Metals: Syntheses and Applications	1
1.1 Introduction.....	1
1.2 Spin Crossover in Transition Metal Complexes	2
1.3 Excited State Properties in Transition Metal Complexes.....	5
1.4 Outline of Dissertation Chapters	7
1.5 References.....	9
Chapter 2. Structural and Electronic Comparison of 1 st Row Transition Metal Complexes of a Tripodal Iminopyridine Ligand	13
2.1 Introduction.....	13
2.2 Division of Labor	15
2.3 Experimental Section	15
2.3.1 Preparation of Compounds.....	15
Trimethyl-6,6',6''-((1E,1'E,1''E)-((nitriлотris(ethane-2,1-diyl)tris(azanylylidene))tris(methanylylidene))trinicotinate (L ^{5-OOMe})	16
[Cr(L ^{5-OOMe})](BF ₄) ₂ (2.1).....	16
[Mn(L ^{5-OOMe})](CF ₃ SO ₃) ₂ (2.2).....	17
[Fe(L ^{5-OOMe})](CF ₃ SO ₃) ₂ (2.3)	17
[Co(L ^{5-OOMe})](ClO ₄) ₂ (2.4)	18
[Co(L ^{5-OOMe})](CoCl ₄) (2.4a).....	18
[Ni(L ^{5-OOMe})](ClO ₄) ₂ (2.5).....	18
[Cu(L ^{5-OOMe})](CF ₃ SO ₃) ₂ (2.6).....	19
[Zn(L ^{5-OOMe})](CF ₃ SO ₃) ₂ (2.7).....	19
2.3.2 X-Ray Structure Determinations	20
2.3.3 Other Physical Methods	23
2.3.4 Electronic Structure Calculations	23
2.4 Results.....	24
2.4.1 Syntheses	24
2.4.2 Structural Comparisons.....	25
2.4.3 Comparison of Magnetic Properties	27
2.4.4 Electronic Absorption Comparisons.....	28
2.4.5 Simulated Electronic Absorption Spectra.....	28
2.4.6 Electrochemistry	30

2.5 Discussion.....	32
2.5.1 Electronic Structure Considerations for the “Cr(II)” Complex.....	33
2.5.2 Trends in Electronic Transitions for L ^{5-OOMe} Complexes.....	34
2.5.3 Electronic Structure Considerations for Spin-State Switching	35
2.6 Conclusions and Outlook	37
2.8 References.....	39
Chapter 3. Synthesis of Functionalized Hexadentate Fe(II) Complexes: Toward Anion-Dependent Spin Switching in Polar Media.....	42
3.1 Introduction.....	42
3.2 Division of Labor.....	46
3.3 Experimental Section	46
3.3.1 Preparation of Compounds.....	46
5-(Hydroxymethyl)picolinaldehyde (3.1)	47
[Fe(L ^{5-OH})]SO ₄ (3.2).....	48
[Fe(L ^{5-OH})](BF ₄) ₂ (3.3).....	48
[Fe(L ^{5-OH})](BPh ₄) ₂ (3.4).....	48
[Fe(L ^{6-OH})](SO ₃ CF ₃) ₂ (3.5).....	49
[Fe(L ^{6-OH})](BF ₄) ₂ (3.6).....	49
[Fe(L ^{6-OH})]I ₂ (3.7)	49
[Fe(L ^{6-OH})]Br ₂ (3.8).....	50
[Fe(L ^{6-OH})]Cl ₂ (3.9).....	50
[Fe(L ^{6-OH})](BPh ₄) ₂ (3.10).....	50
{[Fe(L ^{5-ONH<i>t</i>Bu})]-Cl} ₂ [FeCl ₄] (3.11)	51
[Fe(L ^{5-ONH<i>t</i>Bu})](BF ₄) ₂ (3.12).....	51
[Fe(L ^{5-ONH<i>t</i>Bu})](BPh ₄) _{1.5} Cl _{0.5} (3.13).....	52
[Fe(L ^{6-ONH<i>t</i>Bu})]Cl ₂ (3.14)	53
[Fe(L ^{6-ONH<i>t</i>Bu})](SO ₃ CF ₃) ₂ (3.15)	53
3.3.2 X-Ray Structure Determinations.....	53
3.3.3 Other Physical Methods	55
3.4 Results and Discussion.....	55
3.4.1 Syntheses	55
3.4.2 Solid State Structural Characterization.....	59
3.4.3 Solution Spin-State Studies.....	62
3.4.4 Solution Anion-Binding Studies	63
3.5 Conclusions and Outlook	68
3.7 References.....	71

Chapter 4. Synthesis and Solution Phase Characterization of Strongly Photooxidizing Heteroleptic Cr(III) Tris-Dipyridyl Complexes.....	73
4.1 Introduction.....	73
4.2 Division of Labor.....	75
4.3 Experimental Section.....	75
4.3.1 Preparation of Compounds.....	75
[(phen) ₂ Cr(4-dmcbpy)](OTf) ₃ (4.1).....	76
[(Ph ₂ phen) ₂ CrCl ₂]Cl (4.2).....	76
[(Ph ₂ phen) ₂ Cr(OTf) ₂]OTf (4.3).....	76
[(Ph ₂ phen) ₂ Cr(4-dmcbpy)](OTf) ₃ (4.4).....	77
[(Me ₂ bpy) ₂ CrCl ₂]Cl (4.5).....	77
[(Me ₂ bpy) ₂ Cr(OTf) ₂]OTf (4.6).....	77
[(Me ₂ bpy) ₂ Cr(4-dmcbpy)](OTf) ₃ (4.7).....	78
[Cr(4-dmcbpy) ₃](BF ₄) ₃ (4.8).....	78
4.3.2 X-Ray Structure Determinations.....	78
4.3.3 Photophysical Measurements.....	79
4.3.4 Other Physical Methods.....	81
4.4 Results and Discussion.....	82
4.4.1 Synthesis and Characterization of Heteroleptic Cr(III) Complexes.....	82
4.4.2 Exploration of photophysics and electrochemistry of Cr(III) systems in solution.....	84
4.4.2a Electronic Absorption.....	84
4.4.2b Static Emission.....	88
4.4.2c Time-Resolved Emission.....	91
4.4.2d Ground and Excited State Reduction Potentials.....	94
4.4.2e Transient Absorption.....	96
4.5 Conclusions and Outlook.....	99
4.7 References.....	101
Chapter 5. Syntheses and Photophysical Investigations of Cr(III) Hexadentate Iminopyridine Complexes and Their Tris(Bidentate) Analogues.....	105
5.1 Introduction.....	105
5.2 Division of Labor.....	106
5.3 Experimental Section.....	107
5.3.1 Preparation of Compounds.....	107
[Cr(L1)](BF ₄) ₃ (5.1).....	107
[Cr(L2)](BF ₄) ₃ (5.2).....	108
(E)-N-(pyridin-2-ylmethylene)ethanamine (L3).....	108
[Cr(L3) ₃](BF ₄) ₃ (5.3).....	109
(E)-methyl 6-((ethylimino)methyl)nicotinate (L4).....	109

[Cr(L4) ₃](BF ₄) ₃ (5.4)	110
5.3.2 X-Ray Structure Determinations	110
5.3.3 Photophysical Methods	112
5.3.4 Other Physical Methods	113
5.3.5 Electronic Structure Calculations	114
5.4 Results and Discussion	115
5.4.1 Synthesis and Ground-State Characterization of Cr(III) Complexes	115
5.4.2 Electrochemistry	118
5.4.3 Electronic Absorption	120
5.4.4 Probing Complex Stability in Solution	122
5.4.5 Emission Spectroscopy	123
5.4.6 Electronic Structure Considerations	127
5.5 Conclusions and Outlook	132
5.7 References	134
Chapter 6. Synthesis of “Cr(II)” and “Cr(I)” Polypyridyl Complexes	137
6.1 Introduction	137
6.2 Division of Labor	138
6.3 Experimental Section	138
6.3.1 Preparation of Compounds	138
[Cr(4-dmcbpy) ₃](BF ₄) ₂ (6.1)	138
[Cr(4-dmcbpy) ₃](BF ₄) (6.2)	138
[Cr(tren(imp) ₃)](BF ₄) ₂ (6.3)	139
6.3.2 Bulk Electrolyses	139
6.3.3 X-Ray Structure Determinations	140
6.3.4 Other Physical Methods	141
6.4 Results and Discussion	142
6.4.1 Syntheses	142
6.4.2 Solid-State Structural Characterization	144
6.4.3 Electrochemical Characterization and Bulk Electrolysis	145
6.5 Conclusions and Outlook	149
6.7 References	151
Chapter 7. Final Remarks and Future Work	152

7.1 References.....	158
Appendix A1. Supporting Information for Chapter 2.....	160
A1.1 Full Reference 25 from Chapter 2	160
Appendix A2. Supporting Information for Chapter 3.....	166
A2.1 Additional Information on Calculating Binding Constants Using ¹ H NMR Data.....	166
A2.2 References.....	181
Appendix A3. Supporting Information for Chapter 4.....	181
A3.1 Experimental Section	182
A3.1.1 X-Ray Structure Determination Details	182
A3.1.2 Detailed Instrumentation and Methods for Photophysical Measurements	183
A3.2 References.....	190
Appendix A4. Supporting Information for Chapter 5.....	190
A4.1 Full Reference 21 from Chapter 5	191
A4.2 Details of Computational Analyses	200
Appendix A5. Supporting Information for Chapter 6.....	209
Appendix A6. Notebook Cross-references for Iminopyridine, Polypyridine and Related Compounds...	215

LIST OF TABLES

Table 2.1. Crystallographic data for compounds 2.1-2.5 and 2.7.....	22
Table 2.3. Selected iminopyridine ligand bond lengths.....	33
Table 3.1. Crystallographic data for compounds 3.3, 3.8 and 3.11.....	54
Table 3.2 Key bond distances and angles in crystal structures.....	60
Table 3.3. Hydrogen bonding interactions and close contacts to anions in crystal structures.....	61
Table 4.1. Crystallographic Data for [(phen) ₂ Cr(4-dmcbpy)](OTf) ₃ ·1.3CH ₃ CN (4.1·1.3CH ₃ CN).....	79
Table 4.2. Room temperature electronic absorptions for Cr(III) tris-dipyridyl complexes.....	86
Table 4.3. Photophysical data for Cr(III) polypyridyl complexes.....	90
Table 4.4. Ground and excited state reduction potentials for Cr(III) polypyridyl complexes.....	95
Table 5.1. Crystallographic data for [Cr(L2)](BF ₄) ₃ ·CH ₃ CN (5.2·CH ₃ CN) and [Cr(L4) ₃](BF ₄) ₃ (5.4) ...	112
Table 5.2. Ground-state reduction potentials for Cr(III) iminopyridine complexes.....	119
Table 5.3. Computed excitation energies (EE) for selected complexes.....	128
Table 6.1. Crystallographic data for compounds 6.1 and 6.3.....	141
Table 6.2. Selected ligand diimine ligand bond lengths.....	145
Table 6.3. Reduction potentials for 4-dmcbpy and (tren(imp) ₃) Cr complexes.....	146
Table A1.1. Selected geometric data for complexes 2.1-2.5 and 2.7.....	161
Table A3.1. Selected bond lengths and angles for [(phen) ₂ Cr(4-dmcbpy)](OTf) ₃ ·1.3CH ₃ CN.....	186
Table A3.2. Ground state reduction potentials and peak separations for Cr(III) polypyridyl complexes.....	189
Table A4.1. Selected bond lengths [Å] and angles [°] for 5.2·CH ₃ CN.....	206
Table A4.2. Selected bond lengths [Å] and angles [°] for 5.4.....	207

LIST OF FIGURES

Figure 1.1. Spin-spin state dependent electronic configurations.....	3
Figure 1.2. Simplified Jablonski diagram for an octahedral Cr(III) complex.....	6
Figure 2.1. Side-on view of the $[M(L^{5-OOMe})]^{2+}$ complex cation in the structure of 2.5·2CH ₃ CN.....	25
Figure 2.2. Geometry of the first coordination sphere around the M(II) ions and distance to tether N atom of ligand L ^{5-OOMe}	26
Figure 2.3. Experimental (top) and TD-DFT simulated (bottom) visible electronic absorption spectra for 2.1-2.7.....	29
Figure 2.4. Cyclic voltammograms of the M(II) complexes in 2.1-2.7.....	31
Figure 2.5. Comparison of net spin density plots.....	34
Figure 3.1. Complex cation and interacting anions in 3.3·CH ₃ CN (left), 3.11·3CH ₃ CN·(CH ₃ CH ₂) ₂ O (center), and 3.8·0.5 CH ₃ OH·0.5 CH ₃ CH ₂ OH (right).....	59
Figure 3.2. Variable temperature magnetic susceptibility data for 6-position Fe(II) complexes in solution.....	63
Figure 3.3. 300 MHz ¹ H NMR of $[Fe(L^{5-OH})](BF_4)_2$ in CD ₃ CN at 24.9 C (top) and after addition of TBACl (bottom).....	65
Figure 3.4. Chemical shift values for aromatic protons in $[Fe(L^{5-ONHtBu})](BF_4)_2$ (3.12) during titration of TBACl.....	66
Figure 3.5. Chemical shift values for bulk TMS peak relative to capillary TMS in sample of $[Fe(L^{5-ONHtBu})](BF_4)_2$ (3.12) after addition of varying amounts of TBACl.....	67
Figure 4.1. Structure of the $[(phen)_2Cr(4-dmcbpy)]^{3+}$ complex cation.....	84
Figure 4.2. Electronic absorption spectra for Cr(III) dipyriddy complexes.....	85
Figure 4.3. Electronic absorption spectra for Cr(III) complexes containing phenanthroline-based ligands.....	87
Figure 4.4. Emission spectra for Cr(III) polypyridyl complexes.....	89

Figure 4.5. Temperature dependence of the observed rate constant $k_{obs} = 1/\tau_{obs}$ for $[\text{Cr}(\text{bpy})_3]^{3+}$ and 4.8..	92
Figure 4.6. Comparison of cyclic voltammograms for the 4-dmcbpy containing complexes 4.1, 4.4, 4.7, and 4.8	94
Figure 4.7. Transient absorption spectra on a μs timescale for 4.8 (left) and 4.4 (right)	98
Figure 5.1. Structures of the Cr(III) iminopyridine complex cations	117
Figure 5.2. Comparison of cyclic voltammograms for 5.1-5.4	119
Figure 5.3. Electronic absorption spectra collected in acetonitrile for Cr(III) complexes 5.1-5.4	121
Figure 5.4. Emission spectra for freshly prepared solutions of 5.2 and 5.4	124
Figure 5.5. ^2E excitation spectrum for a fresh prepared solution of 5.4	124
Figure 5.6. ^2E emission kinetic trace for 5.4	125
Figure 5.7. Computed excitation energies for selected Cr(III) complexes	129
Figure 5.8. Natural transition Orbitals (NTOs) for the lowest (a) doublet and (b) quartet transitions	130
Figure 6.1. Comparison of electronic absorption spectra of $[\text{Cr}(4\text{-dmcbpy})_3]^{n+}$ complexes in CH_3CN ...	143
Figure 6.2. The complex cation for 6.1 (left) and two views of the complex cation for 6.3 (center and right)	144
Figure 6.3. Comparison of cyclic voltammograms for 4-dmcbpy and $\text{tren}(\text{imp})_3$ Cr complexes	146
Figure 6.4. Stirring experiment cyclic voltammogram of $[\text{Cr}(4\text{-dmcbpy})_3](\text{BF}_4)$ done to determine oxidation state in bulk solution	147
Figure A1.1. Side-on views of the $[\text{ML}^{5\text{-OOMe}}]^{2+}$ complex cations in the structures of 2.1-5 and 2.7	161
Figure A1.2. UV absorption spectra of complexes 2.1-2.7	162
Figure A1.3. Simulated electronic absorption spectra and select natural transition orbital (NTO) pairs for (a) $\text{L}^{5\text{-OOMe}}$ and (b) its anion, $(\text{L}^{5\text{-OOMe}})^-$	162
Figure A1.4. Simulated electronic absorption spectra and select natural transition orbitals (NTOs) for compounds 2.1-2.7'	164
Figure A1.5. Orbital amplitude surface for the HOMO of trimethylamine	165
Figure A2.1. Full crystal structure for 3.8	167

Figure A2.2. Full crystal structure for 3.3·CH ₃ CN.....	168
Figure A2.3. Full crystal structure for 3.11	169
Figure A2.4. ¹ H NMR spectra of 3.3 in CD ₃ CN before (top) and after addition of 2 equivalents TBACl (bottom)	170
Figure A2.5. Aromatic region in ¹ H NMR-monitored chloride titration of 3.12.....	171
Figure A2.6. Room temperature ¹ H NMR spectrum of L ^{5-OH}	172
Figure A2.7. Room temperature ¹ H NMR spectrum of 3.3	173
Figure A2.8. Room temperature ¹ H NMR spectrum of 3.4	174
Figure A2.9. Room temperature ¹ H NMR spectrum of L ^{6-OH}	175
Figure A2.10. Room temperature ¹ H NMR spectrum of L ^{5-ONHtBu}	176
Figure A2.11. Room temperature ¹ H NMR spectrum of 3.11.....	177
Figure A2.12. Room temperature ¹ H NMR spectrum of 3.12.....	178
Figure A2.13. Room temperature ¹ H NMR spectrum of 3.13.....	179
Figure A2.14. Room temperature ¹ H NMR spectrum of L ^{6-ONHtBu}	180
Figure A3.1. Full crystal structure for complex 4.1·1.3CH ₃ CN.....	186
Figure A3.2. Transient absorption spectra on a μs timescale for Cr(III) polypyridyl complexes.....	187
Figure A3.3. Temperature dependence of the observed rate constant ($k_{obs} = 1/\tau_{obs}$) for Cr(III) polypyridyl complexes	188
Figure A4.1. ¹ H NMR of L2.....	192
Figure A4.2. ¹³ C NMR of L2.....	192
Figure A4.3. ¹ H NMR of L3.....	193
Figure A4.4. ¹³ C NMR of L3.....	193
Figure A4.5. ¹ H NMR of L4.....	194
Figure A4.6. ¹³ C NMR of L4.....	194
Figure A4.7. Absorption spectra of L1 and L2 in acetonitrile and L3 and L4 in pentane	195

Figure A4.8. The full complex cation, and crystallographically independent anion and solvent molecules in the structure of 5.2·CH ₃ CN.....	195
Figure A4.9. Alternate view of Cr(III) complex cation in the structure of 5.2·CH ₃ CN	196
Figure A4.10. Absorption spectra for complexes 5.1, 5.2, 5.4, and [Cr(phen) ₃](OTf) ₃ in 1M HCl _(aq) over 24 hours.	197
Figure A4.11. Absorption spectra for complexes 5.2, 5.4, and [Cr(phen) ₃](OTf) ₃ in acetonitrile over 24 hours.	197
Figure A4.12. (a) Transient absorption spectrum for complex 5.4 recorded in deoxygenated acetonitrile at room temperature. (b) A typical transient absorption kinetic trace at 420 nm	198
Figure A4.13. Emission spectra for complexes 5.2 and 5.4 in acetonitrile right after dissolution and at 24 hours	198
Figure A4.14. Excitation spectra for complexes 5.2 and 5.4 in acetonitrile at 0 and 24 hours after dissolution.....	198
Figure A4.15. The full structure of 5.4.....	199
Figure A4.16. Calculated doublet and quartet excited state absorption spectra of [Cr(bpy) ₃] ³⁺ (left) and transient absorption spectrum of [Cr(bpy) ₃] ³⁺ (right).....	199
Figure A4.17. Computed excitation energies for selected Cr(III) complexes	201
Figure A4.18. Natural transition orbital (NTO) analyses for the 3.1-3.5 eV range for 5.2.....	202
Figure A4.19. Natural transition orbital (NTO) analyses for the 2.6-3.1 eV range for 5.2.....	203
Figure A4.20. Natural transition orbital (NTO) analyses for the 2.1-2.6 eV range for 5.2.....	204
Figure A4.21. Natural transition orbitals (NTOs) for [Cr(4-dmcbpy) ₃] ³⁺ (left), 5.2 (middle) and 5.4' (right)	205
Figure A5.1. Full structure of 6.1	209
Figure A5.2. Full structure of 6.3	210
Figure A5.3. Electronic absorption spectra showing aerobic oxidation of 6.2.....	211
Figure A5.4. Positive ion mass spectrum of [Cr(4-dmcbpy) ₃](BF ₄) 6.2	212

Figure A5.5. Experimental isotopic pattern of the 868.07 m/z peak ($[\text{Cr}(4\text{-dmcby})_3]^+$) of 6.2 in CH_3CN	212
Figure A5.6. Simulated isotopic pattern of the 868.07 m/z peak ($[\text{Cr}(4\text{-dmcby})_3]^+$) of 6.2 in CH_3CN ..	213
Figure A5.7. Cyclic voltammogram of reaction product from reduction of $[\text{Cr}(4\text{-dmcby})_3](\text{BF}_4)_2$ with sodium diphenylketyl radical	213
Figure A5.8. KBr pellet IR spectrum of working compartment product from reduction of $[\text{Cr}(4\text{-dmcby})_3](\text{BF}_4)_2$ by bulk electrolysis	214
Figure A5.9. Cyclic voltammogram of solid reaction product from reduction of $[\text{Cr}(\text{tren}(\text{impy})_3)](\text{BF}_4)_2$ by bulk electrolysis	214

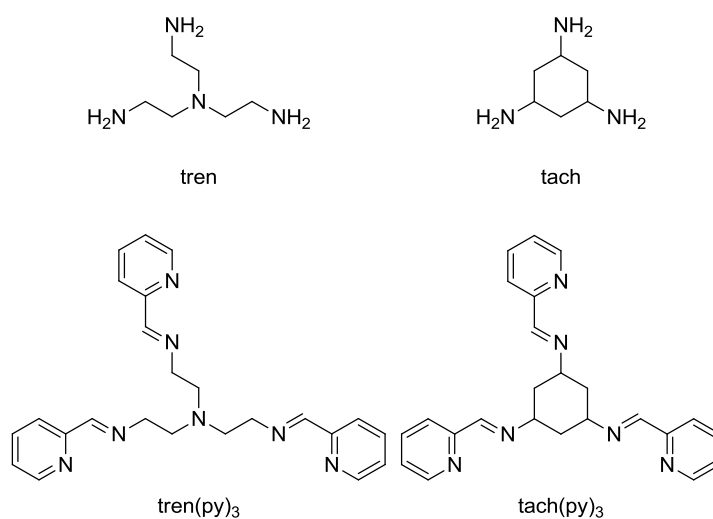
LIST OF SCHEMES

Scheme 1.1. Multidentate iminopyridines	1
Scheme 2.1. Example iminopyridine ligands	13
Scheme 2.2. Syntheses of the ligand L ^{5-OOMe} (top) and the divalent complex salts 2.1-2.7 (bottom)	24
Scheme 3.1. Tripodal hexadentate ligands	44
Scheme 3.2. Potential anion-binding functional groups (left), tripodal ditopic ligand family used in this work (center), and actual ligand configurations used (right)	45
Scheme 3.3. Synthetic pathways for ligands L ^{5-OH} and L ^{6-OH}	56
Scheme 3.4. Synthetic pathway for ligand L ^{5-ONHtBu}	56
Scheme 4.1. Target structures of [(NN) ₂ Cr(4-dmcbpy)] ³⁺ complexes	75
Scheme 4.2. Synthesis of heteroleptic Cr(III) polypyridyl complexes	82
Scheme 4.3. Synthesis of homoleptic 4.8	83
Scheme 5.1. Hexadentate tripodal (L1 and L2) and bidentate iminopyridine (L3 and L4) ligands	106
Scheme 5.2. Preparation of Cr(III) iminopyridine complex salts	116
Scheme A2.1. Synthesis of the ligand aldehyde precursor	160

Chapter 1. Iminopyridine Complexes of First Row Transition Metals: Syntheses and Applications

1.1 Introduction

Iminopyridine ligands are a class of diimine ligand formed by Schiff-base condensation. These types of ligands can be synthesized from functional variants of 2-pyridinecarboxaldehyde and practically any primary amine starting material; this modularity gives them enormous versatility. The resultant ligands provide at least two nitrogen-based coordination sites, act as good σ donors, and provide relatively strong ligand fields. Iminopyridine ligands can range from bidentate to multidentate. Their denticity can be controlled by changing the number of amine groups or aldehyde groups on the individual starting materials. Tripodal multidentate iminopyridine ligands, such as those formed by condensation with the amines tris(2-aminoethyl)amine (tren) or 1,3,5-triaminocyclohexane (tach) shown in Scheme 1.1, are able to accommodate flexible coordination geometries. Tripodal iminopyridines have been shown to support a range of coordination modes from trigonal prismatic to trigonal antiprismatic and even seven-coordinate species.¹



Scheme 1.1. Multidentate iminopyridines. Primary amines (top) used to synthesize multidentate tripodal iminopyridines (bottom).

Functionally, iminopyridine complexes can be useful catalysts. There has been a great deal of research into the activity of iron,² cobalt,^{2b,c,2e,f,3} and nickel^{3i,4} bis(imino)pyridine complexes toward ethylene polymerization and oligomerization. In these systems, the tridentate ligands include sterically bulky aryl groups attached to the imines to access low coordinate metal species in order to provide empty coordination sites for catalytic activity. In another instance of catalysis, copper iminopyridine complexes are efficient catalysts for the asymmetric Henry (nitro-aldol) reaction⁵, which is a very useful C-C bond-forming reaction where nitroalkanes add to carbonyls to yield β -nitroalkanol. Additionally, a wide array of transition metal iminopyridine complexes has also demonstrated the ability to activate dinitrogen.⁶

We became interested in iminopyridine ligands because of their similarity to diimine ligands such as bipyridine and phenanthroline. In our work we are interested in ligands which support long-lived excited states, can potentially act as electron reservoirs, or have intermediate ligand fields in order to engender spin-crossover. The study of transition metal complexes featuring multidentate iminopyridine ligand sets is the primary focus of the work described in this dissertation. This introductory chapter includes an overview of the spin crossover phenomenon, followed by an overview of excited-state properties in transition metals. Lastly, there is an outline of the work to be presented in the remainder of this dissertation.

1.2 Spin Crossover in Transition Metal Complexes

Spin crossover was first observed in 1931 for a Fe(III) compound;⁷ however, Fe(II) is the most commonly studied ion which undergoes spin crossover. For any octahedrally coordinated transition metal ion with a valence electronic configuration of d^4 to d^7 , two distinct electronic ground states are possible. As shown in Figure 1.1, if the pairing energy (Π) is larger than the ligand field splitting energy (Δ_O), d electrons will fill both the t_{2g} and e_g orbitals. This results in the high-spin state which maximizes the number of unpaired electrons, and in the case of Fe(II) this leads to a paramagnetic state where $S = 2$. Conversely, if Π is less than Δ_O , electrons will preferentially populate the t_{2g} orbitals which minimizes the number of unpaired electrons. This leads to the low-spin state which is diamagnetic in Fe(II) with $S = 0$.

When Π and Δ_O are very close in magnitude it is possible for both the low-spin state and the high-spin state to be thermally accessible, and for a metal ion to switch between low-spin and high-spin ground states. This spin-switching transition can be triggered by multiple inputs (thermal, irradiation, pressure, magnetic field, and chemical environment),⁸ and is exquisitely dependent on the nature of the ligands coordinating the metal center and the strength of the ligand field they provide.

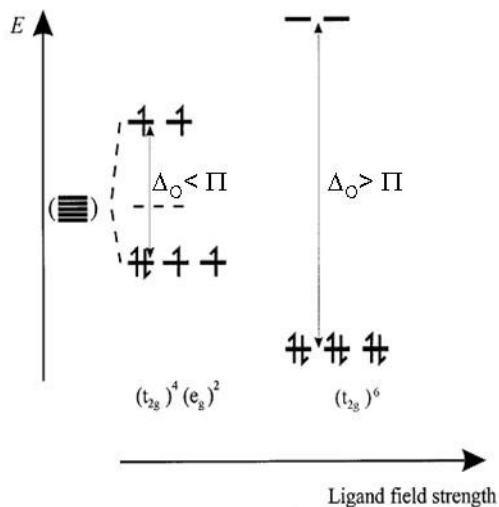


Figure 1.1. Spin-spin state dependent electronic configurations. Electronic configuration of the high-spin state (left) and low-spin state (right) of a Fe(II) ion. Adapted from Ref. 8.

We are interested in combining spin-state switching functionality with anion sensing such that binding of an anion to a receptor on a Fe(II) complex causes a spin transition. In a previous report featuring the ditopic ligand H_2bip (1,1',4,4',5,5',6,6'-octahydro-2,2'-bipyrimidine), anion-dependent spin crossover was observed in the solid state. The authors suggested the spin-state change could be due to alteration of the ligand field by direct anion binding.⁹ Our group's initial work focused on demonstrating anion-dependent spin-state switching in solution for homoleptic¹⁰ and heteroleptic¹¹ H_2bip Fe(II) complexes. Work on these complexes has shown that anion-dependent spin-state switching is achievable in solution. Addition of halides (such as Br^- via tetrabutylammonium bromide) to solutions of H_2bip Fe(II) complexes with weakly coordinating anions (such as tetraphenylborate) cause the complexes to

shift toward the low-spin state. This occurs because halides interact with the –NH moieties on H₂bip and the interaction increases the σ donating ability of the ligand.¹⁰

The main drawback to these tris(bidentate) systems is the lability of high-spin Fe(II) complexes. These complexes are generally stable to anion titration only in solvents of low polarity such as dichloromethane, while heteroleptic complexes are prone to ligand scrambling unless primarily strong-field ligands are used. Our goal was to redesign the ligand environment to enhance kinetic stability and to make sensing possible in polar solvents. Multidentate iminopyridine ligands were an obvious candidate to try to achieve this goal, as their higher denticity over bidentate ligands could help improve kinetic stability. Additionally, their modular assembly nature would make synthesizing ligands, with variations in the identity and position of anion binding moiety, relatively facile.

Due to their similarity to other diimine ligands such as bipyridine and biimidazole, iminopyridine ligands have been utilized in spin crossover research. As stated earlier, ions with electron configurations of d^4 - d^7 have the capacity for spin crossover, but only with certain metal and ligand field combinations is spin crossover practically accessible. There are few examples of spin crossover for 4d and none for 5d transition metals since smaller Π and larger Δ_o values for these metals heavily favor the low-spin state. There are significantly more instances of spin crossover for 3d transition metals, however spin crossover is more common for certain electron configurations than others. Many theoretically d^4 divalent Cr species are better described as Cr(III)–ligand radicals where spin crossover on the metal is not possible,¹² and truly Cr(II) compounds displaying spin crossover do not use iminopyridine ligand sets.¹³ Most d^4 Mn(III) complexes are exclusively high-spin, and of the very few Mn(III) complexes which display spin crossover, all feature anionic ligands and none are iminopyridines.¹³⁻¹⁴ For divalent Mn (d^5), spin crossover is extremely difficult to access,¹³ most Mn(II) complexes are high-spin and no octahedral Mn(II) spin crossover compounds are currently known. Spin crossover is more accessible in Fe(III) (d^5) systems but it requires ligands with mixed N, O donors or chelation exclusively by chalcogens.¹⁵ The vast majority of Co(III) (d^6) complexes are exclusively low-spin, and those that exhibit spin crossover use ligands where oxygen is the chelating atom.¹³ For Co(II) (d^7), terpyridine type ligands are usually favored

for their strong ligand fields and ability to accommodate Jahn-Teller distortions which accompany spin switching.¹⁶ However, the iminopyridine complex $[\text{Co}(\text{pmi})_3](\text{ClO}_4)_2$ (pmi = 2-pyridinalmethylimine) displays spin crossover behavior in the solid state.¹⁷

Finally, a great many Fe(II) (d^6) complexes display spin crossover behavior and those featuring diimine ligands are well known.¹⁸ Tripodal iminopyridine complexes of Fe(II) tend to be low-spin unless steric bulk is present to prevent close approach of the ligand to the metal.¹⁹ This can be achieved by installation of any group at the 6-position (α to the pyridine N atom). The resulting longer metal–nitrogen bonds favor the high-spin state. Tripodal iminopyridine ligands where every pyridine has non-hydrogen substituents at the 6-position undergo thermal spin crossover at temperatures below 200 K and remain high-spin in solution.^{19a,19d} Conversely, those that have only hydrogen substituents at the 6-position are exclusively low spin in the solid state and in solution.^{19a} For ligands with mixed hydrogen/non-hydrogen substituent at the pyridine 6-positions, the resultant complexes undergo thermal spin crossover in both the solid state and in solution.^{19a} If there are two hydrogens and one non-hydrogen group, the complex is mostly low spin at room temperature in the solid state and in solution, whereas if two non-hydrogen groups and one hydrogen is present, the resulting complex is mostly high spin in solution and in the solid state.^{19b}

1.3 Excited State Properties in Transition Metal Complexes

In contrast to the varying ground state properties of iminopyridine complexes, such as spin switching seen in Fe(II) and Co(II), there has been little work reported describing the excited state behaviors of these types of complexes. A great deal of research has gone into studying the excited state properties of aromatic diimine transition-metal complexes, most notably those of Cr(III)²⁰ and Ru(II)²¹ polypyridyls. These metal complexes display accessible μs to ms lifetime excited states which, when combined with redox activity, have made them very attractive materials for solar energy conversion. For Ru(II) complexes there has been an explosion of research on their use as sensitizers for wide bandgap metal oxides as part of dye-sensitized solar cells (DSSCs)^{21c,22} since the seminal paper by Grätzel and O'Regan

published in 1991.²³ In Ru(II)-based DSSCs, the sensitizer acts as a *photo-reductant* which injects an electron into the conduction band of the wide band gap semiconductor on which it is attached. Conversely, the *photo-oxidizing* nature of Cr(III) complexes was recognized for its potential use in solar photoconversion,²⁴ but much less work has been done on these types of materials. Reasons for the lower apparent interest in the Cr(III) systems may include: less favorable visible light absorption than similar Ru(II) complexes, increased ligand lability of the “Cr(II)” species after electron transfer, and redox catalyzed aquation of Cr(III) complexes in aqueous systems.^{24a} Additionally, the primary p-type semiconductor used for sensitized hole injection, NiO, has inherent problems (lower electrical conductivity, lower hole mobility, and band edge potentials which are relatively incompatible with mediator species) not present for the TiO₂ used with sensitized electron injection.²⁵

As a consequence of the large body of literature on Cr(III) polypyridyl complexes, their photophysical behavior is well understood. Absorption of a photon excites the complex from the ⁴A ground state to a high energy ⁴T excited state, which undergoes rapid internal conversion (IC) to a lower energy ⁴T excited state. This is followed by intersystem crossing (ISC) from the ⁴T state to a ²E state as shown in Figure 1.2.^{20e}

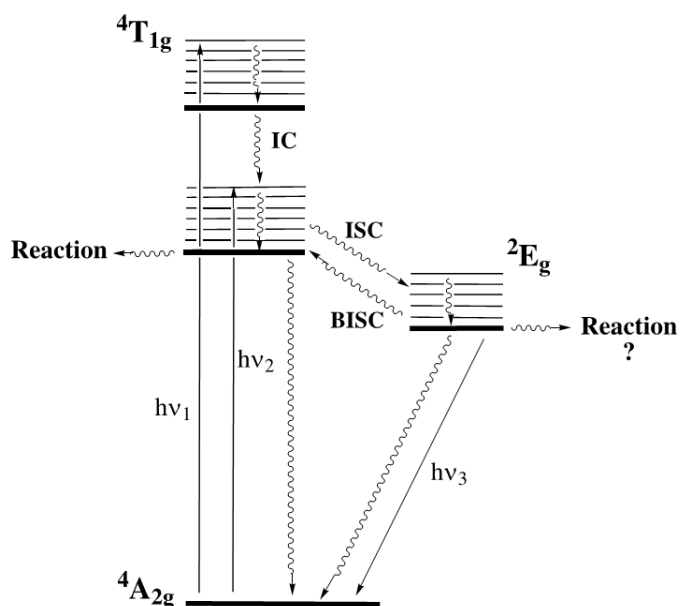


Figure 1.2. Simplified Jablonski diagram for an octahedral Cr(III) complex. Adapted from Ref. 20e.

In polypyridyl Cr(III) complexes back intersystem crossing (BISC) is generally not favored, resulting in long lived excited states with lifetimes on the hundreds of μs range.^{20b} The doublet excited state decays back to the quartet ground state via phosphorescence, denoted as $h\nu_3$ in Figure 1.2. The energy of the emission band varies little across different polypyridine ligand sets and is typically ~ 1.7 eV.

While these excited state processes enhance the prospect of charge injection in a sensitizer-wide band gap hybrid material, Cr(III) polypyridyls are hampered by a significant weakness. These complexes have small molar absorptivities at $\lambda > 450$ nm,^{20b} which makes them less suitable for visible light sensitizers. However, the iminopyridine complex $[\text{Cr}(\text{tren}(\text{py})_3)](\text{ClO}_4)_3$ was reported as ‘wine red’,²⁶ indicating that changes in the ligand set could improve visible light absorption. Compared to polypyridyl complexes, there is little information on excited state processes in iminopyridine type complexes. Work by McCusker on the photophysical behavior of $[\text{Fe}(\text{tren}(\text{py})_3)]^{2+}$ is one of the few reported examples.²⁷

While there is a dearth of information on the excited state behavior of iminopyridine complexes, their redox behavior is relatively well documented. Iminopyridines have been shown to easily take up reducing equivalents added to transition-metal²⁸ and main-group metal²⁹ complexes. In particular, there has been much recent work by Wieghardt and coworkers looking at Cr–ligand radical complexes involving iminopyridine and polypyridyl ligands.^{12a,12c-e,28c} This redox non-innocence opens the door to potential uses as electron reservoirs which can be tapped to facilitate difficult, multielectron chemical processes.

1.4 Outline of Dissertation Chapters

The following chapters include work featuring polypyridyl and iminopyridine ligands, and focus on the synthesis and characterization of first row transition metal complexes. Chapter 2 describes the synthesis, characterization and computational analysis of a series of divalent tripodal hexadentate iminopyridine complexes of first row transition metals and has been submitted to *Inorganic Chemistry*.³⁰ Chapter 3 describes the synthesis, anion binding properties, and spin-state switching abilities in solution of Fe(II) iminopyridine complexes which feature hydrogen bonding moieties. The initial work described on $\text{L}^{6-\text{OH}}$ complexes was elaborated by Christina Klug which resulted in publication in *Dalton*

Transactions.^{19d} The work on L^5 complexes has been submitted to *European Journal of Inorganic Chemistry*.³¹ Chapter 4 describes the synthesis, ground state and excited state characterization of heteroleptic Cr(III) polypyridyl complexes and has been published in *Inorganic Chemistry*.³² Chapter 5 describes the synthesis, ground state and excited state characterization, and computational analysis of tripodal hexadentate and tris(bidentate) iminopyridine Cr(III) complexes and has been submitted to *Inorganic Chemistry*.³³ Chapter 6 describes the synthesis and characterization of “Cr(II)” and “Cr(I)” iminopyridine and polypyridyl complexes. Chapter 7 contains some final remarks about the previous five chapters and has suggestions for future work in light of what was learned while conducting the research for this thesis.

1.5 References

1. Larsen, E.; LaMar, G. N.; Wagner, B. E.; Parks, J. E.; Holm, R. H. *Inorg. Chem.* **1972**, *11*, 2652-2668.
2. (a) Britovsek, G. J. P.; Cohen, S. A.; Gibson, V. C.; Maddox, P. J.; Van, M. M. *Angew. Chem., Int. Ed.* **2002**, *41*, 489-491; (b) Chen, Y.; Chen, R.; Qian, C.; Dong, X.; Sun, J. *Organometallics* **2003**, *22*, 4312-4321; (c) Chen, Y.; Qian, C.; Sun, J. *Organometallics* **2003**, *22*, 1231-1236; (d) Barabanov, A. A.; Bukatov, G. D.; Zakharov, V. A.; Semikolenova, N. V.; Echevskaja, L. G.; Matsko, M. A. *Macromol. Chem. Phys.* **2005**, *206*, 2292-2298; (e) Gibson, V. C.; Long, N. J.; Oxford, P. J.; White, A. J. P.; Williams, D. J. *Organometallics* **2006**, *25*, 1932-1939; (f) Zhang, S.; Vystorop, I.; Tang, Z.; Sun, W.-H. *Organometallics* **2007**, *26*, 2456-2460; (g) Ionkin, A. S.; Marshall, W. J.; Adelman, D. J.; Bobik, F. B.; Fish, B. M.; Schiffhauer, M. F. *Organometallics* **2008**, *27*, 1902-1911; (h) Raucoules, R.; de, B. T.; Raybaud, P.; Adamo, C. *Organometallics* **2008**, *27*, 3368-3377; (i) Cruz, V. L.; Ramos, J.; Martinez-Salazar, J.; Gutierrez-Oliva, S.; Toro-Labbe, A. *Organometallics* **2009**, *28*, 5889-5895.
3. (a) Margl, P.; Deng, L.; Ziegler, T. *Organometallics* **1999**, *18*, 5701-5708; (b) Gibson, V. C.; Tellmann, K. P.; Humphries, M. J.; Wass, D. F. *Chem. Commun.* **2002**, 2316-2317; (c) Bianchini, C.; Mantovani, G.; Meli, A.; Migliacci, F.; Laschi, F. *Organometallics* **2003**, *22*, 2545-2547; (d) Bianchini, C.; Giambastiani, G.; Mantovani, G.; Meli, A.; Mimeo, D. *J. Organomet. Chem.* **2004**, *689*, 1356-1361; (e) Bianchini, C.; Gatteschi, D.; Giambastiani, G.; Rios, I. G.; Ienco, A.; Laschi, F.; Mealli, C.; Meli, A.; Sorace, L.; Toti, A.; Vizza, F. *Organometallics* **2007**, *26*, 726-739; (f) Su, B.-Y.; Zhao, J.-S.; Gao, Q.-C. *Chin. J. Chem.* **2007**, *25*, 121-124; (g) Sun, W.-H.; Hao, P.; Li, G.; Zhang, S.; Wang, W.; Yi, J.; Asma, M.; Tang, N. *J. Organomet. Chem.* **2007**, *692*, 4506-4518; (h) Toti, A.; Giambastiani, G.; Bianchini, C.; Meli, A.; Luconi, L. *Adv. Synth. Catal.* **2008**, *350*, 1855-1866; (i) Zhang, X.; Duan, B.; Sun, W.; Hsu, S. L.; Yang, X. *Sci. China, Ser. B: Chem.* **2009**, *52*, 48-55; (j) Hojilla, A. C. C.; Milsmann, C.; Lobkovsky, E.; Chirik, P. J. *Angew. Chem., Int. Ed.* **2011**, *50*, 8143-8147; (k) Damavandi, S.; Zohuri, G. H.; Sandaroods, R.; Ahmadjo, S. *J. Polym. Res.* **2012**, *19*, 1-5.
4. (a) Benito, J. M.; de Jesus, E.; de la Mata, F. J.; Flores, J. C.; Gomez, R.; Gomez-Sal, P. *Organometallics* **2006**, *25*, 3876-3887; (b) Zhang, S.; Wang, H.; Yang, J. *Chem.: Indian J.* **2006**, *3*, 190-196; (c) Zhang, S.; Wang, H.; Yang, J. *Chem.: Indian J.* **2006**, *3*, 54-60; (d) Adewuyi, S.; Li, G.; Zhang, S.; Wang, W.; Hao, P.; Sun, W.-H.; Tang, N.; Yi, J. *J. Organomet. Chem.* **2007**, *692*, 3532-3541; (e) Brasse, M.; Campora, J.; Palma, P.; Alvarez, E.; Cruz, V.; Ramos, J.; Reyes, M. L. *Organometallics* **2008**, *27*, 4711-4723; (f) Pelletier, J. D. A.; Fawcett, J.; Singh, K.; Solan, G. A. *J. Organomet. Chem.* **2008**, *693*, 2723-2731; (g) Zhang, W.; Wang, Y.; Yu, J.; Redshaw, C.; Hao, X.; Sun, W.-H. *Dalton Trans.* **2011**, *40*, 12856-12865; (h) Antonov, A. A.; Semikolenova, N. V.; Zakharov, V. A.; Zhang, W.; Wang, Y.; Sun, W.-H.; Talsi, E. P.; Bryliakov, K. P. *Organometallics* **2012**, *31*, 1143-1149.
5. (a) Blay, G.; Climent, E.; Fernandez, I.; Hernandez-Olmos, V.; Pedro, J. R. *Tetrahedron: Asymmetry* **2006**, *17*, 2046-2049; (b) Blay, G.; Climent, E.; Fernandez, I.; Hernandez-Olmos, V.; Pedro, J. R. *Tetrahedron: Asymmetry* **2007**, *18*, 1603-1612; (c) Blay, G.; Hernandez-Olmos, V.; Pedro, J. R. *Org. Biomol. Chem.* **2008**, *6*, 468-476; (d) Blay, G.; Hernandez-Olmos, V.; Pedro, J. R. *Synlett* **2011**, 1195-1211; (e) Palomo, C.; Oiarbide, M.; Laso, A. *Eur. J. Org. Chem.* **2007**, 2561-2574.

6. (a) Scott, J. L.; Gambarotta, S.; American Chemical Society: 2004, p GEN-359; (b) Vidyaratne, I.; Gambarotta, S.; Korobkov, I.; Budzelaar, P. H. M. *Inorg. Chem.* **2005**, *44*, 1187-1189; (c) Bart, S. C.; Lobkovsky, E.; Bill, E.; Chirik, P. J. *J. Am. Chem. Soc.* **2006**, *128*, 5302-5303; (d) Scott, J.; Vidyaratne, I.; Korobkov, I.; Gambarotta, S.; Budzelaar, P. H. M. *Inorg. Chem.* **2008**, *47*, 896-911; (e) Tondreau, A. M.; Lobkovsky, E.; Chirik, P. J. *Org. Lett.* **2008**, *10*, 2789-2792; (f) Russell, S. K.; Lobkovsky, E.; Chirik, P. J. *J. Am. Chem. Soc.* **2009**, *131*, 36-37; (g) Sylvester, K. T.; Chirik, P. J. *J. Am. Chem. Soc.* **2009**, *131*, 8772-8774; (h) Bowman, A. C.; Milsmann, C.; Bill, E.; Lobkovsky, E.; Weyhermüller, T.; Wieghardt, K.; Chirik, P. J. *Inorg. Chem.* **2010**, *49*, 6110-6123; (i) Russell, S. K.; Lobkovsky, E.; Chirik, P. J. *J. Am. Chem. Soc.* **2011**, *133*, 8858-8861; (j) Darmon, J. M.; Turner, Z. R.; Lobkovsky, E.; Chirik, P. J. *Organometallics* **2012**, *31*, 2275-2285.
7. (a) Cambi, L.; Gagnasso, A. *Atti. Accad. Naz. Lincei* **1931**, *13*, 809; (b) Gütllich, P.; Hauser, A.; Spiering, H. *Angew. Chem., Int. Ed. Engl.* **1994**, *33*, 2024-2054.
8. Gütllich, P.; Garcia, Y.; Goodwin, H. A. *Chem. Soc. Rev.* **2000**, *29*, 419-427.
9. Burnett, M. G.; McKee, V.; Nelson, S. M. *J. Chem. Soc., Dalton Trans.* **1981**, 1492-1497.
10. Ni, Z.; Shores, M. P. *J. Am. Chem. Soc.* **2008**, *131*, 32-33.
11. (a) Ni, Z.; McDaniel, A. M.; Shores, M. P. *Chem. Sci.* **2010**, *1*, 615-621; (b) Ni, Z.; Shores, M. P. *Inorg. Chem.* **2010**, *49*, 10727-10735; (c) Ni, Z.; Fiedler, S. R.; Shores, M. P. *Dalton Trans.* **2011**, *40*, 944-950.
12. (a) Lu, C. C.; Bill, E.; Weyhermüller, T.; Bothe, E.; Wieghardt, K. *J. Am. Chem. Soc.* **2008**, *130*, 3181-3197; (b) Banerjee, P.; Sproules, S.; Weyhermüller, T.; DeBeer George, S.; Wieghardt, K. *Inorg. Chem.* **2009**, *48*, 5829-5847; (c) Scarborough, C. C.; Sproules, S.; Weyhermüller, T.; DeBeer, S.; Wieghardt, K. *Inorg. Chem.* **2011**, *50*, 12446-12462; (d) Scarborough, C. C.; Lancaster, K. M.; DeBeer, S.; Weyhermüller, T.; Sproules, S.; Wieghardt, K. *Inorg. Chem.* **2012**, *51*, 3718-3732; (e) Scarborough, C. C.; Sproules, S.; Doonan, C. J.; Hagen, K. S.; Weyhermüller, T.; Wieghardt, K. *Inorg. Chem.* **2012**, *51*, 6969-6982.
13. Garcia, Y.; Gütllich, P.; Gütllich, P., Goodwin, H. A., Eds.; Springer Berlin / Heidelberg: 2004; Vol. 234, p 786-786.
14. (a) Sim, P. G.; Sinn, E. *J. Am. Chem. Soc.* **1981**, *103*, 241-243; (b) Wang, S.; Ferbinteanu, M.; Marinescu, C.; Dobrinescu, A.; Ling, Q.-D.; Huang, W. *Inorg. Chem.* **2010**, *49*, 9839-9851; (c) Morgan, G. G.; Murnaghan, K. D.; Müller-Bunz, H.; McKee, V.; Harding, C. J. *Angew. Chem., Int. Ed.* **2006**, *45*, 7192-7195; (d) Pandurangan, K.; Gildea, B.; Murray, C.; Harding, C. J.; Müller-Bunz, H.; Morgan, G. G. *Chem. – Eur. J.* **2012**, *18*, 2021-2029.
15. van Koningsbruggen, P. J.; Maeda, Y.; Oshio, H.; Gütllich, P., Goodwin, H. A., Eds.; Springer Berlin / Heidelberg: 2004; Vol. 233, p 259-324.
16. Goodwin, H. A.; Gütllich, P., Goodwin, H. A., Eds.; Springer Berlin / Heidelberg: 2004; Vol. 234, p 786-786.
17. Mueller, E. W.; Spiering, H.; Gütllich, P. *Inorg. Chem.* **1984**, *23*, 119-120.

18. (a) Goodwin, H. A.; Gütllich, P., Goodwin, H. A., Eds.; Springer Berlin / Heidelberg: 2004; Vol. 233, p 59-90; (b) Halcrow, M. A. *Polyhedron* **2007**, *26*, 3523-3576.
19. (a) Hoselton, M. A.; Wilson, L. J.; Drago, R. S. *J. Am. Chem. Soc.* **1975**, *97*, 1722-1729; (b) Wilson, L. J.; Georges, D.; Hoselton, M. A. *Inorg. Chem.* **1975**, *14*, 2968-2975; (c) Kirchner, R. M.; Mealli, C.; Bailey, M.; Howe, N.; Torre, L. P.; Wilson, L. J.; Andrews, L. C.; Rose, N. J.; Lingafelter, E. C. *Coord. Chem. Rev.* **1987**, *77*, 89-163; (d) Klug, C. M.; McDaniel, A. M.; Fiedler, S. R.; Schulte, K. A.; Newell, B. S.; Shores, M. P. *Dalton Trans.* **2012**, *41*, 12577-12585; (e) Toftlund, H.; McGarvey, J. J.; Gütllich, P., Goodwin, H. A., Eds.; Springer Berlin / Heidelberg: 2004; Vol. 233, p 151-166.
20. (a) Serpone, N.; Jamieson, M. A.; Henry, M. S.; Hoffman, M. Z.; Bolletta, F.; Maestri, M. *J. Am. Chem. Soc.* **1979**, *101*, 2907-2916; (b) Jamieson, M. A.; Serpone, N.; Hoffman, M. Z. *Coord. Chem. Rev.* **1981**, *39*, 121-179; (c) Serpone, N.; Jamieson, M. A.; Sriram, R.; Hoffman, M. Z. *Inorg. Chem.* **1981**, *20*, 3983-3988; (d) Kirk, A. D. *Chem. Rev.* **1999**, *99*, 1607-1640; (e) Kane-Maguire, N. In *Photochemistry and Photophysics of Coordination Compounds I* 2007, p 37-67; (f) Forster, L. S. *Chem. Rev.* **1990**, *90*, 331-353.
21. (a) Juris, A.; Balzani, V.; Barigelletti, F.; Campagna, S.; Belser, P.; Vonzelewsky, A. *Coord. Chem. Rev.* **1988**, *84*, 85-277; (b) Anderson, N. A.; Lian, T. *Coord. Chem. Rev.* **2004**, *248*, 1231-1246; (c) Polo, A. S.; Itokazu, M. K.; Iha, N. Y. M. *Coord. Chem. Rev.* **2004**, *248*, 1343-1361; (d) McCusker, J. K. *Acc. Chem. Res.* **2003**, *36*, 876-887.
22. (a) Grätzel, M. *J. Photochem. Photobiol., C* **2003**, *4*, 145-153; (b) Grätzel, M. *Inorg. Chem.* **2005**, *44*, 6841-6851; (c) Hagfeldt, A.; Grätzel, M. *Acc. Chem. Res.* **2000**, *33*, 269-277; (d) Schwarzburg, K.; Ernstorfer, R.; Felber, S.; Willig, F. *Coord. Chem. Rev.* **2004**, *248*, 1259-1270; (e) Kalaigan, G.; Kang, Y. *J. Photochem. Photobiol., C* **2006**, *7*, 17-22; (f) Robertson, N. *Angew. Chem., Int. Ed. Engl.* **2006**, *45*, 2338-2345; (g) Nazeeruddin, M.; Grätzel, M. In *Photofunctional Transition Metal Complexes* 2007, p 113-175; (h) Neil, R. *ChemSusChem* **2008**, *1*, 977-979; (i) Robertson, N. *Angew. Chem., Int. Ed. Engl.* **2008**, *47*, 1012-1014; (j) Grätzel, M. *Acc. Chem. Res.* **2009**, *42*, 1788-1798; (k) Hagfeldt, A.; Boschloo, G.; Sun, L.; Kloo, L.; Pettersson, H. *Chem. Rev.* **2010**, *110*, 6595-6663.
23. O'Regan, B.; Grätzel, M. *Nature* **1991**, *353*, 737-740.
24. (a) Hoffman, M. Z.; Serpone, N. *Isr. J. Chem.* **1982**, *22*, 91-97; (b) Ballardini, R.; Varani, G.; Indelli, M. T.; Scandola, F.; Balzani, V. *J. Am. Chem. Soc.* **1978**, *100*, 7219-7223.
25. (a) Odobel, F.; Le Pleux, L.; Pellegrin, Y.; Blart, E. *Acc. Chem. Res.* **2010**, *43*, 1063-1071; (b) He, J.; Lindström, H.; Hagfeldt, A.; Lindquist, S.-E. *Sol. Energy Mater. Sol. Cells* **2000**, *62*, 265-273.
26. McLachlan, G. A.; Fallon, G. D.; Spiccia, L. *Acta Crystallogr., Sect. C: Cryst. Struct. Commun.* **1996**, *52*, 309-312.
27. (a) Monat, J. E.; McCusker, J. K. *J. Am. Chem. Soc.* **2000**, *122*, 4092-4097; (b) Juban, E. A.; Smeigh, A. L.; Monat, J. E.; McCusker, J. K. *Coord. Chem. Rev.* **2006**, *250*, 1783-1791.
28. (a) Budzelaar, P. H. M.; de Bruin, B.; Gal, A. W.; Wieghardt, K.; van Lenthe, J. H. *Inorg. Chem.* **2001**, *40*, 4649-4655; (b) Knijnenburg, Q.; Hettterscheid, D.; Kooistra, T. M.; Budzelaar, Peter H. M. *Eur. J. Inorg. Chem.* **2004**, *2004*, 1204-1211; (c) Lu, C. C.; DeBeer, G. S.; Weyhermueller,

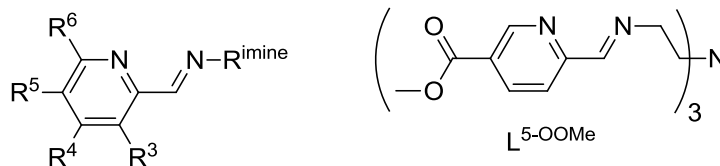
- T.; Bill, E.; Bother, E.; Wieghardt, K. *Angew. Chem., Int. Ed.* **2008**, *47*, 6384-6387; (d) Lu, C. C.; Weyhermueller, T.; Bill, E.; Wieghardt, K. *Inorg. Chem.* **2009**, *48*, 6055-6064; (e) van, G. M.; Lu, C. C.; Wieghardt, K.; Lubitz, W. *Inorg. Chem.* **2009**, *48*, 2626-2632; (f) Wile, B. M.; Trovitch, R. J.; Bart, S. C.; Tondreau, A. M.; Lobkovsky, E.; Milsman, C.; Bill, E.; Wieghardt, K.; Chirik, P. J. *Inorg. Chem.* **2009**, *48*, 4190-4200; (g) Russell, S. K.; Bowman, A. C.; Lobkovsky, E.; Wieghardt, K.; Chirik, P. J. *Eur. J. Inorg. Chem.* **2012**, *2012*, 535-545.
29. (a) Myers, T. W.; Kazem, N.; Stoll, S.; Britt, R. D.; Shanmugam, M.; Berben, L. A. *J. Am. Chem. Soc.* **2011**, *133*, 8662-8672; (b) Kowolik, K.; Shanmugam, M.; Myers, T. W.; Cates, C. D.; Berben, L. A. *Dalton Trans.* **2012**; (c) Myers, T. W.; Berben, L. A. *J. Am. Chem. Soc.* **2011**, *133*, 11865-11867.
30. McDaniel, A. M.; Rappé, A. K.; Shores, M. P., *Submitted to Inorg. Chem.*
31. McDaniel, A. M.; Shores, M. P., *Submitted to Eur. J. Inorg. Chem.*
32. McDaniel, A. M.; Tseng, H.-W.; Damrauer, N. H.; Shores, M. P. *Inorg. Chem.* **2010**, *49*, 7981-7991.
33. McDaniel, A. M.; Tseng, H.-W.; Hill, E. A.; Damrauer, N. H.; Rappé, A. K.; Shores, M. P., *Submitted to Inorg. Chem.*

Chapter 2. Structural and Electronic Comparison of 1st Row Transition Metal Complexes of a Tripodal Iminopyridine Ligand

Reproduced with permission from *Inorganic Chemistry*, submitted for publication. Unpublished work copyright 2012 American Chemical Society.

2.1 Introduction

Iminopyridine ligands generate interesting chemistry when bound to a wide variety of metal ions. These types of ligands can engender unique magnetic properties such as frameworks which support spin-crossover with Fe(II),¹ and can promote unusual and novel reactivity in other first row transition metals. Complexes with iminopyridine ligands have been studied as polymerization catalysts,² dinitrogen activators,³ water reduction catalysts⁴, and reservoirs for electrons (i.e. non-innocent ligands).⁵



Scheme 2.1. Example iminopyridine ligands. Left: Generalized example of an iminopyridine ligand. Functionalization at R⁵ can be used to attach the ligand to substrates. Functionalization at R⁶ can be used to favor high-spin states in Fe(II) complexes. Alteration of R^{imine} can affect coordination geometry. Right: the tripodal ligand L^{5-OOMe} studied in this work.

We are particularly interested in *tripodal* iminopyridine ligands, which may support novel magnetic and/or electronic properties in first-row transition-metal complexes. In principle, such a multidentate ligand set should improve solution stability, provide steric and electronic tunability, and offer coordination modes for anisotropic interfacing of the complex with its environment. To illustrate, efforts to demonstrate anion-dependent spin-state switching or solar photo-conversion require that substitutionally labile species (e.g. high-spin Fe(II), Cr(II), excited states of Cr(III)) be corralled in solution.⁶

More specifically, the coordination environments and chemical properties of tren-based tripodal iminopyridine ligands have been a subject of previous studies.^{1a,7} These scaffolds have seven potential metal-binding sites for chelation, are flexible enough to support different coordination modes depending on the metal center, and tend to be amenable to modular synthetic schemes. Minor alterations in ligand functionalization can produce substantial changes in the coordination environment of the chelated metal. The ability of the tripodal ligand to twist about the M–N_{tether} three-fold axis can give rise to coordination modes ranging from trigonal antiprismatic (locally octahedral) to trigonal prismatic geometries. Previously reported tren-based tripodal iminopyridine complexes tend toward trigonal antiprismatic geometries.^{7a}

Along with variation in the trigonal twist angle, functional groups appended to the pyridine moiety can alter the metal coordination environment. The steric bulk of groups at the 6 position hinders close approach of the pyridine N to the metal center, causing the M–N bonds to lengthen as compared to the unfunctionalized complexes. This is of particular importance in the case of Fe(II), where longer M–N bonds favor the high-spin state over the low-spin state.⁸ Structural variations of this nature can lead to dramatic changes in the compounds' physical, chemical and magnetic properties.^{8b,9}

One avenue of potential property perturbation that has not been widely explored is the modification of ligand electronics by addition of functional groups that do not sterically interact with the bound metal center. Focusing on iminopyridine-type ligands,¹⁰ aside from methyl incorporation at various points on the pyridine,^{7a} the only other type of functionalization that has been explored for tren-based iminopyridine ligands has been inclusion of long chain alkyl groups at the 5-position to produce metallomesogens.¹¹ These types of functionalizations typically alter the way molecules pack, but do not seem to impart significant effects on the complexes' electronics.

In this work, we probe how incorporation of an electron-withdrawing substituent on a tren-based iminopyridine ligand affects the structural and electronic properties of divalent metal complexes. The impetus for this research is to tune complex electronic structure for possible exploitation in solar photoconversion (Cr, Zn) and spin-crossover (Cr, Mn, Fe, Co) applications. In addition, changes in ion

size and d electron count across the 1st transition series may reasonably be expected to offer several coordination modes, highlighting the ligand's structural flexibility. To study how electronic alterations to the ligand affect properties, we selected an ester functionalization at the 5-position of the pyridine. The ester acts as an electron withdrawing group and can significantly affect the electronics of the ligand and its resulting complexes in [Cr(polypyridine)₃]³⁺ analogues.^{6b} In addition to its electron withdrawing properties, the ester group provides: (a) precursors for anchoring complexes to semiconductor substrates,¹² directly related to our ongoing studies in solar photoconversion;^{6b} and (b) convenient entry points to access other types of functionalization, including potential anion binding sites, which may be used to influence spin-crossover in solution and in the solid-state.^{6a,13}

Here we present a comparison of the properties of new [M(L^{5-OOMe})]²⁺ complexes, where L^{5-OOMe} is trimethyl-6,6',6''-((1E,1'E,1"E)-((nitrilotris(ethane-2,1-diyl))tris(azanylylidene))tris(methanylylidene))trinicotinate, and M = Cr, Mn, Fe, Co, Ni, Cu, Zn. We observe coordination flexibility throughout the 3d series as well as interesting behavior in the [Cr(L^{5-OOMe})]²⁺ complex, which differs significantly from the rest of the complexes studied.

2.2 Division of Labor

All DFT calculations, interpretation of DFT data, and spectra simulations were performed by Prof. Anthony Rappé. All syntheses and experimental characterization were done by Ashley McDaniel.

2.3 Experimental Section

2.3.1 Preparation of Compounds. Unless otherwise noted, compound manipulations were performed either inside a dinitrogen-filled glovebox (MBRAUN Labmaster 130) or via Schlenk techniques on an inert gas (N₂) manifold. The preparations of dimethylpyridine-2,5-dicarboxylate,¹⁴ methyl 6-(hydroxymethyl)nicotinate,¹⁵ [Cr(CH₃CN)₄(BF₄)₂],¹⁶ and Fe(CF₃SO₃)₂·2CH₃CN¹⁷ have been described elsewhere. Methyl-6-formylnicotinate was synthesized according to a modified literature procedure,¹⁸ where methyl 6-(hydroxymethyl)nicotinate was substituted as the oxidation substrate.

Pentane was distilled over sodium metal and subjected to three freeze-pump-thaw cycles. Other solvents were sparged with dinitrogen, passed over molecular sieves, and degassed prior to use. All other reagents were obtained from commercial sources and were used without further purification.

Caution! While we have not encountered any difficulties with compounds **2.4** and **2.5** at the 90 to 115 mg scales described here, perchlorate-containing compounds pose an explosion hazard, and should be handled with care and only in small quantities.

Trimethyl-6,6',6''-((1E,1'E,1''E)-((nitrilotris(ethane-2,1-diyl))tris(azanylylidene))tris(methanylylidene))trinicotinate (L^{5-OOMe}). A solution of tren (0.05 g, 0.36 mmol) in 3 mL of anhydrous methanol was added to a solution of methyl-6-formylnicotinate (0.21 g, 1.25 mmol) in 5 mL of anhydrous methanol; the resulting solution was stirred at room temperature. Within 10 minutes, a white precipitate formed; the mixture was stirred for an additional 2 h. The solid was isolated by filtration, washed with anhydrous methanol (3×2 mL) and diethyl ether (3×2 mL) and dried in vacuo to afford 0.17 g (79%) of product. 1H NMR ($CDCl_3$): 3.00 (6H, t), 3.80 (6H, t), 3.97 (9H, s) 7.97 (3H, d), 8.27 (3H, dd). 8.35 (3H, s), 9.16 ppm (3H, d). ^{13}C NMR ($CDCl_3$): 52.71, 55.29, 60.18, 120.84, 126.64, 137.77, 150.81, 157.80, 162.26, 165.67 ppm. IR (KBr pellet): $\nu_{C=O}$ 1723, $\nu_{C=N}$ 1646 cm^{-1} . Absorption spectrum (CH_3CN): λ_{max} 203, 245, 256 (sh), 279 nm. HRES+MS (CH_3OH): m/z 588.2580 ($L^{5-OOMe+H}$) $^+$, 610.2395 ($L^{5-OOMe+Na}$) $^+$.

$[Cr(L^{5-OOMe})](BF_4)_2$ (2.1**)**. A solution of $[Cr(MeCN)_4(BF_4)_2]$ (0.132 g, 0.340 mmol) in 5 mL of acetonitrile was added to a suspension of L^{5-OOMe} (0.200 g, 0.340 mmol) in 8 mL of acetonitrile. The resulting dark-brown solution was stirred at room temperature for 16 h. After concentrating the solvent in vacuo to ~ 2 mL, the addition of 20 mL of diethyl ether produced a dark brown precipitate. The powder was collected by filtration, washed with diethyl ether (3×4 mL) and pentane (3×2 mL), and dried in vacuo to afford 0.225 g (81%) of product. IR (KBr pellet): $\nu_{C=O}$ 1733, $\nu_{C=N}$ 1603 cm^{-1} . Absorption spectrum (MeCN): λ_{max} (ϵ_M) 199 (53000), 228 (31000, sh), 290 (20000), 478 (3500), 586 (1600, sh), 738 (1200), 1068 nm ($1900 M^{-1}cm^{-1}$). μ_{eff} (295 K): 3.40 μ_B . μ_{eff} (5 K): 2.83 μ_B . ES+MS (MeCN): m/z 319.73 ($[Cr(L^{5-OOMe})]^{2+}$). Anal. Calcd. for $C_{30}H_{33}B_2CrF_8N_7O_6$: C, 44.31; H, 4.09; N, 12.06. Found: C, 44.22; H,

4.38; N, 12.35. Crystals of **2.1**·CH₃OH suitable for X-ray analysis were obtained by slow diffusion of diethyl ether into a methanolic solution of the compound.

[Mn(L^{5-OOme})](CF₃SO₃)₂ (2.2**). A solution of Mn(CF₃SO₃)₂ (0.06 g, 0.17 mmol) in 3 mL of methanol was added to a suspension of L^{5-OOme} (0.10 g, 0.17 mmol) in 5 mL of methanol. The resulting light yellow solution was stirred at room temperature for 16 h. After concentrating the solvent in vacuo to ~2 mL, the addition of 20 mL of diethyl ether produced a yellow precipitate. The powder was collected by filtration, washed with diethyl ether (3 × 2 mL) and dried in vacuo to afford 0.143 g (89%) of product. IR (KBr pellet): $\nu_{C=O}$ 1733, $\nu_{C=N}$ 1601 cm⁻¹. Absorption spectrum (MeCN): λ_{max} (ϵ_M) 195 (58000), 239 (35000), 280 (26000, sh), 287 (31000), 297 (25000, sh), 342 nm (850 M⁻¹cm⁻¹). μ_{eff} (295 K): 6.46 μ_B . μ_{eff} (5 K): 6.01 μ_B . ES+MS (MeCN): m/z 791.20 ([Mn(L^{5-OOme})(CF₃SO₃)₂]⁺). Anal. Calcd. for C₃₂H₃₃F₆MnN₇O₁₂S₂: C, 40.86; H, 3.54; N, 10.42. Found: C, 40.72; H, 3.26; N, 10.42. Crystals of **2.2** suitable for X-ray analysis were obtained by slow diffusion of diethyl ether into an acetonitrile solution of the compound.**

[Fe(L^{5-OOme})](CF₃SO₃)₂ (2.3**). A solution of Fe(CF₃SO₃)₂·2CH₃CN (0.045 g, 0.102 mmol) in 3 mL of acetonitrile was added to a suspension of L^{5-OOme} (0.060 g, 0.102 mmol) in 5 mL of acetonitrile. The resulting dark purple solution was stirred for 16 h. After concentrating the solvent in vacuo to ~2 mL, the addition of 20 mL of diethyl ether produced a purple-black precipitate. The powder was collected by filtration, washed with diethyl ether (3 × 2 mL) and pentane (3 × 2 mL), and dried in vacuo to afford 0.082 g (85%) of product. IR (KBr pellet): $\nu_{C=O}$ 1731, $\nu_{C=N}$ 1601 cm⁻¹. Absorption spectrum (MeCN): λ_{max} (ϵ_M) 200 (66000), 239 (26000), 281 (40000), 289 (36000, sh), 382 (570), 540 (760, sh), 594 nm (1160 M⁻¹cm⁻¹). ¹H NMR (CD₃CN): 9.67 (br s, 3H); 8.66 (dd, 3H); 8.48 (dd, 3H); 7.74 (br s, 3H); 3.96 (br m, 6H); 3.81 (s, 9H); 3.19 (m, 6H). μ_{eff} (295 K): 0.94 μ_B . ES+MS (MeCN): m/z 792.13 ([Fe(L^{5-OOme})(CF₃SO₃)₂]⁺), 321.73 ([Fe(L^{5-OOme})₂]²⁺). Anal. Calcd. for C₃₂H₃₃F₆FeN₇O₁₂S₂: C, 40.82; H, 3.53; N, 10.41. Found: C, 40.58; H, 3.25; N, 10.47. Crystals of **2.3**·0.62 Et₂O suitable for X-ray analysis were obtained by slow diffusion of diethyl ether into an acetonitrile solution of the compound.**

[Co(L^{5-00Me})](ClO₄)₂ (2.4). A solution of Co(ClO₄)₂·6H₂O (0.044 g, 0.119 mmol) in 3 mL of methanol was added to a stirring suspension of L^{5-00Me} (0.070 g, 0.119 mmol) in 5 mL of methanol. Within 10 minutes, an orange precipitate formed; the mixture was stirred for 16 h. The solid was collected by filtration, washed with methanol (3 × 3 mL) and diethyl ether (3 × 2 mL), and dried in vacuo to afford 0.091 g (91%) of product. IR (KBr pellet): $\nu_{\text{C=O}}$ 1719, $\nu_{\text{C=N}}$ 1603 cm⁻¹. Absorption spectrum (MeCN): λ_{max} (ϵ_{M}) 194 (61400), 239 (33000), 285 (29200), 385 nm (3100 M⁻¹cm⁻¹). μ_{eff} (295 K): 4.38 μ_{B} . μ_{eff} (5 K): 4.15 μ_{B} . ES+MS (MeCN): m/z 745.13 ([Co(L^{5-00Me})(ClO₄)]⁺). Anal. Calcd. for C₃₀H₃₃Cl₂CoN₇O₁₄: C, 42.62; H, 3.93; N, 11.60. Found: C, 42.66; H, 3.98; N, 11.49. Crystalline material can be obtained by slow diffusion of diethyl ether into an acetonitrile solution of the compound, but the crystals were not suitable for X-ray analysis.

[Co(L^{5-00Me})]CoCl₄ (2.4a). A solution of CoCl₂ (0.021 g, 0.17mmol) in 3 mL of methanol was added to a stirring suspension of L^{5-00Me} (0.100 g, 0.17 mmol) in 5 mL of methanol. Initially an orange solution formed; it was stirred for an additional 16 h, whereupon the color slowly turned brown-green. A brown-green powder was precipitated by addition of diethyl ether. The solid was collected by filtration, washed with diethyl ether (3 × 2 mL), and recrystallized by diethyl ether diffusion into methanol to yield green crystals of the product. IR (KBr pellet): $\nu_{\text{C=O}}$ 1727, $\nu_{\text{C=N}}$ 1600 cm⁻¹. Absorption spectrum (MeCN): λ_{max} 194, 239, 285, 385, 616 nm. ES+MS (MeCN): m/z 681.07 ([Co(L^{5-00Me})(Cl)]⁺), 323.13 ([Co(L^{5-00Me})]²⁺).

[Ni(L^{5-00Me})](ClO₄)₂ (2.5). A solution of Ni(ClO₄)₂·6H₂O (0.065 g, 0.177 mmol) in 3 mL of methanol was added to a stirring suspension of L^{5-00Me} (0.105 g, 0.177 mmol) in 5 mL of methanol. In the first 10 minutes, an orange precipitate forms and the mixture is allowed to stir for 16 h. The solid was collected by filtration, washed with methanol (3 × 3 mL) and diethyl ether (3 × 2 mL), and dried in vacuo to afford 0.13 g (87%) of product. IR (KBr pellet): $\nu_{\text{C=O}}$ 1723, $\nu_{\text{C=N}}$ 1604 cm⁻¹. Absorption spectrum (MeCN): λ_{max} (ϵ_{M}) 199 (65000), 239 (33000), 284 (28000), 396 (1500), 866 nm (9.8 M⁻¹cm⁻¹). μ_{eff} (295K): 3.44 μ_{B} . ES+MS (MeCN): m/z 744.20 ([Ni(L^{5-00Me})(ClO₄)]⁺), 322.73 ([Ni(L^{5-00Me})]²⁺). Anal.

Calcd. for $C_{30}H_{33}Cl_2N_7NiO_{14}$: C, 42.63; H, 3.94; N, 11.60. Found: C, 42.45; H, 3.83; N, 12.03. Crystals of **5**·2CH₃CN suitable for X-ray analysis were obtained by slow diffusion of diethyl ether into an acetonitrile solution of the compound.

[Cu(L^{5-00Me})](CF₃SO₃)₂ (2.6). A solution of Cu(CF₃SO₃)₂ (0.065 g, 0.18 mmol) in 3 mL of acetonitrile was added to a stirring suspension of L^{5-00Me} (0.106 g, 0.18 mmol) in 5 mL of acetonitrile. The resulting mossy green solution was stirred for two hours, and then was concentrated in vacuo to ~2 mL. Mossy-green crystals were obtained from slow diffusion of diethyl ether into the concentrated acetonitrile solution, and were collected by filtration. The collected crystals were washed with diethyl ether (3 × 2 mL) and pentane (3 × 2 mL) to afford 0.129 g (75%) of product. IR (KBr pellet): $\nu_{C=O}$ 1728, $\nu_{C=N}$ 1606 cm⁻¹. Absorption spectrum (MeCN): λ_{max} (ϵ_M) 195 (55000), 236 (38000), 286 (28000), 295 (25000, sh), 353 (1300, sh), 713 nm (85 M⁻¹cm⁻¹). μ_{eff} (295 K): 2.27 μ_B . μ_{eff} (5 K): 1.80 μ_B ES+MS (MeCN): m/z 799.07 ([Cu(L^{5-00Me})(CF₃SO₃)₂]⁺). Anal. Calcd. for C₃₂H₃₃CuF₆N₇O₁₂S₂: C, 40.49; H, 3.50; N, 10.33. Found: C, 40.66; H, 3.70; N, 10.64. Crystalline samples of **2.6** can be obtained by slow diffusion of diethyl ether into methanol or acetonitrile; the crystals tend to be very large but very thin sheets/needles, and thus far have not been suitable for X-ray analysis.

[Zn(L^{5-00Me})](CF₃SO₃)₂ (2.7). A solution of Zn(CF₃SO₃)₂ (0.123 g, 0.34 mmol) in 4 mL of methanol was added to a stirring suspension of L^{5-00Me} (0.200 g, 0.34 mmol) in 3 mL of acetonitrile. The resulting yellow solution was stirred for two hours, and then was concentrated in vacuo to ~2 mL. Crystals were obtained from slow diffusion of diethyl ether into the concentrated methanol solution, and were collected by filtration. The collected crystals were washed with diethyl ether (3 × 2 mL) and pentane (3 × 2 mL) to afford 0.276 g (85%) of product. IR (KBr pellet): $\nu_{C=O}$ 1726, $\nu_{C=N}$ 1601 cm⁻¹. Absorption spectrum (MeCN): λ_{max} (ϵ_M) 195 (59000), 240 (39000), 287 (32000), 294 (26000, sh), 340 nm (910 M⁻¹cm⁻¹, sh). ¹H NMR (CD₃CN): 8.74 (s, 3H); 8.72 (dd, 3H); 8.13 (dd, 3H); 7.60 (d, 3H); 3.80 (s, 9H); 3.76 (m, 3H); 3.58 (dd, 3H); 3.23 (dd, 3H); 2.90 (td, 3H). ES+MS (MeCN): m/z 800.20 ([Zn(L^{5-00Me})(CF₃SO₃)₂]⁺), 325.67 ([Zn(L^{5-00Me})]²⁺). Anal. Calcd. for C₃₂H₃₃F₆N₇O₁₂S₂Zn: C, 40.41; H, 3.50; N, 10.31. Found: C,

40.37; H, 3.29; N, 10.15. Crystals of **2.7** suitable for X-ray analysis were obtained by slow diffusion of diethyl ether into an acetonitrile solution of the compound.

2.3.2 X-Ray Structure Determinations. Crystals suitable for X-ray analysis were coated with Paratone-N oil and supported on a Cryoloop before being mounted on a Bruker Kappa Apex II CCD diffractometer under a stream of dinitrogen. Data collection was performed at 120 K with Mo $K\alpha$ radiation and a graphite monochromator, targeting complete coverage and 4-fold redundancy. Initial lattice parameters were determined from at least 270 reflections harvested from 36 frames; these parameters were later refined against all data. Crystallographic data and metric parameters are presented in Table 2.1. Data were integrated and corrected for Lorentz and polarization effects by using SAINT, and semiempirical absorption corrections were applied by using SADABS.¹⁹ The structure was solved by direct methods and refined against F^2 with the program XL from the SHELXTL 6.14 software package.²⁰ Unless otherwise noted, displacement parameters for all non-hydrogen atoms were refined anisotropically. Hydrogen atoms were added at idealized positions and were refined by using a riding model where the displacement parameters were set at 1.2 times those of the attached carbon atom (1.5 for methyl protons).

For the structure of **2.1**, both BF_4^- anions show significant disorder. The anion containing B1 is rotationally disordered over two positions (57:43 ratio) about the axis containing the B1-F1 bond. The anion containing F8 is disordered over two positions, where only F7 and F8 are common between the two. The major part (83%) contains B2a, F6a and F5a, and the fluorine atoms in the major part were refined anisotropically. The major component of this anion was used to constrain the other BF_4^- bond distances and bond angles by the SAME command. All of the thermal parameters for the other disordered BF_4^- components were treated isotropically. A methanol solvate molecule was initially refined with partial site occupancy (84%) and was finally modeled with full occupation as this is more chemically reasonable; the thermal parameters were treated anisotropically.

In the structure of **2.2**, neither obvious disorder nor solvate molecules are observed; however, the highest residual peak is $2 \text{ e}^-/\text{\AA}^3$ and the deepest hole is $0.97 \text{ e}^-/\text{\AA}^3$. The residual electron density appears

between S1 and C31 on one of the triflate anions, consistent with minor untreated triflate disorder.

In the structure of **2.3**, residual electron density in the trigonal “pocket” formed by the ester groups of the ligand cannot be modeled satisfactorily; they likely represent disordered and/or partially occupied molecules of diethyl ether (no $\nu_{\text{C}=\text{N}}$ resonances are observed in the IR spectrum for crystals of **2.3**). This electron density was treated with SQUEEZE,²¹ which finds a 144.8 Å³ solvent void with 26 e⁻/unit cell, corresponding to a partially occupied (62%) diethyl ether molecule. The data in Table 1 do not include the components removed by SQUEEZE.

For **2.4**, crystals of the perchlorate salt diffract well, but have not produced reasonable structure solutions, possibly due to twinning. An alternative anion, [CoCl₄]²⁻, produces a well-defined structure (**2.4a**) with no included solvent present and no disorder.

In the structure of **2.7**, the anions and cation reside on special positions with three-fold symmetry. One of the triflate anions is disordered over two symmetry-related positions such that O and F atoms are located at the same position. This disorder was modeled simply as each site being occupied by a single type of atom (O or F) with half of the sites assigned to O and half assigned to F. Meanwhile, the triflate C-S axis does not coincide with the crystallographic three-fold axis: this generates four sites over which the C and S are disordered. The disorder was modeled with two sites set as C and two set as S, but no mixing of S and C positions.

Table 2.1. Crystallographic data for compounds **2.1-2.5** and **2.7**.^a

	2.1·CH₃OH	2.2	2.3	2.4a	2.5·2CH₃CN	2.7
formula	C ₃₁ H ₃₇ B ₂ CrF ₈ N ₇ O ₇	C ₃₂ H ₃₃ F ₆ MnN ₇ O ₁₂ S ₂	C ₃₂ H ₃₃ F ₆ FeN ₇ O ₁₂ S ₂	C ₃₀ H ₃₃ Cl ₄ Co ₂ N ₇ O ₆	C ₃₄ H ₃₉ C ₁₂ N ₉ NiO ₁₄	C ₃₂ H ₃₃ F ₆ N ₇ O ₁₂ S ₂ Zn
fw	845.30	940.71	941.62	847.29	927.35	951.14
color, habit	brown needles	yellow plates	purple plates	green plates	orange plates	yellow blocks
<i>T</i> , K	120(2)	120(2)	120(2)	120(2)	120(2)	120(2)
space group	<i>P</i> $\bar{1}$	<i>P</i> $\bar{1}$	<i>P</i> 2 ₁ <i>c</i>	<i>P</i> 2 ₁ 3	<i>P</i> $\bar{1}$	<i>R</i> 3
<i>Z</i>	2	2	4	4	2	3
<i>a</i> , Å	11.8630(4)	12.5586(11)	15.6283(13)	15.4332(4)	12.3690(8)	10.042(2)
<i>b</i> , Å	12.9273(5)	12.6047(11)	19.4132(16)	15.4332(4)	12.7685(8)	10.042(2)
<i>c</i> , Å	13.1753(5)	12.8933(11)	14.4401(13)	15.4332(4)	13.9210(9)	35.268(9)
α , deg	81.305(2)	93.705(5)	90	90	73.345(3)	90
β , deg	71.683(2)	94.262(5)	115.895(4)	90	86.927(3)	90
γ , deg	71.499(2)	103.718(5)	90	90	73.045(3)	120
<i>V</i> , Å ³	1816.04(12)	1970.1(3)	3941.2(6)	3675.94(17)	2013.7(2)	3079.8(12)
<i>d</i> _{calc.} , g/cm ³	1.546	1.586	1.587	1.531	1.529	1.538
GOF	1.028	1.042	1.016	1.036	1.034	1.068
<i>R</i> ₁ (<i>wR</i> ₂) ^b , %	5.05 (12.81)	4.34 (11.60)	4.04 (10.53)	2.31 (5.56)	3.70 (10.24)	4.23 (12.47)

^a Obtained with graphite-monochromated Mo K α ($\lambda = 0.71073$ Å) radiation.

^b $R_1 = \Sigma||F_o| - |F_c|| / \Sigma|F_o|$, $wR_2 = \{\Sigma [w(F_o^2 - F_c^2)^2] / \Sigma[w(F_o^2)^2]\}^{1/2}$ for $F_o > 4\sigma(F_o)$.

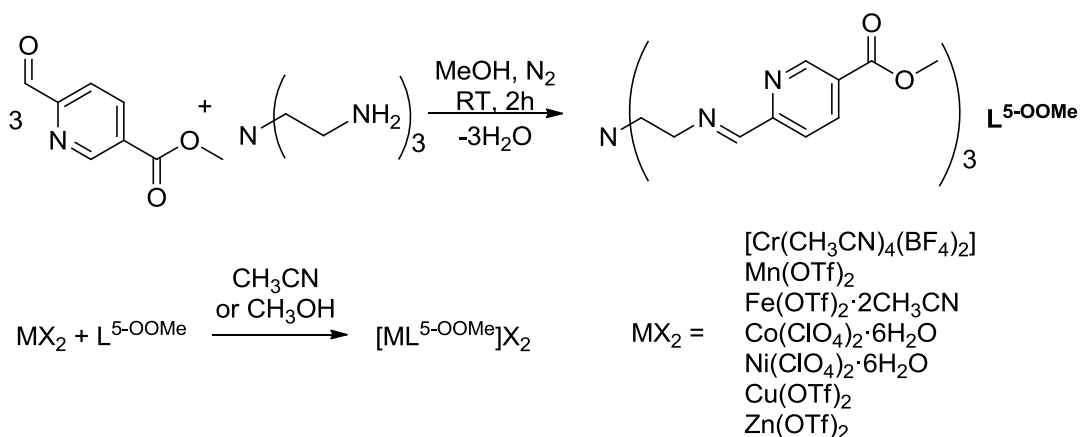
2.3.3 Other Physical Methods. Absorption spectra were obtained with a Hewlett-Packard 8453 spectrophotometer in quartz cuvettes with 1 cm or 1 mm path lengths in air (or in an airfree glass cuvette under dinitrogen for **2.1**); all experiments were performed at room temperature. Infrared spectra were measured with a Nicolet 380 FT-IR spectrometer. Mass spectrometric measurements were performed in the positive ion mode on a Finnigan LCQ Duo mass spectrometer, equipped with an analytical electrospray ion source and a quadrupole ion trap mass analyzer. Cyclic voltammetry experiments were carried out inside a dinitrogen-filled glove box in 0.1 M solutions of $(\text{Bu}_4\text{N})\text{PF}_6$ in acetonitrile unless otherwise noted. The voltammograms were recorded with either a CH Instruments 1230A or 660C potentiostat, using a 0.25 mm Pt disk working electrode, Ag wire quasi-reference electrode, and a Pt wire auxiliary electrode. All voltammograms shown were measured with a scan rate of 0.1 V/s. Reported potentials are referenced to the ferrocenium/ferrocene (Fc^+/Fc) redox couple and were determined by adding ferrocene as an internal standard at the conclusion of each electrochemical experiment. Solid-state magnetic susceptibility measurements were performed using a Quantum Design model MPMS-XL SQUID magnetometer at 295 and 5 K on finely ground samples prepared under a dinitrogen atmosphere. The data were corrected for the magnetization of the sample holder by subtracting the susceptibility of an empty container; diamagnetic corrections were applied using Pascal's constants.²² ^1H NMR spectra were measured using Varian INOVA 300 MHz or 400 MHz instruments. Magnetic susceptibilities in CD_3CN or d_6 -DMSO solution were determined by the Evans method.²³ Elemental analyses were performed by Robertson Microlit Laboratories, Inc. in Madison, NJ.

2.3.4 Electronic Structure Calculations. Unrestricted B3LYP hybrid density functional SCF and TD-DFT studies²⁴ were carried out in the G09 suite of electronic structure codes.²⁵ The geometries for $[\text{M}(\text{L}^{5\text{-OOMe}})](\text{BF}_4)_2$ and $[\text{Cr}(\text{L}^{5\text{-OOMe}})](\text{BF}_4)_3$ were optimized as isolated, gas phase ion pairs; note that BF_4^- anions were used for all computed structures. Due to the importance of the amine nitrogen in the electronic spectroscopy, the $\text{M}-\text{N}_{\text{amine}}$ distance was constrained to the respective experimental distances shown in Figure 2.2. For Cu this distance optimized to 3.243 Å. The Cr cation and BF_4^- anions were removed to generate the coordinates for $\text{L}^{5\text{-OOMe}}$. The LANL2 basis sets and effective core potentials were

used for the transition metals;²⁶ H, B, C, N, O and F were described with a 6-31g* model.²⁷ Simulated electronic absorption spectra utilized a Gaussian line shape, computed oscillator strengths and peak positions as well as a 0.15 eV linewidth.

2.4 Results

2.4.1 Syntheses. Shown in Scheme 2.2, the ligand L^{5-OOMe} is synthesized via Schiff-base condensation of tren (tris-2(aminoethyl)amine) and a slight stoichiometric excess of methyl-6-formylnicotinate. The reaction produces a white precipitate and can be isolated in good yield. The ligand is slightly soluble in polar organic solvents such as methanol, acetonitrile, chloroform and dichloromethane, but is insoluble in hydrocarbons and diethyl ether.



Scheme 2.2. Syntheses of the ligand L^{5-OOMe} (top) and the divalent complex salts **2.1-2.7** (bottom).

The preparations of the divalent metal complex salts are straightforward (Scheme 2.2). The complexes form upon mixing polar-organic solutions of MX_2 with slurries of the ligand in the same solvent under an inert atmosphere. The choice of solvent is primarily dictated by the metal precursor—methanol was used for bare or hydrated metal salts, while acetonitrile was used for acetonitrile-solvated metal salts. The metalation reaction proceeds quickly as evidenced by almost immediate changes in the colors of the reaction mixtures. The tetrafluoroborate and triflate salts **2.1-2.3**, **2.6** and **2.7** remain soluble

but can be isolated by concentrating the reaction mixture, followed by precipitation with diethyl ether. The perchlorate salts **2.4** and **2.5** precipitate directly from solution and can be isolated by filtration. The isolated yields for the complexes are typically >80%. The product complexes are all generally air stable in the solid-state and in solution; however, the Cr complex is air-sensitive in solution and must be handled under inert atmosphere. Crystalline material can be isolated by slowly diffusing diethyl ether into concentrated acetonitrile solutions of each of the complexes, although methanol gives better crystals for **2.1**. While Cr(II) complexes have been reported to disproportionate in protic solutions,²⁸ we observe no evidence of disproportionation of **2.1** in methanol.

2.4.2 Structural Comparisons. The X-ray structures determined for the compounds reported here (Table 2.1, Figures 2.1 and A1.1) reveal cationic mononuclear complexes which are in general well-separated from each other by charge balancing anions.

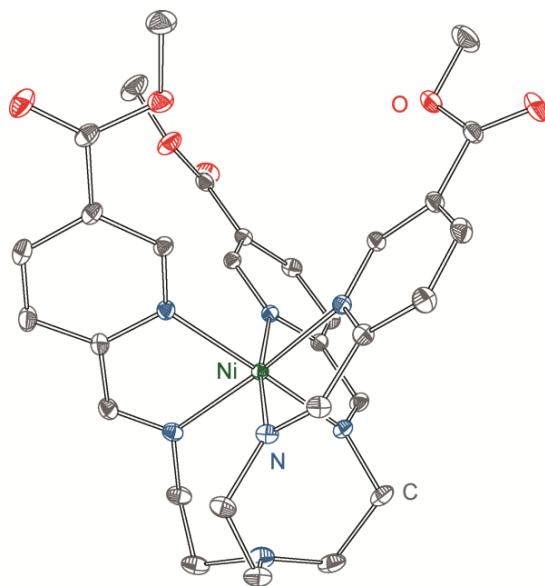


Figure 2.1. Side-on view of the $[M(L^{5-OOMe})]^{2+}$ complex cation in the structure of **2.5**·2CH₃CN, rendered with 40% probability ellipsoids. Green, red, dark blue and gray ellipsoids represent Ni, O, N and C atoms, respectively. All hydrogen atoms are omitted for clarity. Similar views for the complexes in **2.1-2.4** and **2.7** are provided in Figure A1.1.

All iminopyridine nitrogen atoms are bound to the metal ion; in the cases of the Mn and Co complexes **2.2** and **2.4**, the bridgehead (tren) nitrogen atom is significantly closer to the metal center (Figure 2.2).

The average trigonal twist angle ϕ^{7a} (Table A1.1) varies from 39.9° to 54.5°, which indicates that all of

the complexes are closer in geometry to octahedral/trigonal antiprismatic rather than trigonal prismatic. The complexes most distorted away from octahedral local geometry contain Mn (**2.2**), Co (**2.4a**) and Zn (**2.7**) ions.

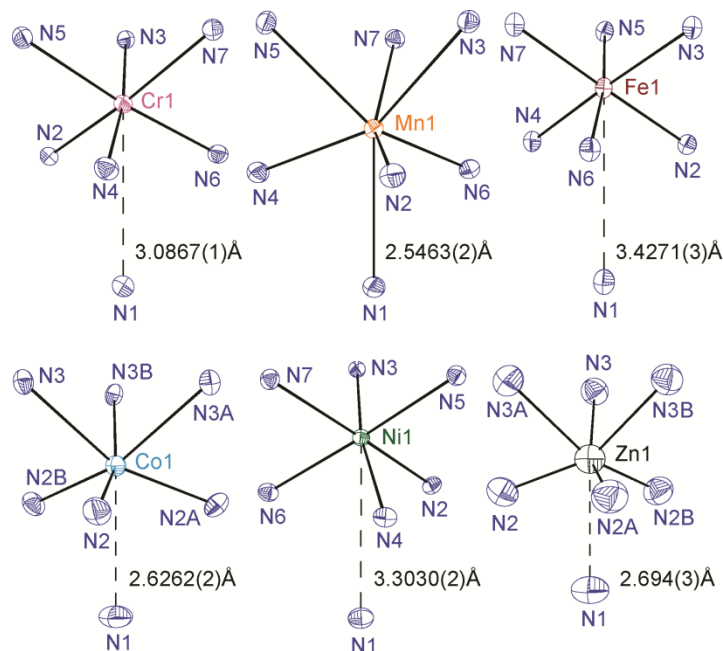


Figure 2.2. Geometry of the first coordination sphere around the M(II) ions and distance to tether N atom of ligand L^{5-OOMe} . Ellipsoids are drawn at 40% probability. N1 is the apical tether nitrogen, even- and other odd-numbered N atoms are within imine and pyridine moieties, respectively. Solid lines denote coordination bonds with distances less than the sum of the van der Waals radii for the two atoms. Dashed lines show the distance between apical N1 and the metal center, but do not necessarily indicate bonding interactions.

For this family of complexes, the metal nitrogen bonds follow a pattern where the $M-N_{imine}$ bonds are shorter than the $M-N_{pyridine}$ bonds. In the more regularly octahedral complexes **2.1**, **2.3**, and **2.5**, this difference is small (~ 0.03 Å), while in the structures that are markedly distorted from octahedral (**2.2**, **2.4a**, and **2.7**), the differences are much larger (0.15-0.25 Å). Chromium-containing **2.1** displays unusual variation between different arms of the tripodal ligand in addition to the metal-pyridine/imine bond variations. The Cr–N bonds on one of the ligand arms are shorter by at least 0.04 Å compared to the other two arms. This is accompanied by shortening of the C–C bond bridging between the two coordinating N atoms and lengthening of both N–C bonds. These differences are consistent with radical anion character

localized on the ligand arm interacting with a Cr(III) center; such bond alternation has been observed recently in other reduced forms of Cr diimine and iminopyridine compounds.^{5,29}

In these complexes, the ester groups are part of the conjugated system including the pyridine and imine. Generally, the esters are nearly coplanar with the pyridines, and all complexes have ester-pyridine torsion angles of less than 20°. The Ni complex **2.5** has both the maximum (19.60°) and minimum (1.89°) torsion angles of all the complexes. It is interesting to note that for every complex except Fe-containing **2.3**, the ester groups all point the same direction on all three arms, with the carbonyl oxygen pointing away from the metal center. However, in the Fe case, only one of the ester groups adopts this position. Additionally, the three ester groups can be thought to form a trigonal pocket. For complexes **2.1**, **2.3**, **2.4** and **2.5**, the sides of the trigonal pocket³⁰ range from 5.3 to 6.5 Å. For complexes in **2.2** and **2.7**, the distances are much shorter and range from 3.9 to 4.6 Å. The smaller trigonal pocket coincides with the much smaller twist angles for these two complexes, and distortion away from octahedral geometry.

2.4.3 Comparison of Magnetic Properties. The room temperature magnetic moments for **2.1-2.6** indicate that compounds **2.2**, **2.4**, and **2.5** contain high-spin ions with 5, 3 and 2 unpaired electrons, respectively. Meanwhile, the data for **2.1** and **2.3** are consistent with low-spin Cr(II) and Fe(II) ions, containing 2 and 0 unpaired electrons, respectively. Note that for **2.1** the magnetic data is equally consistent with strong antiferromagnetic coupling between a ligand radical anion and a Cr(III) cation to give an $S = 1$ ground spin state, and such coupling has been previously observed for $[\text{Cr}^{\text{III}}(\text{bpy})_2(\text{bpy}^-)]^{2+}$ -type complexes.²⁹ In addition to the solid-state magnetic moment measurements, solution susceptibility measurements carried out on **2.3** show that the Fe(II) ion remains low spin and diamagnetic up to 80 °C in d_6 -DMSO. For Ni(II) and Cu(II), single electron configurations with two and one unpaired electrons, respectively, are expected, and these are observed for compounds **2.5** and **2.6**. A solid-state magnetic moment was not collected for complex **2.7** due to the d^{10} configuration for Zn(II); diamagnetism in solution is confirmed by Evans' method (¹H NMR) susceptibility measurements. Magnetic moments of **2.1**, **2.2**, and **2.4** collected at 5 K indicate that the low temperature spin states are unchanged from the room temperature determinations.

2.4.4 Electronic Absorption Comparisons. The ground state UV-Visible absorption properties of each of the complexes were studied in acetonitrile solution at room temperature. Shown in Figure A1.2, each of the complexes shows three intense absorption bands in the ultraviolet part of the spectrum, with molar absorptivities greater than $25000 \text{ M}^{-1}\cdot\text{cm}^{-1}$. These bands are analogous to three UV bands present for the free ligand but shifted slightly: the band at 245 nm in the free ligand is blue-shifted to 239 nm in each of the complexes, and the lowest energy UV band at 279 nm in the free ligand is red-shifted by 5-8 nm in the complexes.

The visible absorption spectra for **2.1-2.7** are shown in Figure 2.3 (top). The high-spin complexes (**2.2**, **2.4**, and **2.5**) and complexes **2.6** and **2.7** are all similar and devoid of strong features at wavelengths longer than 500 nm. Complex **2.2** has no absorption bands in the visible region, while complexes **2.4** and **2.7** have a band of moderate intensity centered at 386 and 340 nm, respectively. The Ni complex **2.5** has a moderately intense band centered at 395 nm and a very weak band at 866 nm; the latter is indicative of a d-d transition. The Ni(II) d-d band at 866 nm can be used to calculate Δ_o , the energy difference between the t_{2g} and e_g orbitals in this approximately octahedral ligand field. For **2.5**, Δ_o corresponds to 11550 cm^{-1} . Complex **2.6** displays similar features to **2.5**, with a moderately intense band at 353 nm and a weak band at 713 nm. The low-spin complex **2.3** has a rich visible absorption spectrum compared to the previously discussed species: the Fe complex displays bands of moderate intensity at 382, 540 and 594 nm.

The Cr compound **2.1** exhibits moderately intense absorption throughout the visible and into the near IR, with prominent peaks at 478, 586, 738, and 1068 nm. This behavior is qualitatively different from the other divalent metal complexes reported here. We note that transitions through the visible and into the near IR of similar band intensity are observed for Cr(III) complexes chelated to anionic bipyridine ligand radicals.²⁹

2.4.5 Simulated Electronic Absorption Spectra. In order to understand the observed periodic trends in the visible absorption spectra, TD-DFT and natural transition orbital (NTO) analyses have been carried out on the free $\text{L}^{5\text{-OOMe}}$ ligand and its anion (Figure A1.3) and complexes **2.1-2.7** (Figures 2.3 and A1.4). Select NTO pairs are associated with the relevant transitions (Figure A1.4).

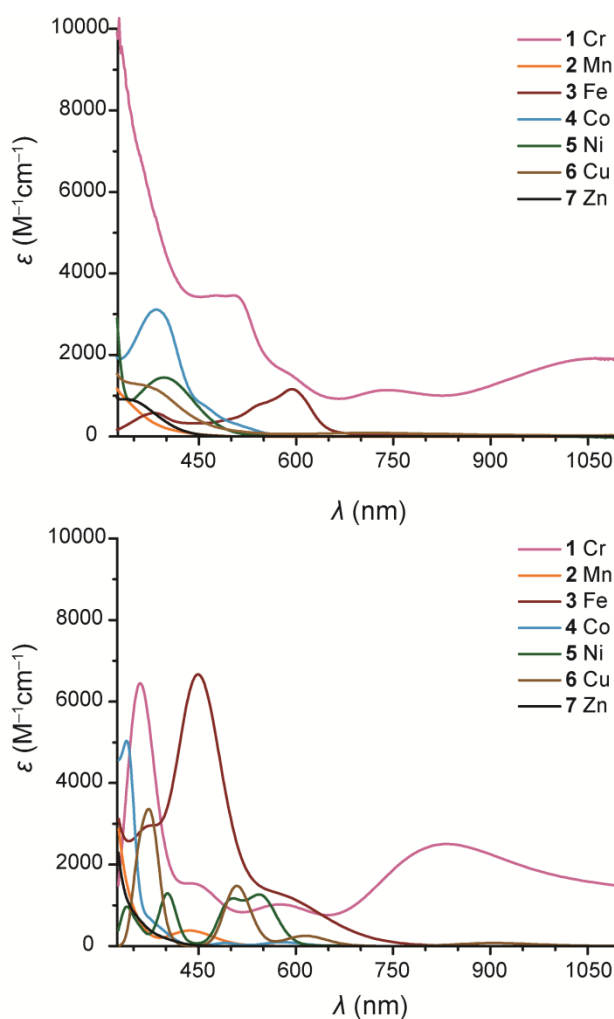


Figure 2.3. Experimental (top) and TD-DFT simulated (bottom) visible electronic absorption spectra for **2.1-2.7**, plotted on the same relative scales. Experimental data were collected on solutions in acetonitrile.

For the free ligand $\mathbf{L}^{5\text{-OOMe}}$, at the computed geometry for **2.1**, the lowest energy transitions ($\lambda < 550$ nm) correspond to transitions from the bridgehead nitrogen lone pair \rightarrow iminopyridine π^* orbitals. The HOMO of trimethylamine is provided in Figure A1.5 to illustrate the orbital character of a typical amine lone pair. When the free ligand is reduced, the bridgehead nitrogen lone pair transitions shift to lower wavelength and new iminopyridine \rightarrow iminopyridine π^* bands appear at 600 nm and 900 nm.

The experimental and computed complex visible spectra collected in Figure 2.3 in the same scale suggest that the computed spectra reproduce the major differential features of the observed visible

spectra. Specifically, **2.1** displays a number of high wavelength ($\lambda > 500$ nm) features. The Fe(II) complex **2.3** has a significant transition around 600 nm. The Mn(II), Co(II), and Zn(II) transitions in **2.2**, **2.4**, and **2.7**, respectively, are weaker and tend toward lower wavelengths, while the computed Ni(II) and Cu(II) spectra (**2.5** and **2.6**) display high wavelength features not present in the observed spectra.

Select NTOs collected in Figure A1.4(b-h) provide viable interpretations for the observed features. For the computed spectrum of **2.1** provided in Figure 2.3 (bottom) a number of low intensity transitions contribute to the broad band above 550 nm: they correspond to iminopyridine \rightarrow iminopyridine π^* bands (Figure A1.4b), comparable to those computed for the anion of \mathbf{L}^{5-00Me} discussed above (Figure A1.3). Bridgehead nitrogen lone pair \rightarrow iminopyridine π^* transitions are computed to occur around 450 nm, and transitions with significant $t_{2g} \rightarrow e_g^*$ character are found below 400 nm. For **2.2** (Figure A1.4c) low intensity bridgehead nitrogen lone pair \rightarrow iminopyridine π^* transitions are computed near 450 nm and iminopyridine \rightarrow iminopyridine π^* bands below 400 nm. As expected for low spin **2.3** (Figure A1.4d) there is significant metal d orbital participation in the prominent 400-450 nm features correspond to a metal (t_{2g}) \rightarrow iminopyridine π^* transitions, while the weaker ($\lambda > 600$ nm) transitions represent bridgehead nitrogen lone pair \rightarrow iminopyridine π^* character. For the Co(II) complex **2.4** (Figure A1.4e) the highest wavelength transitions display bridgehead nitrogen lone pair \rightarrow iminopyridine π^* character. For the Ni(II) complex **2.5** (Figure A1.4f), the highest wavelength transition possesses significant metal $t_{2g} \rightarrow e_g^*$ character; bridgehead nitrogen lone pair \rightarrow iminopyridine π^* transitions occurring at lower wavelength. For the Cu(II) complex **2.6** (Figure A1.4g) a high wavelength bridgehead nitrogen lone pair $\rightarrow e_g^*$ transition is inserted into the spectrum. When Zn(II) is inserted into the ligand to make **2.7** (Figure A1.4h) the bridgehead nitrogen lone pair \rightarrow iminopyridine π^* transition shifts to lower wavelength ($\lambda < 450$ nm), relative to the free ligand.

2.4.6 Electrochemistry. Each of the complexes displays rich electrochemical behavior (Figure 2.4). The hallmark of these species is the presence of multiple reversible reductions. For **2.2-2.5** and **2.7**, three reversible reductions between -1.0 and -1.75 V (vs $Fc^{0/+}$) and one irreversible reduction at potentials more negative than -2.10 V are observed. For each of the complexes, an irreversible oxidation is

observed at positive potentials greater than 1.0 V. The electrochemical events common to all complexes are most likely ligand-based since they vary little with the identity of the chelated metal. Additionally, the participation of other iminopyridine ligands in redox behavior has been previously observed for divalent 1st row transition-metal complexes.⁵

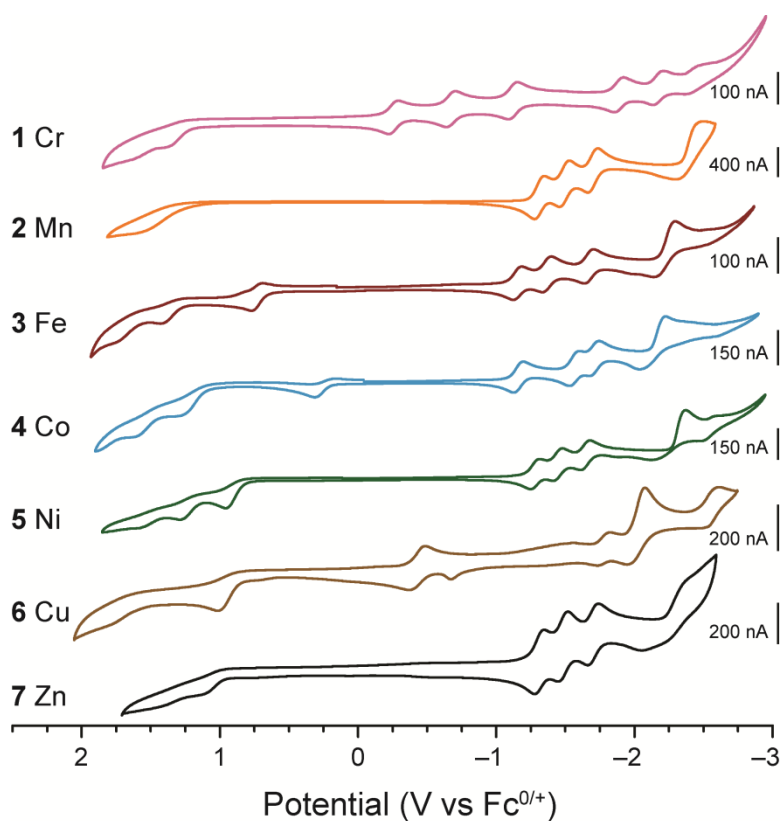


Figure 2.4. Cyclic voltammograms of the M(II) complexes in **2.1-2.7**, collected in 0.1 M TBAPF₆ acetonitrile solution with a scan rate of 100 mV/s. The potentials are referenced to ferrocene.

In addition to the redox events described above, involvement of the metal ion is also evident for **2.3-2.6**. Compounds **2.3** and **2.4** also display one reversible oxidation at +0.71 and +0.26 V, respectively, which are tentatively assigned to metal-based 3+/2+ couples. The very positive potential for oxidation of the Fe complex falls between reported potentials assigned to the 3+/2+ couple for similar [Fe(iminopyridine)₃]²⁺ complexes.³¹ The assigned 3+/2+ couple for Co-containing **2.4** also matches closely to the potential reported for a similar [Co(iminopyridine)₃]²⁺ complex.^{31b} The Ni complex **2.5**

exhibits an additional quasi-reversible reduction at -2.51 V, tentatively assigned to the $2+/1+$ couple, which occurs at slightly more negative potentials than those reported for hexacoordinate iminopyridine Ni(II) complexes.³² An irreversible oxidation occurs at $+1.04$ V and is tentatively assigned to the oxidation of Ni(II) to Ni(III). The Cu complex **2.6** displays an additional reversible reduction at -0.43 V which is assigned to the $2+/1+$ couple. This falls between the reported oxidation potentials for a di-Cu(I) iminopyridine cryptand and the reduction potentials of its di-Cu(II) aminopyridine cryptand analogue which are each assigned to the Cu $2+/1+$ couple.³³

The behavior for the Cr complex **2.1** is qualitatively different than that of the other metal complexes. For **2.1**, four reversible reductions, one quasi-reversible reduction right at the edge of the solvent window, and one reversible oxidation are observed. The $E_{1/2}$ potentials for the events in **2.1** are nearly identical to those reported for the trivalent analogue, $[\text{Cr}(\text{L}^{5\text{-OOMe}})](\text{BF}_4)_3$.³⁴ However, the rest potentials for **2.1** and for $[\text{Cr}(\text{L}^{5\text{-OOMe}})](\text{BF}_4)_3$ are separated by the $3+/2+$ wave. In addition to the nature of the redox events, the spacing of the waves in **2.1** is different compared to complexes **2.2-2.5**. The redox events for **2.1** begin at more positive potentials and are more widely spaced in relation to each other than those for **2.2-2.5**. The more positive potentials are likely due to the Cr center being trivalent instead of divalent, which would also affect the spacing between reduction waves.

2.5 Discussion

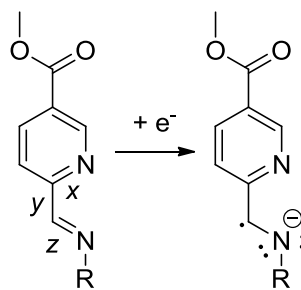
The tripodal iminopyridine ligand $\text{L}^{5\text{-OOMe}}$ displays considerable geometric flexibility in ligating first row transition-metal ions (Figure 2.1). Despite the structural diversity, when comparing the behavior of first row metal complexes **2.1-2.7**, the absorption spectra, electrochemical behavior, and many of the structural characteristics of this family of complexes are similar, and reflect the dominance of the ligand in determining physical properties. Below, we discuss in more detail some instances where significant metal-ligand interactions arise, including ligand field parameters relevant to spin-crossover applications, as well as the very different behavior of the Cr-containing compound **2.1** relative to the other species.

2.5.1 Electronic Structure Considerations for the “Cr(II)” Complex. Comparison of **2.1** and the one electron oxidized counterpart $[\text{Cr}(\text{L}^{5\text{-OOMe}})](\text{BF}_4)_3$ ³⁴ provides a more complete picture of the true electronic character of **2.1**. The cyclic voltammograms of the two Cr complexes are basically identical, with the only difference being the nature of the event at most positive potential. In **2.1** this event is an oxidation, while in $[\text{Cr}(\text{L}^{5\text{-OOMe}})](\text{BF}_4)_3$ it is a reduction.

Structurally, the two complexes are similar; however, several key distances in the iminopyridine ligand are different. Shown in Table 2.3, the lengthening of the C-N bond on the imine (*z*) and to a lesser extent on the pyridine (*x*), coupled with shortening of the C-C iminopyridine bridge (*y*) upon reduction from $[\text{Cr}(\text{L}^{5\text{-OOMe}})]^{3+}$ to $[\text{Cr}(\text{L}^{5\text{-OOMe}})]^{2+}$ is a hallmark of localization of the reducing equivalent on one arm of the iminopyridine ligand.⁵

Table 2.3. Selected iminopyridine ligand bond lengths for **2.1** and average iminopyridine ligand bond lengths for complexes **2.2-2.5**, **2.7**, and $[\text{Cr}(\text{L}^{5\text{-OOMe}})](\text{BF}_4)_3$.

Complex (metal)	<i>x</i> (Å)	<i>y</i> (Å)	<i>z</i> (Å)
2.1 (Cr)	1.361(3)	1.454(3)	1.288(3)
	1.365(2)	1.465(3)	1.280(3)
	1.376(3)	1.420(3)	1.311(3)
2.2 (Mn)	1.352 [3] ^a	1.474[3] ^a	1.271[3] ^a
2.3 (Fe)	1.362[3] ^a	1.451[3] ^a	1.287[3] ^a
2.4 (Co)	1.351(1) ^b	1.469(2) ^b	1.267(2) ^b
2.5 (Ni)	1.353[2] ^a	1.468[2] ^a	1.274[2] ^a
2.7 (Zn)	1.350(5) ^b	1.468(5) ^b	1.255(6) ^b
$[\text{Cr}(\text{L}^{5\text{-OOMe}})](\text{BF}_4)_3$ ^c	1.364(2) ^b	1.463(2) ^b	1.275(2) ^b



^a The errors for these bond distances were calculated by averaging the bond distances for each type of bond and taking the square root of the sum of the squares of the bond esds.

^b There is only one crystallographically independent bond of this type, so there are no average bond distances.

^c See Chapter 5.

Comparison of the iminopyridine ligand bond lengths in **2.1** shows that one *x* and *z* in **2.1** are significantly longer than analogous average bond lengths in the other structurally characterized divalent complexes (also Table 2.3). Similarly, the one *y* in **2.1** is significantly shorter than its counterpart average in **2.2-2.5** and **2.7**. Along with the changes in ligand bond lengths, numerous intense bands in the

absorption spectrum of **2.1**, including bands in the near IR, are features common to other complexes in which Cr(III) is bound by ligand radical anion species.²⁹

Unrestricted B3LYP hybrid density functional results are consistent with the structural and spectroscopic studies. A comparison of **2.1** and $[\text{Cr}(\text{L}^{5\text{-OOMe}})](\text{BF}_4)_3$ show that spin density on the metal center and first coordination sphere are nearly identical; in the divalent species (**2.1**), significant spin density is located in the π system of a single arm of the ligand $\text{L}^{5\text{-OOMe}}$, as shown in Figure 2.5.

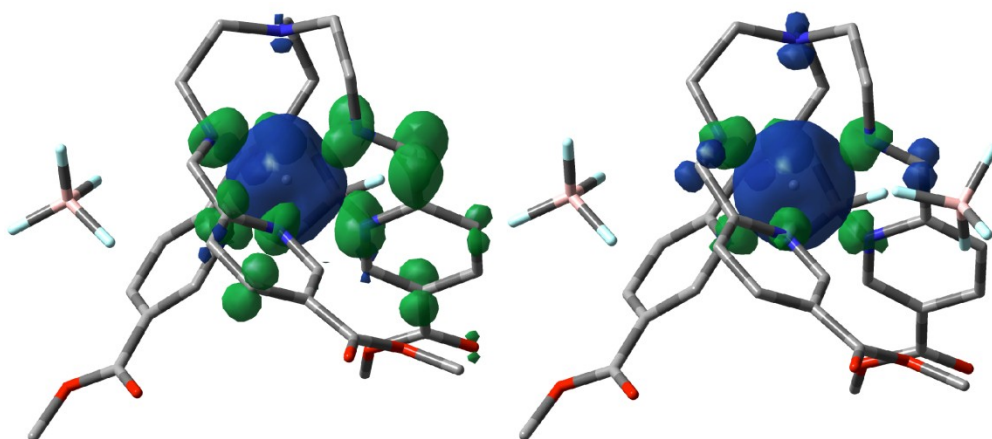


Figure 2.5. Comparison of net spin density plots for **2.1** (left) and $[\text{Cr}(\text{L}^{5\text{-OOMe}})](\text{BF}_4)_3$ (right), scaled at 0.003 atomic units. Triplet and quartet states, respectively, are displayed. Blue surfaces correspond to net α spin density and green to net β spin density. Note additional β spin density on one pyridine “arm” of the iminopyridine ligand in the “Cr(II)” complex.

The $M_S = 1$ spin density plot for **2.1** can be characterized as a Cr(III) ($S = 3/2$) ion antiferromagnetically coupled to a ligand-based electron. Comparison of low energy transitions ($\lambda > 550$ nm) for **2.1** and the anion of the free ligand support this model (Figures A1.3 and A1.4). The magnetic moment indicating $S = 1$ is also consistent with strong antiferromagnetic coupling. All of these data point to the true identity of **2.1** as being $[\text{Cr}^{\text{III}}(\text{L}^{5\text{-OOMe}})](\text{BF}_4)_2$.

2.5.2 Trends in Electronic Transitions for $\text{L}^{5\text{-OOMe}}$ Complexes. Good qualitative agreement between experimental and TD-DFT-computed absorption spectra allow us to establish the orbital character of key features (via NTO analyses), important for the application of these kinds of complexes in

solar photo-conversion schemes. First, the importance of the bridgehead nitrogen atom is evident in the spectrum of the free ligand: all transitions involve the amine as a starting point. In turn, it is reasonable to expect that tuning the N···M distance in transition metal complexes will strongly perturb photophysical properties.

Second, it is evident that for most of the first row complexes studied, the ligand dominates the transitions in the visible spectrum. The lowest energy transitions for **2.1** (Cr), **2.2** (Mn), **2.4** (Co) and **2.7** (Zn) show predominantly LLCT character, although it should be noted that the near-IR absorptions for **2.1** are related to a reduced ligand and are qualitatively different from the other compounds. Transitions featuring larger metal orbital contributions occur higher in energy, although with some overlap in the visible spectrum. The low-spin Fe(II) complex **2.3** is a clear exception, as its lowest energy transitions are largely MLCT in character. The lowest energy transition for the Ni(II) complex **2.5** is ligand field, as expected. A LMCT transition for the Cu(II) analogue **2.6** is predicted but not observed, at least not at the sample concentrations used. Overall, the L^{5-OOMe} ligand shows interesting potential for photophysical exploitation, provided that increased metal participation can be achieved. Compound **2.1** indicates that use of trivalent metals is promising; substituent tuning offers an alternative route.

2.5.3 Electronic Structure Considerations for Spin-State Switching. For metals with d^4 to d^7 electron configurations in locally octahedral coordination environments, two spin states with different numbers of unpaired electrons are possible, depending on whether electrons preferentially populate the e_g orbitals before filling the t_{2g} orbitals. The two energetic terms which dictate whether a complex has a high-spin (where S is maximized) or a low-spin (where S is minimized) configuration are the pairing energy, Π , required to pair electrons in the t_{2g} orbitals and the energy difference between the e_g and the t_{2g} orbitals, Δ_o .³⁵

As discussed above, the “Cr(II)” complex in **2.1** is better described as an antiferromagnetically coupled d^3 ligand radical anion system, and the high spin state is not accessible due to the strength of the coupling between the metal and ligand spin centers. Additionally, the ligand sets that have formerly demonstrated spin switching in Cr(II) and Mn(II) complexes do not include diimines or iminopyridines.³⁶

Spin switching has been observed for the d^4 $[\text{Cr}(\text{depe})_2\text{I}_2]$,³⁷ where depe is 1,2-bis(diethylphosphino)ethane, and for methyl and ethyl mono-alkylated Mn(II) manganocenes and the parent unfunctionalized compound, which all have d^5 configuration. Therefore it is unsurprising that **2.1** remains $S = 1$ and **2.2** remains $S = 5/2$ down to the lowest temperatures probed (5 K). For the ligand system discussed here, we will only focus on the d^6 and d^7 species.

In d^6 Fe(II) complexes, iminopyridine ligands provide strong enough ligand fields³⁸ that unless functional groups ortho to the pyridine N are installed to sterically stabilize the high-spin state, the complexes are exclusively low spin at room temperature. We hypothesized that an electron withdrawing group at the 5-position may reduce the ligand field strength of the iminopyridine by pulling electron density away from the pyridine N, making it a weaker σ donor, and thus allow access to the spin-switching regime. The value of Δ_o (also, $10D_q$) calculated from the Ni(II) spectrum can be used to predict spin-crossover tendency in Fe(II) complexes using the same ligand set. For Ni(II) D_q values between 1120 and 1240 cm^{-1} , the corresponding Fe(II) complexes are expected to fall in the spin-crossover range.^{38a,39} Therefore, based on the Ni(II) ligand field parameter alone, which is $0.1 \cdot \Delta_o$ or 1155 cm^{-1} , this Fe(II) complex would be expected to exhibit spin-crossover. In this work, the available solution and solid-state data indicate that the Fe(II) complex **2.3** remains low-spin at all conditions tested, signifying that the ester incorporation does not sufficiently weaken the ligand field for spin-crossover to manifest. We note that the ligand field parameters discussed above are merely guides for evaluating spin-crossover behavior with N_6 coordination environments, and that there are many exceptions which do not follow this trend. In this case, there may be geometric constraints introduced by tethering the three arms of the ligand together which preclude spin-crossover, which are not present in more commonly studied tris(diimine) Fe(II) complexes.⁴⁰

For Co(II), strong ligand fields are necessary to force spin pairing in the d^7 species.⁴¹ Previously, a $[\text{Co}(\text{iminopyridine})_3]^{2+}$ complex had been reported as high-spin at room temperature, with gradual spin-crossover starting at approximately 250 K.⁴² In the case of the tripodal ligand $\mathbf{L}^{5\text{-OOMe}}$, while the magnetic moment for **2.4** does decrease as the temperature is lowered, it ultimately remains high spin in the solid-

state down to 5 K with a μ_{eff} of 4.15 μ_{B} . For an $S = 3/2$ ion and $g = 2$, the spin only μ_{eff} is expected to be 3.87 μ_{B} ; the actual μ_{eff} for Co(II) species is frequently greater than this due to unquenched orbital angular momentum and g values are greater than 2. The stability of the high-spin state could be due to the weakened ligand field provided by the ester functionalized ligand, or it could be due to geometric constraints imposed by the tren capping group which prevent reaching the low spin state. Notably, the hexadentate ligand may not allow for the exploitation of Jahn-Teller distortions common to bis-tridentate Co(II) complexes shown to be spin-crossover species, such as $[\text{Co}(\text{terpy})_2]^{2+}$.^{41,43} In these systems, stronger π -interaction occurs between the center N donor moieties on each of the ligands in comparison to the two flanking N donor moieties on each ligand. This effectively acts as a tetragonal compression along the z -axis, which favors the low-spin state over the high-spin state in Co(II) (less population of antibonding orbitals). Since there cannot be preferential imine versus pyridine coordination along the z -axis with $\text{L}^{5\text{-OOMe}}$, the Jahn-Teller-induced distortions observed in **2.4a** tend to be C_3 symmetric rather than tetragonal, and the low-spin state is not stabilized in **2.4** and **2.4a** even though the ligand field is strong enough to prevent access of the high-spin state in the Fe(II) analogue **2.3**.

2.6 Conclusions and Outlook

The survey of ester-functionalized iminopyridine complexes presented in this work display an interesting variety of coordination environments around the chelated metal ions. The complexes encompass geometries from very regular octahedral coordination, to highly strained trigonal antiprismatic, to seven-coordinate centers. Despite the wide variation in coordination, most of the complexes have very similar absorption spectra; they seem to divide into high-spin or low-spin electron configurations. Along with the absorption spectra, the electrochemical behaviors of the complexes are remarkably similar. These species display several ligand-based redox events which are mostly unperturbed by the metal identity. However, the redox state of the chelated metal dramatically affects these ligand-based redox events. In reality, the Cr complex **2.1** is best described as a Cr(III) metal center coordinated to a ligand radical anion, whereas complexes **2.2-2.7** are truly divalent metals chelated by a

neutral ligand. Exploitation of ligand non-innocence in solar and/or thermal chemical transformations is underway. Additionally, ligand field considerations suggest that the Fe(II) analogue **2.3** is poised to display spin-crossover; however, **2.3** remains low-spin even at elevated temperatures. Exploring the role of ligand geometric constraints on spin-crossover accessibility will be pursued in due course.

2.8 References

1. (a) Hoselton, M. A.; Wilson, L. J.; Drago, R. S. *J. Am. Chem. Soc.* **1975**, *97*, 1722-1729; (b) Seredyuk, M.; Gaspar, A. B.; Ksenofontov, V.; Galyametdinov, Y.; Kusz, J.; Gütlich, P. *Adv. Funct. Mater.* **2008**, *18*, 2089-2101; (c) Bowman, A. C.; Milsmann, C.; Bill, E.; Turner, Z. R.; Lobkovsky, E.; DeBeer, S.; Wieghardt, K.; Chirik, P. J. *J. Am. Chem. Soc.* **2011**, *133*, 17353-17369.
2. (a) Chen, Y.; Qian, C.; Sun, J. *Organometallics* **2003**, *22*, 1231-1236; (b) Bianchini, C.; Mantovani, G.; Meli, A.; Migliacci, F.; Laschi, F. *Organometallics* **2003**, *22*, 2545-2547; (c) Tang, X.; Sun, W.-H.; Gao, T.; Hou, J.; Chen, J.; Chen, W. *J. Organomet. Chem.* **2005**, *690*, 1570-1580.
3. Vidyaratne, I.; Scott, J.; Gambarotta, S.; Budzelaar, P. H. M. *Inorg. Chem.* **2007**, *46*, 7040-7049.
4. Stubbert, B. D.; Peters, J. C.; Gray, H. B. *J. Am. Chem. Soc.* **2011**, *133*, 18070-18073.
5. Lu, C. C.; Bill, E.; Weyhermüller, T.; Bothe, E.; Wieghardt, K. *J. Am. Chem. Soc.* **2008**, *130*, 3181-3197.
6. (a) Ni, Z.; McDaniel, A. M.; Shores, M. P. *Chem. Sci.* **2010**, *1*, 615-621; (b) McDaniel, A. M.; Tseng, H.-W.; Damrauer, N. H.; Shores, M. P. *Inorg. Chem.* **2010**, *49*, 7981-7991.
7. (a) Larsen, E.; LaMar, G. N.; Wagner, B. E.; Parks, J. E.; Holm, R. H. *Inorg. Chem.* **1972**, *11*, 2652-2668; (b) McLachlan, G. A.; Fallon, G. D.; Spiccia, L. *Acta Crystallogr., Sect. C: Cryst. Struct. Commun.* **1996**, *52*, 309-312; (c) Qian, M.; Gou, S. H.; He, L.; Zhou, Y. M.; Duan, C. Y. *Acta Crystallogr., Sect. C: Cryst. Struct. Commun.* **1999**, *55*, 742-744; (d) Li, S.-N.; Ren, Y.-W.; Li, J.; Zhang, F.-X.; Hu, M.-C. *Acta Crystallogr., Sect. E: Struct. Rep. Online* **2006**, *62*, m498-m499; (e) Kirchner, R. M.; Mealli, C.; Bailey, M.; Howe, N.; Torre, L. P.; Wilson, L. J.; Andrews, L. C.; Rose, N. J.; Lingafelter, E. C. *Coord. Chem. Rev.* **1987**, *77*, 89-163.
8. (a) Gütlich, P.; Hauser, A. *Coord. Chem. Rev.* **1990**, *97*, 1-22; (b) Gütlich, P.; Garcia, Y.; Goodwin, H. A. *Chem. Soc. Rev.* **2000**, *29*, 419-427; (c) Halcrow, M. A. *Chem. Soc. Rev.* **2011**, *40*, 4119-4142; (d) Halcrow, M. A. *Polyhedron* **2007**, *26*, 3523-3576; (e) Klug, C. M.; McDaniel, A. M.; Fiedler, S. R.; Schulte, K. A.; Newell, B. S.; Shores, M. P. *Dalton Trans.* **2012**, *41*, 12577-12585.
9. Toftlund, H. *Coord. Chem. Rev.* **1989**, *94*, 67-108.
10. We note that cyclic imines other than pyridine have been condensed with tren to generate multidentate tripodal ligands.^{19,20} However, for this work our focus is on iminopyridine species.
11. (a) Seredyuk, M.; Gaspar, A. B.; Ksenofontov, V.; Galyametdinov, Y.; Kusz, J.; Gütlich, P. *J. Am. Chem. Soc.* **2008**, *130*, 1431-1439; (b) Seredyuk, M. *Inorg. Chim. Acta* **2012**, *380*, 65-71.
12. Qu, P.; Meyer, G. J. *Langmuir* **2001**, 6720-6728.
13. Ni, Z.; Shores, M. P. *J. Am. Chem. Soc.* **2008**, *131*, 32-33.
14. Oila, M. J.; Tois, J. E.; Koskinen, A. M. P. *Tetrahedron Lett.* **2005**, *46*, 967-969.

15. Jabre, N. D.; Respondek, T.; Ulku, S. A.; Korostelova, N.; Kodanko, J. J. *J. Org. Chem.* **2010**, *75*, 650-659.
16. Henriques, R. T.; Herdtweck, E.; Kuhn, F. E.; Lopes, A. D.; Mink, J.; Romao, C. C. *J. Chem. Soc., Dalton Trans.* **1998**, 1293-1297.
17. Hagen, K. S. *Inorg. Chem.* **2000**, *39*, 5867-5869.
18. Shavaleev, N. M.; Scopelliti, R.; Gumy, F.; Bünzli, J.-C. G. *Inorg. Chem.* **2009**, *48*, 6178-6191.
19. *APEX 2*, Bruker Analytical X-Ray Systems, Inc.: Madison, WI, 2008.
20. Sheldrick, G. M. *SHELXTL*, Version 6.14; Bruker Analytical X-Ray Systems, Inc.: Madison, WI, 1999.
21. Spek, A. L. *J. Appl. Crystallogr.* **2003**, *36*, 7-13.
22. Bain, G. A.; Berry, J. F. *J. Chem. Educ.* **2008**, *85*, 532-536.
23. (a) Evans, D. F. *J. Chem. Soc.* **1959**, 2003-2005; (b) Live, D. H.; Chan, S. I. *Anal. Chem.* **1970**, *42*, 791-792; (c) Ostfeld, D.; Cohen, I. A. *J. Chem. Educ.* **1972**, *49*, 829; (d) Schubert, E. M. *J. Chem. Educ.* **1992**, *69*, 62; (e) Grant, D. H. *J. Chem. Educ.* **1995**, *72*, 39.
24. Becke, A. D. *J. Chem. Phys.* **1993**, *98*, 5648-5652.
25. Frisch, M. J.; et. al. *Gaussian 03*, Gaussian, Inc.: Wallingford CT, 2004
26. Hay, P. J.; Wadt, W. R. *J. Chem. Phys.* **1985**, *82*, 299-310.
27. (a) Ditchfield, R.; Hehre, W. J.; Pople, J. A. *J. Chem. Phys.* **1971**, *54*, 724-728; (b) Hehre, W. J.; Ditchfield, R.; Pople, J. A. *J. Chem. Phys.* **1972**, *56*, 2257-2261; (c) Binkley, J. S.; Pople, J. A.; Hehre, W. J. *J. Am. Chem. Soc.* **1980**, *102*, 939-947; (d) Francl, M. M.; Pietro, W. J.; Hehre, W. J.; Binkley, J. S.; Gordon, M. S.; DeFrees, D. J.; Pople, J. A. *J. Chem. Phys.* **1982**, *77*, 3654-3665.
28. Herzog, S.; Aul, H. *Z. Naturforsch.* **1960**, *15b*, 617.
29. Scarborough, C. C.; Sproules, S.; Weyhermüller, T.; DeBeer, S.; Wieghardt, K. *Inorg. Chem.* **2011**, *50*, 12446-12462.
30. The trigonal pocket side lengths were taken as the distances between the oxygen atoms in each ester group which faced *toward* the metal center. In all cases except the Fe(II) complex **3**, this was the noncarbonyl oxygen atom of each ester.
31. (a) Chum, H. L.; Rock, M.; Murakami, N. Y.; Jordan, I.; Rabockai, T. *J. Electroanal. Chem.* **1977**, *76*, 277-285; (b) Choudhury, S.; Deb, A. K.; Goswami, S. *Polyhedron* **1994**, *13*, 1062-1068.
32. (a) Da Luz, D.; Franco, C. V.; Vencato, I.; Neves, A.; Mascarenhas, Y. P. *J. Coord. Chem.* **1992**, *26*, 269-283; (b) Kryatov, S. V.; Mohanraj, B. S.; Tarasov, V. V.; Kryatova, O. P.; Rybak-Akimova, E. V.; Nuthakki, B.; Rusling, J. F.; Staples, R. J.; Nazarenko, A. Y. *Inorg. Chem.* **2002**, *41*, 923-930.

33. (a) Marrs, D. J.; McKee, V.; Nelson, J.; Lu, Q.; Harding, C. J. *Inorg. Chim. Acta* **1993**, *211*, 195-202; (b) Qin, L.; Nelson, J.; McCann, M. *J. Inorg. Biochem.* **1993**, *51*, 633-639.
34. McDaniel, A. M.; Tseng, H.-W.; Hill, E. A.; Damrauer, N. H.; Rappé, A. K.; Shores, M. P., *Submitted to Inorg. Chem.*
35. Hauser, A.; Gütllich, P., Goodwin, H. A., Eds.; Springer Berlin / Heidelberg: 2004; Vol. 233, p 49-58.
36. Garcia, Y.; Gütllich, P.; Gütllich, P., Goodwin, H. A., Eds.; Springer Berlin / Heidelberg: 2004; Vol. 234, p 786-786.
37. (a) Halepoto, D. M.; Holt, D. G. L.; Larkworthy, L. F.; Leigh, G. J.; Povey, D. C.; Smith, G. W. *J. Chem. Soc., Chem. Commun.* **1989**, 1322-1323; (b) Halepoto, D. M.; Holt, D. G. L.; Larkworthy, L. F.; Povey, D. C.; Smith, G. W.; Leigh, G. J. *Polyhedron* **1989**, *8*, 1821-1822.
38. (a) Goodwin, H. A.; Gütllich, P., Goodwin, H. A., Eds.; Springer Berlin / Heidelberg: 2004; Vol. 233, p 59-90; (b) Toftlund, H.; McGarvey, J. J.; Gütllich, P., Goodwin, H. A., Eds.; Springer Berlin / Heidelberg: 2004; Vol. 233, p 151-166.
39. Robinson, M. A.; Curry, J. D.; Busch, D. H. *Inorg. Chem.* **1963**, *2*, 1178-1181.
40. We note that the apparent ligand field parameter is actually stronger for the ester-containing ligand L^{5-00Me} (1155 cm^{-1}) as compared to its counterpart without ester functionalization (1124 cm^{-1}).³⁸ This is unexpected since the addition of an electron withdrawing group is expected to decrease σ donation ability and provide a weaker ligand field. We also note that there is a scaling factor (between 1.1 - 1.0)³⁹ for converting between the Ni(II) ligand field to the Fe(II) ligand field which could account for the discrepancy in the apparent ligand field parameters vs. the nature of the ligand functional groups.
41. Goodwin, H. A.; Gütllich, P., Goodwin, H. A., Eds.; Springer Berlin / Heidelberg: 2004; Vol. 234, p 786-786.
42. Mueller, E. W.; Spiering, H.; Gütllich, P. *Inorg. Chem.* **1984**, *23*, 119-120.
43. Figgins, P. E.; Busch, D. H. *J. Phys. Chem.* **1961**, *65*, 2236-2240.

Chapter 3. Synthesis of Functionalized Hexadentate Fe(II) Complexes: Toward Anion-Dependent Spin Switching in Polar Media

Reproduced in part with permission from *European Journal of Inorganic Chemistry*, submitted for publication. Unpublished work copyright 2012 Wiley-Blackwell.

3.1 Introduction

We and others are interested in understanding the factors that control spin-state switching in solution in order to develop new applications for spin-crossover (SC)-based materials.¹ Since small energies separate high-spin (HS) and low-spin (LS) states in a typical Fe(II) SC system, non-covalent interactions between a complex and its environment significantly impact the observed spin states. Under the right conditions — a suitably balanced ligand field, complex solution stability and sufficiently perturbing host-guest interactions — spin-state switching may act as a reporter in a chemical sensing scheme.

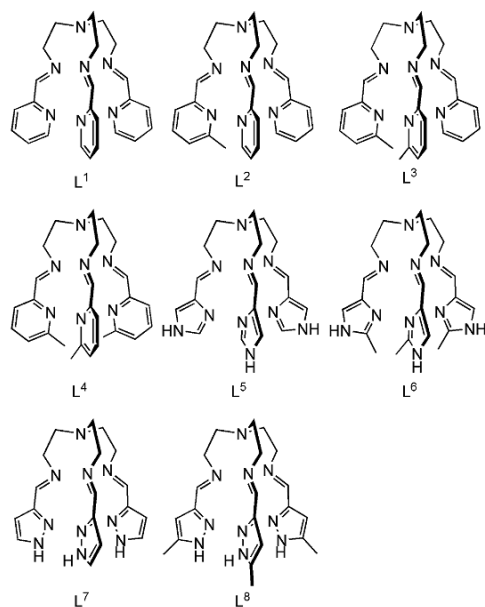
Anions provide an attractive substrate for sensing since they play important roles in biology and the environment.² Recognizing the impacts on living systems, interest in effective anion sensing has spurred work designing molecular sensor species.^{2a,3} Metal incorporation into sensing architectures has become increasingly widespread: they are used to influence complex geometry, add additional reporting functionality (e.g., optical, electrochemical, or magnetic differences in the anion-free and -associated states) or to be the site of anion-binding itself.^{2a,4} Specific to spin-state switching schemes, it appears that anion-sensing and spin-crossover complexes are a natural fit, since an electrostatic cation-anion interaction offers a strong chemical trigger for SC property perturbation and most SC complexes are cationic.

Hydrogen-bonding interactions are particularly well suited for anion sensing; installation of hydrogen bond donors has led to successful anion recognition and binding in metal-based complex cations in solution. Our efforts have focused on incorporation of Fe(II) metal centers into complexes with hydrogen bond donor moieties which are capable of anion recognition. The anion-binding event can induce Fe(II)

center spin-crossover in an appropriately tuned ligand field, resulting in dramatic changes in complex magnetic and optical properties.⁵ The changes in magnetic properties can be probed by solid state and solution magnetic susceptibility measurements as well as by direct monitoring of proton chemical shifts in the ¹H NMR. The optical properties are often easily followed by electronic absorption spectroscopy and are sometimes apparent by visual inspection.

Fe(II) complexes featuring the bidentate ditopic ligand H₂bip demonstrate solution phase anion-dependent spin switching.^{5a-c} Recently we have demonstrated that homo- and heteroleptic Fe(II) complexes using H₂bip, a diimine ligand with –NH hydrogen bonding moieties, demonstrate solution phase anion-dependent spin switching.^{5a-c} However, in order to minimize ligand exchange in solution, these studies must be performed in dichloromethane, a solvent of low polarity. Extending this proof-of-concept work into more polar media (such as alcohols, acetonitrile, or water) would be more relevant to the aqueous conditions of biological media or environmental samples. In order to do this, ligand lability must be minimized.

One way to reduce enhance complex thermodynamic stability is by exploiting the chelate effect. Increasing ligand denticity should improve the thermodynamic stability of the resulting metal complex while in solution, and a single hexadentate ligand would be ideal. Hexadentate ligands based on the Schiff-base condensation of tris(2-aminoethyl)amine (tren) with pyridinealdehydes combine with Fe(II) to produce SC species;⁶ a variety of Fe(II) complexes with related tripodal ligands (shown in Scheme 3.1) also demonstrate tunable SC behavior. Hoselton and coworkers synthesized SC complexes using the ligands L¹-L⁴.⁶ The authors found that L⁴ formed exclusively HS complexes in solution between 185 K and 435 K, whereas L¹ formed only LS complexes up to 350 K. Only the mixed ligands L² and L³ formed complexes capable of spin-crossover, and spin transition onset temperature was seen to decrease with increasing methyl substitution, as expected from increasing steric bulk.

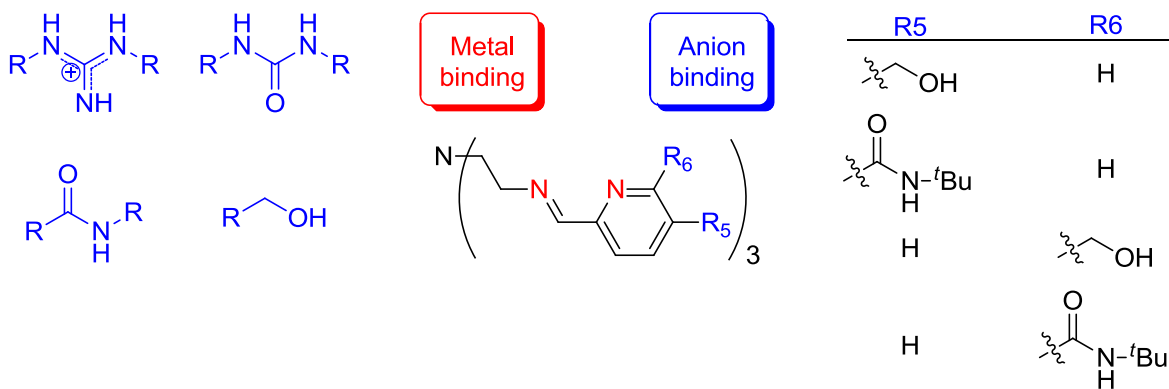


Scheme 3.1. Tripodal hexadentate ligands. Adapted from Ref. 7.

While spin switching has been demonstrated in several Fe(II) complexes which have been synthesized using tren-based tripodal ligands, most include either pyridine or imidazole moieties containing varying degrees of aliphatic or aryl steric bulk as shown in Scheme 3.1. However, none of these complexes have been shown to act as an anion receptor,⁸ which is unsurprising given the absence of anion-binding functional groups. Ideally, it would be possible to couple an appropriately tuned ligand field provided by a hexadentate ligand with the electronic or steric/geometric influence of guest binding to generate the SC regime. Alteration of non-inner sphere anions has been shown to have a dramatic effect on SC transitions of identically chelated Fe(II) cations.⁹ It is reasonable to hypothesize that direct anion-ligand interaction has the potential to perturb the ligand field enough to cause a spin state transition in a cation poised for spin-crossover since spin-state transitions only require energy perturbations on the order of $k_B T$ (~ 2.5 kJ/mol at room temperature).

Competent anion-binding is optimized when multiple hydrogen bonding groups are oriented toward a single binding site or pocket, and when hydrogen bonding is coupled with electrostatic interactions.¹⁰ Poising $-NH$ and $-OH$ groups can encourage direct anion-ligand interaction in tripodal complexes

(Scheme 3.2). Metal-based anion receptors can effectively combine these two binding modes, as shown in the recent work by Fabbrizzi and coworkers on a trisimidazolium cage organized around a Fe(II) ion, that is capable of binding spherical and linear anions.¹¹ A second example uses Cu²⁺ ions to preorganize a tripodal ligand to sense phosphates.¹²



Scheme 3.2. Potential anion-binding functional groups (left), tripodal ditopic ligand family used in this work (center), and actual ligand configurations used (right).

To observe Fe(II) anion-dependent spin switching in solution, several criteria need to be met. The complex must competently bind anions, which means appropriate anion-binding motifs must be incorporated into the ligand architecture. The host-guest association must sufficiently perturb the ligand field to prompt spin-state switching and the spin switching event must take place in a relatively narrow temperature range: between 0°C to 100°C for aqueous solutions, and in slightly larger temperature windows for polar-organic solvents such as methanol or acetonitrile. These last two criteria are highly dependent on the ligand field.

In this work, we targeted ligands based on pyridines functionalized at the 5- or 6-position as shown in the center of Scheme 3.2. Functionalization at these positions would include groups capable of hydrogen bonding, such as –OH and –NH, as shown on the right of Scheme 3.2. Chelation of the ligand to a Fe(II) center would provide positive charge to attract anions and also organize the hydrogen bond donor groups into a pocket where anions could bind. The ligand field provided by the diimine ligand arms would be

near the SC regime.¹³ Lastly, we hypothesized that successful anion-binding could do two possible things. Similar to the behavior observed for H₂bip complexes,⁵ successful anion-binding would increase ligand field strength in HS 6-position complexes to cause HS → LS switching. Or anion-binding to LS 5-position complexes could cause geometric perturbation of the Fe(II) center by pushing ligand arms out, leading to lengthening of Fe–N bonds and transition to the HS state. Herein, we report on the spin behavior of Fe(II) complexes of **L**^{5-OH}, **L**^{5-ONH*t*Bu}, **L**^{6-OH}, and **L**^{6-ONH*t*Bu} where we find competent cation-chloride interactions in polar solution and potential evidence for spin-state switching as a result of anion-binding for the 5-position complexes.

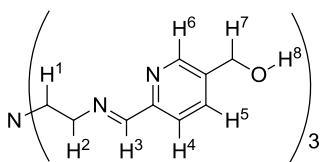
3.2 Division of Labor

All experimental work was performed by Ashley McDaniel. The preliminary work on complexes of **L**^{6-OH} described here was continued by Christina Klug.^{13a}

3.3 Experimental Section

3.3.1 Preparation of Compounds. Unless otherwise noted, compound manipulations were performed either inside a dinitrogen-filled glovebox (MBRAUN Labmaster 130) or via Schlenk techniques on an inert gas (N₂) manifold. The preparations of [Fe(SO₃CF₃)₂(CH₃CN)₂]¹⁴, diethyl pyridine-2,5-dicarboxylate,¹⁵ 2,5-pyridinedimethanol,¹⁶ 6-(Hydroxymethyl)picolinaldehyde,¹⁷ and 6-(methoxycarbonyl)nicotinic acid¹⁸ have been described previously. Literature procedures for generating amides from acid chlorides¹⁹ were modified to use 6-(methoxycarbonyl)nicotinic acid as the starting material and *tert*-butylamine as the reagent to give methyl 5-(*tert*-butylcarbamoyl)picolinate. N-(*tert*-butyl)-6-formylnicotinamide was synthesized analogously to methyl 6-formylnicotinate.²⁰ Pentane was distilled over sodium metal and subjected to three freeze-pump-thaw cycles. Other solvents were sparged with dinitrogen, passed over molecular sieves, and degassed prior to use. All other reagents were obtained from commercial sources and were used without further purification.

5-(Hydroxymethyl)picolinaldehyde (3.1). A synthesis has been reported in a patent²¹ using SeO₂ as the oxidant, while in this synthesis MnO₂ is used as an alternative oxidizing agent.¹ 2,5-pyridinedimethanol (0.486 g, 3.49 mmol) was dissolved in CHCl₃ (100 mL). Activated MnO₂ (6.07 g, 69.9 mmol) was added and the suspension was stirred at room temperature. After 45 min, the mixture was filtered through Celite, the solids were washed with CHCl₃ (3 × 100 mL), and the filtrate was collected. The solvent was removed by rotary evaporation to give a yellow solid, which was purified by column chromatography (EtOAc on silica gel) to give 0.165 g (34%) of light yellow powder. ¹H NMR (300 MHz, CDCl₃, δ): 4.86 (s, 2H, -CH₂OH), 7.90 (d, 1H, H³), 7.96 (d, 1H, H⁴), 8.75 (s, 1H, H⁶), 10.05 (s, 1H, CHO), which qualitatively matches previously reported chemical shifts.²¹



(6,6',6''-((1E,1'E,1''E)-((nitrilotris(ethane-2,1-

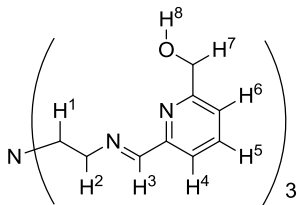
diyl))tris(azanylylidene))tris(methanylylidene))tris(pyridine-6,3-diyl))trimethanol (L^{5-OH}). In air, 5-(Hydroxymethyl)picolinaldehyde (0.203 g, 1.46 mmol) was dissolved in methanol (6 mL). A methanolic solution (5 mL) of tris(2-aminoethyl)amine (tren) (0.071 g, 0.486 mmol) was added and the resulting yellow solution was heated at reflux for 14 hours. The solvent was removed by rotary evaporation, leaving 0.245 g (97%) of an orange oil. ¹H NMR (300 MHz, CDCl₃, δ): 2.94 (t, 6H, H¹), 3.50 (t, 3H, H⁸), 3.70 (t, 6H, H²), 4.73 (s, 6H, H⁷), 7.62 (dd, 3H, H⁵), 7.82 (d, 3H, H⁴), 8.08 (s, 3H, H³), 8.54 (d, 3H, H⁶), and is included as Figure A2.6. ESI-MS (MeOH): 526.27 m/z ([L^{5-OH}Na]⁺).

¹ While working on the L^{5-OOMe} ligand described in Chapter 2, a literature procedure using SeO₂ as the oxidant to generate the aldehyde precursor was employed. However residual Se gave the isolated product a brick red color and unrecognized transesterification from the previous synthetic step made the reaction look unsuccessful. An alternative literature reported oxidant, MnO₂, was subsequently used and gave the desired product. This methodology was extended to the ligands reported in this chapter. Use of MnO₂ has drawbacks; it is required in 10-20 fold excess and the yields are typically lower than those for reactions using SeO₂. In the future, SeO₂ is probably a better choice for oxidation.

[Fe(L^{5-OH})]SO₄ (3.2). A solution of FeSO₄·7H₂O (13.7 mg, 0.049 mmol) in methanol (3 mL) was added to a stirring solution of L^{5-OH} (24.5 mg, 0.049 mmol) in methanol (2 mL). Upon combination, the reaction mixture immediately turned violet-fuchsia followed by formation of a fuchsia precipitate. The mixture was stirred for an additional 16 h, after which the precipitate was collected by filtration to give 24.3 mg (75%) of product. ESI-MS (MeOH): 558.07 m/z ([Fe(L^{5-OH}-H)]⁺), 279.73 m/z ([Fe(L^{5-OH})]²⁺).

[Fe(L^{5-OH})](BF₄)₂ (3.3). Solid Fe(BF₄)₂·6H₂O (50.3 mg, 0.149 mmol) was added to a stirring methanolic solution (3 mL) of L^{5-OH} (73.4 mg, 0.146 mmol), resulting in an immediate color change to violet-plum. The mixture was stirred for 2 hours and a dark plum precipitate formed. The precipitate was collected by filtration to give 94.5 mg (88%) of plum-colored solid. ESI-MS (CH₃CN): 279.67 m/z ([Fe(L^{5-OH})]²⁺). ¹H NMR (300 MHz, CD₃CN, δ): 3.08 (m, 6H, H¹), 3.39 (m, 3H, H⁸), 3.53 (m, 6H, H²), 4.50 (d, 6H, H⁷), 6.96 (s, 3H, H³), 8.06 (d, 3H, H⁵), 8.19 (d, 3H, H⁴), 9.09 (d, 3H, H⁶) and is included as Figure A2.7. Calcd. for C₂₇H₃₃B₂F₈FeN₇O₃: C, 44.24; H, 4.54; N, 13.38. Found: C, 43.70; H, 5.02; N, 13.36 and, upon repeat analysis, C, 43.56; H, 4.80; N, 13.25. Crystals suitable for X-ray diffraction were grown by diethyl ether diffusion into a concentrated solution of the complex in acetonitrile.

[Fe(L^{5-OH})](BPh₄)₂ (3.4). An aqueous solution (3 mL) of NaBPh₄ (14.7 mg, 0.043 mmol) sparged with dinitrogen was added to a stirring, dinitrogen-sparged aqueous solution (2 mL) of [FeL^{5-OH}]₂SO₄ (12.1 mg, 0.018 mmol), resulting in the immediate formation of a fuchsia precipitate. The solid was collected by filtration, washed with dinitrogen-sparged distilled water (10 mL) and dried in vacuo to give 16.0 mg (72%) of fuchsia powder. ¹H NMR (300 MHz, CD₃CN, δ): 3.03 (6H, H¹), 3.38 (3H, H⁸), 3.46 (6H, H²), 4.49 (6H, H⁷), 6.83 (8H, BPh₄), 6.90 (s, 3H, H³), 6.97 (16H, BPh₄), 7.26 (16H, BPh₄), 8.04 (3H, H⁵), 8.15 (3H, H⁴), 8.94 (3H, H⁶) and is included as Figure A2.8. ESI-MS (CH₃CN): 878.07 m/z ([Fe(L^{5-OH})BPh₄]⁺), 279.67 m/z ([Fe(L^{5-OH})]²⁺).



(6,6',6''-((1E,1'E,1''E)-((nitrilotris(ethane-2,1-

diyl))tris(azanylylidene))tris(methanylylidene))tris(pyridine-6,2-diyl))trimethanol (L^{6-OH}). 6-

(Hydroxymethyl)picolinaldehyde (0.150g, 1.10 mmol) was dissolved in methanol (30 mL). To this, a methanolic solution (10 mL) of tren (0.053 g, 0.37 mmol) was added and the resulting yellow solution was brought to reflux. After 16 hours the resulting orange solution was cooled and the solvent was removed by rotary evaporation to give 0.181 g (100%) of an orange oil. 1H NMR (300 MHz, $CDCl_3$, δ): 2.98 (t, 6H, H^1), 3.74 (t, 6H, H^2), 4.12 (br s, 3H H^8), 4.75 (s, 6H, H^7), 7.25 (d, 3H, H^6), 7.68 (d, 3H, H^4), 7.81 (t, 3H, H^5), 8.26 (s, 3H, H^3) and is included as Figure A2.9. ESI-MS (MeOH): 526.27 m/z ($[(L^{6-OH})Na]^+$).

$[Fe(L^{6-OH})](SO_3CF_3)_2$ (**3.5**). A solution of L^{6-OH} (0.486 g, 0.965 mmol) in methanol (3 mL) was added to a stirring solution of $[Fe(SO_3CF_3)_2(CH_3CN)_2]$ (0.421 g, 0.965 mmol) in methanol (1 mL). The resulting dark-red solution was stirred for 16 hours, and then the solvent was removed in vacuo to give a red residue. The residue was triturated with diethyl ether (10 mL) to give a dark red powder. The powder was collected by filtration and washed with diethyl ether (3×3 mL) to give 0.756 g (91%) of product. ESI-MS (CH_3OH): 558.20 m/z ($[Fe(L^{6-OH}-H)]^+$).

$[Fe(L^{6-OH})](BF_4)_2$ (**3.6**). Solid $Fe(BF_4)_2 \cdot 6H_2O$ (58.8 mg, 0.174 mmol) was placed under dinitrogen. To this, a dinitrogen-sparged methanolic solution (5 mL) of L^{6-OH} (85.6 mg, 0.170 mmol) was added by syringe. The resulting solution immediately turned deep red. The solution was stirred for 10 min, after which the solvent was removed in vacuo to give a dark red residue 98 mg (79%). ESI-MS (CH_3OH): 558.20 m/z ($[Fe(L^{6-OH}-H)]^+$).

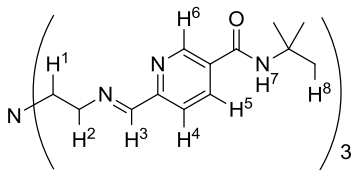
$[Fe(L^{6-OH})]I_2$ (**3.7**). A solution of tetrabutylammonium iodide (TBAI) (0.178 g, 0.481 mmol) in acetonitrile (5 mL) was slowly added to a stirring solution of $[Fe(L^{6-OH})](SO_3CF_3)_2$ (0.178 g, 0.208 mmol) in acetonitrile (3 mL). Upon addition, a red precipitate formed and the mixture was stirred for 16 hours.

The precipitate was collected by filtration and washed with cold acetonitrile (3 × 3 mL) and diethyl ether (3 × 3 mL) to give 0.119 g (70%) of product. ESI-MS (CH₃OH): 558.20 m/z ([Fe(L^{6-OH}-H)]⁺).

[Fe(L^{6-OH})]Br₂ (3.8). A solution of FeBr₂ (0.042 g, 0.199 mmol) in methanol (3 mL) was slowly added to a stirring solution of L^{6-OH} (0.100 g, 0.199 mmol) in methanol (4 mL). The resulting dark-red solution was stirred for 1 hour, and then the solvent was removed in vacuo to give a red residue. The residue was triturated with pentane (10 mL) to give a dark-red powder. The powder was collected by filtration and washed with pentane (3 × 3 mL) to give 0.114 g (80%) of product. ESI-MS (CH₃OH): 558.20 m/z ([Fe(L^{6-OH}-H)]⁺). Crystals suitable for X-ray diffraction were grown by pentane diffusion into a concentrated solution of the complex in a mixture of ethanol and methanol.

[Fe(L^{6-OH})]Cl₂ (3.9). A solution of solution of L^{6-OH} (0.200 g, 0.397 mmol) in methanol (4 mL) was slowly added to a stirring solution of FeCl₂ (0.051 g, 0.397 mmol) in methanol (2 mL). The resulting red-purple solution was stirred for 16 hours, and then the solvent was removed in vacuo to give a dark-red residue. The residue was triturated with diethyl ether (10 mL) to give a dark-red powder. The powder was collected by filtration and washed with diethyl ether (3 × 3 mL) to give 0.193 g (77%) of product. ESI-MS (CH₃OH): 558.20 m/z ([Fe(L^{6-OH}-H)]⁺).

[Fe(L^{6-OH})](BPh₄)₂ (3.10). A solution of NaBPh₄ (0.233 g, 0.680 mmol) in acetonitrile (4 mL) was added to a stirring solution of FeCl₂ (0.043 g, 0.340 mmol) in acetonitrile (4 mL). The mixture was stirred for 2 hours at room temperature, finally producing a colorless solution and a white precipitate. The precipitated NaCl was removed by filtration. The filtrate was added to a solution of L^{6-OH} (0.171 g, 0.340 mmol) in acetonitrile (8 mL), immediately forming a dark-red solution. The solution was concentrated in vacuo to 5 mL and filtered to remove residual NaCl. The solvent was removed from the filtrate in vacuo, leaving a sticky purple-red residue which was triturated with methanol (3 × 3 mL) and diethyl ether (3 × 3 mL) to give a purple-red powder. The powder was collected by filtration, washed with diethyl ether (3 × 3 mL), and dried in vacuo to give 0.363 g (89%) of a brick red solid. ESI-MS (CH₃CN): 279.60 ([Fe(L^{6-OH})²⁺], 558.20 m/z ([Fe(L^{6-OH}-H)]⁺).



6,6',6''-((1E,1'E,1''E)-((nitrilotris(ethane-2,1-

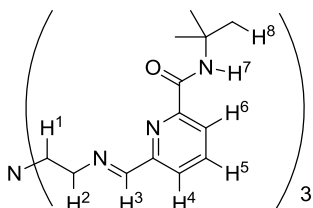
diyl))tris(azanylylidene))tris(methanylylidene))tris(N-(tert-butyl)nicotinamide) L^{5-ONHtBu}. A solution of tren (0.131 g, 0.88 mmol) in acetonitrile (2 mL) was added to a solution of N-(*tert*-butyl)-6-formylnicotinamide (0.60 g, 2.91 mmol) in acetonitrile (8 mL). Upon addition, the reaction mixture darkened to a dark-yellow color. The reaction mixture was stirred at room temperature for 16 hours, and then the solvent was removed in vacuo to leave 0.52 g (85%) of yellow powder product. ¹H NMR (300 MHz, CD₃CN, δ): 1.45 (s, 27H, H⁸), 2.92 (t, 6H, H¹), 3.72 (t, 6H, H²), 6.86 (s, 3H, H⁷), 7.85 (d, 3H, H⁴), 8.00 (dd, 3H, H⁵), 8.22 (s, 3H, H³), 8.78 (d, 3H, H⁶), and is included as Figure A2.10. ESI-MS (CH₃OH): 733.53 ([L^{5-ONHtBu})Na]⁺)

{[Fe(L^{5-ONHtBu})]Cl₂}[FeCl₄] (3.11). A solution of L^{5-ONHtBu} (0.070 g, 0.098 mmol) in acetonitrile (3 mL) was added to FeCl₂ (0.019 g, 0.147 mmol) stirring in acetonitrile (1 mL). The resulting dark-purple solution was stirred for 2 hours at room temperature, and then the solvent was removed in vacuo to give a purple residue. This solid was triturated with diethyl ether (10 mL) to give a dark-purple powder. The powder was collected by filtration and washed with diethyl ether (3 × 3 mL) to give 0.064 g (72%) of product. ¹H NMR (400 MHz, CD₃CN, δ): 1.23 (27H, H⁸), 3.08 (6H, H¹), 3.42 (3H, H²), 3.56 (3H, H²), 7.56 (3H, H⁶), 8.22 (3H, H⁴), 8.34 (3H, H⁵), 8.98 (3H, H⁷), 9.07 (3H, H³), and is included as Figure A2.11. ESI-MS (CH₃CN): 801.33 m/z ([Fe(L^{5-ONHtBu})Cl]⁺), 383.27 m/z ([Fe(L^{5-ONHtBu})]²⁺). Calcd for C₇₈H₁₀₈Cl₆Fe₃N₂₀O₆: C, 51.99; H, 6.04; N, 15.55. Found: C, 51.87; H, 6.16; N, 15.33. Crystals suitable for X-ray diffraction were grown by diethyl ether diffusion into a concentrated solution of the complex in acetonitrile.

[Fe(L^{5-ONHtBu})](BF₄)₂ (3.12). A solution of Fe(BF₄)₂·6H₂O (0.024 g, 0.076 mmol) in acetonitrile (3mL) was added to a solution of L^{5-ONHtBu} (0.054 g, 0.076 mmol) in acetonitrile (2 mL) . The resulting dark-purple solution was stirred for 2 hours at room temperature, and then the solvent was removed in

vacuo to give a purple residue. This solid was triturated with diethyl ether (10 mL) to give a dark-purple powder. The powder was collected by filtration, washed with diethyl ether (3 × 3 mL) and dried in vacuo to give 0.061 g of product. ¹H NMR (400 MHz, CD₃CN, δ): 1.31 (27H, H⁸), 3.09 (6H, H¹), 3.56 (3H, H²), 3.71 (3H, H²), 6.79 (3H, H⁷), 7.37 (3H, H⁶), 8.34 (3H, H⁴), 8.45 (3H, H⁵), 9.27 (3H, H³), and is included as Figure A2.12. ESI-MS (CH₃CN): 853.0 m/z ([Fe(L^{5-ONH*t*Bu})(BF₄)]⁺), 383.27 m/z ([Fe(L^{5-ONH*t*Bu})]²⁺). Calcd for C₃₉H₅₆B₂F₈FeN₁₀O₄ (3·H₂O): C, 48.88; H, 5.89; N, 14.61. Found: C, 48.94; H, 5.74; N, 14.35.

[Fe(L^{5-ONH*t*Bu})](BPh₄)_{1.5}Cl_{0.5} (3.13). A solution of {[Fe(L^{5-ONH*t*Bu})]-Cl}₂[FeCl₄] (0.040 g, 0.022 mmol) in dichloromethane (3 mL) was added to a stirring mixture of NaBPh₄ (0.034 g, 0.100 mmol) in dichloromethane (3 mL). The resulting dark-purple mixture was stirred for 16 hours, and then filtered to remove precipitated NaCl. The solvent was removed in vacuo from the dark-purple filtrate to give a dark-blue residue. The residue was triturated with diethyl ether (10 mL) to give a dark purple powder. The powder was collected by filtration and washed with diethyl ether (3 × 3 mL) to give 0.051 g (90%) of product. Based on ¹H NMR integration and peak shifts, this is a mixed salt with incomplete anion exchange. ¹H NMR (400 MHz, CD₃CN, δ): 1.25 (27H, H⁸), 3.06 (6H, H¹), 3.43 (3H, H²), 3.58 (3H, H²), 6.82 (6.5 H, BPh₄), 6.98 (13H, BPh₄), 7.26 (13H, BPh₄), 7.49 (3H, H⁶), 8.20 (3H, H⁴), 8.34 (br, 3H, H⁷), 8.34 (3H, H⁵), 9.05 (3H, H³), and is included as Figure A2.13. ESI-MS (CH₃CN): 1085.20 m/z ([Fe(L^{5-ONH*t*Bu})(BPh₄)]⁺), 383.20 m/z ([Fe(L^{5-ONH*t*Bu})]²⁺).



6,6',6''-((1E,1'E,1''E)-((nitrilotris(ethane-2,1-

diyl))tris(azanylylidene))tris(methanylylidene))tris(N-(tert-butyl)picolinamide) (L^{6-ONH*t*Bu}). A

solution of tren (0.025 g, 0.171 mmol) in acetonitrile (1 mL) was added to a solution of N-(*tert*-butyl)-6-formylpicolinamide (0.136 g, 6.59 mmol) in acetonitrile (2 mL) to give a golden-yellow solution. The reaction mixture was stirred at room temperature for 16 hours, and then the solvent was removed in vacuo, resulting in a sticky residue. The residue was triturated with pentane (3 × 2 mL) to yield 0.085 g

(70%) of yellow powder. ^1H NMR (300 MHz, CDCl_3 , δ) 1.49 (s, 27H, H^8), 3.04 (t, 6H, H^1), 3.84 (t, 6H, H^2), 7.84 (t, 3H, H^5), 7.97 (s, 3H, H^7), 8.05 (d, 3H, H^6), 8.19 (d, 3H, H^4), 8.38 (s, 3H, H^3) and is included as Figure A2.14.

$[\text{Fe}(\text{L}^{6\text{-ONHtBu}})]\text{Cl}_2$ (3.14). A solution of FeCl_2 (0.007 g, 0.056 mmol) in methanol (1 mL) was added to a stirring solution of $\text{L}^{6\text{-ONHtBu}}$ (0.040 g, 0.0561 mmol) in methanol (3 mL). The resulting dark-purple solution was stirred for 16 hours, and then the solvent was removed in vacuo to give a purple residue. The residue was triturated with diethyl ether (5 mL) to give a dark-purple powder. The powder was collected by filtration and washed with diethyl ether (3×3 mL) to give the final product. ESI-MS (CH_3OH): 765.40 m/z ($[\text{Fe}(\text{L}^{6\text{-ONHtBu}}-\text{H})]^+$).

$[\text{Fe}(\text{L}^{6\text{-ONHtBu}})](\text{SO}_3\text{CF}_3)_2$ (3.15). A solution of $[\text{Fe}(\text{SO}_3\text{CF}_3)_2(\text{CH}_3\text{CN})_2]$ (0.024 g, 0.056 mmol) in methanol (1 mL) was added to a stirring solution of $\text{L}^{6\text{-ONHtBu}}$ (0.040 g, 0.0561 mmol) in methanol (3 mL). The resulting dark-purple solution was stirred for 16 hours, and then the solvent was removed in vacuo to give a purple residue. The residue was triturated with diethyl ether (5 mL) to give a dark-purple powder. The powder was collected by filtration and washed with diethyl ether (3×3 mL) to give the final product. ESI-MS (CH_3OH): 947.07 m/z ($[\text{Fe}(\text{L}^{6\text{-ONHtBu}})(\text{SO}_3\text{CF}_3)_2 \cdot \text{CH}_3\text{OH}]^+$), 916.20 m/z ($[\text{Fe}(\text{L}^{6\text{-ONHtBu}})(\text{SO}_3\text{CF}_3)]^+$), 765.40 m/z ($[\text{Fe}(\text{L}^{6\text{-ONHtBu}}-\text{H})]^+$).

3.3.2 X-Ray Structure Determinations. Crystals suitable for X-ray analyses were coated with Paratone-N oil and supported on a Cryoloop before being mounted on a Bruker Kappa Apex II CCD diffractometer under a stream of dinitrogen. Data collection was performed at 100 or 120 K with Mo $\text{K}\alpha$ radiation and a graphite monochromator, targeting complete coverage and 4-fold redundancy. Initial lattice parameters were determined from at least 500 reflections harvested from 36 frames; these parameters were later refined against all data. Crystallographic data and metric parameters are presented in Table 3.1. Data were integrated and corrected for Lorentz and polarization effects by using SAINT, and semiempirical absorption corrections were applied by using SADABS.²² The structure was solved by direct methods and refined against F^2 with the program XL from the SHELXTL 6.14 software package.²³

Unless otherwise noted, displacement parameters for all non-hydrogen atoms were refined anisotropically. Hydrogen atoms were added at idealized positions and were refined by using a riding model where the displacement parameters were set at 1.2 times those of the attached carbon atom (1.5 for methyl protons).

Table 3.1. Crystallographic data for compounds **3.3**, **3.8** and **3.11**.^a

	3.3 ·CH ₃ CN	3.8 ·0.5MeOH·0.5 EtOH	3.11 ·3CH ₃ CN·(CH ₃ CH ₂) ₂ O
formula	C ₂₉ H ₃₆ B ₂ F ₈ FeN ₈ O ₃	C _{28.50} H ₃₈ Br ₂ FeN ₇ O ₄	C ₈₈ H ₁₁₇ Cl ₆ Fe ₃ N ₂₃ O ₇
fw	774.13	757.32	1989.30
color, habit	purple blocks	red plates	purple plates
<i>T</i> , K	100(2)	100(2)	120(2)
space	<i>Pna</i> 2 ₁	<i>P</i> 2 ₁ / <i>c</i>	<i>P</i> $\bar{1}$
<i>Z</i>	8	4	2
<i>a</i> , Å	15.4403(3)	10.0980(2)	11.9443(11)
<i>b</i> , Å	12.2839(2)	14.0077(3)	21.0685(18)
<i>c</i> , Å	34.8855(6)	22.0804(5)	21.1533(18)
α , deg	90	90	73.208(4)
β , deg	90	94.7740(10)	89.076(4)
γ , deg	90	90	84.615(4)
<i>V</i> , Å ³	6616.6(2)	3112.43(11)	5073.4(8)
<i>d</i> _{calc} , g/cm ³	1.554	1.616	1.302
GOF	1.056	1.055	1.023
<i>R</i> ₁ (<i>wR</i> ₂) ^b	4.42 (10.28)	3.61 (8.71)	6.00(14.33)

^a Obtained with graphite-monochromated Mo K α ($\lambda = 0.71073$ Å) radiation.

^b $R_1 = \sum||F_o| - |F_c||/\sum|F_o|$, $wR_2 = \{\sum[w(F_o^2 - F_c^2)^2]/\sum[w(F_o^2)^2]\}^{1/2}$ for $F_o > 4\sigma(F_o)$.

In the structure of **3.3**·CH₃CN, positional disorder in one of the BF₄ anions was treated by splitting atoms F15 and F16 over two positions (refined to a 56:44 ratio); all thermal parameters were treated anisotropically.

In the structure of **3.8**·0.5CH₃OH·0.5 CH₃CH₂OH, one of the bromide counter ions is disordered over two positions that refine to a 47:53 ratio. Both parts of Br1 were treated anisotropically. There is also positional disorder for the hydroxyl group containing O3 that is disordered over two positions in a 69:21 ratio. Both parts of O3 were also treated anisotropically. There is additionally disorder in the alcohol solvent molecules within the unit cell. The disordered solvent was refined as 50% methanol and 50%

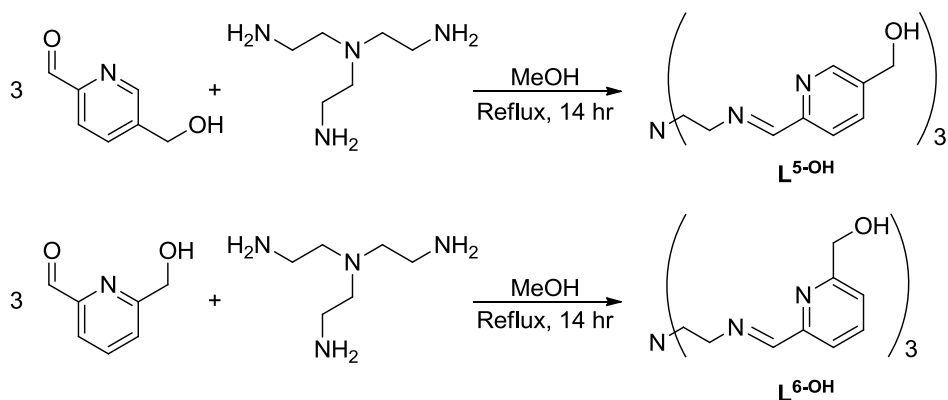
ethanol disordered over two positions with the oxygen atom O4 common to both and at full occupation. All atoms in the disordered solvent were treated anisotropically and the restraints SIMU and DELU were applied.

Solvate molecule disorder in the structure of **3.11**·3CH₃CN·(CH₃CH₂)₂O was modeled in the following manner. Two acetonitrile molecules were modeled at full occupancy. The occupancy of the third acetonitrile molecule was originally tied to a free variable that refined to 70-80% occupancy; this was rounded to full occupancy to give a more chemically reasonable value. Positive residual electron density near the terminal C atom (C82) may be due to further disorder. SAME, DELU and SIMU restraints were used on each of the acetonitrile molecules with the acetonitrile containing N21, C79, and C80 as the model for SAME. Meanwhile, the diethyl ether molecule is disordered over two positions at two sites. Because of the large amount of disorder in this solvent molecule, H atoms were not added to the model. Both disordered solvent molecules were treated isotropically.

3.3.3 Other Physical Methods. Absorption spectra were obtained with a Hewlett-Packard 8453 spectrophotometer in glass cuvettes with 1 cm path lengths in air and near IR spectra were recorded using a Cary 500 spectrophotometer; all experiments were performed at room temperature. Mass spectrometric measurements were performed in either the positive ion or negative ion mode on a Finnigan LCQ Duo mass spectrometer, equipped with an analytical electrospray ion source and a quadrupole ion trap mass analyzer. ¹H NMR spectra were measured using Varian INOVA 300 MHz or 400 MHz instruments. Magnetic susceptibilities in solution were determined by the Evans method²⁴ and diamagnetic corrections were applied using Pascal's constants.²⁵

3.4 Results and Discussion

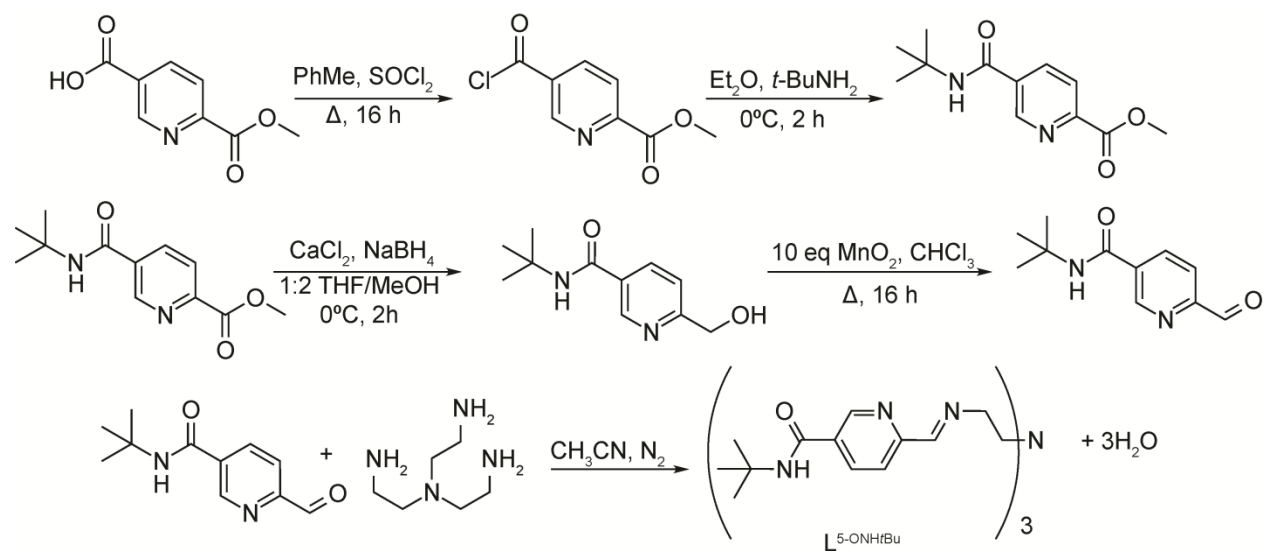
3.4.1 Syntheses. The ligand syntheses for L^{5-OH} and L^{6-OH} are relatively straightforward and necessitate only one step using precursors found in the literature and tren, which is commercially available, as shown in Scheme 3.3.



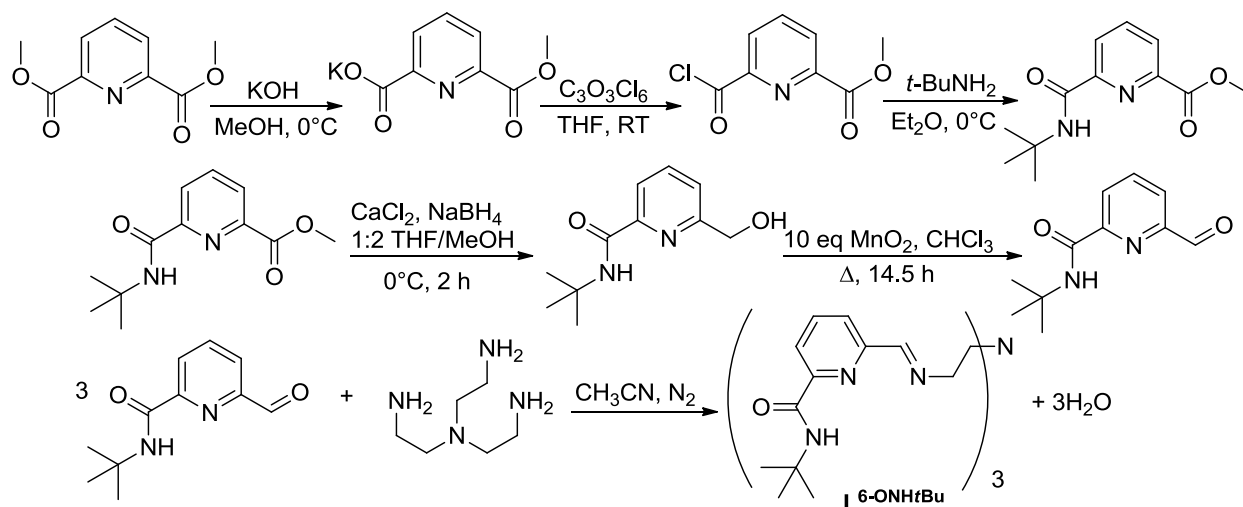
Scheme 3.3. Synthetic pathways for ligands L^{5-OH} and L^{6-OH} .

The 5-hydroxy- or 6-hydroxy-substituted aldehyde starting materials react cleanly with tren to afford the desired tripodal ligands. Neither L^{5-OH} nor L^{6-OH} precipitate from solution and both are isolated as oils. This is a notable difference from the ester based ligand described in Chapter 6 (L^{5-OOMe}) and the two amide based ligands $L^{5-ONHtBu}$ and $L^{6-ONHtBu}$, all of which are isolated as free flowing powders.

The syntheses of ligands $L^{5-ONtBu}$ and $L^{6-ONHtBu}$ provide some challenges and are more elaborate, as shown in Schemes 3.4 and 3.5.



Scheme 3.4. Synthetic pathway for ligand $L^{5-ONHtBu}$. The steps in the top row of the synthetic scheme are modified from Ref. 49. The steps in the middle row are adapted from Ref. 33.



Scheme 3.5. Synthetic pathway for ligand $L^{6\text{-OH}t\text{Bu}}$.

Initially, a published synthetic route²⁶ was used to try to install a 5-position amide via the transformation of 5-position methyl ester precursors. However, this methodology proved unsuccessful, perhaps due to the increased steric bulk of the *t*-butyl amine relative to diaminopropane. A successful alternative synthetic path involves protecting the 2-position as a methyl ester and generating an acid chloride from an unprotected acid or carboxylate at the 5- or 6-positions, respectively. The acid chloride for $L^{5\text{-OH}t\text{Bu}}$ can be successfully synthesized using thionyl chloride; however, violent decomposition of the 6-position acid chloride in the presence of excess thionyl chloride and air in the synthesis of $L^{6\text{-OH}t\text{Bu}}$ prompted the use of a different chlorinating agent. One possibility for the difference in acid chloride stability could be the increased reactivity of the 6-position over the 5-position. Triphosgene (which is highly toxic) is effective for forming the 2-position acid chloride and it is more safely handled than its monomeric counterpart. The obtained acid chlorides react readily with *t*-butylamine to generate the desired amide functionalizations. The amide functionalizations are untouched by the reduction and oxidation steps needed to convert the 2-position ester to the aldehyde, and which are analogous to the steps described for the synthesis of ligands $L^{5\text{-OH}}$ and $L^{6\text{-OH}}$.

Each of the ligands was characterized by ^1H NMR and positive ion ESI-MS. The major ESI-MS peak for each of the isolated ligands corresponds to the sodium adduct of the ligand. The ^1H NMR for each ligand clearly shows loss of the aldehyde resonance downfield of 10 ppm, and a new resonance in the 8-8.4 ppm region due to imine formation. In each ligand, the three arms that tether to the apical N atom of the tren are equivalent on the ^1H NMR timescale and the peaks are split in ways consistent with the 3-fold symmetric ligand structure.

Metalation of the ligands by Fe(II) is straightforward. Solutions of bare or solvated Fe(II) salts react rapidly to form the desired complexes when introduced to solutions of the free ligand. The Fe(II) complexes $[\text{Fe}(\text{L}^{5\text{-OH}})]\text{X}$ ($\text{X} = \text{SO}_4^{2-}$ (**3.2**), $(\text{BF}_4^-)_2$ (**3.3**), $(\text{BPh}_4^-)_2$ (**3.4**)) and $[\text{Fe}(\text{L}^{5\text{-ONHtBu}})]\text{X}$ ($\text{X} = (\text{Cl}^-)([\text{FeCl}_4]^{2-})_{0.5}$ (**3.11**), $(\text{BF}_4^-)_2$ (**3.12**), $(\text{BPh}_4^-)_{1.5}(\text{Cl}^-)_{0.5}$ (**3.13**)) are purple and are all stable in air. Interestingly, attempts to directly make the chloride salt of $[\text{Fe}(\text{L}^{5\text{-ONtBu}})]^{2+}$ result instead in the formation of a salt that contains both chloride and $[\text{FeCl}_4]^{2-}$ anions. Evans' method room temperature ^1H NMR spectra indicate the complexes are all low-spin, which makes their air stability unsurprising. In these complexes the spin state seems to be insensitive to anion identity at ambient temperature, and weakly interacting counter anions (e.g. triflate or tetraphenylborate) give rise to the same low-spin state as the counter anions that can interact strongly or coordinate to hydrogen bond donors (e.g., sulfate or halides). As with the 5-position methyl ester complex discussed in Chapter 1, alteration of complex electronics by ligand functionalization is insufficient to prompt spin transition.

The 6-position functionalized ligand $\text{L}^{6\text{-OH}}$ reacts to form Fe(II) complexes $[\text{Fe}(\text{L}^{6\text{-OH}})]\text{X}$ ($\text{X} = (\text{CF}_3\text{SO}_3^-)_2$ (**3.5**) $(\text{BF}_4^-)_2$ (**3.6**), $(\Gamma)_2$ (**3.7**), $(\text{Br}^-)_2$ (**3.8**), $(\text{Cl}^-)_2$ (**3.9**), $(\text{BPh}_4^-)_2$ (**3.10**)) which are generally red in color and are air-sensitive in solution, whereas Fe(II) complexes with the ligand $\text{L}^{6\text{-ONHtBu}}$ $[\text{Fe}(\text{L}^{6\text{-ONHtBu}})]\text{X}$ ($\text{X} = (\text{Cl}^-)_2$ (**3.14**), $(\text{CF}_3\text{SO}_3^-)_2$ (**3.15**)) are purple and air sensitive in solution. Room temperature ^1H NMR spectra of the 6-position complexes show peaks that are paramagnetically broadened and shifted in the range of 200 to -50 ppm. The complexes have $\chi_{\text{M}}T$ values calculated by the Evans' method that are typical for high-spin Fe(II) centers. Similar to the 5-position complex discussed above, alteration of the counter anion has no effect on the spin state at room temperature in the solid state and does not prompt

spin switching at lowered temperatures in solution. Further investigation of solid state spin switching for complexes of L^{6-OH} was carried out by Christina Klug.^{13a}

3.4.2 Solid State Structural Characterization. In order to explore anion-cation interactions in the solid state and to potentially access solid-state spin transitions at low temperature, crystals of $3.3 \cdot CH_3CN$ and $3.8 \cdot 0.5 MeOH \cdot 0.5 EtOH$ were structurally characterized at 100 K and crystals of $3.11 \cdot 3CH_3CN \cdot (CH_3CH_2)_2O$ were structurally characterized at 120 K. The Fe-containing cation for each complex is shown in Figure 3.1.

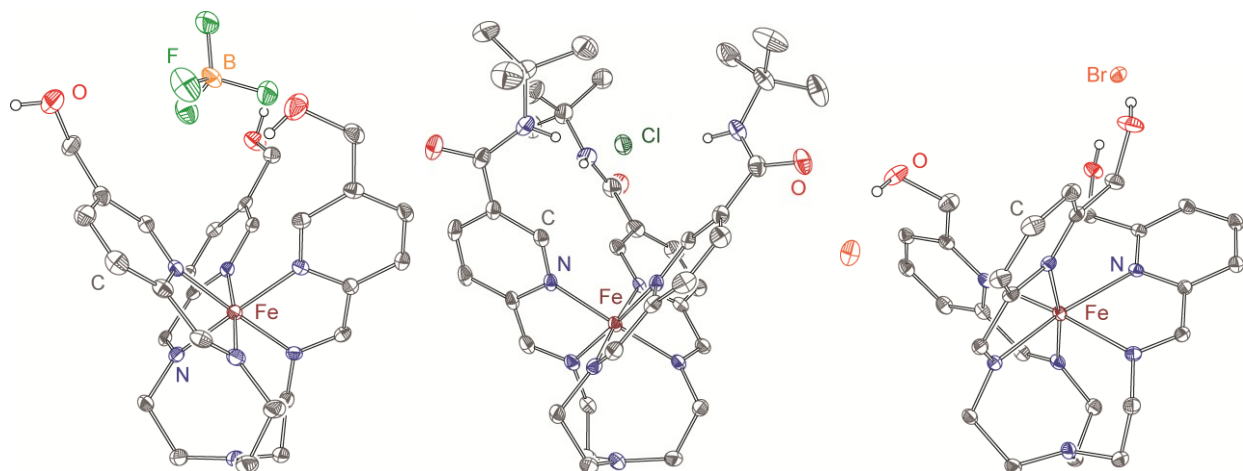


Figure 3.1. Complex cation and interacting anions in $3.3 \cdot CH_3CN$ (left), $3.11 \cdot 3CH_3CN \cdot (CH_3CH_2)_2O$ (center), and $3.8 \cdot 0.5 CH_3OH \cdot 0.5 CH_3CH_2OH$ (right) shown at 40% probability. Hydrogen atoms bonded to carbon and minor disorder components have been omitted for clarity.

The Fe–N bond distances for the 5-position functionalized $3.3 \cdot CH_3CN$ and $3.11 \cdot 3CH_3CN \cdot (CH_3CH_2)_2O$ are typical of low-spin Fe(II),^{13b} and range from 1.948(3) to 1.996(3) Å and 1.848(3) to 1.991(3) Å, respectively. The apical N lies 3.460(4) Å from the Fe center in $3.3 \cdot CH_3CN$, and has nearly planar geometry with C–N–C angles of 119.3(4) to 120.9(4)°. Similarly, the apical N in $3.11 \cdot 3CH_3CN \cdot (CH_3CH_2)_2O$ is also nearly planar and lies 3.489(3) Å from the Fe center, with C–N–C angles of 118.9(3) to 120.6(3)°. These values contrast with the 6-position functionalized $3.8 \cdot 0.5 MeOH \cdot 0.5 EtOH$, which remains high-spin at 100 K. The Fe–N bond distances are longer than those found in low-spin Fe(II) complexes and range from 2.1386(16) to 2.3728(18) Å. The apical N is also

clearly pyramidalized with more acute C–N–C angles that range from 116.90(17) to 117.28(17)° and a shorter N-Fe distance of 3.242(2) Å. Key Fe–N distances and the angles around the apical N atom for each of the structures are tabulated in Table 3.2.

Table 3.2 Key bond distances and angles in crystal structures.

Complex	Distance (Å)		Angle (°)
[FeL^{5-OH}](BF₄)₂·CH₃CN (3.3)			
Fe ¹ –N _{imine}	1.948(3)	C–N _{apical} –C	119.8(4)
	1.950(4)		120.2(4)
	1.966(4)		120.1(4)
Fe ¹ –N _{pyridine}	1.975(3)		
	1.978(3)		
	1.981(3)		
Fe ¹ –N _{apical}	3.460(4)		
Fe ² –N _{imine}	1.951(3)	C–N _{apical} –C	120.9(4)
	1.955(3)		119.8(4)
	1.961(3)		119.3(4)
Fe ² –N _{pyridine}	1.957(3)		
	1.972(3)		
	1.996(3)		
Fe ² –N _{apical}	3.463(4)		
{[Fe(L^{5-ONHtBu})]₂Cl₂}[FeCl₄]·3CH₃CN·(CH₃CH₂)₂O (3.11)			
Fe ¹ –N _{imine}	1.948(3)	C–N _{apical} –C	118.9(3)
	1.953(3)		120.6(3)
	1.954(3)		120.4(3)
Fe ¹ –N _{pyridine}	1.973(3)		
	1.984(3)		
	1.991(3)		
Fe ¹ –N _{apical}	3.489(3)		
Fe ² –N _{imine}	1.952(3)	C–N _{apical} –C	120.5(3)
	1.959(3)		119.2(3)
	1.966(3)		120.3(4)
Fe ² –N _{pyridine}	1.971(3)		
	1.994(3)		
	1.994(3)		
Fe ² –N _{apical}	3.472(4)		
[FeL^{6-OH}]Br₂·0.5CH₃OH·0.5CH₃CH₂OH (3.8)			
Fe ¹ –N _{imine}	2.1386(16)	C–N _{apical} –C	116.90(17)
	2.1538(16)		117.23(17)
	2.1619(17)		117.59(17)
Fe ¹ –N _{pyridine}	2.2834(16)		
	2.3139(16)		
	2.3728(18)		
Fe ¹ –N _{apical}	3.242(2)		

The complex cations in each of the structures participate in hydrogen bonding interactions in the solid state. The atoms involved and distances for these hydrogen bonding interactions are tabulated in Table 3.3. In the case of **3.3**·CH₃CN, where no free halide ions are present, all but one of the hydroxyl groups participate in hydrogen bonding interactions with hydroxyl groups on adjacent cations. The O–O distances compare closely to an average reported O–O distance of 2.76(10) Å for –OH to –OH interactions.²⁷

Table 3.3. Hydrogen bonding interactions and close contacts to anions in crystal structures.

Complex	Interacting atoms (DH–A)	Distance (Å)
Hydrogen bonding interactions		
[FeL ^{5-OH}](BF ₄) ₂ ·CH ₃ CN (3.3)	O1–O4	2.744(5)
	O3–O6	2.882(5)
	O4–O5	2.755(5)
{[Fe(L ^{5-OH<i>t</i>Bu})]Cl} ₂ [FeCl ₄]·3CH ₃ CN·(CH ₃ CH ₂) ₂ O (3.11)	N4–Cl1	3.169(4)
	N7–Cl1	3.186(3)
	N10–Cl1	3.194(4)
	N14–Cl2	3.199(4)
	N17–Cl2	3.220(4)
	N20–Cl2	3.201(3)
[FeL ^{6-OH}]Br ₂ ·0.5CH ₃ OH·0.5 CH ₃ CH ₂ OH (3.8)	O1–Br1	3.336(4)
	O3A–Br1	3.204(5)
	O2–Br2	3.213(2)
Non-hydrogen bonding anion close contacts		
[FeL ^{5-OH}](BF ₄) ₂ ·CH ₃ CN (3.3)	O1–F9	2.725(5)
	O2–F3	2.930(5)
	O3–F13	2.807(4)
	O6–F7	2.814(4)
{[Fe(L ^{5-OH<i>t</i>Bu})]Cl} ₂ [FeCl ₄]·3CH ₃ CN·(CH ₃ CH ₂) ₂ O (3.11)	C8–Cl1	3.276(3)
	C21–Cl1	3.378(4)
	C34–Cl1	3.300(4)
	C47–Cl2	3.365(5)
	C60–Cl2	3.289(4)
	C21–Cl4	3.281(4)
	C29–Cl4	3.355(3)
	Cl5–C31	3.353(4)
Cl5–C55	3.170(3)	

In the complexes containing halide anions, there are multiple direct hydrogen bonds between the anions present and the hydrogen bonding functional groups on the pyridine. In **3.8**·0.5 MeOH·0.5 EtOH, the O–Br distances are typical of hydrogen bonding interactions seen in the literature, where the mean O–Br distance for an –OH to Br interaction is 3.254(8) Å.²⁸ Similarly, the N–Cl distances in **3.11**·3CH₃CN·(CH₃CH₂)₂O are very close to the reported mean N–Cl distance of 3.181(6) Å for *sp*² NH··Cl interactions.²⁸

While there are no interactions between the cation and anions in **3.3**·CH₃CN with distances small enough to be considered hydrogen bonds, there are several close contacts between the BF₄[–] anions and the hydroxyl groups on the complex cation. These distances and cation-anion close contacts for **3.11** are also included in Table 3.3. In **3.11**, many of the close contacts occur between the 6-position on the pyridine and the bound Cl[–]; however, the 6-position H atoms are not pointing directly into the cavity holding the chloride. Additionally, there are close contacts between the imine group and the chlorine atoms of the [FeCl₄]^{2–} anion.

3.4.3 Solution Spin-State Studies. Although cation-anion interactions have been observed in the solid state for Fe(II) complexes with 5- or 6-position functionalized tripodal ligands, and salts of [Fe(L^{6-OH})]²⁺ show temperature-dependent changes in solid-state interactions and spin states,^{13a} neither anion-binding in solution nor anion-dependent spin-state behavior has been observed in solution for tripodal ligand Fe(II) complexes. Despite the clear anion-cation interactions in the structures discussed above, in the solid state none of these complexes show any perturbation of their spin-states away from the expected states for tripodal ligands with either all H-atoms (LS, L⁵) or all non-H atoms at the 6-position (HS, L⁶). However, conditions can be very different in solution, compared to the solid state.²⁹

Room temperature solution magnetic susceptibility measurements confirm that the complexes of L^{5-OH} and L^{5-ONHtBu} are low-spin, and complexes L^{6-OH} and L^{6-ONHtBu} are high-spin regardless of anion. Due to their low-spin nature at room temperature, and the lack of temperature dependent spin-switching in solution for [Fe(L^{5-OOMe})]²⁺ (in **2.3**, see Chapter 2)²⁰, temperature dependent spin-switching was not investigated for complexes of L^{5-OH} and L^{5-ONHtBu}. For complexes of L^{6-OH} and L^{6-ONHtBu}, χ_{MT} values in

solution range between 2.98 and 3.45 $\text{emu}\cdot\text{K}\cdot\text{mol}^{-1}$. Each of the 6-position complexes studied by variable temperature ^1H NMR remains high-spin in solution as the temperature is lowered to 183 K as shown in Figure 3.2, and no anion dependence on spin state is evident.

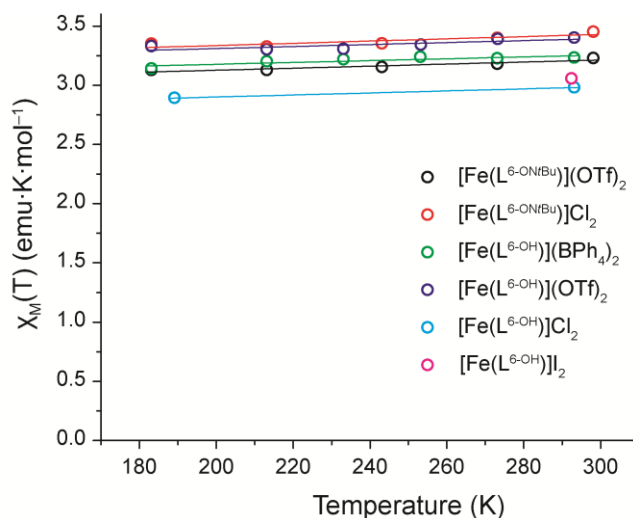


Figure 3.2. Variable temperature magnetic susceptibility data for 6-position Fe(II) complexes in solution. The lines are provided as a guide to the eye.

Errors associated with Evans' method susceptibility measurements are on the order of 5%-10%,³⁰ which can account for the variation in $\chi_{\text{M}}T$ values between the different samples. Additional studies on complexes of $\text{L}^{6\text{-OH}}$ in both solution and in the solid state were carried out by Christina Klug.^{13a} Initial solution state measurements on $[\text{FeL}^{6\text{-OH}}]\text{I}_2$ where $\chi_{\text{M}}T$ values dropped as temperature decreased were found to be due to poor solubility of the complex at low temperatures, and not due to spin-crossover in solution.

3.4.4 Solution Anion-Binding Studies. The high-spin nature of the L^6 -type complexes makes assessing anion-binding in solution difficult because peaks can rarely be positively assigned in the ^1H NMR spectra due to paramagnetic broadening and shifting. For these reasons, we have primarily focused anion-binding studies on the 5-position species. Intrigued by the evidence of strong chloride binding in the solid state structure containing **3.11**, we explored the solution behavior of these tripodal complexes toward anion interaction.

The degree of interaction can be probed by ^1H NMR spectroscopy. In diamagnetic compounds, strong interactions between anions and the $-\text{OH}$ or $-\text{NH}$ protons result in downfield shifts of the proton resonances due to electrostatic deshielding. Addition of excess Cl^- in CD_3CN to Ru(II)-based amide anion receptors produces downfield shifts of nearly 2 ppm for protons involved in hydrogen bonding.³¹ Similar shifts are observed for hydrogen bonding protons in LS Fe(II)-based imidazolium anion receptors.¹¹ The LS nature of complexes like **3.3** and **3.12** should allow for the unambiguous detection of anion-binding. If spin-state switching accompanies anion-binding, susceptibility increases can be detected by the Evans method.

The ^1H NMR spectrum in CD_3CN of the $\text{Fe}(\text{BF}_4)_2$ salt of $\text{L}^{5-\text{OH}}$, **3.3**, does not display paramagnetic peak shifting or broadening, indicating the complex remains LS in solution. All of the peaks in the ^1H NMR spectrum can be assigned, including that of the $-\text{OH}$ proton at 3.38 ppm. The position of this peak is not shifted greatly from the chemical shift for the $-\text{OH}$ proton in the free ligand, 3.50 ppm in CDCl_3 . The similarity of the peak positions argues that tetrafluoroborate is not interacting strongly with the hydroxyl groups in solution. However, upon addition of excess TBACl to a solution of **3.3**, the ^1H NMR spectrum changes (Figures 3.3 and A2.4).

Small downfield shifts of 0.05 and 0.22 ppm are observed for the imine proton (H^3) and the proton at the 6-position (H^6), respectively. More dramatically, the $-\text{OH}$ proton (H^8) shifts 1.6 ppm downfield to 5.0 ppm. The magnitude of this shift indicates that there is strong interaction in CD_3CN between the $-\text{OH}$ proton and the added Cl^- . In addition to the large δ shift, the splittings of the $-\text{OH}$ proton and the adjacent methylene protons (H^7) change: they now each appear as a doublet of doublets with an integration of three protons, indicating that the methylene protons are no longer equivalent. A likely explanation for this is that the interacting Cl^- effectively locks the methanol group in a single conformation, orienting one hydrogen atom on the methylene toward the metal center and the other away from it, resulting in magnetically inequivalent positions.

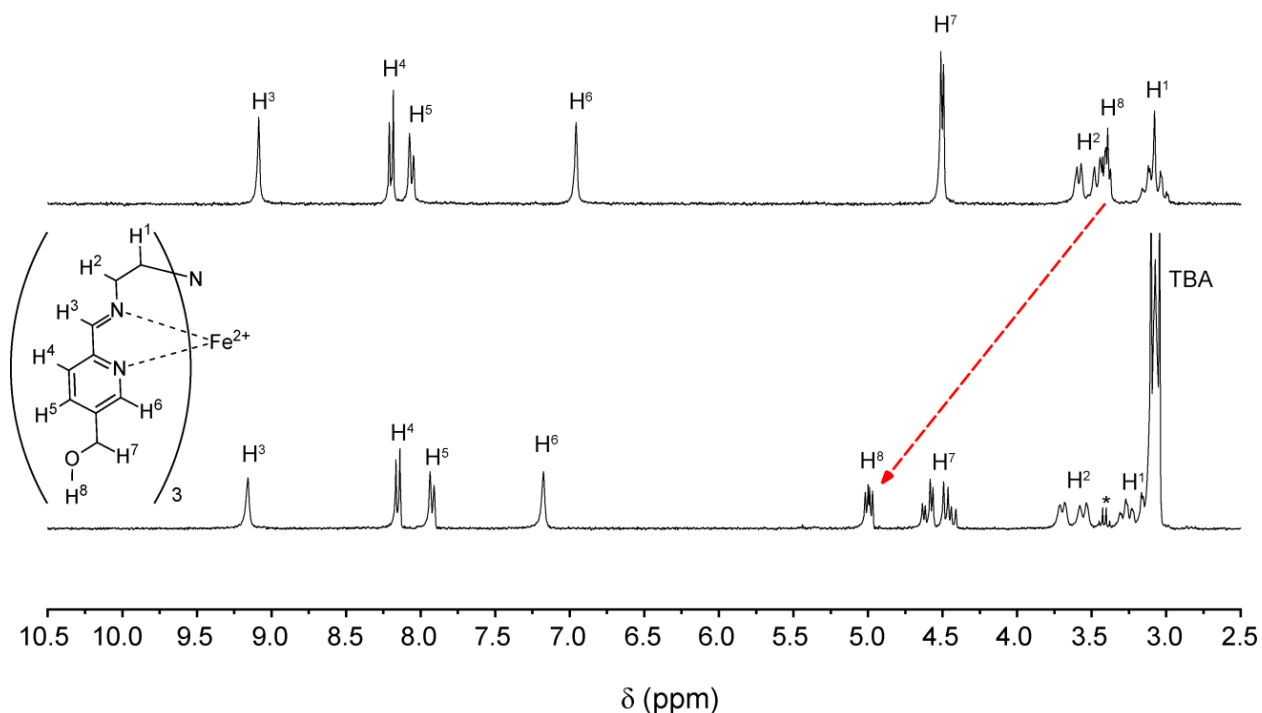


Figure 3.3. 300 MHz ^1H NMR of $[\text{Fe}(\text{L}^{5\text{-OH}})](\text{BF}_4)_2$ in CD_3CN at 24.9 C (top) and after addition of TBACl (bottom).

Complexes of $\text{L}^{5\text{-ONHtBu}}$ show similar anion-dependence in their ^1H NMR spectra. For both $\{[\text{Fe}(\text{L}^{5\text{-ONHtBu}})]\text{Cl}\}_2[\text{FeCl}_4]$ (**3.11**) and $[\text{Fe}(\text{L}^{5\text{-ONHtBu}})](\text{BF}_4)_2$ (**3.12**), all proton resonances can be assigned, including those of the -NH protons, which lie at 9.12 and 6.79 ppm, respectively. Alteration of the counter anion does not obviously influence the spin state of the $[\text{Fe}(\text{L}^{5\text{-ONHtBu}})]^{2+}$ complex cation at room temperature, but the large difference in -NH chemical shift implies anion-binding is operative in solutions containing Cl^- .

In order to further study the solution interaction between chloride and $[\text{Fe}(\text{L}^{5\text{-ONHtBu}})]^{2+}$, TBACl was used to titrate 1.25 equivalents of Cl^- to a solution of **3.12**, and the proton shifts were monitored by ^1H NMR (Figures 3.4 and A2.5). From the titration data, downfield shifts are seen for the amide proton, as expected from comparison of the separately collected spectra of **3.11** and **3.12**. The amide peak ultimately shifts +2.2 ppm, indicating very strong cation-anion interactions. The proton in the 6-position also shows modest downfield shifts upon chloride titration, consistent with its proximity to the bound anion. The other aromatic protons on the pyridine and the imine proton all show small *upfield* shifts, as shown in

Figure 3.4. Similar upfield shifts for protons pointing away from the anion-containing cavity are observed for the tris(imidazolium) Fe(II) complex studied by Fabbrizzi and coworkers.¹¹

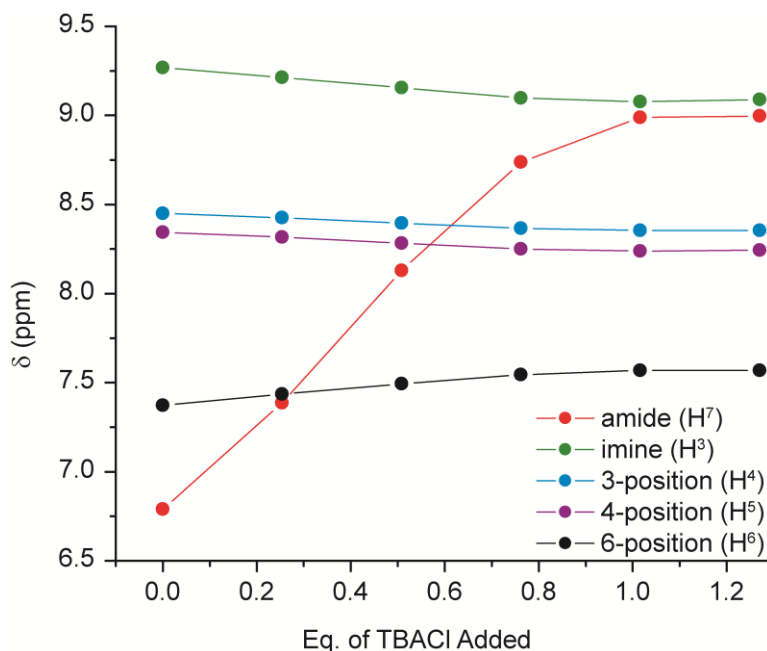


Figure 3.4. Chemical shift values for aromatic protons in $[\text{Fe}(\text{L}^{5\text{-OH}t\text{Bu}})](\text{BF}_4)_2$ (**3.12**) during titration of TBACl. ^1H NMR spectra were collected in CD_3CN at 400 MHz and 23.5°C . Lines are provided as guides to the eye.

Focusing on the large downfield shifts, it is useful to compare this result to the heteroleptic Ru(II) complex reported by Beer and coworkers (also studied in CD_3CN), where a bipyridine ligand decorated with two *t*-butyl amide groups is poised for selective anion chelation.³¹ For this Ru(II) complex, the amide -NH undergoes a 1.62 ppm shift upon addition of 1 equivalent of Cl^- and quantitative analysis of the titration data gives a stability constant of 6700 M^{-1} . In the Fe(II) systems described here, we expect comparable association constants for the $\text{L}^{5\text{-OH}}$ system and even stronger association for the $\text{L}^{5\text{-OH}t\text{Bu}}$ system. This improved anion-binding is likely due to the tripodal pocket created by Fe(II) complexation, in contrast to the bidentate chelation available in the Ru(II) system. Fabbrizzi's tris(imidazolium) Fe(II) system has been also been studied through ^1H NMR titrations and association constants calculated (6300 M^{-1} for Cl^- in 4:1 $\text{CD}_3\text{CN}:\text{D}_2\text{O}$).¹¹ However, direct comparison to our iminopyridine systems is difficult

because anion-binding is highly sensitive to solvent polarity and competing hydrogen bonding interactions. Titrations with a very similar tris(imidazolium) Fe(II) complex have been done in CD₃CN: these give imidazolium C–H peak shifts of 2.67 ppm after addition of one equivalent of TBACl and yield an association constant for Cl[−] of 1.4×10⁶ M^{−1}.³² It is likely that [Fe(L^{5-ONHtBu})]²⁺ would not bind anions as strongly as these systems since it is a dicationic species, whereas the tris(imidazolium) Fe(II) complex cations have charges of 5+.

One intriguing observation from the chloride titration study of **3.12** is that the TMS capillary and bulk solvent TMS peaks are split upon addition of TBACl, which is indicative of a slight increase in magnetic susceptibility. The chemical shifts and apparent $\chi_M T$ value continue to increase until one equivalent of TBACl has been added, to a value of 0.22 emu·K·mol^{−1} based on the concentration of [Fe(L^{5-ONHtBu})](BF₄)₂. After 1 equivalent of TBACl has been added, the chemical shift between the two peaks remains constant (Figure 3.5).

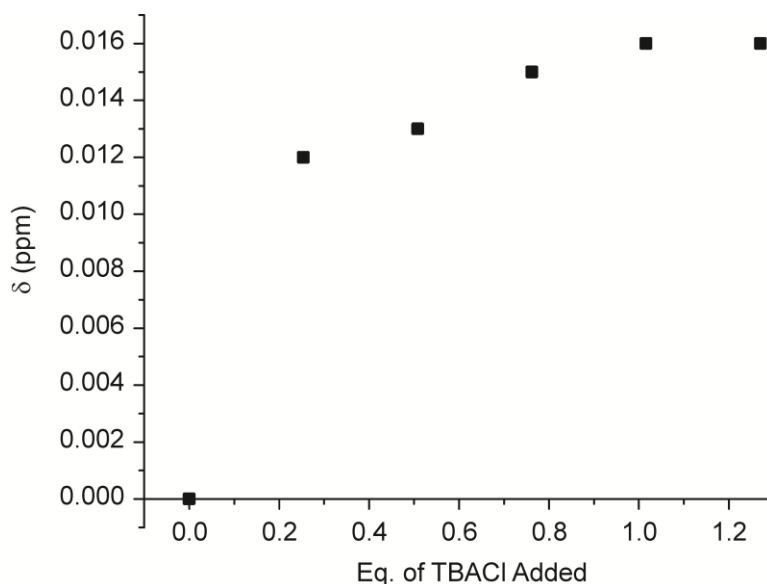


Figure 3.5. Chemical shift values for bulk TMS peak relative to capillary TMS in sample of [Fe(L^{5-ONHtBu})](BF₄)₂ (**3.12**) after addition of varying amounts of TBACl. ¹H NMR spectra collected in CD₃CN at 400 MHz and at 23.5° C.

Possible causes for an increase in magnetic susceptibility include (a) oxidation of the LS Fe(II) center to Fe(III), (b) paramagnetic impurities in TBACl, (c) formation of HS tetrahedral [FeCl₄]^{2−}, or (d) an

authentic increase in the HS fraction of $[\text{Fe}(\text{L}^{5\text{-ONHtBu}})]^{2+}$ in solution, possibly due to interaction with the added Cl^- ions. Regarding scenario (a), spectra collected on solutions of $[\text{Fe}(\text{L}^{5\text{-ONHtBu}})](\text{BF}_4)_2$ kept rigorously airfree show the same splitting of the TMS reference peaks upon addition of TBACl, so oxidation to Fe(III) by air is unlikely to be the cause of the apparent increase in χ_{MT} . Responding to (b), impurities in the TBACl would continue to accumulate with each new addition of TBACl to the sample, yet this is not observed — the lack of further change after addition of one equivalent of TBACl suggests that impurities are not the cause of the splitting in the TMS peaks. Regarding (c), electronic absorption spectroscopic measurements of solutions of **3.12**+TBACl do not show $[\text{FeCl}_4]^{2-}$. We note that the small molar absorptivity value of the absorption ($\sim 70 \text{ M}^{-1}\text{cm}^{-1}$ at 2466 nm^{33}) makes this ion difficult to detect at the concentrations used for the NMR-monitored titrations. On the other hand, we also note that the ^1H NMR spectra for **3.11** and **3.12**+TBACl are similar but not identical (Figures A2.5, A2.11-12).

Additionally, for a HS Fe(II) ion, such as that in $[\text{FeCl}_4]^{2-}$, a χ_{MT} value of $3.0 \text{ cm}^3\text{Kmol}^{-1}$ is expected. To achieve this χ_{MT} value with the TMS peak splitting observed, solely through the formation of $[\text{FeCl}_4]^{2-}$, a minimum concentration of 0.28 mM $[\text{FeCl}_4]^{2-}$ must be formed upon the first addition of TBACl. This would be 84% conversion of all TBACl added to $[\text{FeCl}_4]^{2-}$ and would give rise to more than 5% of the ligand $\text{L}^{5\text{-ONHtBu}}$ present as free ligand, which would be apparent in the ^1H NMR. Since none of the resonances for the free ligand are observed in the ^1H NMR spectrum after addition of TBACl, it is unlikely that $[\text{FeCl}_4]^{2-}$ is being formed in large enough quantities to account for the TMS peak splitting. Although determining the mechanism requires further study, the available evidence is consistent with scenario (d): chloride binding to $[\text{Fe}(\text{L}^{5\text{-ONHtBu}})]^{2+}$ appears to be linked to an increase in the Fe(II) HS:LS ratio.

3.5 Conclusions and Outlook

Four new tripodal ligands have been synthesized and successfully used to make Fe(II) coordination complexes. Complexes formed from $\text{L}^{6\text{-OH}}$ are air-sensitive, remain high-spin from room temperature down to 183K in solution, and alteration of counter anion does not change their properties. Structural

characterization of $[\text{FeL}^{6\text{-OH}}]\text{Br}_2 \cdot 0.5\text{EtOH} \cdot 0.5\text{MeOH}$ shows anion interaction between the hydroxyl groups and the bromide anions; however, the complex remains high-spin in the solid state down to 100 K. Ligands with functionalization at the 5-pyridine position form exclusively low-spin complexes at room temperature that are air stable in the solid state and in solution. While these complexes do not show anion-dependent spin state properties, they do interact strongly with anions in the solid state and in solution. Structural characterization of $\{[\text{Fe}(\text{L}^{5\text{-ONHtBu}})]\text{Cl}\}_2[\text{FeCl}_4]$ clearly shows a chloride anion bound by the three amide protons in the pocket created by Fe(II) coordination to the ligand. In addition to the solid state evidence for anion-binding, addition of chloride to **3.3** and **3.12** produce large downfield shifts for hydroxyl and amide protons, respectively, indicating strong cation-anion interactions in solution.

The intriguing observation of magnetic susceptibility increases in solutions of $[\text{Fe}(\text{L}^{5\text{-ONHtBu}})]^{2+}$ titrated with chloride suggests that anion-triggered spin-state switching may emerge in Fe(II) complexes where the ligand field is slightly weaker. For tripodal iminopyridine ligands, the available results^{6,13a,20} demonstrate that functionalization at all three 6- and 5- positions generate exclusively HS and LS Fe(II) complexes, respectively. Moving toward the spin-crossover regime may be achieved by employing mixed arm tripodal ligands: Drago and coworkers have demonstrated HS:LS tunability by adjusting steric bulk at the 6-position;⁶ the incorporation of anion-binding moieties has not been explored.

In order to combine spin switching with anion-binding in these types of tripodal complexes it would be necessary to produce mixed-arm tripodal ligands that include $-\text{NH}$ or $-\text{OH}$ groups. One variant would contain two arms with anion-binding functional groups at the 5-position and a single arm with a simple functionalization at the 6-position, such as a methyl group. Based on the behavior of mixed arm tripodal complexes reported by Drago and coworkers,⁶ these types of complexes are expected to be mostly low-spin at in solution at room temperature and transition to mostly high-spin when the temperature is elevated.

A second variant that may be more appropriate for observing spin-switching near room temperature would include one arm without any functionalization on the pyridine and two arms with anion-binding

groups at the 6-position. This type of complex is expected to be mostly high-spin at room temperature and transition to mostly low-spin at reduced temperature in solution. This combination may be more useful since anion-binding with only two arms is unlikely to cause dramatic conformational changes in the complex, and instead electronic properties must be perturbed to induce spin state switching. Anion-binding has been shown to increase ligand field strength, promoting transition to the low-spin state for high-spin species in solution.^{5a-c} However, it is not known if 6-position functionalizations such as the *t*-butyl amide groups create a pocket that is suitable for anion-binding as structural data have not yet been obtained for these species.

Alternatively, changing trigonal twisting³⁴ by modification or substitution of the tren backbone may afford spin-crossover complexes without impacting an already demonstrated robust anion-binding pocket. Both of these strategies are being pursued in our laboratory to target anion-triggered spin-state switching in polar media.

3.7 References

1. Shores, M. P.; Klug, C. M.; Fiedler, S. R. In *Spin-Crossover Materials – Properties and Applications*; Halcrow, M. A., Ed.; John Wiley & Sons : Chichester, UK: 2012.
2. (a) Vilar, R. *Eur. J. Inorg. Chem.* **2008**, *2008*, 357-367; (b) Bianchi, A.; Bowman-James, K.; García-España, E. *Supramolecular chemistry of anions*; Wiley-VCH, 1997; (c) Sessler, J. L.; Gale, P. A.; Cho, W.-S. *Anion Receptor Chemistry*; The Royal Society of Chemistry: Cambridge, UK, 2006.
3. (a) Beer, P. D.; Gale, P. A. *Angew. Chem., Int. Ed.* **2001**, *40*, 486-516; (b) Gale, P. A.; Garcia-Garrido, S. E.; Garric, J. *Chem. Soc. Rev.* **2008**, *37*, 151-190; (c) Steed, J. W. *Chem. Soc. Rev.* **2009**, *38*, 506-519.
4. (a) Beer, P. D.; Bayly, S. R.; Stibor, I., Ed.; Springer Berlin / Heidelberg: 2005; Vol. 255, p 373-378; (b) Rice, C. R. *Coord. Chem. Rev.* **2006**, *250*, 3190-3199.
5. (a) Ni, Z.; McDaniel, A. M.; Shores, M. P. *Chem. Sci.* **2010**, *1*, 615-621; (b) Ni, Z.; Shores, M. P. *Inorg. Chem.* **2010**, *49*, 10727-10735; (c) Ni, Z.; Shores, M. P. *J. Am. Chem. Soc.* **2008**, *131*, 32-33; (d) Ni, Z.; Fiedler, S. R.; Shores, M. P. *Dalton Trans.* **2011**, *40*, 944-950.
6. Hoselton, M. A.; Wilson, L. J.; Drago, R. S. *J. Am. Chem. Soc.* **1975**, *97*, 1722-1729.
7. Lazar, H. Z.; Forestier, T.; Barrett, S. A.; Kilner, C. A.; Letard, J.-F.; Halcrow, M. A. *Dalton Trans.* **2007**, 4276-4285.
8. (a) Lazar, H. Z.; Forestier, T.; Barrett, S. A.; Kilner, C. A.; Letard, J.-F.; Halcrow, M. A. *Dalton Trans.* **2007**, 4276-4285; (b) Halcrow, M. A. *Polyhedron* **2007**, *26*, 3523-3576; (c) Seredyuk, M.; Gaspar, A. B.; Kusz, J.; Gütllich, P. *Z. Anorg. Allg. Chem.* **2011**, *637*, 965-976.
9. Lemerrier, G.; Bréfuel, N.; Shova, S.; Wolny, J. A.; Dahan, F.; Verelst, M.; Paulsen, H.; Trautwein, A. X.; Tuchagues, J.-P. *Chemistry- A European Journal* **2006**, *12*, 7421-7432.
10. Beer, P. D.; Gale, P. A.; Smith, D. K. *Supramolecular chemistry*; Oxford University Press: Oxford ; New York, 1999.
11. Amendola, V.; Boiocchi, M.; Colasson, B.; Fabbrizzi, L.; Douton, M.-J. R.; Ugozzoli, F. *Angew. Chem., Int. Ed.* **2006**, *45*, 6920-6924.
12. Tobey, S. L.; Jones, B. D.; Anslyn, E. V. *J. Am. Chem. Soc.* **2003**, *125*, 4026-4027.
13. (a) Klug, C. M.; McDaniel, A. M.; Fiedler, S. R.; Schulte, K. A.; Newell, B. S.; Shores, M. P. *Dalton Trans.* **2012**, *41*, 12577-12585; (b) Goodwin, H. A.; Gütllich, P., Goodwin, H. A., Eds.; Springer Berlin / Heidelberg: 2004; Vol. 233, p 59-90.
14. Hagen, K. S. *Inorg. Chem.* **2000**, *39*, 5867-5869.
15. Bisel, P.; Gies, J. P.; Schlewer, G.; Wermuth, C. G. *Bioorg. Med. Chem. Lett.* **1996**, *6*, 3025-3028.

16. Dawson, M. I.; Chan, R.; Hobbs, P. D.; Chao, W.; Schiff, L. J. *J. Med. Chem.* **1983**, *26*, 1282-1293.
17. Artali, R.; Botta, M.; Cavallotti, C.; Giovenzana, G. B.; Palmisano, G.; Sisti, M. *Org. Biomol. Chem.* **2007**, *5*, 2441-2447.
18. Isagawa, K.; Kawai, M.; Fushizaki, Y. *Nippon Kagaku Zasshi* **1967**, *88*, 553-556.
19. (a) Wang, B. J.-S. *J. Chem. Educ.* **1974**, *51*, 631; (b) Pavia, D. L.; Lampman, G. M.; Kriz, G. S.; Engel, R. G. *Introduction to Organic Laboratory Techniques: A Small Scale Approach*; First ed.; Saunders College Publishing, Harcourt Brace & Company: Fort Worth, TX, 1998.
20. McDaniel, A. M.; Rappé, A. K.; Shores, M. P., *Submitted to Inorg. Chem.*
21. Dawson, M. I.; Chan, R. L. S.; Hobbs, P. D.; SRI International, USA . 1985, p 9 pp.
22. *APEX 2*, Bruker Analytical X-Ray Systems, Inc.: Madison, WI, 2008.
23. Sheldrick, G. M. *SHELXTL*, Version 6.14; Bruker Analytical X-Ray Systems, Inc.: Madison, WI, 1999.
24. (a) Evans, D. F. *J. Chem. Soc.* **1959**, 2003-2005; (b) Live, D. H.; Chan, S. I. *Anal. Chem.* **1970**, *42*, 791-792; (c) Ostfeld, D.; Cohen, I. A. *J. Chem. Educ.* **1972**, *49*, 829; (d) Schubert, E. M. *J. Chem. Educ.* **1992**, *69*, 62; (e) Grant, D. H. *J. Chem. Educ.* **1995**, *72*, 39.
25. Bain, G. A.; Berry, J. F. *J. Chem. Educ.* **2008**, *85*, 532-536.
26. Chong, H. S.; Torti, S. V.; Ma, R.; Torti, F. M.; Brechbiel, M. W. *J. Med. Chem.* **2004**, *47*, 5230-5234.
27. Wallwork, S. *Acta. Cryst.* **1962**, *15*, 758-759.
28. Steiner, T. *Acta Crystallogr., Sect. B: Struct. Sci.* **1998**, *54*, 456-463.
29. (a) Weber, B.; Walker, F. A. *Inorg. Chem.* **2007**, *46*, 6794-6803; (b) Burnett, M. G.; McKee, V.; Nelson, S. M. *J. Chem. Soc., Dalton Trans.* **1981**, 1492-1497.
30. Yatsunyk, L. A.; Walker, F. A. *Inorg. Chem.* **2003**, *43*, 757-777.
31. Beer, P. D.; Dent, S. W.; Wear, T. J. *J. Chem. Soc., Dalton Trans.* **1996**, 2341-2346.
32. Sato, K.; Sadamitsu, Y.; Arai, S.; Yamagishi, T. *Tetrahedron Lett.* **2007**, *48*, 1493-1496.
33. Furlani, C.; Cervone, E.; Valenti, V. *J. Inorg. Nucl. Chem.* **1963**, *25*, 159-163.
34. (a) Reger, D. L.; Elgin, J. D.; Smith, M. D.; Grandjean, F.; Rebbouh, L.; Long, G. J. *Polyhedron* **2006**, *25*, 2616-2622; (b) Reger, D. L.; Gardinier, J. R.; Elgin, J. D.; Smith, M. D.; Hautot, D.; Long, G. J.; Grandjean, F. *Inorg. Chem.* **2006**, *45*, 8862-8875.

Chapter 4. Synthesis and Solution Phase Characterization of Strongly Photooxidizing Heteroleptic Cr(III) Tris-Dipyridyl Complexes

Reproduced with permission from McDaniel, A. M.; Tseng, H.-W.; Damrauer, N. H.; Shores, M. P. *Inorg. Chem.* **2010**, *49*, 7981-7991. Copyright 2010 American Chemical Society and available at <http://pubs.acs.org/doi/abs/10.1021/ic1009972>.

4.1 Introduction

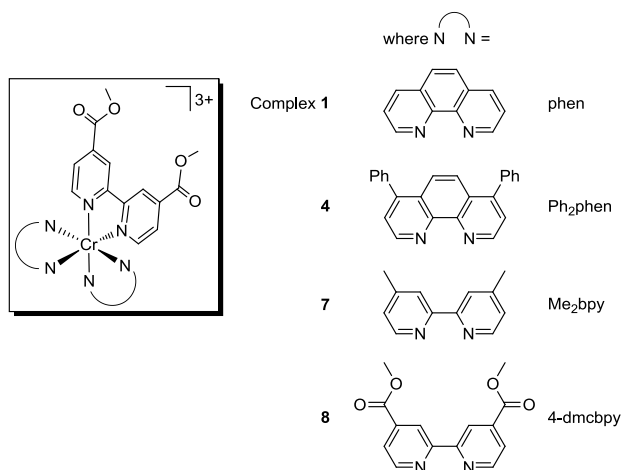
A large body of research has clarified the physical and synthetic prerequisites for achieving efficient light-to-electrical energy conversion in dye-sensitized solar cells (DSSCs) wherein excited states of inorganic chromophores can inject electrons into wide band-gap ceramic semiconductors.¹ Early experimental successes, promising economic factors, and the sheer magnitude of the scientific issues involved have meant that other paradigms for dye-sensitization of charge transport remain relatively unexplored. One such opportunity involves photoinduced interfacial *hole* transfer. Optimization of this paradigm would expose numerous opportunities in solar energy conversion, including initiation of catalytic oxidative reactions critical for water splitting,² photocathodic solar cells (where current runs in the direction opposite to Grätzel cells),³ and tandem photovoltaic cells,⁴ where both electrodes are photoactive.^{4b,5}

Despite these promises, relatively little is known about the physio-chemical factors that must be controlled if photoinduced hole injection processes are to be exploited for solar energy conversion. To our knowledge, there are only a few reports in the literature where this initial photophysical mechanism drives a photocathodic current in a DSSC device.^{3d,6} There are only three systems reported where hole injection is time-resolved and shown to be ultrafast^{3a,7} and only three disclosures where hole transfer participates in a dye-sensitized heterojunction solar cell.⁸ Finally, only in three reports has hole injection functioned as one half of a tandem photovoltaic cell.^{4b,9} The latter of these is the current efficiency record holder for *p*-type DSSCs (0.20% overall efficiency). Clearly, whereas the paucity of results alludes to the significant

challenges involved in this area, it also offers the freedom to explore new materials and methods for controlling energetics and carrier-transfer rates.

Searching for molecular sensitizers capable of initiating excited-state oxidation of wide band-gap semiconductors, we note tris-dipyridyl complexes of Cr(III) as one promising class of compounds. Serpone and Hoffman studied homoleptic analogues for solar energy conversion purposes ca. 25 years ago.¹⁰ Parent complexes such as $[\text{Cr}(\text{bpy})_3]^{3+}$ or $[\text{Cr}(\text{phen})_3]^{3+}$ have excited state redox potentials sufficient to oxidize water to dioxygen if $4e^-$ oxidation could be achieved. They also have long excited state lifetimes, which should promote hole injection into an attached semiconductor surface. Although they absorb visible light ~50 times more weakly than $[\text{Ru}(\text{bpy})_3]^{2+}$ (at 450 nm),^{10a,11} chromium is several orders of magnitude more abundant than ruthenium¹² and ligand modifications can improve absorption properties (vide infra).

Heteroleptic polypyridyl complexes of Cr(III) represent potentially functional model systems, which to our knowledge have not been studied as components of hybrid materials. Dipyridyl ligands with carboxylate functional groups located at the 4 and 4' positions can serve to anchor the sensitizer to metal oxide surfaces, as has been demonstrated extensively in Ru(II)-containing analogues.¹ As discussed in this paper, the electronic properties of the Cr(III) center can be tuned by judicious choice of the ancillary dipyridyl-type ligands (NN). Although structurally homologous with Ru(II) complexes, the synthesis of heteroleptic Cr(III) dipyridyl complexes is not straightforward, as efforts to activate the inert metal center often result in ligand scrambling.¹³ Nevertheless, a recently disclosed methodology employing $[(\text{NN})_2\text{Cr}(\text{OTf})_2]^+$ complexes as synthons¹³⁻¹⁴ shows the way to a new class of molecular species with potential for efficient hole injection into semiconductor substrates. Herein, we describe the preparations as well as electrochemical and photophysical investigations of a family of structurally related heteroleptic Cr(III) dipyridyl complexes (Scheme 4.1). The solution phase investigation of these compounds demonstrates their ability to act as strong photooxidants, and the electronic flexibility afforded by ligand substitution allows us to explore fundamental structure/function relationships in our search for efficient hole transfer to semiconductor substrates.



Scheme 4.1. Target structures of $[(\text{NN})_2\text{Cr}(4\text{-dmcbpy})]^{3+}$ complexes. The (NN) ligands impart electronic tunability, while 4-dmcbpy makes possible covalent attachment to semiconductor surfaces.

4.2 Division of Labor

Interpretation of photophysical data was done by Huan-Wei Tseng and Prof. Niels Damrauer at the University of Colorado, Boulder. All photophysical characterization was conducted by Huan-Wei Tseng. Initial synthetic work using [2,2'-bipyridine]-4,4'-dicarboxylic acid (dcbpy) was carried out by Dr. Md. K. Kabir. All other synthetic work and ground-state characterization was done by Ashley McDaniel.

4.3 Experimental Section

4.3.1 Preparation of Compounds. Unless otherwise noted, the syntheses of heteroleptic tris-dipyridyl Cr(III) complexes were performed in air with atmospheric moisture excluded by use of a CaCO_3 -filled drying tube. For synthetic routes employing Cr(II) starting materials and for preparation of $[\text{Cr}(\text{NN})_2(\text{OTf})_2]\text{OTf}$ (OTf = trifluoromethanesulfonate), compound manipulations were performed either inside a dinitrogen-filled glovebox (MBRAUN Labmaster 130) or via Schlenk techniques on an inert gas (N_2) manifold. The commercially-obtained ligand 4,4'-dimethyl-2,2'-bipyridine (Me_2bpy) was recrystallized from ethyl acetate before use. The ligand dimethyl 2,2'-bipyridine-4,4'-dicarboxylate (4-dmcbpy) was synthesized according to the literature.¹⁵ The preparations of $[(\text{phen})_2\text{Cr}(\text{OTf})_2](\text{OTf})$,

$[(\text{bpy})_2\text{Cr}(\text{OTf})_2](\text{OTf})$, and $[\text{Cr}(\text{CH}_3\text{CN})_4(\text{BF}_4)_2]$ have been described elsewhere.¹⁶ The homoleptic complexes $[\text{Cr}(\text{NN})_3](\text{OTf})_3$, where (NN) is phen, Ph_2phen , or Me_2bpy , were prepared by refluxing $[\text{Cr}(\text{NN})_2(\text{OTf})_2]\text{OTf}$ in CH_2Cl_2 , with five equivalents of the same (NN) ligand for 16 h and collecting the precipitated yellow solids by filtration. The complex $[\text{Cr}(\text{bpy})_3](\text{BF}_4)_3$ was prepared analogously to $[\text{Cr}(4\text{-dmc bpy})_3](\text{BF}_4)_3$ (**4.8**), using bpy in place of 4-dmc bpy. Electronic absorption spectra,^{10a} ESI-MS and clean electrochemical traces confirmed the identity and purity of the previously reported homoleptic complexes. Pentane was distilled over sodium metal and subjected to three freeze-pump-thaw cycles. Other solvents were sparged with dinitrogen, passed over alumina, and degassed prior to use. All other reagents were obtained from commercial sources and were used without further purification.

$[(\text{phen})_2\text{Cr}(4\text{-dmc bpy})](\text{OTf})_3$ (4.1). Solid 4-dmc bpy (0.71 g, 2.62 mmol) was added to a solution of $[(\text{phen})_2\text{Cr}(\text{OTf})_2]\text{OTf}$ (1.50 g, 1.75 mmol) in 125 mL of dichloromethane and heated to reflux. Over 5 days, a bright-yellow precipitate formed. The solid was isolated by filtration, washed with dichloromethane (3×30 mL) and dried in vacuo to afford 1.86 g (94%) of product. IR (KBr pellet): $\nu_{\text{C=O}}$ 1728 cm^{-1} . μ_{eff} (295 K): 3.90 μ_{B} . ES⁺MS (CH_3CN): m/z 228.27 ($[\mathbf{4.1-3OTf}]^{3+}$), 981.67 ($[\mathbf{4.1-OTf}]^+$). Anal. Calcd. for $\text{C}_{41}\text{H}_{28}\text{N}_6\text{CrF}_9\text{O}_{13}\text{S}_3$: C, 43.51; H, 2.49; N, 7.42. Found: C, 43.23; H, 2.33; N, 7.27. Crystals suitable for X-ray analysis were obtained by slow diffusion of diethyl ether into an acetonitrile solution of the compound.

$[(\text{Ph}_2\text{phen})_2\text{CrCl}_2]\text{Cl}$ (4.2). Solid anhydrous CrCl_3 (0.10 g, 0.60 mmol) was added to a suspension of Ph_2phen (0.40 g, 1.20 mmol) in 35 mL of absolute ethanol. A trace amount (< 2 mg) of zinc dust was added and the mixture was heated to reflux for 1 hr, resulting in a green-brown mixture. The mixture was filtered and an olive green solid was isolated from the filtrate by rotary evaporation to afford 0.49 g (98%) of product. IR (KBr pellet): $\nu_{\text{C=N}}$ 1620 cm^{-1} . ES⁺MS (CH_3CN): m/z 788.27 ($[\mathbf{4.2-Cl}]^+$). The compound was used in the next synthetic step without further purification or characterization.

$[(\text{Ph}_2\text{phen})_2\text{Cr}(\text{OTf})_2]\text{OTf}$ (4.3). Under a dinitrogen atmosphere, trifluoromethanesulfonic acid (2 mL, 22.60 mmol) was slowly added to solid **4.2** (0.40 g, 0.49 mmol) to give a red-orange solution.

Dinitrogen was bubbled through the stirring solution for 24 hr, after which the solution was cooled in an ice bath and 250 mL of diethyl ether was added. After standing 4 hr, a beige-peach colored solid precipitated from solution. The solid was isolated by vacuum filtration and rinsed with diethyl ether (3 × 30 mL) to afford 0.47 g (83%) of product. IR (KBr pellet): $\nu_{\text{C=N}}$ 1625 cm^{-1} . ES⁺MS (CH₃CN): m/z 1014.20 ([**4.3**-OTf]⁺). The compound was used in the next synthetic step without further purification or characterization.

[(Ph₂phen)₂Cr(4-dmcbpy)](OTf)₃ (4.4). Solid 4-dmcbpy (0.140 g, 0.515 mmol) was added to a solution of **4.3** (0.209 g, 0.17 mmol) in 30 mL of dichloromethane and heated to reflux. Over 14 days, a yellow precipitate formed. The solid was isolated by filtration, washed with dichloromethane (3 × 10 mL) and collected to afford 0.07 g (27%) of product. IR (KBr pellet): $\nu_{\text{C=O}}$ 1734 cm^{-1} . μ_{eff} (295 K): 3.36 μ_{B} . ES⁺MS (CH₃CN): m/z 329.80 ([**4.4**-3OTf]³⁺), 1285.60 ([**4.4**-OTf]⁺). Anal. Calcd. for C₆₅H₄₄N₆CrF₉O₁₃S₃: C, 54.36; H, 3.09; N, 5.85. Found: C, 54.12; H, 3.05; N, 5.75.

[(Me₂bpy)₂CrCl₂]Cl (4.5). Solid anhydrous CrCl₃ (0.43 g, 2.71 mmol) was added to a solution of Me₂bpy (1.00 g, 5.43 mmol) in 60 mL of absolute ethanol. A trace amount (< 4 mg) of zinc dust was added and the mixture heated to reflux for 1 hr, resulting in a green-brown solution. A grey-green solid precipitated from the reaction mixture upon cooling. It was collected by filtration, washed with cold absolute ethanol (3 × 10 mL) and dried in vacuo to afford 1.12 g (78%) of product. IR (KBr pellet): $\nu_{\text{C=N}}$ 1616 cm^{-1} . ES⁺MS (CH₃CN): m/z 490.00 ([**4.5**-Cl]⁺). The compound was used in the next synthetic step without further purification or characterization.

[(Me₂bpy)₂Cr(OTf)₂]OTf (4.6). Under a dinitrogen atmosphere, trifluoromethanesulfonic acid (2 mL, 22.60 mmol) was added to solid **4.5** (0.35 g, 0.67 mmol) to give a red-orange solution. Dinitrogen was bubbled through the stirring solution for 24 hr, after which the solution was cooled in an ice bath. Diethyl ether (250 mL) was slowly added to form a pink precipitate. The solid was isolated by filtration and rinsed with diethyl ether (3 × 50 mL) to afford 0.53 g (92%) of product. IR (KBr pellet): $\nu_{\text{C=N}}$ 1627

cm⁻¹. ES⁺MS (CH₃CN): *m/z* 718.13 ([**4.6**-OTf]⁺). The compound was used in the next synthetic step without further purification or characterization.

[(Me₂bpy)₂Cr(4-dmcbpy)](OTf)₃ (4.7**). Solid 4-dmcbpy (0.07 g, 0.26 mmol) was added to a solution of **4.6** (0.20 g, 0.23 mmol) in 30 mL of dichloromethane and heated to reflux. Over 9 days, a light-yellow precipitate was formed. The solid was isolated by filtration, washed with dichloromethane (3 × 10 mL) and dried in vacuo to afford 0.13 g (48%) of product. IR (KBr pellet): $\nu_{\text{C=O}}$ 1739 cm⁻¹. μ_{eff} (295 K): 4.01 μ_{B} . ES+MS (CH₃CN): *m/z* 230.93 ([**4.7**-3OTf]³⁺), 989.60 ([**4.7**-OTf]⁺). Anal. Calcd. for C₄₁H₃₆N₆CrF₉O₁₃S₃: C, 43.20; H, 3.18; N, 7.37. Found: C, 42.94; H, 3.11; N, 7.28.**

[Cr(4-dmcbpy)₃](BF₄)₃ (4.8**). Under a dinitrogen atmosphere, a solution of [Cr(CH₃CN)₄(BF₄)₂] (0.13 g, 0.74 mmol) in 4 mL of acetonitrile was added to a suspension of 4-dmcbpy (0.33 g, 2.44 mmol) in 4 mL of acetonitrile to form a forest green solution. The solvent was removed in vacuo to afford a forest-green solid. Addition of AgBF₄ (0.04 g, 0.19 mmol) to a solution of the isolated green solid (0.20 g, 0.19 mmol) in 5 mL of acetonitrile resulted in a yellow solution along with a light-grey solid. The solution was filtered and the filtrate was treated with 15 mL of diethyl ether to precipitate a bright-yellow solid. The solid was recrystallized by diethyl ether diffusion into acetonitrile resulting in bright-yellow crystals. The crystals were collected by filtration, washed with dichloromethane (3 × 3 mL) followed by diethyl ether (3 × 5 mL) and dried in vacuo to afford 0.10 g (45%) of product. IR (mineral oil): $\nu_{\text{C=O}}$ 1737 cm⁻¹. μ_{eff} (295 K): 4.15 μ_{B} . ES⁺MS (CH₃CN): *m/z* 289.67 ([**4.8**-3BF₄]³⁺). Anal. Calcd. for C₄₂H₃₆N₆CrF₁₂B₃O₁₂: C, 44.67; H, 3.21; N, 7.44. Found: C, 44.46; H, 3.08; N, 7.28.**

4.3.2 X-Ray Structure Determinations. A suitable crystal of **4.1**·1.3CH₃CN was coated with Paratone-N oil and supported on a Cryoloop before being mounted on a Bruker Kappa Apex II CCD diffractometer under a stream of dinitrogen. Data collection was performed at 110 K with Mo K α radiation and a graphite monochromator. Crystallographic data and metric parameters are presented in Table 4.1. Data were integrated and corrected for Lorentz and polarization effects by using SAINT, and semiempirical absorption corrections were applied by using SADABS.¹⁷ The structure was solved by

direct methods and refined against F^2 with the program XL from the SHELXTL 6.14 software package.¹⁸ Unless otherwise noted, displacement parameters for all non-hydrogen atoms were refined anisotropically. Hydrogen atoms were added at idealized positions and were refined by using a riding model where the displacement parameters were set at 1.2 times those of the attached carbon atom (1.5 for methyl protons). In the structure of **4.1**·1.3CH₃CN, two of the triflate anions show positional disorder and one solvent molecule is only partially occupied. Complete experimental parameters and disorder treatment is discussed in Appendix 3.

Table 4.1. Crystallographic Data for [(phen)₂Cr(4-dmcbpy)](OTf)₃·1.3CH₃CN (**4.1**·1.3CH₃CN).^a

	4.1 ·1.3CH ₃ CN
formula	C _{43.60} H _{31.90} CrF ₉ N _{7.30} O ₁₃ S ₃ S ₃
fw	1185.24
color, habit	yellow plates
<i>T</i> , K	110(2)
space group	$P\bar{1}$ (triclinic)
<i>Z</i>	2
<i>a</i> , Å	12.6215(7)
<i>b</i> , Å	13.9620(8)
<i>c</i> , Å	17.2034(15)
α , deg	99.574(4)
β , deg	106.338(4)
γ , deg	115.479(2)
<i>V</i> , Å ³	2477.6(3)
<i>d</i> _{calc} , g/cm ³	1.589
GOF	1.026
<i>R</i> ₁ (<i>wR</i> ₂) ^b , %	4.64 (10.17)

^a Obtained with graphite-monochromated Mo K α ($\lambda = 0.71073$ Å) radiation.

^b $R_1 = \sum ||F_o| - |F_c|| / \sum |F_o|$, $wR_2 = \{ \sum [w(F_o^2 - F_c^2)^2] / \sum [w(F_o^2)^2] \}^{1/2}$ for $F_o > 4\sigma(F_o)$.

4.3.3 Photophysical Measurements. All photophysical measurements were undertaken with complexes dissolved in 1 M HCl_(aq). This alters the nucleophilicity of the solvent, thereby decreasing the quantum yield of associative excited state reactions (formation of seven-coordinate solvento species) which ultimately would lead to polypyridyl ligand substitution by solvent molecules.^{10a,19} The ground-

state absorption spectra were obtained with a Hewlett-Packard 8453 spectrophotometer in quartz cuvettes with 1 cm or 1 mm path lengths; experiments were performed at room temperature. Quartz cuvettes (1 cm × 1 cm) with silicone septa seal screw caps were used for the following measurements. Transient absorption spectra were performed at 20-21 °C without deoxygenation (see Supporting Information for details). Emission spectra, emission quantum yields, and single-temperature emission lifetime experiments were measured at 23-24 °C with deoxygenation on dilute samples (see Supporting Information for details). Teflon tubing was used to introduce a stream of argon into the solution. Prior to measurements, samples were purged with argon for 30 min to remove oxygen. For the longer lifetime species such as $[\text{Cr}(\text{phen})_3]^{3+}$, which are highly sensitive to $^3\text{O}_2$ concentrations, this methodology proved far more effective and facile at achieving reproducible results than using freeze-pump-thaw cycles. Each measurement was done with argon flowing on top of the solution. In these emission experiments the temperature of the sample was controlled using a water-jacket cuvette holder connected to a constant-temperature circulator. For temperature-dependent experiments, emission lifetimes were measured every 10 °C from 10 to 80 °C and the lifetime measured at 23-24 °C was also included.

For the normalized emission quantum yields reported in Table 4.3, we compared the integrated emission of each complex relative to that of the standard $[\text{Cr}(\text{phen})_3]^{3+}$ in 1 M $\text{HCl}_{(\text{aq})}$ according to the Eq. 4.1.²⁰ Both measurements are made back to back.

$$\Phi_{unk} = \Phi_{std} \left(\frac{I_{unk}}{A_{unk}} \right) \left(\frac{A_{std}}{I_{std}} \right) \left(\frac{\eta_{unk}}{\eta_{std}} \right)^2 \quad (4.1)$$

In this expression, Φ_{unk} and Φ_{std} are the emission quantum yields of the unknown and standard, respectively, under the conditions of the measurement. To our knowledge Φ_{std} (for $[\text{Cr}(\text{phen})_3]^{3+}$) has not been previously measured and is set to *one* in this column of Table 3 as has been done previously.^{10a,19b} The quantities I_{unk} and I_{std} are the integrated emission intensities of the sample and the standard, respectively, at 650-850 nm. The quantities A_{unk} and A_{std} are the absorbances of the sample and the standard, respectively, at the excitation wavelength (320 nm). Care was taken to ensure that these are both close to 0.1 as mentioned above. Finally η_{unk} and η_{std} are the indices of refraction of the sample and the

standard solution, respectively. Since the same solvent was used in both measurements, the last term in Eq. 1 can be ignored. For these measurements, no differences were observed in absorption spectra collected before and after the emission measurements.

To determine the emission quantum yields reported in Table 4.3, we first measured Φ_{unk} for $[\text{Cr}(\text{phen})_3](\text{OTf})_3$ in 1 M $\text{HCl}_{(\text{aq})}$ relative to $[\text{Ru}(\text{bpy})_3](\text{PF}_6)_2$ in acetonitrile for which the absolute quantum yield (Φ_{std}) of 0.062 is known.²¹ The refractive indices of pure acetonitrile and 1 M $\text{HCl}_{(\text{aq})}$ were used in the calculation. The quantum yields for the rest of the seven complexes were then calculated with respect to Φ_{unk} determined for $[\text{Cr}(\text{phen})_3]^{3+}$. The error bars reported with these seven quantum yields are determined by combining the percentage experimental errors from the individual normalized emission quantum yields (A%) with the percentage error in the measurement made between $[\text{Cr}(\text{phen})_3]^{3+}$ and $[\text{Ru}(\text{bpy})_3]^{2+}$ (B%) according to the equation: $\text{Error}\% = \sqrt{A^2 + B^2}\%$

Further detailed information about instrumentation and methods for photophysical measurements are included in Appendix 3.

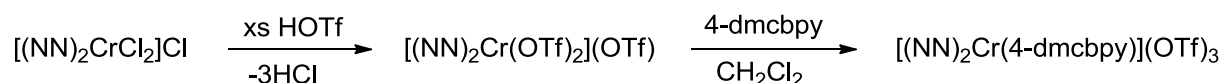
4.3.4 Other Physical Methods. Infrared spectra were measured with a Nicolet 380 FT-IR spectrometer. Mass spectrometric measurements were performed in the positive ion mode on a Finnigan LCQ Duo mass spectrometer, equipped with an analytical electrospray ion source and a quadrupole ion trap mass analyzer. Cyclic voltammetry experiments were carried out inside a dinitrogen filled glove box in 0.1 M solutions of $(\text{Bu}_4\text{N})\text{PF}_6$ in acetonitrile unless otherwise noted. The voltammograms were recorded with either a CH Instruments 1230A or 660C potentiostat using a 0.25 mm Pt disk working electrode, Ag wire quasi-reference electrode, and at Pt mesh auxiliary electrode. All voltammograms shown were measured with a scan rate of 0.1 V/s. Reported potentials are referenced to the ferrocenium/ferrocene (Fc^+/Fc) redox couple and were determined by adding ferrocene as an internal standard at the conclusion of each electrochemical experiment. Solid-state magnetic susceptibility measurements were performed on finely ground samples prepared in air using a Quantum Design model MPMS-XL SQUID magnetometer at 295 K. The data were corrected for the magnetization of the sample

holder by subtracting the susceptibility of an empty container; diamagnetic corrections were applied using Pascal's constants.²² Elemental analyses were performed by Robertson MicroLit Laboratories, Inc. in Madison, NJ.

4.4 Results and Discussion

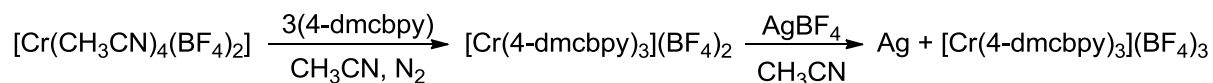
4.4.1 Synthesis and Characterization of Heteroleptic Cr(III) Complexes. Although there is literature precedent for heteroleptic Cr(III) dipyriddy complexes, the preparation of species that contain at least one carboxylate group (for eventual attachment to semiconductor surfaces) was not known prior to our efforts. The preparative routes we have developed are outlined in Schemes 4.2-4.3. Typically, heteroleptic dipyriddy complexes of Cr(III) are synthesized using [(NN)₂Cr(OTf)₂](OTf) precursors: the weakly coordinating triflate anions can be easily removed from otherwise inert Cr(III) centers, and replaced by a third diimine species with minimal ligand scrambling.¹³⁻¹⁴ Initial attempts to prepare complexes using 2,2'-bipyridine-4,4'-dicarboxylic acid (dcbpy) or its disodium salt do not afford pure products. Whereas mass spectral analysis show peaks at anticipated *m/z* ratios (consistent with [(phen)₂Cr(4-dcbpy)]⁺), analysis of isotopic distribution patterns reveal 2+ charges for those ions. We speculate that the products actually formed are dimeric [(NN)₂Cr(4-dcbpy)]₂²⁺ species, where carboxylates coordinate in preference to the imines due to the oxophilic nature of Cr(III), allowing the 4-dcbpy ligand to bridge between two metal centers. Masking the carboxylates on dcbpy by conversion to methyl ester groups (4-dmcbpy) avoids undesirable metal coordination by the carboxylates. Where (NN) is phen, Ph₂phen, or Me₂bpy, the ester-protected ligand 4-dmcbpy is found to react cleanly, albeit sluggishly, with [(NN)₂Cr(OTf)₂](OTf) via Scheme 4.2 to form the heteroleptic complexes **4.1**, **4.4**, and **4.7**, respectively, as yellow solids.

Scheme 4.2. Synthesis of heteroleptic Cr(III) polypyridyl complexes.



The homoleptic complex salt $[\text{Cr}(4\text{-dmcbpy})_3](\text{OTf})_3$ (**4.8**) cannot be prepared via Scheme 4.2, since deprotection of the esters during triflate exchange with $[\text{Cr}(4\text{-dmcbpy})_2\text{Cl}_2]\text{Cl}$ results in dimerization of the Cr complexes. Instead, we find that a Cr(II) solvento complex, $[\text{Cr}(\text{CH}_3\text{CN})_4(\text{BF}_4)_2]$, can serve as a suitable starting material.^{16b} The labile Cr(II) ion is easily ligated by three equivalents of the 4-dmcbpy ligand. Oxidation by Ag(I) affords the tetrafluoroborate salt of the homoleptic Cr(III) complex in reasonable yield (Scheme 4.3).

Scheme 4.3. Synthesis of homoleptic **4.8**.



In contrast to the phen-containing heteroleptic complex **4.1**, the bpy-containing analogue $[(\text{bpy})_2\text{Cr}(4\text{-dmcbpy})]^{3+}$ resists formation via Scheme 4.2, although the reasons for this are not known at this time. To our knowledge, only two successful syntheses of bpy-containing heteroleptic complexes have been reported, $[(\text{bpy})_2\text{Cr}(\text{phen})](\text{OTf})_3$ ¹³ and $[(\text{bpy})_2\text{Cr}(\text{DPPZ})](\text{OTf})_3$ (where DPPZ is dipyridophenazine).²³ We speculate that the ring-locked configuration and higher basicity of the phenanthroline-type ligands minimize opportunities for deleterious ligand exchange before replacement of the more labile triflate anions, whereas the less rigid dipyriddy ligands offer greater opportunity for ligand scrambling. Attempts to make heteroleptic bpy-containing complexes via the more reactive Cr(II) synthon (a la Scheme 4.3) have led thus far to intractable mixtures of homo- and hetero-leptic products.

Besides the usual methods employed for identification and characterization of the complexes, the solid state structure of the phen-containing complex **4.1** has been confirmed by X-ray crystallography (Figure 4.1). All bond distances and angles are as expected for a Cr(III) ion in a tris-chelate ligand environment. Relevant crystallographic data are shown in Table 4.1; additional structural and geometric data are included in Appendix 3.

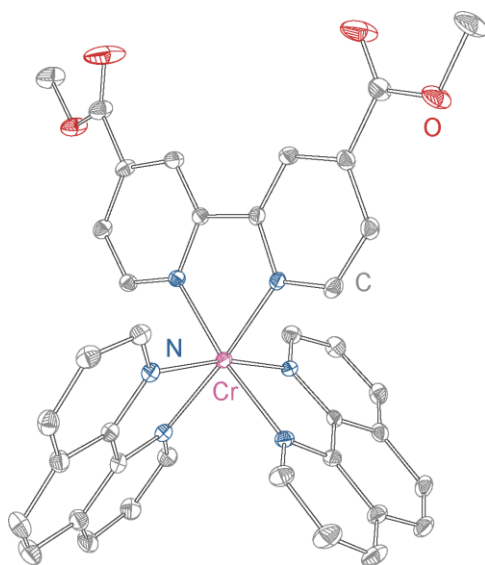


Figure 4.1. Structure of the $[(\text{phen})_2\text{Cr}(4\text{-dmcbpy})]^{3+}$ complex cation, as observed in $4.1 \cdot 1.3\text{CH}_3\text{CN}$, rendered with 40% ellipsoids. H atoms are omitted for clarity. The complex resides on a general position. Bond distances and angles are available in Appendix 3.

4.4.2 Exploration of photophysics and electrochemistry of Cr(III) systems in solution. We have explored the basic photophysical and electrochemical properties of these systems in order to better understand the nascent and long-lived excited-states that will be called upon to drive hole-injection following photo-excitation in later studies. Key questions to be addressed here include: (1) how efficient are these complexes as optical absorbers? (2) how much energy is stored in the excited state? (3) for how long is it stored in unbound solution phase systems? (4) what driving force might we expect for hole transfer photochemistry? and (5) what are the transient absorption features we might use in later femtosecond pump/probe studies to determine hole-injection rates?

4.4.2a Electronic Absorption. Sensitization of hole transfer photochemistry demands light absorption in the material-bound metal complex as an initial step. If Cr(III) polypyridyl complexes are to serve in this role it is important that ligand modifications render visible light absorption more efficient than pure spin-allowed ligand-field excitation ($\epsilon = 50\text{--}100 \text{ M}^{-1}\text{cm}^{-1}$). UV-visible absorption spectra in $1 \text{ M HCl}_{(\text{aq})}$ for complexes containing substituted bipyridine ligands are shown in Figure 4.2. Also included for purposes of comparison are spectra for $[\text{Cr}(\text{bpy})_3]^{3+}$ and $[\text{Cr}(\text{Me}_2\text{bpy})_3]^{3+}$. Absorption data for

all complexes considered in this manuscript are presented in Table 4.2. Note that spectra for previously reported homoleptic complexes^{10a} were reacquired to allow for unambiguous quantitative comparisons to the new heteroleptic complexes.

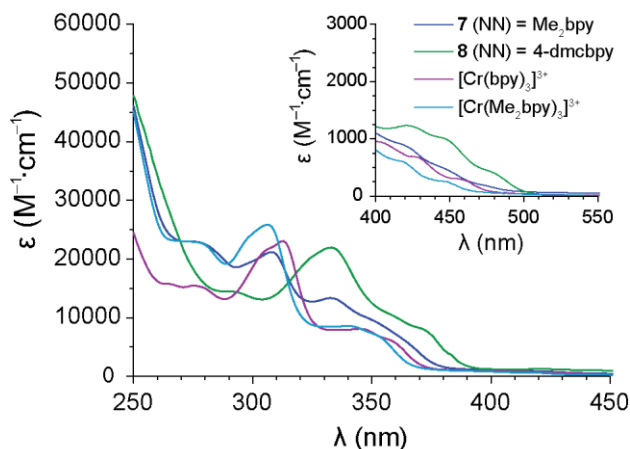


Figure 4.2. Electronic absorption spectra for Cr(III) dipyriddy complexes in 1 M HCl_(aq) at room temperature.

As shown above, these complexes are strongly absorptive in the UV owing to ligand-centered $\pi \rightarrow \pi^*$ transitions; these are also observed in the free ligands. For $[\text{Cr}(\text{bpy})_3]^{3+}$, $[\text{Cr}(\text{Me}_2\text{bpy})_3]^{3+}$, and **4.7**, this includes the band in the vicinity of 300 nm. Ligand-centered $\pi \rightarrow \pi^*$ transitions due to the presence of 4-dmcbpy are seen red shifted by ~ 10 nm in **4.7** and ~ 30 nm in **4.8**. For $[\text{Cr}(\text{bpy})_3]^{3+}$, $[\text{Cr}(\text{Me}_2\text{bpy})_3]^{3+}$, and **4.7**, the band in the vicinity of 350 nm appears to be charge transfer in nature based on its intensity (see Table 4.2) and the fact that it is absent in the free ligand. A similar band is observed for **4.8** as a shoulder at ~ 375 nm. This red shift is consistent with expectations for MLCT given the presence of electron withdrawing substituents on the 4-dmcbpy ligands. However, one might also expect red shifting for LMCT if such ligands serve to reduce electron–electron repulsion in the metal-centered orbitals. It is noted that the ~ 350 nm band in $[\text{Cr}(\text{bpy})_3]^{3+}$ is most often attributed to LMCT^{16a,24} since there is an energetic penalty for oxidizing Cr(III) to Cr(IV) as would formally occur during MLCT.

Table 4.2. Room temperature electronic absorptions for Cr(III) tris-dipyridyl complexes.

Complex	$\lambda_{\text{max}}/\text{nm}$ ($\epsilon/\text{M}^{-1}\text{cm}^{-1}$)
$[\text{Cr}(\text{phen})_3]^{3+}$	269 (52500); 285 (31800), sh; 323 (11200), sh; 342 (6810), sh; 358 (3710); 405 (821), sh; 435 (558), sh; 454 (285), sh
$[\text{Cr}(\text{Ph}_2\text{phen})_3]^{3+}$	283 (103000); 307 (108000); 362 (35300), sh; 380 (26200), sh; 445 (2820), sh; 484 (1730), sh
$[\text{Cr}(\text{bpy})_3]^{3+}$	265 (15700); 275 (15500); 305 (21300), sh; 313 (23100); 346 (8100); 360 (5680), sh; 402 (950), sh; 428 (682), sh; 458 (291), sh
$[\text{Cr}(\text{Me}_2\text{bpy})_3]^{3+}$	278 (23100); 307 (25800); 342 (8530); 354 (6590), sh; 394 (892), sh; 418 (602), sh; 446 (256), sh
$[(\text{phen})_2\text{Cr}(4\text{-dmcbpy})]^{3+}$ (in 4.1)	269 (50600); 285 (29900), sh; 329 (14300); 368 (5020), sh; 418 (1130), sh; 450 (634), sh; 480 (163), sh
$[(\text{Ph}_2\text{phen})_2\text{Cr}(4\text{-dmcbpy})]^{3+}$ (in 4.4)	284 (63300); 311 (59300); 368 (21500), sh; 389 (11600), sh; 455 (1950), sh; 491 (1270), sh
$[(\text{Me}_2\text{bpy})_2\text{Cr}(4\text{-dmcbpy})]^{3+}$ (in 4.7)	279 (23000), sh; 308 (21500); 333 (13500); 351 (9570), sh; 369 (4410), sh; 398 (1140), sh; 422 (866), sh; 451 (429), sh
$[\text{Cr}(4\text{-dmcbpy})_3]^{3+}$ (in 4.8)	294 (14800), sh; 322 (20000), sh; 333 (22700); 360 (10500), sh; 372 (8210), sh; 420 (1280), sh; 448 (1020), sh; 480 (415), sh

For each of the bpy-containing complexes, a broad and modestly structured absorption feature is observed tailing into the visible spectrum (Figure 4.2 inset). Even for the known tris-homoleptic complexes $[\text{Cr}(\text{bpy})_3]^{3+}$ and $[\text{Cr}(\text{Me}_2\text{bpy})_3]^{3+}$, the observed molar absorptivities are larger than would be expected for pure spin-allowed ligand field transitions (${}^4\text{A}_2 \rightarrow {}^4\text{T}_2$), and have been discussed in the literature.^{16a} Here we accept that trigonal splitting is small ($\sim 20 \text{ cm}^{-1}$)²⁵ and that these systems can be discussed with state designations normally reserved for systems with octahedral symmetry. The origin of this intensity enhancement is currently uncertain, but it has been claimed that spin-spin coupling between the (${}^4\text{A}_2$) Cr(III) center and the triplet states of the aromatic ligand is a possible source.^{16a,26} Juban and McCusker have argued that visible absorption enhancement in $[\text{Cr}(\text{bpy})_3]^{3+}$ is due to intensity borrowing from ligand-centered transitions.²⁷ This should be kept in mind as a possible mechanism in future

explorations of 4-dmcbpy ligand-containing systems. It is noted here that for a Cr(III) species, $[\text{Cr}(4\text{-dmcbpy})_3]^{3+}$ (**4.8**) shows appreciable sensitization of visible light, with a molar absorptivity of $940 \text{ M}^{-1}\text{cm}^{-1}$ at 450 nm. This portends eventual control of this critical property through judicious structural and electronic modifications.

Figure 4.3 presents UV-visible absorption spectra for homo- and heteroleptic complexes containing phen-based ligands. Addition of 2% MeOH by volume to 1 M $\text{HCl}_{(\text{aq})}$ was necessary to increase solubility for the Ph_2phen -containing complexes.^{10a} Like the bipyridine-containing complexes discussed in Figure 4.2, intense ligand-centered $\pi \rightarrow \pi^*$ transitions are observed in the UV. For complexes with the unsubstituted phen ligand, this is most prominently observed at ~ 270 nm with very little shifting relative

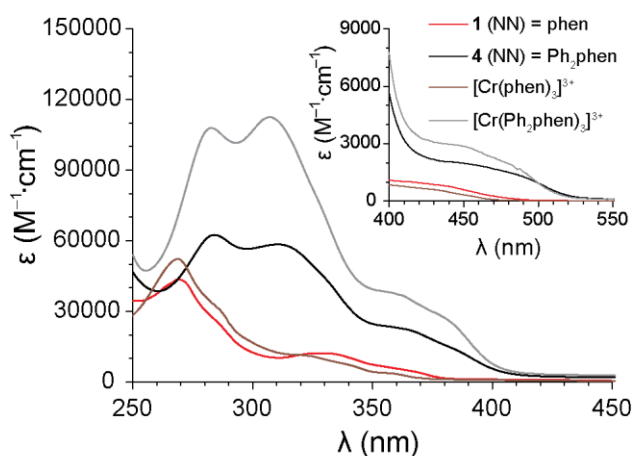


Figure 4.3. Electronic absorption spectra for Cr(III) complexes containing phenanthroline-based ligands: $[\text{Cr}(\text{phen})_3]^{3+}$ and **4.1** in 1 M $\text{HCl}_{(\text{aq})}$, $[\text{Cr}(\text{Ph}_2\text{phen})_3]^{3+}$ and **4.4** in 1 M $\text{HCl}_{(\text{aq})}$ with MeOH (2 % v/v). All spectra were collected at room temperature.

to the free ligand (264 nm for phen in CH_2Cl_2). Such transitions are significantly stronger and red shifted in complexes containing the Ph_2phen ligand as evidenced by intense absorption bands at ~ 285 nm and ~ 310 nm. This is likely due to the presence of a larger and more delocalized π -system. For these two complexes, $[\text{Cr}(\text{Ph}_2\text{phen})_3]^{3+}$ and **4.4**, new absorption features appear at ~ 375 nm upon formation of the metal complex. It is also noted that the intensity of the ~ 310 nm band mentioned above changes significantly relative to the free ligand where it appears as a shoulder to the bluer $\pi \rightarrow \pi^*$ band. We

believe these substantive changes upon complexation herald charge transfer transitions (again, LMCT, MLCT, or both). For $[\text{Cr}(\text{phen})_3]^{3+}$ and **4.1**, features absent in the free ligand spectra are observed at ~ 340 nm. The Ph_2phen -containing species **4.4** shows even more promising absorption of the visible spectrum than $[\text{Cr}(4\text{-dmcby})_3]^{3+}$ (**4.8**) discussed above: at 450 nm $\varepsilon = 1960 \text{ M}^{-1}\text{cm}^{-1}$ and at 480 nm $\varepsilon = 1490 \text{ M}^{-1}\text{cm}^{-1}$.

4.4.2b Static Emission. Each of the bis-heteroleptic polypyridyl Cr(III) complexes that we have synthesized (**4.1**, **4.4**, **4.7**, and **4.8**) is emissive at room temperature following electronic excitation. Emission spectra are shown in Figure 4.4 for dilute samples of the four ester-containing species in thoroughly deoxygenated 1 M $\text{HCl}_{(\text{aq})}$ following excitation at 320 nm. The peaks of these spectra have been scaled to reflect relative intensity with respect to the nearly simultaneous measurement of a standard $[\text{Cr}(\text{phen})_3]^{3+}$ in thoroughly deoxygenated 1 M $\text{HCl}_{(\text{aq})}$. We note that the wavelength of maximum emission at ~ 730 nm in **4.1**, **4.7**, and **4.8** is largely invariant to any changes made to the polypyridyl ligands. As shown in Table 4.3, the model homoleptic species $[\text{Cr}(\text{phen})_3]^{3+}$, $[\text{Cr}(\text{bpy})_3]^{3+}$, and $[\text{Cr}(\text{Me}_2\text{bpy})_3]^{3+}$ emit most strongly at this approximate wavelength. Such emission λ_{max} invariance is common to Cr(III) polypyridyl species and indicates that the lowest-energy excited state is insensitive to the ligand field, as would be the case for a ${}^2\text{E}$ state with a t_{2g}^3 configuration involving a spin flip.^{10g} By analogy to a large number of known emissive Cr(III) polypyridyl complexes, the main emission band seen at ~ 730 nm is assigned to the ${}^2\text{E} \rightarrow {}^4\text{A}$ (ground state) transition and the shoulder that occurs at ~ 700 nm is assigned to the ${}^2\text{T} \rightarrow {}^4\text{A}$ (ground state) transition.^{10a} Interestingly, and somewhat counter to the above discussion, Figure 4.4 and Table 4.3 show that the two species containing the Ph_2phen ligand, $[\text{Cr}(\text{Ph}_2\text{phen})_3]^{3+}$ and $[(\text{Ph}_2\text{phen})_2\text{Cr}(4\text{-dmcby})]^{3+}$ (**4.4**), have an emission λ_{max} that is shifted ~ 14 nm to the red. For $[\text{Cr}(\text{Ph}_2\text{phen})_3]^{3+}$ this has also been reported elsewhere, although no explanation has been offered.^{10a} Electron delocalization via the larger π -system of the aryl-substituted ligand would reduce electron-electron repulsion in the t_{2g}^3 configuration of the ${}^2\text{E}$ state. However, a complete explanation of emission shifting must be more subtle as a similar reduction of repulsion in the t_{2g}^3 configuration of the ${}^4\text{A}$ ground state might be expected to cancel the effect in the excited state, thereby leading to no shift in the

emission maximum. One plausible explanation lies in the fact that doublet configurations involving spin pairing within individual metal orbitals contribute to the description of the emissive states in all of the these molecules explored herein, but for the aryl-substituted versions, the energetic perturbation due to these configurations is smaller as intraligand electronic delocalization takes effect.²⁸ Ultimately it will be important to determine whether there are connections between these emission-shifting effects and the states playing roles in the absorption intensity borrowing (vide supra).

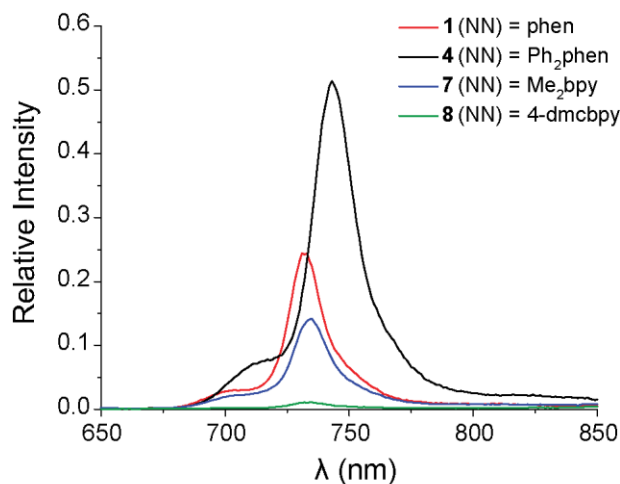


Figure 4.4. Emission spectra for Cr(III) polypyridyl complexes in deoxygenated 1 M HCl_(aq) following excitation at 320 nm. On this intensity scale, the value 1 corresponds to the peak height in emission collected for [Cr(phen)₃]³⁺.

Table 4.3. Photophysical data for Cr(III) polypyridyl complexes in 1 M HCl_(aq).

Complex	Emission ^a λ_{\max} /nm	E_{00} ^b /eV	Normalized Emission Quantum Yield ^{a,c,d}	Emission Quantum Yield ^{a,e} $\times 10^3$	Emission Lifetime ^{a,c} / μ s	$\ln(A)$ ^f	A /s ⁻¹	E_a^f /kJ· mol ⁻¹
[Cr(phen) ₃] ³⁺	730	1.70	1	12±1 ^c	304±4	28.9±0.5	3.5×10 ¹²	51±1
[Cr(Ph ₂ phen) ₃] ³⁺	744	1.67	2.5±0.4	30±5 ^g	425±20	26±1	2.4×10 ¹¹	45±3
[Cr(bpy) ₃] ³⁺	729	1.71	0.21±0.01	2.5±0.2 ^g	69±2	27.0±0.3	5.5×10 ¹¹	43±1
[Cr(Me ₂ bpy) ₃] ³⁺	732	1.70	0.74±0.03	8.9±0.9 ^g	196±8	28.5±0.5	2.3×10 ¹²	49±1
[(phen) ₂ Cr(4-dmcbpy)] ³⁺ (in 4.1)	732	1.70	0.28±0.01	3.4±0.4 ^g	87±3	27.8±0.5	1.2×10 ¹²	46±1
[(Ph ₂ phen) ₂ Cr(4-dmcbpy)] ³⁺ (in 4.4)	742	1.68	0.55±0.02	6.6±0.7 ^g	108±8	27.3±0.5	7.5×10 ¹¹	45±1
[(Me ₂ bpy) ₂ Cr(4-dmcbpy)] ³⁺ (in 4.7)	734	1.70	0.15±0.01	1.8±0.2 ^g	47±1	28.6±0.2	2.6×10 ¹²	46±1
[Cr(4-dmcbpy) ₃] ³⁺ (in 4.8)	733	1.70	0.012±0.002	0.14±0.02 ^g	7.7±0.3	26.7±0.4	4.1×10 ¹¹	37±1

^a The measurements were done at 23-24 °C.^b See text for details on the calculation of E_{00} .^c The errors represent 2 σ (two times of standard deviation) from nine measurements (three independent experiments for each sample, three measurements for each experiment.)^d The normalized emission quantum yields were determined with respect to [Cr(phen)₃]³⁺.^e Emission quantum yields reported are relative to the standard [Ru(bpy)₃]²⁺ in acetonitrile with a 0.062 absolute emission quantum yield. See Experimental for details.^f Errors reported reflect 2 σ from the fitting of a single temperature-data set to a linear Arrhenius model $\ln k_{obs} = \ln A - \frac{E_a}{RT}$.^g See Experimental for details on the calculation of these error bars.

The emission spectra shown in Figure 4.4 allow us to determine the amount of energy stored in the long-lived excited states of these systems. This is a critical piece of information in assessing the oxidation potential available following absorption of UV-visible light. The values reported in Table 4.3 are for E_{00} (equivalent to the ΔG stored in the excited state) where we have modified the observed maximum of the 0-0 vibronic transition (E_0) with its width ($\Delta\bar{\nu}_{0,1/2}$) according to the expression

$$E_{00} = E_0 + (\Delta\bar{\nu}_{0,1/2})^2 / 16k_B T \ln 2 \quad (4.2)$$

For emissive MLCT species (commonly, Ru^{II} , Os^{II} , and Re^{I}) one generally uses a Franck-Condon analysis to determine E_0 and $\Delta\bar{\nu}_{0,1/2}$.²⁹ Here, because emissive features from the ${}^2\text{E} \rightarrow {}^4\text{A}$ ground state are relatively narrow, we determine these quantities directly from the energy and width of the most intense band in the emission spectra.

We also report emission quantum yields in Table 4.3 for **4.1**, **4.4**, **4.7**, **4.8**, and our set of tris-homoleptic species relative to $[\text{Cr}(\text{phen})_3]^{3+}$. The expression for the emission quantum yield ϕ_{em} in terms of radiative (k_r) and non-radiative (k_{nr}) rate constants is shown in Eq 4.3. Here k_{obs} and τ_{obs} are inversely related and refer to the observed rate constant and lifetime, respectively.

$$\phi_{\text{em}} = \frac{\sum k_r}{\sum k_r + \sum k_{\text{nr}}} = \frac{\sum k_r}{k_{\text{obs}}} = \tau_{\text{obs}} \sum k_r \quad (4.3)$$

If a comparison is drawn between $[\text{Cr}(\text{phen})_3]^{3+}$ and $[(\text{phen})_2\text{Cr}(4\text{-dmcbpy})]^{3+}$ (**4.1**), it is seen that introduction of a single 4-dmcbpy ligand drops the quantum yield to 28% of its value in the homoleptic species. For the comparisons between $[\text{Cr}(\text{Me}_2\text{bpy})_3]^{3+}$ and $[(\text{Me}_2\text{bpy})_2\text{Cr}(4\text{-dmcbpy})]^{3+}$ (**4.7**) or between $[\text{Cr}(\text{Ph}_2\text{phen})_3]^{3+}$ and $[(\text{Ph}_2\text{phen})_2\text{Cr}(4\text{-dmcbpy})]^{3+}$ (**4.4**), these values are 21% and 21.5%, respectively. In the comparison between $[\text{Cr}(\text{bpy})_3]^{3+}$ and $[\text{Cr}(4\text{-dmcbpy})_3]^{3+}$ (**4.8**), introduction of three 4-dmcbpy ligands in place of the three bpy ligands drops the quantum yield to ~6% of the value prior to the substitution. The origin of these quantum yield changes is discussed below.

4.4.2c Time-Resolved Emission. To understand these trends in radiative quantum yields, we have measured the observed lifetimes (τ_{obs}) of the emissive ${}^2\text{E}$ states in the full set of complexes and these are

also reported in Table 4.3. For the new complexes reported here, the lowest energy excited-state lifetimes range from 108 μs (for **4.4**) to 7.7 μs (for **4.8**). This is encouraging as it suggests there may be ample time in the ${}^2\text{E}$ excited-state of the respective complexes to engage in hole transfer photochemistry. In the comparison between $[\text{Cr}(\text{phen})_3]^{3+}$ and $[(\text{phen})_2\text{Cr}(4\text{-dmcbpy})]^{3+}$ (**4.1**), the observed lifetime drops from 304 μs to 87 μs upon introduction of the 4-dmcbpy ligand. This latter value is 29% of that measured for the tris-homoleptic species. Similar comparisons made between $[\text{Cr}(\text{Me}_2\text{bpy})_3]^{3+}$ and $[(\text{Me}_2\text{bpy})_2\text{Cr}(4\text{-dmcbpy})]^{3+}$ (**4.7**) or between $[\text{Cr}(\text{Ph}_2\text{phen})_3]^{3+}$ and $[(\text{Ph}_2\text{phen})_2\text{Cr}(4\text{-dmcbpy})]^{3+}$ (**4.4**) yield the values 24% and 25%, respectively. The comparison between $[\text{Cr}(\text{bpy})_3]^{3+}$ and $[\text{Cr}(4\text{-dmcbpy})_3]^{3+}$ (**4.8**) shows that introduction of a full set of ester-containing ligands drops the observed lifetime (7.7 μs) to 11% of the value obtained for $[\text{Cr}(\text{bpy})_3]^{3+}$ (69 μs). The various percentage changes in τ_{obs} shown here are similar to those seen above for ϕ_{em} . This correspondence suggests (by Eq. 4.3) that introduction of the 4-dmcbpy ligand mainly affects the rate constants for non-radiative relaxation pathways (Σk_{nr}).

In order to better understand the origin of the lifetime drop for **4.8**, we have explored the temperature dependence of emission lifetimes for the complete series of complexes over the range 283 K – 353 K.

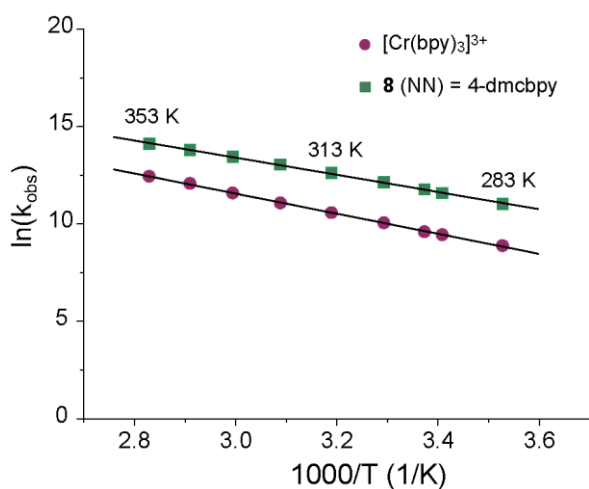


Figure 4.5. Temperature dependence of the observed rate constant $k_{\text{obs}} = 1/\tau_{\text{obs}}$ for $[\text{Cr}(\text{bpy})_3]^{3+}$ and **4.8** in degassed 1 M $\text{HCl}_{(\text{aq})}$.

A representative example is shown in Figure 4.5 for **4.8** compared to $[\text{Cr}(\text{bpy})_3]^{3+}$ as the natural log of the observed rate constant (k_{obs}) versus $1000/T$. Other data sets for the remaining compounds are shown in Figure A3.3.

In all cases we observe temperature dependence. The high-degree of linearity for all data sets suggests that in this temperature range (throughout which we have a fluid solution) the activated process dominates the observed rate constant relative to temperature-independent contributions to k_r and k_{nr} .³⁰ Table 4.3 includes a listing of the measured Arrhenius preexponential (A) and activation energy (E_a) for each system. With this information we can see general trends emerge, especially if we draw comparisons, as before, between pairs of compounds where ancillary ligands are the same. For example in comparing $[\text{Cr}(\text{phen})_3]^{3+}$ and **4.1** it is seen that introduction of the ester-containing ligand serves to drop the activation energy by 5 kJ/mol. Given that the preexponential A drops modestly between $[\text{Cr}(\text{phen})_3]^{3+}$ and **4.1**, the concomitant decrease in E_a is responsible for the shortening of the lifetime from 304 μs to 87 μs . A similar decrease in E_a is also observed between $[\text{Cr}(\text{Me}_2\text{bpy})_3]^{3+}$ and **4.7** and the system with shortest lifetime, **4.8**, also has the smallest E_a , which is 6 kJ/mol less than that measured for $[\text{Cr}(\text{bpy})_3]^{3+}$. These observations can be explained if introduction of the electron-withdrawing ester ligand weakens the ligand field via an inductive effect, thereby decreasing the barrier to excited states having a $t_{2g}^2 e_g$ configuration. Such states would have significant nuclear distortions (primarily metal–ligand bond distances) and through these displacements larger non-radiative decay rates. Given the magnitude of the Arrhenius preexponential A measured for these systems, it is unlikely that these complexes are thermally activated directly through back-intersystem-crossing from the 2E to the 4T manifold. Rather one might need to invoke deactivation through states with appropriate nuclear distortion but also with doublet electron spin character. It is noted that differences in activation energy alone are not sufficient to explain the significant lifetime variation between $[(\text{Ph}_2\text{phen})_2\text{Cr}(4\text{-dmcbpy})]^{3+}$ (**4.4**) where $\tau_{\text{obs}} = 108 \mu\text{s}$, and $[\text{Cr}(\text{Ph}_2\text{phen})_3]^{3+}$ where $\tau_{\text{obs}} = 425 \mu\text{s}$. Here, differences in the Arrhenius preexponential A are the primary origin of the observation. It does not appear to be simply a consequence of the reduced rigidity of the di-ester ligand and related entropic effects as we do not see A increase between $[\text{Cr}(\text{phen})_3]^{3+}$ and

$[(\text{phen})_2\text{Cr}(4\text{-dmcbpy})]^{3+}$ (**4.1**). Detailed theoretical exploration is needed to determine, for example, whether there are changes in the density of electronic states at the activation energy of ~ 45 kJ/mol in the comparison between $[\text{Cr}(\text{Ph}_2\text{phen})_3]^{3+}$ and $[(\text{Ph}_2\text{phen})_2\text{Cr}(4\text{-dmcbpy})]^{3+}$ (**4.4**) that might influence the relative mechanisms for nonradiative decay.

4.4.2d Ground and Excited State Reduction Potentials. Along with emission data, the second critical component for finding excited state redox potentials is the determination of ground state $\text{Cr}^{\text{III/II}}$ and $\text{Cr}^{\text{IV/III}}$ couples. Each of the heteroleptic dipyriddy complexes **4.1**, **4.4**, and **4.7** show 4 reversible $1e^-$ reductions, and in the case of **4.8**, six reversible waves are seen. The $\text{Cr}^{\text{IV/III}}$ couples for these systems have not been observed as they are outside of the acetonitrile solvent oxidation window. These data are presented here in Figure 4.6 and Table 4.4.

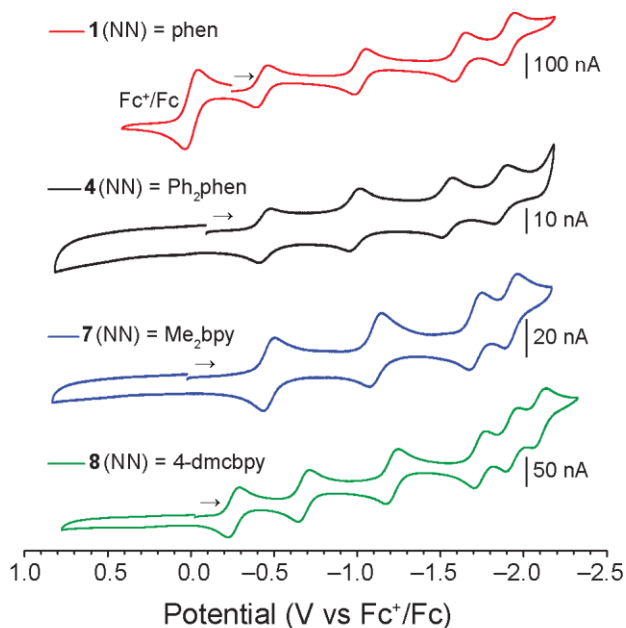


Figure 4.6. Comparison of cyclic voltammograms for the 4-dmcbpy containing complexes **4.1**, **4.4**, **4.7**, and **4.8** in 0.1 M TBAPF₆ acetonitrile solution. Arrows indicate the starting point and direction for each voltammogram. For **4.4**, **4.7**, and **4.8**, the potential is referenced to ferrocene (from a voltammogram which includes Fc collected immediately after the displayed voltammogram).

As shown, the first reduction for complexes containing the ester ligands is facile, with $E_{1/2}$ occurring between -0.47 and -0.42 V versus Fc^+/Fc for all species containing a single ester ligand. We find that the position of the first wave can be tuned through the functional groups present on the attached ligands. The presence of two strongly electron withdrawing ester groups on the ligand 4-dmcbpy shifts the initial ‘Cr^{III/II}’ process to more positive potentials compared to those previously reported for hetero- and homoleptic $[Cr(NN)_3]^{3+}$ complexes.^{14a,19b} This is shown in Table 4.4: for **4.1**, **4.4**, and **4.7**, the first ‘Cr^{III/II}’ reduction occurs at a potential at least 0.22 V more positive than the homoleptic species that lack an ester ligand. For $[Cr(4-dmcbpy)_3]^{3+}$ (**4.8**) this first reduction is remarkably shifted an additional ~ 0.2 V in the positive direction compared to the complexes containing a single 4-dmcbpy. For this species the presence of three ligands carrying electron withdrawing groups is able to move the ‘Cr^{-I/-II}’ and ‘Cr^{-II/-III}’ reductions to within the acetonitrile window, leading to the observation of six reversible waves. While each of these reductions is listed as a change in the Cr formal oxidation state (matching the literature precedent), these processes are more likely due to ligand reduction,^{24b,31} and it is reasonable to surmise that the presence of electron withdrawing groups allow for each 4-dmcbpy ligand to be reduced by two electrons.

Table 4.4. Ground and excited state reduction potentials for Cr(III) polypyridyl complexes.

	$(E_{1/2}$ vs Fc^+/Fc , V) ^a						
	3+/2+	2+/1+	1+/0	0/1-	1-/2-	2-/3-	*3+/2+ ^b
$[Cr(phen)_3]$	-0.65	-1.17	-1.71	-2.21			+1.05
$[Cr(Ph_2phen)_3]$	-0.67	-1.11	-1.63	-2.05			+1.00
$[Cr(bpy)_3]$	-0.63	-1.15	-1.72	-2.34			+1.08
$[Cr(Me_2bpy)_3]$	-0.79	-1.29	-1.82				+0.91
$[(phen)_2Cr(4-dmcbpy)]$ (4.1)	-0.42	-1.01	-1.61	-1.90			+1.28
$[(Ph_2phen)_2Cr(4-dmcbpy)]$ (4.4)	-0.45	-0.99	-1.54	-1.87			+1.23
$[(Me_2bpy)_2Cr(4-dmcbpy)]$ (4.7)	-0.47	-1.11	-1.71	-1.92			+1.23
$[Cr(4-dmcbpy)_3]$ (4.8)	-0.26	-0.68	-1.21	-1.74	-1.93	-2.10	+1.44

^a Conditions for cyclic voltammetry of Cr Complexes: Electrolyte, 0.1 M TBAPF₆ in CH₃CN; WE, Pt; CE, Pt Wire; Scan Rate, 100 mV/s. ^b Calculated from Eq. 4.4.

The half wave reduction potential of the excited state can be estimated using the ground state half wave reduction potential and the one electron potential corresponding to the spectroscopic excited state:³²

$$E_{1/2}(\text{Cr}^{\text{III}*/\text{II}}) = E_{00}(\text{Cr}^{\text{III}*/\text{III}}) + E_{1/2}(\text{Cr}^{\text{III}/\text{II}}) \quad (4.4)$$

The use of E_{00} as a potential (rather than energy) is acceptable in this context because the excited state is only acting as a one-electron acceptor. As discussed in the context of Table 4.3, E_{00} is largely invariant to ligand substitution patterns. Others have noted that the ${}^2\text{E}$ emission maximum in Cr(III) species is solvent insensitive and we have observed that E_{00} does not change between aqueous (where our spectroscopic measurements have been done) and acetonitrile (where our electrochemical measurements have been done) environments. On the other hand, the ground state (first) reduction potentials show ligand dependence (Table 4.4). Thus, the excited state reduction potential is tunable. These values are compiled in Table 4.4 for all the complexes studied. Equation 4 allows us to predict a $\text{Cr}^{\text{III}*/\text{II}}$ couple of +1.22 to +1.27 V versus Fc^+/Fc for the heteroleptic complexes. In order to compare the excited state potentials of these Cr(III) complexes to other photo-electrochemically active species reported in the literature, the measured redox potentials have been converted to reference NHE (Fc^+/Fc is 0.40 V vs SCE in 0.1M TBAPF₆³³ and SCE is 0.241V vs NHE³⁴). We note that this comparison is approximate due to differences in solvent and supporting electrolyte, but it is still useful.³⁵ In the case of **4.8**, the $\text{Cr}^{\text{III}*/\text{II}}$ couple is calculated to be a remarkable +2.08 V versus NHE while **4.1**, **4.4**, and **4.7** are +1.92 V, +1.87 V, and +1.87 V versus NHE, respectively. As a point of reference, a similar ester-functionalized $[\text{Ru}(\text{NN})_3]^{2+}$ complex shows an excited state reduction potential of +1.26 V (vs NHE) for $\text{Ru}^{\text{II}*/\text{I}}$.³⁶ Nocera and coworkers reported +1.78 V (vs NHE) for a $\text{Re}^{\text{I}*/\text{0}}$ complex,³⁷ while Sullivan and coworkers reported +2.71 V (vs NHE) for a $\text{Re}^{\text{II}*/\text{I}}$ complex.³⁸ Reports of $\text{Cr}^{\text{III}*/\text{II}}$ potentials from non-polypyridyl complexes are very rare in the literature, however an amine-based $\text{Cr}^{\text{III}*/\text{II}}$ system has been reported with an excited state reduction potential of +0.77 V (vs NHE).³⁹ Indeed, the ester-containing Cr(III) complexes **4.1**, **4.4**, **4.7** and **4.8** offer themselves as potentially powerful excited-state oxidants.

4.4.2e Transient Absorption. In future studies involving hole transfer photochemistry between Cr(III) systems and wide band-gap semiconductors to which they are bound, it will be important to be

able to interrogate the time-dependent behavior of the lowest energy excited-state manifold in these complexes without relying on emission and on potentially very short time scales. A valuable tool in this context is transient electronic absorption (TA) spectroscopy. With time resolution from tens of femtoseconds to milliseconds, TA spectroscopy has been central to unraveling mechanism in dye-sensitized heterojunction solar cell materials.^{1f,g,40} Here we do not consider the earliest transient events but rather explore absorption features once these molecules are electronically relaxed in the 2E excited states. The spectrometer used here employs ~ 10 ns excitation pulses centered at 355 nm and the transient features probed with white light decay with single exponential behavior on μs timescales. Within such timescales, it is well established that the 2E excited-state of these complexes in fluid solution at room temperature is vibrationally cool and thermally equilibrated with the solvent.^{27-28,41} TA spectra collected for the tris-homoleptic compounds $[\text{Cr}(\text{phen})_3]^{3+}$, $[\text{Cr}(\text{bpy})_3]^{3+}$, $[\text{Cr}(\text{Me}_2\text{bpy})_3]^{3+}$, and $[\text{Cr}(\text{Ph}_2\text{phen})_3]^{3+}$ are shown in Figure A3.2 and these agree with previously reported spectra collected under similar experimental conditions.^{10a} Spectra for the two additional bis-heteroleptic complexes **4.1** and **4.7** are also shown in Figure A3.2. In the case of **4.7**, the spectrum is quite similar to the related tris-homoleptic species $[\text{Cr}(\text{Me}_2\text{bpy})_3]^{3+}$. There are some qualitative differences between **4.1** and $[\text{Cr}(\text{phen})_3]^{3+}$ in terms of relative band intensities but these are unremarkable and are not considered here further. In Figure 4.7 are plotted transient absorption (TA) spectra for **4.8** (left) and **4.4** (right). As discussed above, these species have the most promising molar absorptivities at visible wavelengths and are likely, therefore, to be used in future semiconductor sensitization experiments.

Both difference spectra show a resolved bleach feature centered at 360 nm, a strong absorption feature at ~ 400 nm, and a broad absorption further to the red. In the case of **4.4**, this redder absorbance is very broad and appears to peak at ~ 550 nm. The magnitude of the bleach in both transient spectra provides a useful metric for estimating excited-state molar absorptivities at various wavelengths.

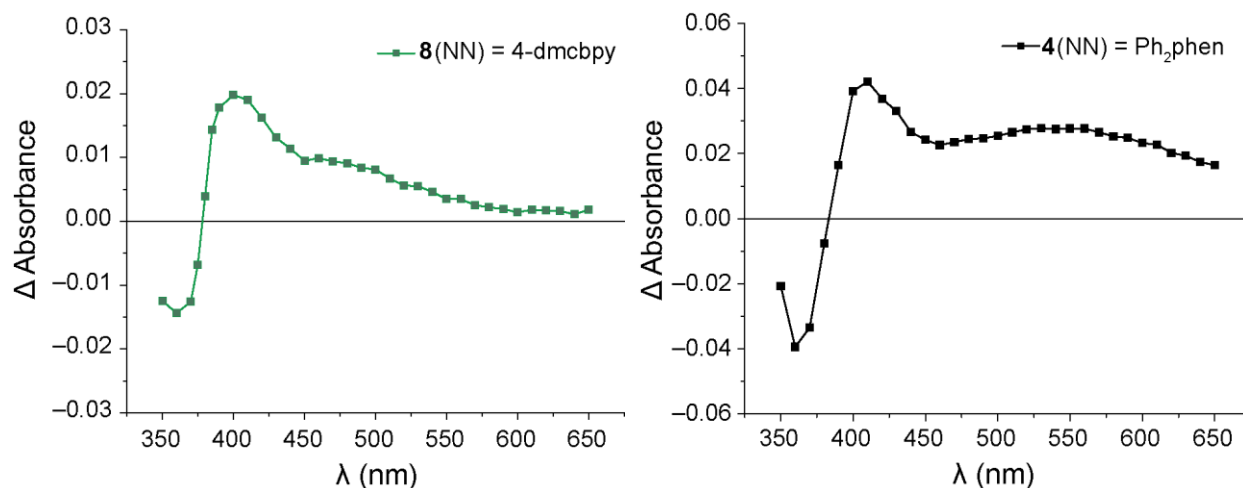


Figure 4.7. Transient absorption spectra on a μs timescale for **4.8** (left) and **4.4** (right) in 1 M $\text{HCl}_{(\text{aq})}$. The spectra were determined from a single exponential fit to transient absorption (or bleach) kinetics collected at each of the wavelengths for which there is a dot. The lines are included as guides to the eye.

In the ground state optical spectra shown in Figure 4.2 and Figure 4.3, complexes **4.8** and **4.4** exhibit molar extinction coefficients at 360 nm of $\epsilon_{360\text{nm}} = 10500 \text{ M}^{-1}\text{cm}^{-1}$ and $\epsilon_{360\text{nm}} = 23400 \text{ M}^{-1}\text{cm}^{-1}$, respectively. In the limiting case that the $-\Delta A$ at 360 nm for these two spectra is entirely due to loss of ground state absorption, then it is possible to assign a lower limit to excited-state molar absorptivities ($\epsilon^*_{(\lambda)}$) for observed absorption features. In the case of **4.8**, we measure $\Delta A = -0.014$ at 360 nm and $\Delta A = 0.020$ at 400 nm such that $\epsilon^*_{400\text{ nm}} \geq 14400 \text{ M}^{-1}\text{cm}^{-1}$. A similar observation is made for **4.4** although the absorptivities are even larger. In this case $\epsilon^*_{400\text{ nm}} \geq 23300 \text{ M}^{-1}\text{cm}^{-1}$ and $\epsilon^*_{550\text{ nm}} \geq 16500 \text{ M}^{-1}\text{cm}^{-1}$. In these spectra (and very likely in the whole series of Cr(III) polypyridyl complexes we have considered), the transient absorption features with appreciable ΔA are clearly not assignable to ligand-field absorption occurring from the t_{2g}^3 configuration of the 2E excited state. The strength of the absorption features suggest these are charge transfer in nature originating from the 2E and 2T excited states, although it is not possible at this time to assign MLCT and/or LMCT to any particular feature. The t_{2g}^3 configuration of the 2E excited state is not expected to significantly perturb the ligand π -system, so ligand centered $\pi \rightarrow \pi^*$ transitions are unlikely to play a prominent role. It may be possible that the observed transitions, especially those near 400 nm, borrow some intensity from such excitations as Juban and McCusker²⁷ have

argued occurs in the ground state of $[\text{Cr}(\text{bpy})_3]^{3+}$. The important point to stress here is that excited-state absorption features in the visible spectrum for these complexes have significant oscillator strength. In more complex environments such as when complexes are bound to heterogeneous semiconductor surfaces, such features may be a useful and easily observable diagnostic of ${}^2\text{E}$ lifetime and related hole-injection rate constants.

4.5 Conclusions and Outlook

The preparation of heteroleptic dipyriddy Cr(III) complexes that contain at least one carboxylate group (for eventual attachment to semiconductor surfaces) was not known prior to our efforts. We have synthesized four such complexes, including three heteroleptic $[(\text{NN})_2\text{Cr}(4\text{-dmcbpy})]^{3+}$ species. We have also explored the basic photophysical and electrochemical properties of these systems in order to better understand the nascent and long-lived excited-states that will be called upon to drive hole-injection following photo-excitation in later studies.

The electronic absorption studies show a combination of ligand-centered, metal-centered ligand field, and charge-transfer transitions. Nevertheless, it is noted here that for a Cr(III) species with Ph_2phen ancillary ligands, $[(\text{Ph}_2\text{phen})_2\text{Cr}(4\text{-dmcbpy})]^{3+}$ (in **4.4**), shows appreciable sensitization of visible light, with a molar absorptivity of $1270 \text{ M}^{-1}\text{cm}^{-1}$ at 491 nm. Time-resolved emission studies show that the introduction of the 4-dmcbpy ligand decreases the doublet excited state lifetimes of the complexes with respect to their tris-homoleptic analogues. Notwithstanding, excited-state lifetimes are sufficiently long that we can anticipate photo-induced hole transfer to suitable semiconductor substrates. Additionally, preliminary electrochemical studies show that the introduction of the 4-dmcbpy significantly shifts reduction potentials of the complexes to more positive values. The combination of cyclic voltammetry and static emission studies indicates that strongly oxidizing excited states are possessed by this class of molecules.

The strongly oxidizing excited states found for the Cr(III) dye complexes coupled with the reported long excited-state lifetimes lead us to believe these species will be capable of hole injection into p-type

semiconductors with suitably aligned valence bands. Further, the excited-state absorption features for these heteroleptic complexes should serve as handles for studying the hybrid dye-sensitized materials. Efforts are underway to incorporate these dye complexes into semiconductors to form hybrid materials.

4.7 References

- (a) O'Regan, B.; Grätzel, M. *Nature* **1991**, *353*, 737-740; (b) Nazeeruddin, M.; Grätzel, M. In *Photofunctional Transition Metal Complexes* 2007, p 113-175; (c) Robertson, N. *Angew. Chem., Int. Ed. Engl.* **2006**, *45*, 2338-2345; (d) Polo, A. S.; Itokazu, M. K.; Iha, N. Y. M. *Coord. Chem. Rev.* **2004**, *248*, 1343-1361; (e) Hagfeldt, A.; Grätzel, M. *Acc. Chem. Res.* **2000**, *33*, 269-277; (f) Ardo, S.; Meyer, G. J. *Chem. Soc. Rev.* **2009**, *38*, 115-164; (g) Martinson, A. B. F.; Hamann, T. W.; Pellin, M. J.; Hupp, J. T. *Chem.–Eur. J.* **2008**, *14*, 4458-4467.
- (a) Gersten, S. W.; Samuels, G. J.; Meyer, T. J. *J. Am. Chem. Soc.* **1982**, *104*, 4029-4030; (b) Lei, Y. B.; Hurst, J. K. *Inorg. Chim. Acta* **1994**, *226*, 179-185; (c) Limburg, J.; Vrettos, J. S.; Liable-Sands, L. M.; Rheingold, A. L.; Crabtree, R. H.; Brudvig, G. W. *Science* **1999**, *283*, 1524-1527; (d) Wada, T.; Tsuge, K.; Tanaka, K. *Angew. Chem., Int. Ed.* **2000**, *39*, 1479-1482; (e) Sens, C.; Romero, I.; Rodriguez, M.; Llobet, A.; Parella, T.; Benet-Buchholz, J. *J. Am. Chem. Soc.* **2004**, *126*, 7798-7799; (f) Zong, R.; Thummel, R. P. *J. Am. Chem. Soc.* **2005**, *127*, 12802-12803; (g) Tseng, H.-W.; Zong, R.; Muckerman, J. T.; Thummel, R. *Inorg. Chem.* **2008**, *47*, 11763-11773; (h) Kanan, M. W.; Nocera, D. G. *Science* **2008**, *321*, 1072-1075; (i) McDaniel, N. D.; Coughlin, F. J.; Tinker, L. L.; Bernhard, S. *J. Am. Chem. Soc.* **2008**, *130*, 210-217; (j) Eisenberg, R.; Gray, H. B. *Inorg. Chem.* **2008**, *47*, 1697-1699, and papers published in the forum.
- (a) Morandeira, A.; Boschloo, G.; Hagfeldt, A.; Hammarström, L. *J. Phys. Chem. C* **2008**, *112*, 9530-9537; (b) Qin, P.; Wiberg, J.; Gibson, E. A.; Linder, M.; Li, L.; Brinck, T.; Hagfeldt, A.; Albinsson, B.; Sun, L. *J. Phys. Chem. C* **2010**, *114*, 4738-4748; (c) Qin, P.; Linder, M.; Brinck, T.; Boschloo, G.; Hagfeldt, A.; Sun, L. *Adv. Mater.* **2009**, *21*, 2993-2996; (d) Qin, P.; Zhu, H.; Edvinsson, T.; Boschloo, G.; Hagfeldt, A.; Sun, L. *J. Am. Chem. Soc.* **2008**, *130*, 8570-8571.
- (a) Nattestad, A.; Mozer, A. J.; Fischer, M. K. R.; Cheng, Y. B.; Mishra, A.; Bauerle, P.; Bach, U. *Nat. Mater.* **2010**, *9*, 31-35; (b) He, J.; Lindström, H.; Hagfeldt, A.; Lindquist, S.-E. *Sol. Energy Mater. Sol. Cells* **2000**, *62*, 265-273; (c) Mizoguchi, Y.; Fujihara, S. *Electrochem. Solid-State Lett.* **2008**, *11*, K78-K80.
- (a) The theoretical efficiency limit for 3rd generation²⁶ photovoltaic tandem cells, where each of the chromophores absorbs a different portion of the solar spectrum, is ~43%.^{23,27} This compares favorably to the maximum 30% efficiency achievable in Grätzel-type cells operating with one active electrode; (b) Green, M. *Third Generation Photovoltaics: Advanced Solar Energy Conversion*; Springer-Verlag: Berlin, 2003; (c) Hanna, M. C.; Nozik, A. J. *J. Appl. Phys.* **2006**, *100*, 074510-074518.
- (a) Nattestad, A.; Ferguson, M.; Kerr, R.; Cheng, Y.-B.; Bach, U. *Nanotechnology* **2008**, *19*, 295304; (b) Mori, S.; Fukuda, S.; Sumikura, S.; Takeda, Y.; Tamaki, Y.; Suzuki, E.; Abe, T. *J. Phys. Chem. C* **2008**, *112*, 16134-16139; (c) Borgström, M.; Blart, E.; Boschloo, G.; Mukhtar, E.; Hagfeldt, A.; Hammarström, L.; Odobel, F. *J. Phys. Chem. B* **2005**, *109*, 22928-22934; (d) Odobel, F.; Le Pleux, L.; Pellegrin, Y.; Blart, E. New Photovoltaic Devices Based on the Sensitization of p-type Semiconductors: Challenges and Opportunities. *Acc. Chem. Res.* [Online Early Access]. DOI: DOI: 10.1021/ar900275b. Published Online: 2010. <http://dx.doi.org/10.1021/ar900275b> (accessed Jun 30, 2010).
- (a) Morandeira, A.; Edvinsson, T.; Pleux, L.; Blart, E.; Boschloo, G.; Hagfeldt, A.; Hammarström, L.; Odobel, F. *J. Phys. Chem. C* **2008**, *112*, 1721-1728; (b) Morandeira, A.; Boschloo, G.; Hagfeldt, A.; Hammarström, L. *J. Phys. Chem. B* **2005**, *109*, 19403-19410.

8. (a) O'Regan, B.; Schwartz, D. T. *J. Appl. Phys.* **1996**, *80*, 4749-4754 ; (b) O'Regan, B.; Lenzmann, F.; Muis, R.; Wienke, J. *Chem. Mater.* **2002**, *14*, 5023-5029; (c) Rusop, M.; Soga, T.; Jimbo, T.; Umeno, M. *Surf. Rev. and Lett.* **2004**, *11*, 577-583.
9. (a) Nakasa, A.; Usami, H.; Sumikura, S.; Hasegawa, S.; Koyama, T.; Suzuki, E. *Chem. Lett.* **2005**, *34*, 500-501; (b) Gibson, E. A.; Smeigh, A. L.; Le Pleux, L.; Fortage, J.; Boschloo, G.; Blart, E.; Pellegrin, Y.; Odobel, F.; Hagfeldt, A.; Hammarström, L. *Angew. Chem., Int. Ed. Engl.* **2009**, *48*, 4402-4405.
10. (a) Serpone, N.; Jamieson, M. A.; Henry, M. S.; Hoffman, M. Z.; Bolletta, F.; Maestri, M. *J. Am. Chem. Soc.* **1979**, *101*, 2907-2916; (b) Serpone, N.; Jamieson, M. A.; Emmi, S. S.; Fuochi, P. G.; Mulazzani, Q. G.; Hoffman, M. Z. *J. Am. Chem. Soc.* **1981**, *103*, 1091-1098; (c) Serpone, N.; Jamieson, M. A.; Sriram, R.; Hoffman, M. Z. *Inorg. Chem.* **1981**, *20*, 3983-3988; (d) Hoffman, M. Z.; Serpone, N. *Isr. J. Chem.* **1982**, *22*, 91-97; (e) Bolletta, F.; Maestri, M.; Moggi, L.; Jamieson, M. A.; Serpone, N.; Henry, M. S.; Hoffman, M. Z. *Inorg. Chem.* **1983**, *22*, 2502-2509; (f) Serpone, N.; Hoffman, M. Z. *J. Chem. Educ.* **1983**, *60*, 853-860; (g) Jamieson, M. A.; Serpone, N.; Hoffman, M. Z. *Coord. Chem. Rev.* **1981**, *39*, 121-179.
11. Juris, A.; Balzani, V.; Barigelletti, F.; Campagna, S.; Belser, P.; Vonzelewsky, A. *Coord. Chem. Rev.* **1988**, *84*, 85-277.
12. Greenwood, N. N.; Earnshaw, A. *Chemistry of the Elements*; 2nd ed.; Elsevier Butterworth-Heinemann: Oxford, 1997.
13. Barker, K. D.; Barnett, K. A.; Connell, S. M.; Glaeser, J. W.; Wallace, A. J.; Wildsmith, J.; Herbert, B. J.; Wheeler, J. F.; Kane-Maguire, N. A. P. *Inorg. Chim. Acta* **2001**, *316*, 41 - 49.
14. (a) Isaacs, M.; Sykes, A.; Ronco, S. *Inorg. Chim. Acta* **2006**, *359*, 3847-3854; (b) Donnay, E. G.; Schaeper, J. P.; Brooksbank, R. D.; Fox, J. L.; Potts, R. G.; Davidson, R. M.; Wheeler, J. F.; Kane-Maguire, N. A. P. *Inorg. Chim. Acta* **2007**, *360*, 3272-3280.
15. Garelli, N.; Vierling, P. *J. Org. Chem.* **1992**, *16*, 3046-3051.
16. (a) Ryu, C. K.; Endicott, J. F. *Inorg. Chem.* **1988**, *27*, 2203-2214; (b) Henriques, R. T.; Herdtweck, E.; Kuhn, F. E.; Lopes, A. D.; Mink, J.; Romao, C. C. *J. Chem. Soc., Dalton Trans.* **1998**, 1293-1297.
17. *APEX 2*, Bruker Analytical X-Ray Systems, Inc.: Madison, WI, 2008.
18. Sheldrick, G. M. *SHELXTL*, Version 6.14; Bruker Analytical X-Ray Systems, Inc.: Madison, WI, 1999.
19. (a) Kalyanasundaram, K. *Photochemistry of Polypyridine and Porphyrin Complexes*; Academic Press: London, 1992; (b) Brunschwig, B.; Sutin, N. *J. Am. Chem. Soc.* **1978**, *100*, 7568-7577.
20. Demas, J. N.; Crosby, G. A. *J. Phys. Chem.* **1971**, *75*, 991-1024.
21. Calvert, J. M.; Caspar, J. V.; Binstead, R. A.; Westmoreland, T. D.; Meyer, T. J. *J. Am. Chem. Soc.* **1982**, *104*, 6620-6627.
22. Bain, G. A.; Berry, J. F. *J. Chem. Educ.* **2008**, *85*, 532-536.

23. Vandiver, M. S.; Bridges, E. P.; Koon, R. L.; Kinnaird, A. N.; Glaeser, J. W.; Campbell, J. F.; Priedemann, C. J.; Rosenblatt, W. T.; Herbert, B. J.; Wheeler, S. K.; Wheeler, J. F.; Kane-Maguire, N. A. P. *Inorg. Chem.* **2010**, *49*, 839-848.
24. (a) Milder, S. J.; Gold, J. S.; Klinger, D. S. *Inorg. Chem.* **1990**, *29*, 2506-2511; (b) König, E.; Herzog, S. *J. Inorg. Nucl. Chem.* **1970**, *32*, 585-599.
25. (a) Hauser, A.; Maeder, M.; Robinson, W. T.; Murugesan, R.; Ferguson, J. *Inorg. Chem.* **1987**, *26*, 1331-1338; (b) Schonherr, T.; Atanasov, M.; Hauser, A. *Inorg. Chem.* **1996**, *35*, 2077-2084.
26. (a) Ohno, T.; Kato, S.; Kaizaki, S.; Hanazaki, I. *Chem. Phys. Lett.* **1983**, *102*, 471-474; (b) Ohno, T.; Kato, S.; Kaizaki, S.; Hanazaki, I. *Inorg. Chem.* **1986**, *25*, 3853-3858.
27. Juban, E. A. Ph.D., University of California, 2006.
28. Kirk, A. D. *Chem. Rev.* **1999**, *99*, 1607-1640.
29. (a) Claude, J. P.; Meyer, T. J. *J. Phys. Chem.* **1995**, *99*, 51-54; (b) Kober, E. M.; Caspar, J. V.; Lumpkin, R. S.; Meyer, T. J. *J. Phys. Chem.* **1986**, *90*, 3722-3734; (c) Chen, P. Y.; Meyer, T. J. *Chem. Rev.* **1998**, *98*, 1439-1477.
30. Forster, L. S. *Coord. Chem. Rev.* **2002**, *227*, 59-92.
31. (a) Saito, Y.; Takemoto, J.; Hutchinson, B.; Nakamoto, K. *Inorg. Chem.* **1972**, *11*, 2003-2011; (b) Creutz, C. *Comments Inorg. Chem.* **1982**, *1*, 293 - 311.
32. Ballardini, R.; Varani, G.; Indelli, M. T.; Scandola, F.; Balzani, V. *J. Am. Chem. Soc.* **1978**, *100*, 7219-7223.
33. Connelly, N. G.; Geiger, W. E. *Chem. Rev.* **1996**, *96*, 877-910.
34. Bard, A. J.; Faulkner, L. R. *Electrochemical methods fundamentals and applications*; 2nd ed.; Wiley: New York, 2001.
35. Pavlishchuk, V. V.; Addison, A. W. *Inorg. Chim. Acta* **2000**, *298*, 97-102.
36. Monserrat, K.; Foreman, T. K.; Grätzel, M.; Whitten, D. G. *J. Am. Chem. Soc.* **1981**, *103*, 6667-6672.
37. Reece, S. Y.; Nocera, D. G. *J. Am. Chem. Soc.* **2005**, *127*, 9448-9458.
38. Del Negro, A. S.; Seliskar, C. J.; Heineman, W. R.; Hightower, S. E.; Bryan, S. A.; Sullivan, B. P. *J. Am. Chem. Soc.* **2006**, *128*, 16494-16495.
39. Ramasami, T.; Endicott, J. F.; Brubaker, G. R. *J. Phys. Chem.* **1983**, *87*, 5057-5059.
40. Grätzel, M. *Inorg. Chem.* **2005**, *44*, 6841-6851.
41. (a) Serpone, N.; Jamieson, M. A.; Hoffman, M. Z. *J. Chem. Soc., Chem. Commun.* **1980**, 1006 - 1007; (b) Serpone, N.; Jamieson, M. A.; Sharma, D. K.; Danesh, R.; Bolletta, F.; Hoffman, M. Z. *Chem. Phys. Lett.* **1984**, *104*, 87-92; (c) Kirk, A. D.; Porter, G. B.; Sharma, D. K. *Chem. Phys.*

Lett. **1986**, *123*, 548-550; (d) Serpone, N.; Hoffman, M. Z. *Chem. Phys. Lett.* **1986**, *123*, 551-552; (e) Rojas, G. E.; Dupuy, C.; Sexton, D. A.; Magde, D. *J. Phys. Chem.* **1986**, *90*, 87-92; (f) Rojas, G. E.; Magde, D. *J. Phys. Chem.* **1987**, *91*, 689-691; (g) Serpone, N.; Hoffman, M. Z. *J. Phys. Chem.* **1987**, *91*, 1737-1743.

Chapter 5. Syntheses and Photophysical Investigations of Cr(III) Hexadentate Iminopyridine Complexes and Their Tris(Bidentate) Analogues

Reproduced with permission from *Inorganic Chemistry*, submitted for publication. Unpublished work copyright 2012 American Chemical Society.

5.1 Introduction

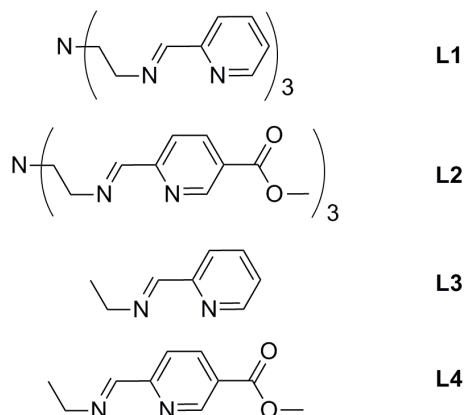
The photophysics and photochemistry of Cr(III) complexes are relevant to third generation solar photoconversion schemes. Chromium is an earth-abundant metal, and surrounding Cr(III) ions with appropriate ligands can produce powerful photooxidants.¹ The excited-state properties of Cr(III) tris-diimine (e.g., bpy, phen) complexes are well known, and the long (μs) lifetimes observed make these compounds potentially useful for dye-sensitized hole-injection photovoltaic devices and/or photooxidative catalytic schemes.^{1b,2} In principle, the photophysical properties are tunable: in the previous chapter on heteroleptic tris-dipyridyl Cr(III) complexes (Chapter 4), we observed subtle changes in the ground-state electronic absorption and more pronounced changes in electrochemical and excited-state photophysical properties when the ligand set was altered.^{1b} Drawbacks to using Cr(III) tris-diimine complexes in photoconversion schemes are: relatively weak absorption of visible light, poor stability in non-acidic aqueous solution, and increased lability of the formally reduced species in a photooxidative scenario following hole transfer.

Enhanced solution stability may be addressed by increasing the denticity of the ligand(s) chelating the chromium center. Photochemical studies on a few chromium complexes ligated by multidentate amine ligands³ or tethered bipyridines⁴ have uncovered long-lived ²E excited-states, although it should be noted that all of these species are yellow and therefore do not absorb strongly in the visible spectrum. However, a structural study for $[\text{Cr}(\text{tren}(\text{impy})_3)](\text{ClO}_4)_3$ reports a ‘wine red’ color for crystals of the hexadentate ligand-containing Cr(III) complex salt,⁵ which contrasts with the typical bright-yellow coloration of the hetero- and homo-leptic tris(bidentate) polypyridyl complexes of Cr(III).^{1b} Thus, complexes featuring

tripodal ligands could have enhanced absorption in the visible wavelengths coupled simultaneously with increased stability against ligand exchange in photoreduced species. Although there are few chromium complexes with hexadentate imine ligands,⁵⁻⁶ the tripodal system shown in Scheme 5.1 offers a ligand set similar to the tris-diimine complexes studied previously, as well as the potential for kinetic stability and electronic and steric tunability. Since bidentate iminopyridine analogues are easily prepared via Schiff-base condensations, we might also straightforwardly evaluate how photophysical and electrochemical properties change between tethered (hexadentate) podand ligands and those without a tether (tris(bidentate)).

Herein, we report the preparations, characterizations, photophysical properties and computational analyses of a family of Cr(III) iminopyridine complexes. A comparison of tripodal hexadentate complexes with their tris(bidentate) analogues reveals very similar ground-state behaviors (e.g., structures, electrochemistry, solution stability), but unexpectedly divergent photophysical properties.

Scheme 5.1. Hexadentate tripodal (**L1** and **L2**) and bidentate iminopyridine (**L3** and **L4**) ligands used in this study.



5.2 Division of Labor

Interpretation of photophysical data was done by Huan-Wei Tseng and Prof. Niels Damrauer at the University of Colorado, Boulder. Stability testing in acetonitrile and all photophysical characterization was conducted by Huan-Wei Tseng. All DFT calculations and NTO analyses were performed by Prof.

Anthony Rappé. Syntheses of **L1**, **L2** and **5.2** were carried out by Ethan Hill under the direction of Ashley McDaniel. All other synthetic work, ground-state characterization, and stability testing in 1M HCl and acetonitrile were done by Ashley McDaniel.

5.3 Experimental Section

5.3.1 Preparation of Compounds. Unless otherwise noted, compound manipulations were performed either inside a dinitrogen-filled glovebox (MBRAUN Labmaster 130) or via Schlenk techniques on an inert gas (N₂) manifold. The preparations of dimethylpyridine-2,5-dicarboxylate,⁷ methyl 6-(hydroxymethyl)nicotinate,⁸ the hexadentate ligand trimethyl 6,6',6''-((1E,1'E,1''E)-((nitrilotris(ethane-2,1-diyl))tris(azanylylidene))tris-(methanylylidene))-trinicotinate (**L2**),⁹ [Cr(CH₃CN)₄(BF₄)₂],¹⁰ and thianthrene tetrafluoroborate (Th⁺BF₄⁻)¹¹ have been described elsewhere. Methyl-6-formylnicotinate was synthesized according to a modified literature procedure,¹² where methyl 6-(hydroxymethyl)nicotinate was substituted as the oxidation substrate. The tripodal ligand tren(impy)₃ (**L1**) (tren = tris-(2-aminoethyl)amine) was synthesized from a reported procedure.¹³ Pentane was distilled over sodium metal and subjected to three freeze-pump-thaw cycles. Other solvents were sparged with dinitrogen, passed over molecular sieves, and degassed prior to use. All other reagents were obtained from commercial sources and were used without further purification.

[Cr(**L1**)](BF₄)₃ (**5.1**). A structure of the perchlorate salt of the [Cr(**L1**)]³⁺ species has been previously reported,⁵ however the synthetic route is not amenable to preparing bulk amounts of material. A solution of [Cr(CH₃CN)₄(BF₄)₂] (0.30 g, 0.78 mmol) in 3 mL of acetonitrile was added to a solution of **L1** (0.32 g, 0.78 mmol) in 5 mL of acetonitrile to form a dark-brown solution. Addition of a solution of Th⁺BF₄⁻ (0.25 g, 0.83 mmol) in 4 mL of acetonitrile caused the solution color to lighten to red-orange. A red-orange solid was precipitated by addition of diethyl ether (30 mL). The solid was isolated by filtration, washed with dichloromethane (3 × 5 mL) and diethyl ether (3 × 5 mL), and then dried in vacuo to afford 0.50 g (88%) of product. IR (KBr pellet): ν_{C=N} 1638 cm⁻¹. Absorption spectrum (CH₃CN): λ_{max} (ε_M) 204

(45900), 292 (12200), 321 nm (8800 M⁻¹·cm⁻¹). μ_{eff} (295K): 3.70 μ_{B} . ES+MS (CH₃CN): m/z 503.17 ([Cr(L1)F₂]⁺). ES-MS (CH₃CN): m/z 813.00 m/z ([Cr(L1)(BF₄)₄]⁻). Anal. Calcd. for C₂₄H₂₇B₃CrF₁₂N₇: C, 39.71; H, 3.75; N, 13.51. Calcd. for 5.1·2H₂O: C, 37.83; H, 4.10; N, 12.87. Found: C, 38.08; H, 4.37; N, 12.69. We note that the 5.1 is hygroscopic, and that broad peaks at 3610 and 3266 cm⁻¹ indicating uptake of water appear in the IR spectrum if the sample is not kept under dry conditions.

[Cr(L2)](BF₄)₃ (5.2). A solution of [Cr(CH₃CN)₄(BF₄)₂] (0.13 g, 0.34 mmol) in 3 mL of acetonitrile was added to a suspension of L2 (0.20 g, 0.34 mmol) in 5 mL of acetonitrile to form a dark brown solution. Upon addition of a solution of Th⁺BF₄⁻ (0.13 g, 0.43 mmol) in 4 mL of acetonitrile the solution lightened to a tan brown color. A tan-brown solid was precipitated by addition of diethyl ether (30 mL) and was isolated by filtration. The isolated powder was washed with dichloromethane (3 × 5 mL), and diethyl ether (3 × 5 mL), and then recrystallized twice by diethyl ether diffusion into a concentrated solution of acetonitrile to yield 0.15 g (49%) of crystalline product. IR (KBr pellet): $\nu_{\text{C=O}}$ 1733, $\nu_{\text{C=N}}$ 1638 and 1610 cm⁻¹. Absorption spectrum (CH₃CN): λ_{max} (ϵ_{M}) 201 (63000), 246 (sh 19000), 303 (16000), 390 nm (2100 M⁻¹·cm⁻¹). μ_{eff} (295 K): 4.57 μ_{B} . ES+MS (CH₃CN): m/z 677.13 ([Cr(L2)F₂]⁺). ES-MS (CH₃CN): m/z 987.07 m/z ([Cr(L2)(BF₄)₄]⁻). Anal. Calcd. for C₃₂H₃₆B₃CrF₁₂N₈O₆ (5.2·CH₃CN): C, 40.84; H, 3.86; N, 11.91. Found: C, 40.58; H, 4.04; N, 11.65. Crystals suitable for X-ray analysis were obtained by slow diffusion of diethyl ether into an acetonitrile solution of the compound.

(E)-N-(pyridin-2-ylmethylene)ethanamine (L3). A solution of 70% ethylamine in water (0.80 g) was added to a solution of 2-pyridinecarboxaldehyde (1.08 g, 10.1 mmol) in 20 mL of methanol containing 4Å molecular sieves. The resulting mixture was stirred at room temperature for 2 h and then filtered to remove the molecular sieves. The solvent was removed from the filtrate in vacuo to afford a tan-colored oil. The oil was extracted into 20 mL of pentane and the solvent was removed in vacuo to afford 1.03 g (76%) of product as a pale-yellow oil. ¹H NMR (CDCl₃): 1.31 (3H, t), 3.70 (2H, quar), 7.29 (1H, dd), 7.72 (1H, td), 7.96 (1H, d), 8.38 (1H, s), 8.63 ppm (1H, d). ¹³C NMR (CDCl₃): 16.24, 55.86, 121.39, 124.79, 136.72, 149.63, 154.89, 161.54 ppm. IR (KBr pellet): $\nu_{\text{C=N}}$ 1649 cm⁻¹. Absorption

spectrum (pentane): λ_{\max} 196, 234, 264 (sh), 271, 280(sh) nm. HRES+MS (CH₃OH): m/z calculated: 135.0922; found: 135.0915 (**L3**+H)⁺.

[Cr(L3)₃](BF₄)₃ (5.3). A solution of [Cr(CH₃CN)₄(BF₄)₂] (0.062 g, 0.159 mmol) in 3 mL of acetonitrile was added to a solution of **L3** (0.066 g, 0.493 mmol) in 4 mL of acetonitrile to form a dark brown solution. Upon addition of a solution of Th⁺BF₄ (0.051 g, 0.167 mmol) in 4 mL of acetonitrile, the dark solution lightened to a yellow color. The solvent volume was reduced to 1 mL in vacuo to precipitate thianthrene as a white solid, which was removed by filtration. The filtrate was treated with diethyl ether (20 mL) to precipitate a yellow solid. The solid was isolated by filtration, washed with dichloromethane (3 × 3 mL) and diethyl ether (3 × 3 mL), and then dried in vacuo to afford 0.104 g (91%) of product. IR (KBr pellet): $\nu_{\text{C=N}}$ 1635 and 1601 cm⁻¹. Absorption spectrum (CH₃CN): λ_{\max} (ϵ_{M}) 208 (51000), 224 (sh 37000) 246 (sh 12400), 298 (13400), 315 nm (sh 11400 M⁻¹·cm⁻¹). μ_{eff} (295 K): 3.86 μ_{B} . ES+MS (CH₃CN): m/z 151.47 ([Cr(**L3**)₃]³⁺), 236.40 ([Cr(**L3**)₃F]²⁺), 358.13 ([Cr(**L3**)₂F₂]⁺). ES-MS (CH₃CN): m/z 802.20 m/z ([Cr(**L3**)₃(BF₄)₄]⁻). Anal. Calcd. for C₂₄H₃₀B₃CrF₁₂N₆: C, 40.32; H, 4.23; N, 11.75. Found: C, 37.75; H, 4.25; N, 10.99. Calcd. for **5.3**·2.5H₂O C, 37.93; H, 4.64; N, 11.06.

(E)-methyl 6-((ethylimino)methyl)nicotinate (L4). A solution of 70% ethylamine in water (0.23 g) was added to a solution of methyl-6-formylnicotinate (0.45 g, 2.72 mmol) in 15 mL of methanol containing 4Å molecular sieves. The resulting mixture was stirred at room temperature for 2 h, and then filtered to remove the molecular sieves. The solvent was removed from the filtrate in vacuo. The resulting orange residue was extracted into 50 mL of pentane and filtered. The solvent was removed from the filtrate in vacuo, resulting in an ivory powder. This was sublimed at reduced pressure and 30 °C to yield 0.44 g (84%) of product as colorless crystals. ¹H NMR (CDCl₃): 1.34 (3H, t), 3.75 (2H, quar), 3.97 (3H, s) 8.07 (1H, d), 8.33 (1H, dd). 8.44 (1H, s), 9.23 ppm (1H, d). ¹³C NMR (CDCl₃): 16.11, 52.67, 56.00, 120.84, 126.64, 137.78, 150.82, 158.05, 160.78, 165.68 ppm. IR (KBr pellet): $\nu_{\text{C=O}}$ 1725, $\nu_{\text{C=N}}$ 1649 cm⁻¹. Absorption spectrum (pentane): λ_{\max} 199, 245, 254 (sh), 278 nm. HRES+MS(CH₃OH): m/z calculated: 193.0977; found: 193.0967 (**L4**+H)⁺.

[Cr(L4)₃](BF₄)₃ (5.4). A solution of [Cr(CH₃CN)₄(BF₄)₂] (0.049 g, 0.125 mmol) in 3 mL of acetonitrile was added to a solution of L4 (0.075 g, 0.388 mmol) in 4 mL of acetonitrile to form a dark brown red solution. Upon addition of a solution of Th⁺BF₄⁻ (0.04 g, 0.13 mmol) in 4 mL of acetonitrile, the dark solution lightened to a yellow color. The solvent volume was reduced to 1 mL in vacuo to precipitate thianthrene as a white solid, which was removed by filtration. The filtrate was treated with diethyl ether (20 mL) to precipitate a yellow solid. The powder was isolated by filtration, washed with dichloromethane (3 × 3 mL) and diethyl ether (3 × 3 mL), and then dried in vacuo to afford 0.090 g (80%) of product. IR (KBr pellet): $\nu_{\text{C=O}}$ 1736, $\nu_{\text{C=N}}$ 1633 and 1607 cm⁻¹. Absorption spectrum (CH₃CN): λ_{max} (ϵ_{M}) 205 (57000), 222 (sh 45000), 299 (17600), 321 nm (sh 14600 M⁻¹·cm⁻¹). μ_{eff} (295 K): 4.11 μ_{B} . ES+MS (CH₃CN): m/z 209.47 ([Cr(L4)₃]³⁺), 474.13 ([Cr(L4)₂F₂]⁺). ES-MS (CH₃CN): m/z 976.13 m/z ([Cr(L4)₃(BF₄)₄]⁻). Anal. Calcd. for C₃₀H₃₆B₃CrF₁₂N₆O₆: C, 40.53; H, 4.08; N, 9.45;. Found: C, 40.45; H, 3.89; N, 9.39. Crystals suitable for X-ray analysis were obtained by slow diffusion of diethyl ether into an acetonitrile solution of the compound.

5.3.2 X-Ray Structure Determinations. Crystals of **5.2** and **5.4** suitable for X-ray analysis were coated with Paratone-N oil and supported on a Cryoloop before being mounted on a Bruker Kappa Apex II CCD diffractometer under a stream of cold dinitrogen. Data collection was performed at 120 K with Mo K α radiation and a graphite monochromator, targeting complete coverage and 4-fold redundancy. Initial lattice parameters were determined from 342 reflections (**5.2**) and 500 reflections (**5.4**) harvested from 36 frames; these parameters were later refined against all data. Crystallographic data and metric parameters for **5.2** and **5.4** are presented in Table 5.1. Data were integrated and corrected for Lorentz and polarization effects by using SAINT, and semiempirical absorption corrections were applied by using SADABS.¹⁴ The structure of **5.2** was solved by direct methods and the structure of **5.4** was solved by Patterson techniques; both structures were refined against F^2 with the program XL from the SHELXTL 6.14 software package.¹⁵ Unless otherwise noted, displacement parameters for all non-hydrogen atoms were refined anisotropically. Hydrogen atoms were added at idealized positions and were refined by using

a riding model where the displacement parameters were set at 1.2 times those of the attached carbon atom (1.5 for methyl protons).

Crystals of complex **5.4** contain loosely-held solvate molecules, which quickly exit the lattice upon removal of the crystals from the mother liquor. This leads to rapid cracking of the crystals, even at 120 K, and results in moderate resolution and mediocre residuals. The residual electron density from the severely disordered/partially occupied solvate molecules could not be modeled satisfactorily, so the data were treated with SQUEEZE,¹⁶ which finds a 851.8 Å³ solvent void with 374 e⁻/unit cell corresponding to approximately 8 diethyl ether molecules. The data in Table 5.1 do not include the components removed by SQUEEZE. In addition to the solvent disorder, there is positional disorder in one ligand and in two anions. The CH₃ portion of the ethyl group on the imine containing C21 is disordered over two sites, and the methyl group on the ester containing C30 is disordered over two sites; the site occupancies refine to 57:43 and 77:23 ratios for the groups containing C21 and C30, respectively. The BF₄⁻ anion containing B2 has two F atoms, F5 and F6, split over two positions in an 81:19 ratio. Additionally, the BF₄⁻ anion containing B3 has also two F atoms, F9 and F12, split over two positions in a 57:43 ratio.

Table 5.1. Crystallographic data for [Cr(L2)](BF4)₃·CH₃CN (**5.2**·CH₃CN) and [Cr(L4)₃](BF4)₃ (**5.4**).^a

	5.2 ·CH ₃ CN	5.4
formula	C ₃₂ H ₃₆ B ₃ CrF ₁₂ N ₈ O ₆	C ₃₀ H ₃₆ B ₃ Cr F ₁₂ N ₆ O ₆
fw	941.12	889.08
color, habit	tan needle	yellow block
<i>T</i> , K	120(2)	120(2)
space group	<i>P</i> 6 ₃	<i>P</i> 2 ₁ / <i>n</i>
<i>Z</i>	2	4
<i>a</i> , Å	12.8725(2)	13.3694(8)
<i>b</i> , Å	12.8725(2)	16.6678(9)
<i>c</i> , Å	13.6811(4)	20.3617(11)
<i>α</i> , deg	90	90
<i>β</i> , deg	90	99.601(4)
<i>γ</i> , deg	120	90
<i>V</i> , Å ³	1963.26(7)	4473.8(4)
<i>d</i> _{calc} , g/cm ³	1.592	1.320
GOF	1.140	1.105
<i>R</i> ₁ (<i>wR</i> ₂) ^b , %	2.94 (7.83)	8.03(24.49)

^a Obtained with graphite-monochromated Mo K_α (λ = 0.71073 Å) radiation.

^b $R_1 = \sum ||F_o| - |F_c|| / \sum |F_o|$, $wR_2 = \{ \sum [w(F_o^2 - F_c^2)^2] / \sum [w(F_o^2)^2] \}^{1/2}$ for $F_o > 4\sigma(F_o)$.

5.3.3 Photophysical Methods. Much of the instrumentation used was the same as our previous report,^{1b} and only salient details are discussed here. For static emission spectra and quantum yield measurements, complexes were dissolved in CH₃CN (HPLC-UV grade, Honeywell B&J High Purity Solvent) at room temperature, placed in quartz cuvettes of 1 cm path length, and diluted to give absorbances of ~0.1 at the excitation wavelength. Sample solutions were purged with argon (ultra pure carrier grade, Airgas Inc.) for 15 minutes to remove oxygen before measurement. The measurements were done with argon flowing on top of the solution to prevent oxygen from re-dissolving into the solution. Samples were excited at 355 nm and emission was recorded at a relative angle of 90°. To avoid Rayleigh scattering contamination in the emission spectra from higher orders of the 355 nm excitation, a 560 nm long-pass filter was placed in front of the grating. The emission spectra were corrected for solvent

scattering background and PMT response. The emission quantum yields were determined by comparing the integrated emission of each complex to the standard $[\text{Ru}(\text{bpy})_3](\text{PF}_6)_2$ with a known quantum yield of 0.095 in room temperature CH_3CN .¹⁷ Note that this quantum yield value for the $[\text{Ru}(\text{bpy})_3](\text{PF}_6)_2$ standard updated relative to the value ($\phi_{\text{em}} = 0.062$)¹⁸ which has been extensively used in past literature.

For the measurement of emission lifetimes, sample solutions were prepared and deoxygenated in exactly the same manner as described above and data were collected at room temperature. The sample was excited by 355 nm laser pulses (10 Hz; $\sim 0.3 \mu\text{J}/\text{pulse}$) with a pulse width of 3-5 ns (FWHM). The emitted light was selected by a notch filter ($750 \pm 5 \text{ nm}$) and detected at 90° with respect to the excitation laser. Each emission transient was obtained by averaging 3000 scans. The data were fit with a single exponential decay model using a LabView program with a code of local origin.

Both static emission and emission lifetime data were acquired from multiple experiments. Measurements were collected on three different days, in each case using freshly prepared solutions due to degradation issues. For each of these samples on each of these days, three data sets were collected. Quantum yield and lifetime values obtained from those nine measurements were averaged and the standard deviations were calculated. The percentage experimental errors ($\pm \text{error } \%$) reported herein represent two times the standard deviation.

5.3.4 Other Physical Methods. Absorption spectra were obtained with a Hewlett-Packard 8453 spectrophotometer in quartz cuvettes with 1 cm or 1 mm path lengths; all experiments were performed at room temperature. Infrared spectra were measured with a Nicolet 380 FT-IR spectrometer. Mass spectrometric measurements were performed in either the positive ion or negative ion mode on a Finnigan LCQ Duo mass spectrometer, equipped with an analytical electrospray ion source and a quadrupole ion trap mass analyzer. High resolution mass spectrometric measurements were performed in positive ion mode on an Agilent 6210 TOF LC/MS instrument, equipped with both electrospray and atmospheric pressure chemical ionization sources and an orthogonal-axis time-of-flight mass analyzer. Cyclic

voltammetry experiments were carried out inside a dinitrogen filled glove box in 0.1 M solutions of (Bu₄N)PF₆ in acetonitrile unless otherwise noted. The voltammograms were recorded with either a CH Instruments 1230A or 660C potentiostat using a 0.25 mm Pt disk working electrode, Ag wire quasi-reference electrode, and a Pt wire auxiliary electrode. All voltammograms shown were measured with a scan rate of 0.1 V/s. Reported potentials are referenced to the ferrocenium/ferrocene (Fc⁺⁰) redox couple and were determined by adding ferrocene as an internal standard at the conclusion of each electrochemical experiment. Solid state magnetic susceptibility measurements were performed using a Quantum Design model MPMS-XL SQUID magnetometer at 295 K on finely ground samples. The data were corrected for the magnetization of the sample holder by subtracting the susceptibility of an empty container; diamagnetic corrections were applied using Pascal's constants.¹⁹ Elemental analyses were performed by Robertson Microlit Laboratories, Inc. in Madison, NJ.

5.3.5 Electronic Structure Calculations. Unrestricted B3LYP hybrid density functional studies²⁰ were carried out in the G09 suite of electronic structure codes.²¹ Geometries were optimized for each of the quartet ground-states. For **L2**, the Cr-N_{amine} was constrained to the experimental bond distance of 3.12 Å. Methyl iminopyridine ligands **L3'** and **L4'** were used instead of the ethyl iminopyridine ligands **L3** and **L4**. The LANL2²² basis sets and effective core potentials were used for Cr; H, B, C, N and F were described with a 6-31g* model.²³ For the spin unrestricted M_S = 3/2 “quartet”, the excited-state energies were computed using TD-DFT, wherein at least the lowest 16 excited-states were computed. The number of excited-states computed was incrementally increased until the excited-state manifold reached approached 3.5 eV; the lowest 13 for [Cr(bpy)₃](BF₄)₃, 23 for [Cr(4-dmcbpy)₃](BF₄)₃, 19 for [Cr(**L2**)](BF₄)₃, and 24 for [Cr(**L4'**)₃](BF₄)₃ quartet excited-states are reported (Figure 5.7). For the doublet manifold, broken symmetry unrestricted solutions were obtained for the ααβ, αβα, and βαα M_S = 1/2 determinants. As described previously,²⁴ these three single determinantal descriptions are combined to form two multi-determinantal (MD-DFT), nearly degenerate doublet states (equations 2-9 in Ref. 24). In addition, the lowest energy of the three single determinantal M_S = 1/2 “doublet” models was used to compute a TD-DFT excited-state manifold;²⁵ again the number of excited-states computed was

incrementally increased until the excited-state manifold reached 3.5 eV (relative to the lowest doublet). The doublet TD-DFT excitation energies were offset relative to the lowest $M_S = 1/2$ “doublet” state. To compare with our MD-DFT results, estimates for spin-projected doublet states were obtained using the Soda et al model,²⁶ reproduced in equation (5.1).

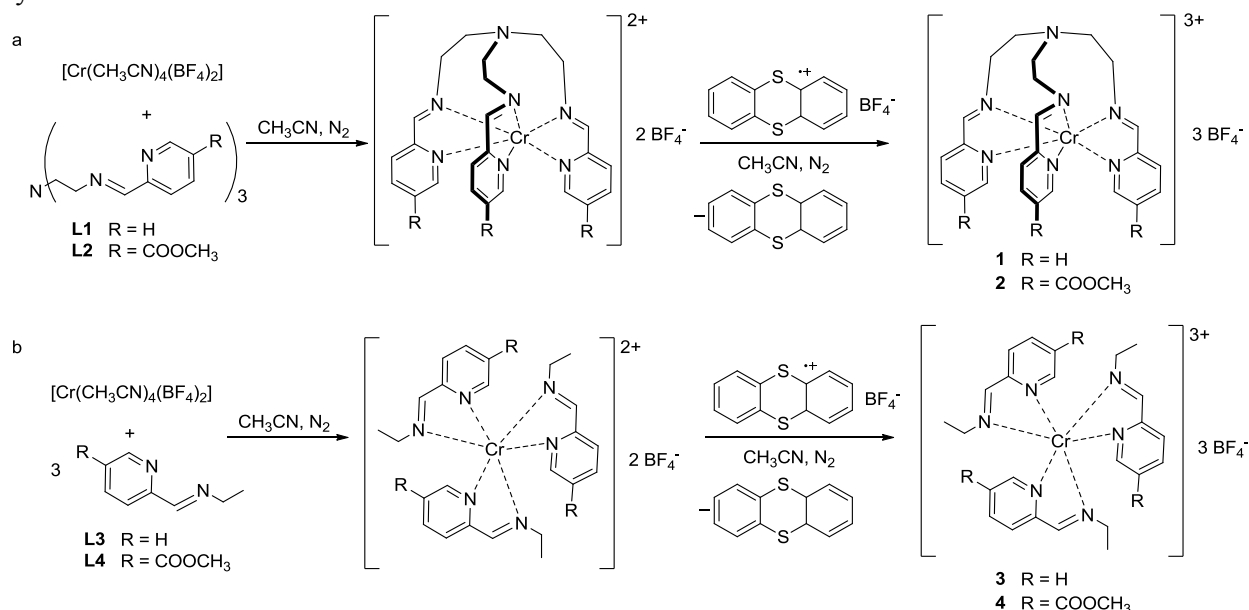
$$E_{3/2} - E_{1/2} = 3 \frac{(E_{HS} - E_{BS})}{\langle S^2 \rangle_{HS} - \langle S^2 \rangle_{BS}} \quad (5.1)$$

In the Soda model and in the predecessor Noodleman-Davidson model,²⁷ the expectation values of S^2 for the high-spin and related spin-flipped single determinantal models are used to project out spin contamination and more accurately estimate the energy for the true low-spin model. In equation (5.1) the $M_S = 3/2$ “quartet” and one of the $M_S = 1/2$ “doublet” models are used as the high-spin and broken symmetry models, respectively. For the $M_S = 5/2$ “sextet” manifold, a spin unrestricted SCF solution was obtained and the lowest 8 excited-states were computed using TD-DFT.

5.4 Results and Discussion

5.4.1 Synthesis and Ground-State Characterization of Cr(III) Complexes. The Cr(III) complex salts **5.1-5.4** are synthesized from the Cr(II) starting material $[\text{Cr}(\text{CH}_3\text{CN})_4(\text{BF}_4)_2]$ by the addition of stoichiometric amounts of the hexadentate tripodal ligands (Scheme 5.2a) or bidentate iminopyridine ligands (Scheme 5.2b), followed by oxidation by the non-coordinating oxidant thianthrene tetrafluoroborate (Th^+BF_4^-). Although there is literature precedent for synthesizing $[\text{Cr}(\mathbf{L1})](\text{ClO}_4)_3$ from Cr(III) precursors,⁵ in our hands we find that an oxidative route provides significantly higher yields. The complex salts $[\text{Cr}(\mathbf{L2})](\text{BF}_4)_3$ (**5.2**) and $[\text{Cr}(\mathbf{L4})_3](\text{BF}_4)_3$ (**5.4**) can be isolated as crystalline solids. X-ray structural data are available for **5.2**· CH_3CN and **5.4** (Table 5.1). Although the structure of $[\text{Cr}(\mathbf{L1})](\text{ClO}_4)_3$ (**5.1a**) has been reported in the literature,⁵ samples of $[\text{Cr}(\mathbf{L1})](\text{BF}_4)_3$ (**5.1**) and $[\text{Cr}(\mathbf{L3})_3](\text{BF}_4)_3$ (**5.3**) have not been crystallized.

Scheme 5.2. Preparation of Cr(III) iminopyridine complex salts: (a) syntheses of **5.1** and **5.2**; (b) syntheses of **5.3** and **5.4**.



Crystals of **5.2**·CH₃CN can be grown by slow diffusion of diethyl ether into acetonitrile solutions of **5.2**. The complex cation is shown in Figure 5.1; complete bond distances and angles are provided in the Supporting Information (cif). The complex crystallizes in the hexagonal space group *P6₃*, where the chromium center and an acetonitrile molecule sit on sites of three-fold symmetry. The chromium center is ligated to the tripodal impy ligand by three imino and three pyridine nitrogen atoms, producing a distorted octahedral environment (Figure A4.9). Due to the metal position on a three-fold symmetric site, only one arm of the ligand is crystallographically independent. Also present in the asymmetric unit is a single crystallographically independent tetrafluoroborate anion.

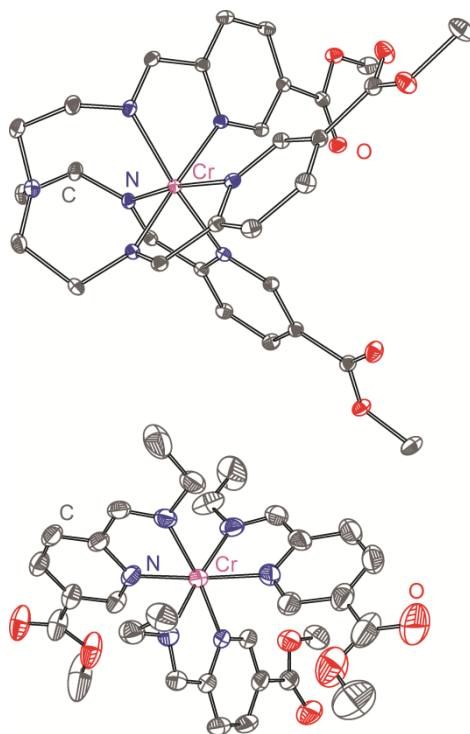


Figure 5.1. Structures of the Cr(III) iminopyridine complex cations $[\text{Cr}(\mathbf{L2})]^{3+}$ (top) and $[\text{Cr}(\mathbf{L4})_3]^{3+}$ (bottom), as observed in $\mathbf{5.2} \cdot \text{CH}_3\text{CN}$ and $\mathbf{5.4}$, respectively, rendered with 40% ellipsoids. Hydrogen atoms and minority disordered components are omitted for clarity.

Comparison of the structure of $\mathbf{5.2} \cdot \text{CH}_3\text{CN}$ and the previously reported structure of $\mathbf{5.1a}$ ($[\text{Cr}(\mathbf{L1})](\text{ClO}_4)_3$)⁵ show many similarities and a few small differences. The local coordination environment for $\mathbf{5.1a}$ and $\mathbf{5.2} \cdot \text{CH}_3\text{CN}$ are very similar. Within error, the Cr–N bond distances are identical: for $\mathbf{5.1a}$ the average Cr–N(py) and Cr–N(imine) distances are 2.062[9] and 2.044[9] Å,²⁸ respectively; for $\mathbf{5.2} \cdot \text{CH}_3\text{CN}$ the Cr–N(py) and Cr–N(imine) distances are 2.067(2) and 2.050(1) Å, respectively. In addition, for both structures the trigonal twist angles are very similar (average 52.54° for $\mathbf{5.1a}$ and 53.00(12)° for $\mathbf{5.2} \cdot \text{CH}_3\text{CN}$) and lower than the 60° expected for an ideal octahedral geometry. The main difference between the two structures is the distance between the Cr and the bridgehead N atoms: in $\mathbf{5.2} \cdot \text{CH}_3\text{CN}$ it is 3.120(2) Å, whereas in $\mathbf{5.1a}$ it is 3.155(5) Å. The difference in the position of the tether N may be due in part to solvation: $\mathbf{5.1a}$ lacks any co-crystallized solvent, whereas $\mathbf{5.2} \cdot \text{CH}_3\text{CN}$ contains an acetonitrile molecule. The shorter Cr···bridgehead N distance in $\mathbf{5.2} \cdot \text{CH}_3\text{CN}$ may also be attributable to weaker binding of the ester-functionalized ligand $\mathbf{L2}$, or other packing effects. The

acetonitrile solvate nitrogen atom is in close contact with the 6-position hydrogen atoms on each of the three pyridine moieties on the iminopyridine ligand at a distance of 2.714(2) Å. There are no close contacts between the solvent molecule and the bridgehead nitrogen, however.

Yellow block crystals of compound **5.4** can also be grown by ether diffusion into acetonitrile solutions of **5.4**. The crystals contain a significant amount of solvent, which quickly exits the lattice upon removal of the crystals from the mother liquor. The volatile nature of the solvent present in the lattice leads to severe solvent disorder and eventual cracking of the crystals. The data for **5.4** are presented herein to establish complex connectivity and provide additional characterization of the compound; solvent disorder does not appear to adversely affect determination of interactions relevant to the Cr-containing species. The complex cation in **5.4** is present as the *mer* isomer (Figure 5.1, bottom), and there is no evidence for *fac/mer* disorder present in the solid-state structure. The Cr–N bond distances in **5.4** are not significantly different from those found in **5.2** and range from 2.044(4) to 2.070(4) Å. Bond distances and angles are available in the Supporting Information (cif).

The isolated salts of **5.1-5.4** are soluble in strongly polar, aprotic solvents such as acetonitrile and nitromethane, but are only slightly soluble in strongly polar protic solvents such as methanol and water. The salts are insoluble in less polar solvents such as dichloromethane, tetrahydrofuran, diethyl ether and hydrocarbons. The complexes dissolve readily in 1M HCl_(aq), but degrade quickly, as discussed below.

5.4.2 Electrochemistry. Cyclic voltammogram (CV) data collected on fresh acetonitrile solutions of the complexes with 0.1 M TBA⁺PF₆⁻ as the supporting electrolyte are shown in Figure 5.2. Each of the Cr(III) complexes undergo multiple reversible reductions on the CV timescale. The reduction potentials for each of the complexes (relative to Fc⁺⁰) are reported in Table 5.2.

When comparing the tripodal to the tris(bidentate) analogues (**5.1** vs **5.3** and **5.2** vs **5.4**, respectively), inclusion of the nitrogen tether atom results in a shift of the first reduction wave to more negative potentials by 50 mV, presumably because of electron-donating properties of the tether nitrogen.²⁹ For successive reduction waves, the differences in potentials between tethered and non-tethered ligands varies between 10 and 40 mV, and is smallest for the 1+/0 wave.

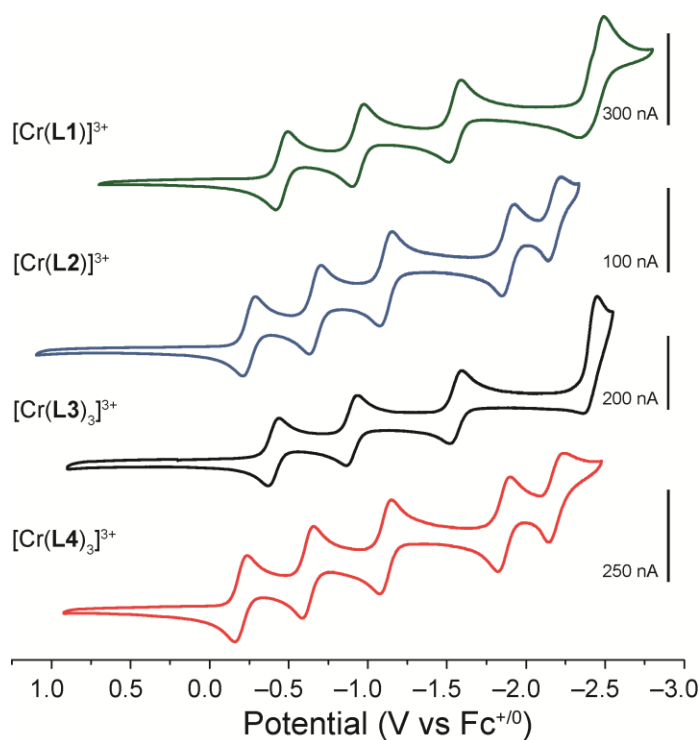


Figure 5.2. Comparison of cyclic voltammograms for **5.1-5.4** in 0.1 M TBAPF₆ acetonitrile solution.

Table 5.2. Ground-state reduction potentials for Cr(III) iminopyridine complexes.

Compound	$E_{1/2}$ ^a 3+/2+	2+/1+	1+/0	0/1-	1-/2-
[Cr(L1)] ³⁺	-0.45 (71)	-0.93 (70)	-1.55 (77)	-2.44 (160) irr	
[Cr(L2)] ³⁺	-0.25 (71)	-0.67 (71)	-1.12 (71)	-1.89 (81)	-2.18 (86)
[Cr(L3)] ³⁺	-0.41 (69)	-0.90 (71)	-1.56 (72)	-2.40 (89) irr	
[Cr(L4)] ³⁺	-0.20 (76)	-0.63 (73)	-1.11 (74)	-1.87 (78)	-2.17 (91)
[Cr(bpy)] ₃ ^{3+b}	-0.63 (72)	-1.15 (71)	-1.72 (69)	-2.34 (74)	
[Cr(phen)] ₃ ^{3+b}	-0.65 (70)	-1.17 (72)	-1.71 (75)	-2.21 (77)	

^a Potentials reported in V vs Fc^{+/0} (ΔE_p in mV). Conditions for cyclic voltammetry of Cr complexes: electrolyte, 0.1 M TBAPF₆ in CH₃CN; WE, Pt; CE, Pt wire; scan rate, 100 mV/s. ^b Data from Reference 2.

A more profound effect involves the inclusion of the electron-withdrawing ester groups, which shift the first reduction waves toward positive potentials by approximately 200 mV. For each successive reduction, the potential difference between the ester-functionalized and parent complexes increases. Additionally, the ester-functionalized complexes have a fifth reversible reduction wave that is accessible within the solvent window, whereas the parent complexes only have four accessible reduction waves and

the waves at the most negative potentials are irreversible. The much larger effect of the ester functionality compared to that of the nitrogen tether is expected given the ester's presence within the conjugated π -system of the iminopyridine ligands.

While there are very few chromium impy complexes reported in the literature,³⁰ the electrochemistry reported here is very similar to electrochemistry for a bis(iminopyridine) Cr(III) complex reported by Wieghardt and coworkers.³¹ For our complexes, each imine on the unfunctionalized parent ligand is able to undergo a one-electron reduction, generating a ligand radical. Addition of a fourth reducing equivalent to the tris-bidentate or tripodal hexadentate complex leads to an irreversible reduction. The inclusion of the electron-withdrawing ester groups allows for two additional reversible reductions to take place for the complex overall. It is likely that a third additional reduction wave would be present, but it is outside the acetonitrile solvent window.

5.4.3 Electronic Absorption. For comparison, ground-state electronic absorption spectra for fresh acetonitrile solutions of each of the complexes are shown in Figure 5.3. The spectra for each of the complexes are similar at short wavelengths, with a strong absorption peak near 205 nm. This peak correlates with a peak observed in the spectra of all free ligands near 200 nm. All of the iminopyridine Cr(III) complexes are moderately strong UV absorbers with ϵ of 10,000-20,000 $\text{M}^{-1}\text{cm}^{-1}$ between 250 and 325 nm. Comparing the two tripodal species **5.1** and **5.2**, a shoulder to the 205 nm peak occurs at 255 nm for each complex. This shoulder correlates to a peak and shoulder at 245 and 254 nm, respectively, found in **L2** (ligand spectra in Figure A4.7). In **L1** the analogous peak is significantly blue shifted and appears at 233 nm. For a comparison of the spectral features from the two tris-bidentate complexes **5.3** and **5.4**, a pronounced shoulder near 235 nm appears in each. This shoulder matches well with a peak that occurs at 234 nm for **L3**, and is shifted slightly from the analogous peak in **L4**, which lies at 245 nm.

When comparing the two parent complexes (**5.1** and **5.3**) to the ester-functionalized species (**5.2** and **5.4**), the ester-containing complexes show higher molar absorptivities in the UV region of $\lambda < 330$ nm. This is most likely due to the additional conjugation the ester groups provide to the iminopyridine ligands,

thus impacting ligand-centered absorptions as well as transitions that derive intensity from charge-transfer character involving the ligands.

In addition to the ultraviolet ligand-based absorptions, there is a broad peak and shoulder feature at ~300 nm and ~325 nm, respectively, for each of the four complexes. These transitions are likely to be charge transfer in nature because of their absence in the free ligands and their relatively strong intensities. The lowest energy shoulder is red shifted by 5-6 nm for the ester-functionalized ligand complexes relative to their parent iminopyridine ligand complexes. This red shift is consistent with expectations for metal-to-ligand charge-transfer (MLCT) given the presence of electron withdrawing substituents on the ester ligands **L2** and **L4**. However, one might also expect red shifting for ligand-to-metal charge transfer (LMCT) if such ligands serve to reduce electron-electron repulsion in the metal-centered orbitals. It is noted that the ~350 nm band in $[\text{Cr}(\text{bpy})_3]^{3+}$ is most often attributed to LMCT,³² since there is an energetic penalty for oxidizing Cr(III) to Cr(IV) as would formally occur during MLCT.^{1b}

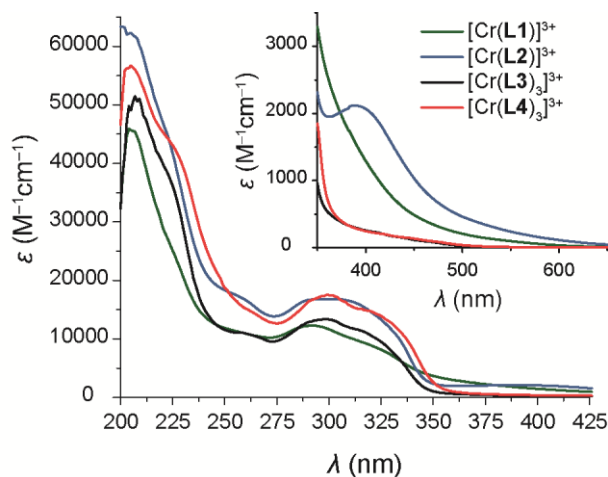


Figure 5.3. Electronic absorption spectra collected in acetonitrile for Cr(III) complexes **5.1-5.4** in the UV range (main) and the visible range (inset). All spectra were collected at room temperature.

The molar absorptivities of the two tris(bidentate) complexes diminish more rapidly at $\lambda > 350$ nm compared to their tripodal counterparts. Optically, this translates to more visible coloration in **5.1** and **5.2** compared to **5.3** and **5.4**. Solutions of complex **5.1** appear as a tan-orange color and solutions of complex

5.2, which has an additional peak centered at 390 nm with an $\epsilon = 2100 \text{ M}^{-1}\text{cm}^{-1}$, are a tan-brown color. Compounds **5.3** and **5.4** appear light yellow in solution as well as in the solid state.

Overall, changes to the ligand structure impact the absorption properties of the metal complexes. We find that addition of ester groups to the iminopyridine ligands helps to increase molar absorptivity for the UV and near-UV region, while addition of the nitrogen tether increases absorptivities in the visible wavelengths between 350 and 650 nm.

5.4.4 Probing Complex Stability in Solution. We hypothesized that tethering of the iminopyridine ligands would increase overall complex stabilities in solution, both in the ground-state and in photo-induced excited-states. Because photophysical properties for related tris(dipyridyl) Cr(III) complexes must be studied in acidic media to avoid photo-excited ligand substitution and/or solvolysis,^{2a} we first probed the properties of **5.1**, **5.2** and **5.4** in 1M HCl_(aq). Within 1 hour of dissolution, their spectra indicate conversion of the initial complex to another species (Figure A4.10). A white precipitate observed in acidic aqueous solutions of **5.2** indicates the loss of the hexadentate ligand, which may be initiated by protonation of the bridgehead nitrogen in acidic media. Yellow-to-pink color changes observed for **5.4** are reminiscent of the color of bis(bidentate) complex [Cr(phen)₂(OTf)₂](OTf) in the solid state and in acetonitrile solution,^{32a} and suggest the loss of one of the iminopyridine ligands with replacement by solvent molecules or coordinating anions. However, we have never observed hydrolysis of the imino groups in 1M HCl_(aq). The fact that **5.1** also changes over time indicates that the presence or absence of the ester functionality does not significantly impact the stability of the complexes in acidic solution.

Since the complexes have good solubility in acetonitrile and we are able to crystallize pure **5.2** and **5.4** from this solvent, we investigated the stability of those compounds in acetonitrile as an alternative to acidic media. Relative to [Cr(phen)₃](OTf)₃, ground-state absorption for **5.2** and **5.4** in acetonitrile (Figure A4.11) show small shifts over 24 hours. One possible explanation for the spectroscopic changes observed in acetonitrile could be related to the hydrolytic sensitivity of the charge-balancing BF₄⁻ anion to trace amounts of water, which is accelerated in the presence of acidic species.³³ Mass spectra of mixed CH₃CN/water solutions of **5.2** and **5.4** show peaks that contain fluorine without boron (e.g. [Cr(L4)₂F₂]⁺).

The loss of BF_4^- as a weakly interacting anion and its replacement by either fluoride- or oxygen-containing hydrolysis products would likely generate Cr species with directly coordinated anions, resulting in qualitatively different absorption spectra. Note that the hygroscopic nature of **5.1** and **5.3** could contribute further to anion instability for those compounds.

We conclude that, at least for the Cr(III) species examined here, thermodynamic stability is not significantly enhanced by use of a hexadentate tripodal ligand relative to the bidentate iminopyridine species on the time scales that were probed: **5.2** and **5.4** show similar solution chemistries. The photophysical studies discussed below are carried out in fresh solutions of the compounds using dry acetonitrile.

5.4.5 Emission Spectroscopy. In the photophysical discussions that follow, we focus on the two compounds (**5.2** and **5.4**) that can be obtained as X-ray quality crystals, and more importantly contain potential attachment points to a semiconductor surface in the form of ester functional groups. Following excitation at 355 nm, compound **5.4** is emissive in deoxygenated acetonitrile at room temperature (Figure 5.4). The spectrum is similar to that observed for Cr(III) tris-bipyridyl complexes.^{1b} The most intense band at 740 nm (1.68 eV) is assigned to $^2\text{E} \rightarrow ^4\text{A}$ phosphorescence. A weaker shoulder observed at 700 nm is expected to originate from the ^2T state, which is thermally equilibrated with the ^2E state. An excitation spectrum of 740 nm emission (Figure 5.5) shows that excited-states produced in the complex via excitation throughout the reddest portion of the UV absorption spectrum convert to the emissive ^2E state.

The ^2E emission quantum yield (ϕ_{em}) of **5.4** is measured (by relative comparison to a $[\text{Ru}(\text{bpy})_3](\text{PF}_6)_2$ standard) to be $0.00061 \pm 14\%$ in deoxygenated acetonitrile at room temperature. This represents a 64% reduction in emissive quantum yield compared to $[\text{Cr}(\text{bpy})_3](\text{OTf})_3$ where we observe $\phi_{\text{em}} = 0.0017 \pm 18\%$ under the same conditions.

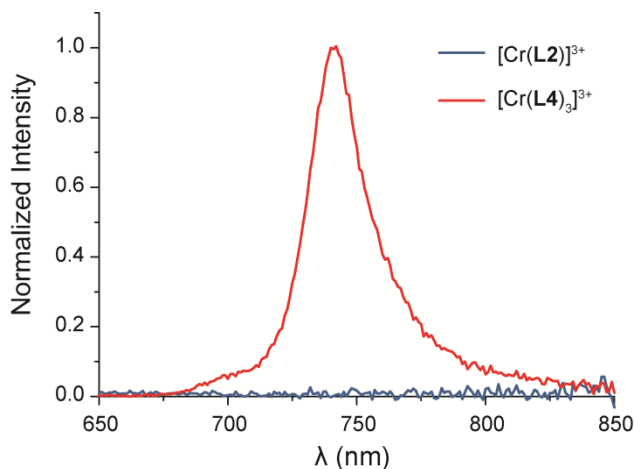


Figure 5.4. Emission spectra for freshly prepared solutions of **5.2** and **5.4** in deoxygenated acetonitrile at room temperature following 355 nm excitation.

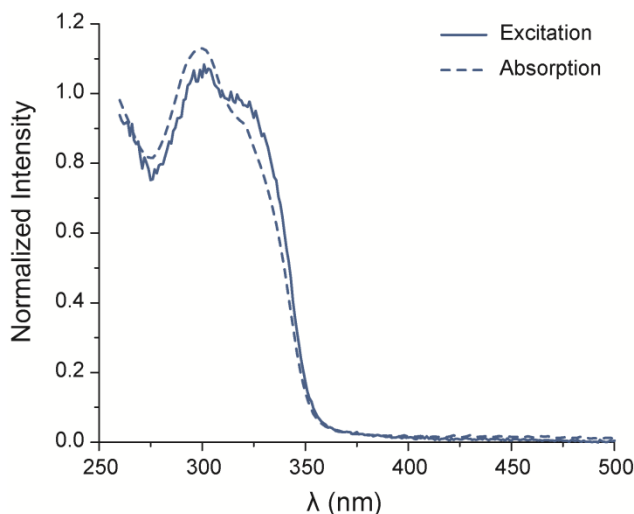


Figure 5.5. 2E excitation spectrum for a fresh prepared solution of **5.4** in deoxygenated acetonitrile at room temperature obtained by monitoring 740 nm emission intensity while varying the excitation wavelength. The excitation spectrum and ground-state absorption spectrum are normalized and overlaid for comparison.

Using nanosecond time-resolved emission spectroscopy, the 2E excited-state lifetime (τ_{obs}) of **5.4** was measured and a typical emission decay kinetic trace is presented in Figure 5.6. These data are fit with a single exponential decay model indicating $\tau_{\text{obs}} = 19 \mu\text{s} \pm 3\%$ in deoxygenated acetonitrile at room temperature. Transient absorption kinetics (following excitation with a ~ 5 ns pulse at 355 nm) have also been measured in deoxygenated acetonitrile at room temperature throughout the near-UV and visible

spectra (350 nm – 590 nm); all data show single-exponential decay of absorption features (Figure A4.12) with a comparable time constant ($\tau_{\text{obs}} = 17 \mu\text{s} \pm 5\%$). The μs time scale of emission (and absorption) decay agrees with the expected behavior of the ^2E state, where the lowest energy radiative pathway is $^2\text{E} \rightarrow ^4\text{A}$ phosphorescence. The observed lifetime is comparable to molecules such as $[\text{Cr}(\text{bpy})_3](\text{OTf})_3$, where $35 \mu\text{s}$ was measured under the same conditions used in this work.

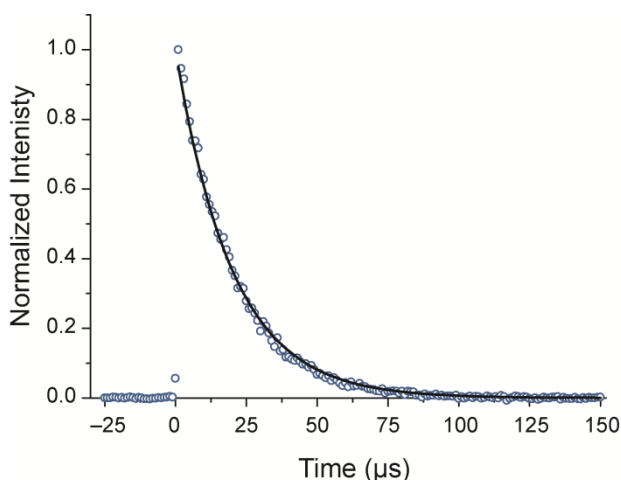


Figure 5.6. ^2E emission kinetic trace for **5.4** monitored at 750 nm in deoxygenated acetonitrile at room temperature following 355 nm laser excitation.

It is common to combine both static and time-resolved emission data to determine non-radiative ($\sum k_{\text{nr}}$) and radiative ($\sum k_{\text{r}}$) rate constants according to Eq. 5.2, where φ_{form} refers to the quantum yield of formation of the lowest energy excited-state from the Franck-Condon state.

$$\varphi_{\text{em}}/\varphi_{\text{form}} = \frac{\sum k_{\text{r}}}{\sum k_{\text{r}} + \sum k_{\text{nr}}} = \frac{\sum k_{\text{r}}}{k_{\text{obs}}} = \tau_{\text{obs}} \sum k_{\text{r}} \quad (5.2)$$

Assuming that φ_{form} is close to unity (an assumption that has not yet been tested extensively for this complex) we find that for compound **5.4**, $\sum k_{\text{r}} = 32 \text{ s}^{-1}$ and $\sum k_{\text{nr}} = 52600 \text{ s}^{-1}$ to be compared with $\sum k_{\text{r}} = 47 \text{ s}^{-1}$ and $\sum k_{\text{nr}} = 27700 \text{ s}^{-1}$ measured for $[\text{Cr}(\text{bpy})_3](\text{OTf})_3$ under the same conditions. Thus for **5.4** relative to $[\text{Cr}(\text{bpy})_3](\text{OTf})_3$, $\sum k_{\text{r}}$ is decreased by 32% while $\sum k_{\text{nr}}$ nearly doubles. Both quantities contribute to the lower emissive quantum yield for **5.4**. Although the excited-state lifetime of **5.4** is shortened relative to

[Cr(bpy)₃](OTf)₃, it is still in the μs time scale. If stability issues were not a concern, **5.4** could be a candidate for performing photo-induced oxidation reactions or interfacial hole-transfer photochemistry, provided that the quantum yield for forming the ²E (i.e., ϕ_{form}) is indeed high.

Unlike the tris(bidentate) complex **5.4**, the hexadentate complex **5.2** has shown no evidence for transient absorption throughout the visible (beyond the ~ 5 ns excitation pulse width) or ²E emission at room temperature. This latter point is shown, for example, in Figure 4 in the wavelength region of 650-850 nm where no emitted light is detected. This region is inclusive of where ²E emission (which is particularly insensitive to ligand or environment for the d³ electronic configuration) would be observed for most Cr(III) species.³⁴ The crystallographic data for **5.2** discussed previously in this paper are unremarkable with respect to the Cr coordination environment and would not preclude a ligand field comparable to what is present in **5.4**. The major difference in the coordination environments between **5.2** and **5.4** is the *facial* versus *meridional* arrangement of the iminopyridine moieties, respectively. However, for [Cr(α -picolylamine)]³⁺, it is reported that *fac*- versus *mer*- coordination imparts only small differences to complex emission properties, and both geometries give rise to ²E emission with lifetimes near 200 μs at 77 K.^{3a} The lack of ²E emission at room temperature in our case therefore suggests that either Σk_{nr} is large or ϕ_{form} is small. The details are important and will be elucidated in future work, including low temperature emission studies and transient absorption studies. Nevertheless, these initial observations, specifically the apparent absence of appreciable ²E lifetime at room temperature, suggest that **5.2** is not ideal as a sensitizer for excited-state redox chemistry.

In addition to the ²E emission found and discussed above for **5.4**, we report the observation of higher energy emitted light in the region of 350-550 nm for samples of **5.4** as well as for **5.2** with much lower intensity (Figure A4.13). Attempts were made to measure the excited-state lifetimes using these emission bands, however, no μs emission kinetics were observed and emission could not be resolved with a laser pulse width of ~ 5 ns. This suggests that excited-state lifetimes elucidated via these emission bands decay on a time scale of ns or shorter.

We first considered whether the higher energy emission for **5.4** suggested dual emission, wherein the Franck-Condon state partitions between 2E formation and decay via other pathways, some of which are radiative at ~ 425 nm (Figure A4.13). Such photophysics would contribute to measurement of a small ϕ_{em} via non-unity ϕ_{form} . There are two observations that lead us to consider that dual emission is unlikely. First, wavelength-dependent excitation scans of emission collected at 470 nm (Figure A4.14) show a stark difference to those collected at 740 nm (Figure 5.5) where there is excellent agreement between the features of ground-state absorbance and the excitation scans. Second, acetonitrile solutions of **5.4** aged for 24 hours exhibit a significant increase in the emission intensity of the ~ 425 nm band without significant change to the 740 nm 2E band (Figure A4.13). These observations suggest the growth of a small amount of a new strongly emissive compound as the samples age in solution. Studies performed on **5.2** give similar results (Figures A4.13-A4.14), although the percentage change is significantly lower than what is observed for the tris(bidentate) complex **5.4**.

Cr(III) complexes with bidentate ligands similar to the iminopyridines reported here have been studied.^{3a} At 77 K, $[\text{Cr}(\alpha\text{-picolyamine})_3]^{3+}$ shows emission at ~ 700 nm, which was assigned to be $^2E \rightarrow ^4A$ phosphorescence, and another emission band at ~ 390 nm was assigned to be ligand-centered emission. One important piece of evidence that supports the authors' assignment was that the free α -picolyamine is emissive under the same condition. However, the free ligands (**L1-L4**) are not emissive in room temperature acetonitrile, suggesting that the 350-550 nm emission observed in **5.4** and **5.2** is unlikely to be due to free ligand in the case of **5.4** or from a dissociated ligand arm in the case of **5.2**.

5.4.6 Electronic Structure Considerations. Photophysical behavior of Cr(III) complexes is generally conceived as involving the quartet and doublet manifolds, where the lowest energy, long-lived doublet state is essentially a linear combination of spin-flipped ($M_S = 1/2$) configurations of the metal-based quartet ground-state. In principle, sextet states may also contribute to the photophysical behavior observed. Based on the results presented here as well as previous work, it is clear that the ligands are heavily involved in complex properties: ground-state reduction of these kinds of complexes places the

reducing equivalent on the ligand,^{9,30d,31} and small changes in the ligand set appear to deactivate emission in **5.2** compared to **5.4**.

To explore a wide range of deactivation scenarios, multi-determinantal (MD) UB3LYP-DFT and TD-DFT computational studies were performed. Excitation energy (EE) diagrams are presented in Figure 5.7, lowest computed excitation energies are collected in Table 5.3, and representative natural transition orbital (NTO) plots are provided in Figure 5.8. For all complexes studied, the lowest doublet excited-states are lower in energy than the various quartet excited-states, indicating that ²E excited-states should be energetically accessible for all the iminopyridine Cr(III) complexes studied. For complex **5.4'** (using methyl iminopyridine ligand **L4'** instead of ethyl iminopyridine **L4**), the MD-DFT calculated first doublet excited-state energy (1.61 eV) is confirmed by experimental result for **5.4** from room temperature static emission (1.68 eV). For [Cr(bpy)₃]³⁺, the reported ²E emission of 1.71 eV compares well with the MD-DFT calculated energy 1.60 eV. In addition, for all four complexes the lowest doublets concentrate spin density in the three Cr t_{2g} orbitals. However, whereas **5.4**, [Cr(bpy)₃]³⁺, and [Cr(4-dmcbpy)₃]³⁺ show emission from the doublet manifold, **5.2** does not. Therefore, the simple presence of a low-lying doublet does not ensure productive emission.

Table 5.3. Computed excitation energies (EE) for selected complexes (eV)

Complex	1 st quartet EE	1 st M _S = ½ EE	1 st doublet EE (proj)	1 st doublet EE (MD-DFT)	1 st sextet EE
[Cr(bpy) ₃](BF ₄) ₃	2.71	1.07	1.58	1.60	3.11
[Cr(4-dmcbpy) ₃](BF ₄) ₃	2.54	1.09	1.59	1.62	2.95
[Cr(L1)](BF ₄) ₃ (5.1)	1.92	1.05	1.55	1.57	3.14
[Cr(L2)](BF ₄) ₃ (5.2)	1.95	1.03	1.52	1.54	3.16
[Cr(L3') ₃](BF ₄) ₃ (5.3') ^a	2.71	1.07	1.59	1.61	3.42
[Cr(L4') ₃](BF ₄) ₃ (5.4') ^a	2.86	1.08	1.61	1.61	3.29

^a Ligands marked by ' are methyl-terminated instead of ethyl-terminated.

In addition to comparison with experiment for the emissive doublet, the accuracies of the doublet manifold energies were further probed by TD-DFT studies. States within 3.5 eV of the lowest energy doublet were computed (since the experimental pumping wavelength of 355 nm is ~ 3.49 eV), absorption spectra were calculated for **5.2** and $[\text{Cr}(\text{bpy})_3]^{3+}$, and the latter computed spectrum was compared to the transient absorption spectrum for $[\text{Cr}(\text{bpy})_3]^{3+}$ (as discussed above the ${}^2\text{E}$ state is not observed for **5.2**). Good qualitative agreement between theory and experiment is observed (Figure A4.16).

Figures 5.7 and 5.8 highlight unique features of the tripodal complex salt **5.2** relative to $[\text{Cr}(\text{bpy})_3]^{3+}$, $[\text{Cr}(4\text{-dmc bpy})_3]^{3+}$, and **5.4'**. For the doublet and quartet spin manifolds, there are sets of lower energy

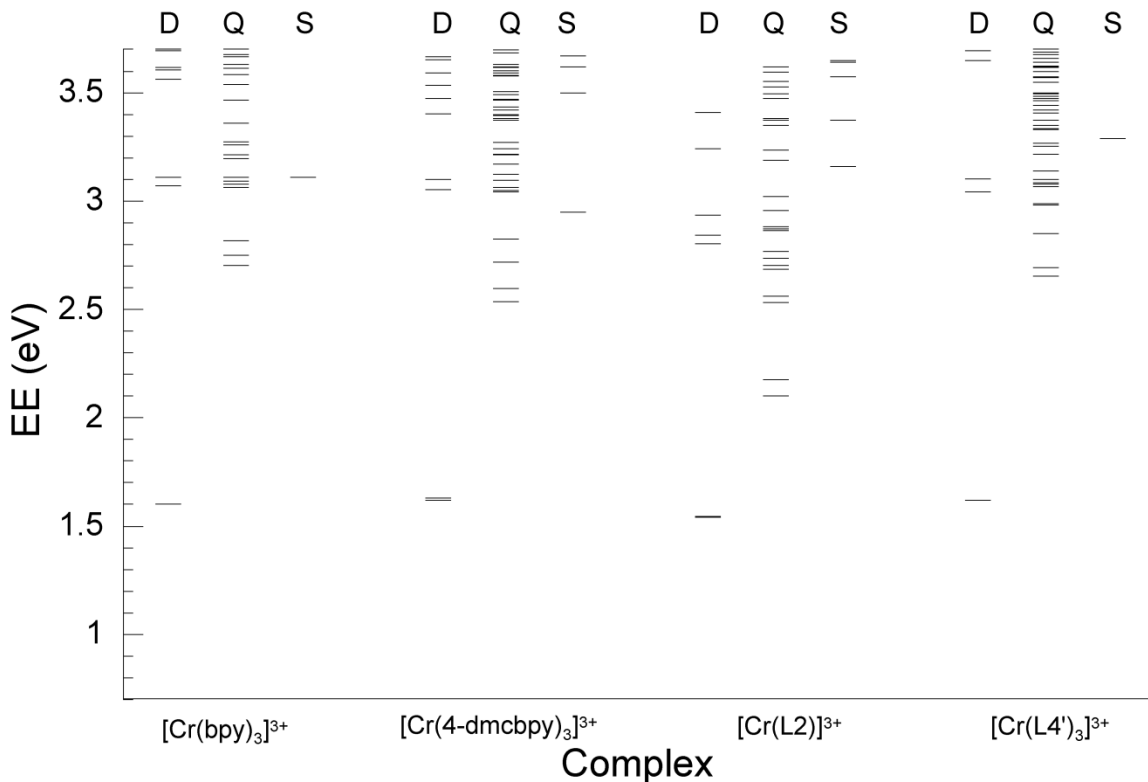


Figure 5.7. Computed excitation energies for selected Cr(III) complexes, where the ground-state quartet energy for each complex is set at zero. For each species, the left column is the doublet manifold (D), the middle column is the quartet manifold (Q), and the right column is the sextet manifold (S).

excited-states for **5.2**, relative to the other three complexes. For the sextet manifold, **5.2** does not have the lowest energy state but does have a significantly higher density of states than **5.1** or **5.4'** (Figure 5.7).

Additionally, the second set of doublet states of **5.2** (~2.8 eV) display different orbital character than those of **5.4'** (Figure 5.8) or $[\text{Cr}(4\text{-dmcbpy})_3]^{3+}$ (Figure A4.21).

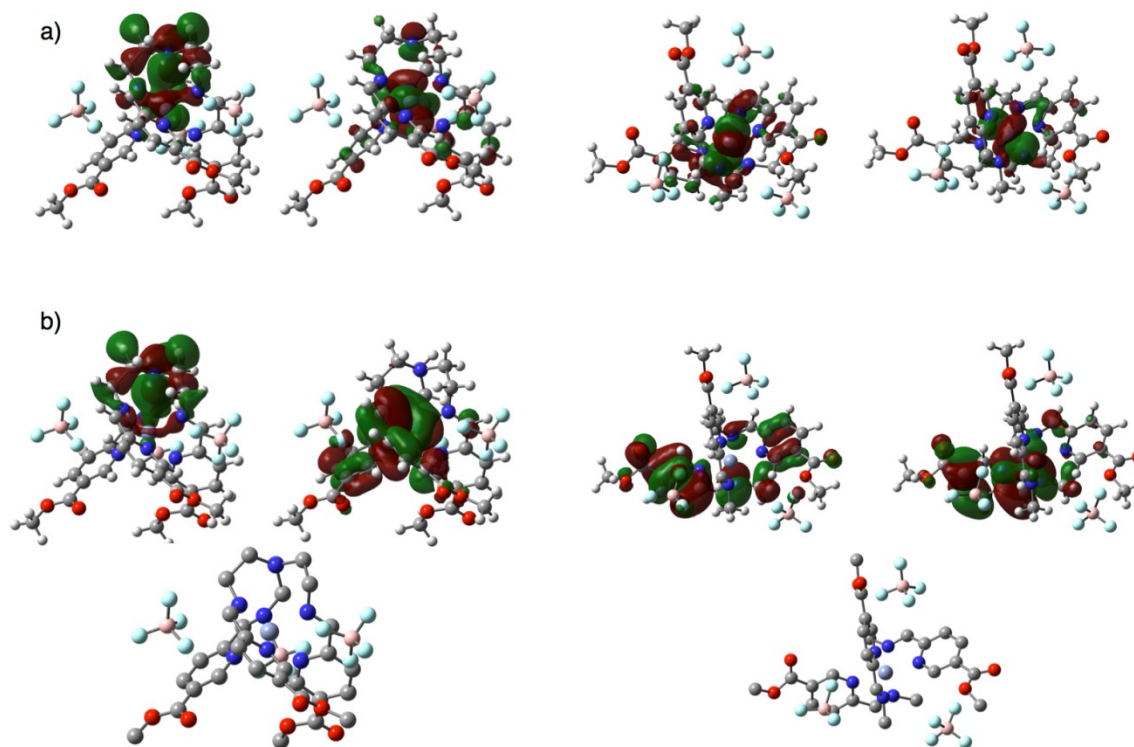


Figure 5.8. Natural transition Orbitals (NTOs) for the lowest (a) doublet and (b) quartet transitions for **5.2** (left) and **5.4'** (right). In each pair, the left NTO corresponds to where the excitation is from while the right NTO is where the excitation is to. Hydrogen atoms have been removed for clarity.

As developed in the Supporting Information (Figure A4.17-A4.21), the energetic position and orbital character of the quartet and doublet excited-states provide an explanation for the absence of observed doublet emission and transient absorption for **5.2**. Briefly, for **5.2**, $[\text{Cr}(4\text{-dmcbpy})_3]^{3+}$, and **5.4'**, the lowest quartet excited-states involve excitation from a ligand (ligand π or N_{amine}) orbital to an orbital that is an admixture of ligand π^* and Cr t_{2g} character. For $[\text{Cr}(4\text{-dmcbpy})_3]^{3+}$ and **5.4'** the second set of doublet states arise from transitions that are dominantly Cr $t_{2g} \rightarrow \text{Cr } t_{2g}$ in character (lowest doublet transitions in Figure 5.8, A4.21), as shown in Eq. 5.3 below:



For both $[\text{Cr}(4\text{-dmcby})_3]^{3+}$ and **5.4'** there is a small admixture of ligand character in the donating orbital, with larger admixture for the iminopyridine than for the bipyridine complex. In contrast, for **5.2**, the admixture of ligand character dominates: the transition for **5.2** is LMCT in nature ($\text{N}_{\text{amine}} \rightarrow \text{Cr } t_{2g}$ transition). For both $[\text{Cr}(4\text{-dmcby})_3]^{3+}$ and **5.4'** the higher energy low spin t_{2g}^3 doublet states can readily undergo internal conversion to the lower t_{2g}^3 doublet states via the large congruence of orbital character, electronic coupling, and ligand geometry. For **5.2**, due to a disparity of orbital character and ligand geometry, internal conversion from higher doublets to the lowest energy set of doublet states competes with intersystem crossing to a set of quartet states with congruent orbital character (and ligand geometry) which shares little orbital character with the lowest doublet states.

In summary, the NTO analyses show several key features. First, the involvement of the ligand's bridgehead nitrogen helps to explain why the tripodal complex **5.2** has much lower energy quartet and doublet excited-states relative to its tris(bidentate) relatives **5.4'** and $[\text{Cr}(4\text{-dmcby})_3]^{3+}$. Second, **5.2** can undergo photo-excitation similar to **5.4'** and $[\text{Cr}(4\text{-dmcby})_3]^{3+}$, and the three complexes have reasonable pathways for intersystem crossing into the doublet manifold. However, distinct from the non-tethered species, intersystem crossing and/or internal conversion events allow photo-excited **5.2** to settle into a low-energy, largely ligand-based quartet excited-state featuring little spatial congruence with the lowest energy metal-based doublet set. This quartet has dominant ligand-based charge transfer character, implying that there will be significant reorganization on both solvent and intramolecular nuclear coordinates relative to the ground-state of the molecule where the quartet character is metal-based. These factors along with the already-noted low energy of the quartet excited-state, will contribute to large non-radiative rates for internal conversion. Indeed, the bridgehead nitrogen of the tripodal ligand introduces "real intruder" ligand-based excited-states for complexes **5.1** and **5.2**.

It is important to note that the original impetus for studying the tripodal ligand complexes – increased absorption in the visible spectrum relative to Cr(III) dipyriddy species – is validated by the computational

results: the tripodal complexes feature increased density-of-states of the quartet manifold at lower energy compared to the other complexes studied (Figure 5.7), which is necessary for more efficient storage of visible spectrum energy. That the bridgehead nitrogen is also a source of efficient deactivation pathways is not readily apparent from a standard coordination chemical analysis of the ligand, especially for a functional group that is neither bound to the metal ion nor conjugated with the binding groups.

5.5 Conclusions and Outlook

We have prepared and studied the photophysical properties of a series of Cr(III) iminopyridine complexes, both in tethered and tris(bidentate) forms. While the solution stability of the complexes is not markedly improved by addition of the tether, the photophysical properties of the species are quite affected by the presence or absence of the bridgehead nitrogen moiety. The tris(bidentate) complex **5.4** shows μs emission at room temperature, similar to aromatic diimine complexes studied previously, and consistent with the existence of a long-lived (doublet) excited-state. In contrast, the tripodal complex **5.2** does not appear to emit from the doublet excited-state or give μs time-scale transient absorption signals. Computational results show the importance of small ligand modifications on photophysical properties. In future studies, we will explore the synthesis of podand-type ligands where the Cr(III) center can be completely incarcerated in the ligand framework, so as to avoid the formation of species due to ligand loss or exchange. We will also seek to replace the bridgehead nitrogen with other species to probe the electronic perturbations on excited-state behavior.

As part of this work, we have developed a computational protocol for quartet-doublet-sextet systems that (a) gives good agreement with available experimental observations, and (b) highlights the importance of ligand-based excited-states. Current and future computational efforts aim to incorporate the key spin-orbit coupling intersystem crossing matrices in a straightforward and efficient manner. Controlling both the quartet and doublet manifolds is important, and this experimentally-validated approach may be useful

in predicting suitable Cr(III) complexes which absorb more strongly in the visible spectrum and continue to allow efficient population of the long-lived doublet excited-state.

5.7 References

1. (a) Balzani, V.; Bolletta, F.; Gandolfi, M.; Maestri, M. In *Organic Chemistry and Theory*; Springer Berlin / Heidelberg: 1978; Vol. 75, p 1-64; (b) McDaniel, A. M.; Tseng, H.-W.; Damrauer, N. H.; Shores, M. P. *Inorg. Chem.* **2010**, *49*, 7981-7991.
2. (a) Serpone, N.; Jamieson, M. A.; Henry, M. S.; Hoffman, M. Z.; Bolletta, F.; Maestri, M. *J. Am. Chem. Soc.* **1979**, *101*, 2907-2916; (b) Hoffman, M. Z.; Serpone, N. *Isr. J. Chem.* **1982**, *22*, 91-97; (c) Pizzocaro, C.; Bolte, M.; Hoffman, M. Z. *J. Photochem. Photobiol., A* **1992**, *68*, 115-119; (d) Cheng, M.; Bakac, A. *J. Am. Chem. Soc.* **2008**, *130*, 5600-5605.
3. (a) Krause, R. A. *J. Phys. Chem.* **1978**, *82*, 2579-2581; (b) Brown, K. N.; Geue, R. J.; Sargeson, A. M.; Moran, G.; Ralph, S. F.; Riesen, H. *Chem. Commun.* **1998**, 2291-2292; (c) Lessard, R. B.; Heeg, M. J.; Buranda, T.; Perkovic, M. W.; Schwarz, C. L.; Yang, R.; Endicott, J. F. *Inorg. Chem.* **1992**, *31*, 3091-3103; (d) Ramasami, T.; Endicott, J. F.; Brubaker, G. R. *J. Phys. Chem.* **1983**, *87*, 5057-5059; (e) Comba, P.; Creaser, I. I.; Gahan, L. R.; Harrowfield, J. M.; Lawrance, G. A.; Martin, L. L.; Mau, A. W. H.; Sargeson, A. M.; Sasse, W. H. F.; Snow, M. R. *Inorg. Chem.* **1986**, *25*, 384-389.
4. (a) Williams, A. L.; Bhuiyan, A. A.; Turner, M. O.; Millett, F.; Durham, B. *J. Coord. Chem.* **2011**, *64*, 48-56; (b) Williams, A. L. Ph.D. dissertation, University of Arkansas, 2009.
5. McLachlan, G. A.; Fallon, G. D.; Spiccia, L. *Acta Crystallogr., Sect. C: Cryst. Struct. Commun.* **1996**, *52*, 309-312.
6. (a) Ziessel, R.; Lehn, J.-M. *Helv. Chim. Acta* **1990**, *73*, 1149-1162; (b) Saraswat, R.; Rana, V. B. *J. Indian Chem. Soc.* **1998**, *75*, 493-495; (c) Singh, D. P.; Shishodia, N.; Yadav, B. P.; Rana, V. B. *J. Indian Chem. Soc.* **2004**, *81*, 287-290; (d) Yang, M.; Li, X.; Chen, Y.; Deng, R. *Huaxue Shiji* **2002**, *24*, 266-267, 270.
7. Oila, M. J.; Tois, J. E.; Koskinen, A. M. P. *Tetrahedron Lett.* **2005**, *46*, 967-969.
8. Jabre, N. D.; Respondek, T.; Ulku, S. A.; Korostelova, N.; Kodanko, J. J. *J. Org. Chem.* **2010**, *75*, 650-659.
9. McDaniel, A. M.; Rappé, A. K.; Shores, M. P., *Submitted to Inorg. Chem.*
10. Henriques, R. T.; Herdtweck, E.; Kuhn, F. E.; Lopes, A. D.; Mink, J.; Romao, C. C. *J. Chem. Soc., Dalton Trans.* **1998**, 1293-1297.
11. Boduszek, B.; Shine, H. J. *J. Org. Chem.* **1988**, *53*, 5142-5143.
12. Shavaleev, N. M.; Scopelliti, R.; Gumy, F.; Bünzli, J.-C. G. *Inorg. Chem.* **2009**, *48*, 6178-6191.
13. Jäntti, A.; Wagner, M.; Suontamo, R.; Kolehmainen, E.; Rissanen, K. *Eur. J. Inorg. Chem.* **1998**, 1555-1562.
14. *APEX 2*, Bruker Analytical X-Ray Systems, Inc.: Madison, WI, 2008.
15. Sheldrick, G. M. *SHELXTL*, Version 6.14; Bruker Analytical X-Ray Systems, Inc.: Madison, WI, 1999.

16. Spek, A. L. *J. Appl. Crystallogr.* **2003**, *36*, 7-13.
17. Suzuki, K.; Kobayashi, A.; Kaneko, S.; Takehira, K.; Yoshihara, T.; Ishida, H.; Shiina, Y.; Oishi, S.; Tobita, S. *Phys. Chem. Chem. Phys.* **2009**, *11*, 9850-9860.
18. Calvert, J. M.; Caspar, J. V.; Binstead, R. A.; Westmoreland, T. D.; Meyer, T. J. *J. Am. Chem. Soc.* **1982**, *104*, 6620-6627.
19. Bain, G. A.; Berry, J. F. *J. Chem. Educ.* **2008**, *85*, 532-536.
20. Becke, A. D. *J. Chem. Phys.* **1993**, *98*, 5648-5652.
21. Frisch, M. J.; et. al. *Gaussian 09, Revision A.1*, Gaussian, Inc.: Wallingford CT, 2009
22. Hay, P. J.; Wadt, W. R. *J. Chem. Phys.* **1985**, *82*, 299-310.
23. (a) Binkley, J. S.; Pople, J. A.; Hehre, W. J. *J. Am. Chem. Soc.* **1980**, *102*, 939-947; (b) Ditchfield, R.; Hehre, W. J.; Pople, J. A. *J. Chem. Phys.* **1971**, *54*, 724-728; (c) Francl, M. M.; Pietro, W. J.; Hehre, W. J.; Binkley, J. S.; Gordon, M. S.; DeFrees, D. J.; Pople, J. A. *J. Chem. Phys.* **1982**, *77*, 3654-3665; (d) Hehre, W. J.; Ditchfield, R.; Pople, J. A. *J. Chem. Phys.* **1972**, *56*, 2257-2261.
24. Hoffert, W. A.; Rappé, A. K.; Shores, M. P. *J. Am. Chem. Soc.* **2011**, *133*, 20823-20836.
25. Stratmann, R. E.; Scuseria, G. E.; Frisch, M. J. *J. Chem. Phys.* **1998**, *109*, 8218-8224.
26. Soda, T.; Kitagawa, Y.; Onishi, T.; Takano, Y.; Shigeta, Y.; Nagao, H.; Yoshioka, Y.; Yamaguchi, K. *Chem. Phys. Lett.* **2000**, *319*, 223-230.
27. Noodleman, L.; Davidson, E. R. *Chem. Phys.* **1986**, *109*, 131-143.
28. The errors for these bond distances were calculated by averaging the bond distances for each type of bond and taking the square root of the sum of the squares of the bond esds.
29. Isaacs, M.; Sykes, A.; Ronco, S. *Inorg. Chim. Acta* **2006**, *359*, 3847-3854.
30. (a) Vidyaratne, I.; Scott, J.; Gambarotta, S.; Budzelaar, P. H. M. *Inorg. Chem.* **2007**, *46*, 7040-7049; (b) Zhang, W.; Sun, W.-H.; Tang, X.; Gao, T.; Zhang, S.; Hao, P.; Chen, J. *J. Mol. Catal. A: Chem.* **2007**, *265*, 159-166; (c) Amolegbe, S. A.; Asma, M.; Zhang, M.; Li, G.; Sun, W. *Aust. J. Chem.* **2008**, *61*, 397-403; (d) Lu, C. C.; DeBeer George, S.; Weyhermüller, T.; Bill, E.; Bothe, E.; Wieghardt, K. *Angew. Chem., Int. Ed.* **2008**, *47*, 6384-6387.
31. Lu, C. C.; Bill, E.; Weyhermüller, T.; Bothe, E.; Wieghardt, K. *J. Am. Chem. Soc.* **2008**, *130*, 3181-3197.
32. (a) Ryu, C. K.; Endicott, J. F. *Inorg. Chem.* **1988**, *27*, 2203-2214; (b) Milder, S. J.; Gold, J. S.; Klinger, D. S. *Inorg. Chem.* **1990**, *29*, 2506-2511; (c) König, E.; Herzog, S. *J. Inorg. Nucl. Chem.* **1970**, *32*, 585-599.

33. (a) Wamser, C. A. *J. Am. Chem. Soc.* **1948**, *70*, 1209-1215; (b) Freire, M. G.; Neves, C. M. S. S.; Marrucho, I. M.; Coutinho, J. A. P.; Fernandes, A. M. *J. Phys. Chem. A* **2009**, *114*, 3744-3749.
34. Forster, L. S. *Coord. Chem. Rev.* **2002**, *227*, 59-92.

Chapter 6. Synthesis of “Cr(II)” and “Cr(I)” Polypyridyl Complexes

6.1 Introduction

In our previous studies of Cr(III) polypyridyl complexes, we employed a synthetic route which used “Cr(II)” precursors. We became interested in the Cr(II) and more reduced analogues of our complexes for two reasons. In hole injection photomaterials that use Cr(III), upon hole injection the 3+ species would be formally reduced to 2+. The reduction increases the lability of the resultant complex ion compared to the inert Cr(III). Understanding the behavior of the labile reduced versions of Cr polypyridyl complexes would help us to better design ligand sets which would improve solution stability and preserve photophysical performance. Additionally, in Cr polypyridyl complexes the polypyridyl ligands can behave non-innocently. As discussed in Chapter 1, the reducing equivalent that separates $[\text{Cr}(\text{L}^{5\text{-OOMe}})]^{2+}$ from $[\text{Cr}(\text{L}^{5\text{-OOMe}})]^{3+}$ actually resides on the $\text{L}^{5\text{-OOMe}}$ ligand, and both complexes are best described as having a Cr(III) metal center. Our group is also interested in the interaction between unpaired spins, and reduced versions of the Cr polypyridyl complexes would contain a Cr(III) center with three unpaired spins and ligand radical species.

In the course of this work, Wieghardt and coworkers published work¹ on the synthesis and characterization of reduced forms of $[\text{Cr}(\text{'bpy})_3]^n$, where 'bpy is 4,4'-di-tert-butyl-2,2'-bipyridine, and $n = 3+, 2+, 1+$ and 0. The work described in this chapter focuses on reduced forms of a similar ligand, 4-dmcbpy, which contains strongly electron withdrawing ester groups in contrast to the electron donating *t*-butyl moieties used in Wieghardt's work. In addition, we describe the reduced form of an iminopyridine complex, $[\text{Cr}(\text{tren}(\text{py})_3)]^{2+}$. The structural and electrochemical data presented here are in agreement with the observations and conclusions presented by Wieghardt and coworkers, specifically that reducing equivalents added to Cr polypyridine¹⁻² or iminopyridine³ complexes do not reside on the metal, and that these complexes are best described as Cr(III) ions ligated to anionic radical ligands.

6.2 Division of Labor

REU student Ethan Hill synthesized $\text{tren}(\text{impy})_3$, $[\text{Cr}(\text{tren}(\text{impy})_3)](\text{BF}_4)_2$, and carried out bulk electrolysis studies on this complex under the direction of Ashley McDaniel. All other experimental work was performed by Ashley McDaniel.

6.3 Experimental Section

6.3.1 Preparation of Compounds. Unless otherwise noted, compound manipulations were performed either inside a dinitrogen-filled glovebox (MBRAUN Labmaster 130) or via Schlenk techniques on an inert gas (N_2) manifold. $[\text{Cr}(\text{CH}_3\text{CN})_4(\text{BF}_4)_2]$ and the ligands dimethyl 2,2'-bipyridine-4,4'-dicarboxylate (4-dmcbpy)⁴ and (E)-N1-(pyridin-2-ylmethylene)-N2,N2-bis(2-((E)-(pyridin-2-ylmethylene)amino)-ethyl)ethane-1,2-diamine ($\text{tren}(\text{impy})_3$)⁵ were synthesized according to the literature. Pentane was distilled over sodium metal and subjected to three freeze-pump-thaw cycles. Other solvents were sparged with dinitrogen, passed over alumina, and degassed prior to use. All other reagents were obtained from commercial sources and were used without further purification.

$[\text{Cr}(4\text{-dmcbpy})_3](\text{BF}_4)_2$ (6.1). Under a dinitrogen atmosphere, a solution of $[\text{Cr}(\text{CH}_3\text{CN})_4(\text{BF}_4)_2]$ (0.148 g, 0.38 mmol) in 3 mL of acetonitrile was added to a suspension of 4-dmcbpy (0.342 g, 1.256 mmol) in 6 mL of acetonitrile to form a forest green solution. The solvent volume was reduced to 3 mL in vacuo and treated with 15 mL of diethyl ether to afford a forest green precipitate. The solution was filtered, the isolated powder was washed with diethyl ether (3×2 mL), and then dried in vacuo to afford 0.385 g (97%) of product. IR (mineral oil): $\nu_{\text{C=O}}$ 1727 cm^{-1} . Absorption spectrum (MeCN) λ_{max} , (ϵ): 313 (25900), 478 (2220), 635 (2630), 770(sh, 1700), >1100 nm (>2000 $\text{M}^{-1}\text{cm}^{-1}$). Crystals suitable for X-ray analysis were obtained by slow diffusion of diethyl ether into an acetonitrile solution of the compound.

$[\text{Cr}(4\text{-dmcbpy})_3](\text{BF}_4)$ (6.2). Solid **6.1** (0.148g, 0.14 mmol) was added to 6 mL of N,N-dimethylformamide. Upon dissolution, the initially green solid formed an indigo colored solution. After stirring overnight, the solution was added to 40 mL of diethyl ether to precipitate an indigo solid. The

solid was collected by filtration and washed with diethyl ether (3×2 mL) and pentane (3×2 mL), and dried in vacuo to afford 0.133 g (98%) of product. IR (KBr pellet): $\nu_{\text{C=O}}$ 1716 cm^{-1} . Absorption spectrum (MeCN) λ_{max} : 414 (sh), 454, 556, 624, 668, 806, >1100 nm. ES+MS (MeCN): m/z 868.07 ($[\text{Cr}(4\text{-dmcbpy})_3]^+$), 596.12 ($[\text{Cr}(4\text{-dmcbpy})_2]^+$), 434.07 ($[\text{Cr}(4\text{-dmcbpy})_3]^{2+}$).

[Cr(tren(impy)₃)](BF₄)₂ (6.3). A solution of $[\text{Cr}(\text{MeCN})_4(\text{BF}_4)_2]$ (0.188 g, 0.484 mmol) in 3 mL of acetonitrile was added to a solution of $\text{tren}(\text{impy})_3$ (0.200 g, 0.484 mmol) in 5 mL of acetonitrile to form a dark brown solution. After stirring for 2 h, the reaction solution was concentrated to ~ 2 mL in vacuo, then added to 18 mL of diethyl ether to produce a dark brown precipitate. The powder was collected by filtration, washed with diethyl ether (3×2 mL) and pentane (3×2 mL), and dried in vacuo to afford 0.299 g (97%) of product. Crystals suitable for X-ray analysis were obtained by slow diffusion of diethyl ether into an acetonitrile solution of the compound.

6.3.2 Bulk Electrolyses. Electrochemical experiments were carried out inside a nitrogen filled glovebox at ambient temperature in a two compartment cell. Each cell compartment contained approximately 30 mL of 0.1M TBAPF₆ acetonitrile solution and the two compartments were separated by a porous glass frit (24.2 mm diameter and 4 mm thick). In the working compartment was kept a coiled Pt wire or Pt mesh attached to a Pt wire electrode as the working electrode and an Ag wire quasi-reference or a non-aqueous Ag/Ag⁺ (0.1M AgNO₃ in CH₃CN, Vycor frit) electrode as the reference electrode and a flea magnetic stirbar to maintain solution agitation. In the auxiliary compartment a solid Pt flag or Pt mesh basket electrode was used as the auxiliary electrode. Between 60 to 200 mg of “Cr(II)” complex was dissolved in the working compartment solution.

Prior to bulk electrolysis experiments, a cyclic voltammogram of the solution in the working compartment was carried out to determine the potential at which to carry out the bulk electrolysis. Bulk electrolysis experiments were carried out in constant potential mode and current and charge passed were monitored. Over the course of the experiment diffusion of the Cr containing species through the frit into

the auxiliary compartment was observed by the yellow coloration of the solution in the auxiliary compartment (indicating presence of Cr(III) species).

Future experiments would benefit from a dual compartment cell with a smaller diameter frit connecting the two compartments. Additionally, better results were obtained when using a Ag/Ag⁺ non-aqueous reference electrode instead of a Ag wire quasi-reference, most likely due to the ability of the Ag quasi-reference potential to ‘float’ as the composition of the solution changed over the course of the experiment.

6.3.3 X-Ray Structure Determinations. Crystals suitable for X-ray analysis were coated with Paratone-N oil and supported on a Cryoloop before being mounted on a Bruker Kappa Apex II CCD diffractometer under a stream of dinitrogen. Data collection was performed at 120 K with Mo K α radiation and a graphite monochromator, affording complete coverage and 4-fold redundancy. Initial lattice parameters were determined from 500 reflections harvested from 36 frames; these parameters were later refined against all data. Crystallographic data and metric parameters are presented in Table 6.1. Data were integrated and corrected for Lorentz and polarization effects by using SAINT, and semiempirical absorption corrections were applied by using SADABS.⁶ The structures were solved by direct methods and refined against F^2 with the program XL from the SHELXTL 6.14 software package.⁷ Unless otherwise noted, displacement parameters for all non-hydrogen atoms were refined anisotropically. Hydrogen atoms were added at idealized positions and were refined by using a riding model where the displacement parameters were set at 1.2 times those of the attached carbon atom (1.5 for methyl protons).

In the structure of **6.1·2** CH₃CN, one of the 4-dmcbpy ligands and one of the BF₄⁻ anions are positionally disordered. In one 4-dmcbpy ligand, an ester group contains a disordered methyl group split over two positions including C29 and C29a. The disorder refines to a 56:44 occupancy ratio and both carbon atoms were treated isotropically. In the BF₄⁻ anion containing B67, each of the four fluorine atoms are disordered over two positions and refine to an 86:14 ratio. The major part of the disorder was treated anisotropically and the minor part was refined isotropically. The bond lengths and angles in the

disordered anion were constrained to match those of the non-disordered anion by using the SAME command.

The structure of **6.3** includes disorder in one of the anions. The BF_4^- anion containing B2 is rotationally disordered along the B2-F5 axis and F6, F7, and F8 are split over two positions. The disorder refines to a 54:46 occupancy ratio and each set of fluorine atoms were treated anisotropically. The bond lengths and angles in the disordered anion were constrained to match those of the anion containing B1 by using the SAME command.

Table 6.1. Crystallographic data for compounds **6.1** and **6.3**.^a

	6.1 ·2CH ₃ CN	6.3
formula	C ₄₆ H ₄₂ B ₂ Cr F ₈ N ₈ O ₁₂	C ₂₄ H ₂₇ B ₂ CrF ₈ N ₇
fw	1124.50	639.15
color, habit	green plates	brown plates
<i>T</i> , K	120(2)	120(2)
space group	<i>P</i> 2 ₁ / <i>c</i>	<i>P</i> 2 ₁ / <i>c</i>
<i>Z</i>	4	4
<i>a</i> , Å	10.1513(4)	15.9010(9)
<i>b</i> , Å	26.2084(9)	10.7443(6)
<i>c</i> , Å	18.3876(7)	17.0864(9)
α , deg	90	90
β , deg	90.192(2)	114.907(3)
γ , deg	90	90
<i>V</i> , Å ³	4892.0(3)	2647.6(3)
<i>d</i> _{calc} , g/cm ³	1.527	1.603
GOF	1.040	1.137
<i>R</i> ₁ (<i>wR</i> ₂) ^b , %	5.51 (13.64)	3.72 (10.68)

^a Obtained with graphite-monochromated Mo K_α ($\lambda = 0.71073$ Å) radiation.

^b $R_1 = \Sigma |F_o| - |F_c| / \Sigma |F_o|$, $wR_2 = \{\Sigma [w(F_o^2 - F_c^2)^2] / \Sigma w(F_o^2)^2\}^{1/2}$ for $F_o > 4\sigma(F_o)$.

6.3.4 Other Physical Methods. Absorption spectra were obtained with a Hewlett-Packard 8453 spectrophotometer in airfree glass cuvettes; all experiments were performed at room temperature. Infrared spectra were measured with a Nicolet 380 FT-IR spectrometer. Mass spectrometric measurements were performed in the positive ion mode on a Finnigan LCQ Duo mass spectrometer, equipped with an analytical electrospray ion source and a quadrupole ion trap mass analyzer. Cyclic voltammetry

experiments were carried out inside a dinitrogen filled glove box in 0.1 M solutions of (Bu₄N)PF₆ in acetonitrile unless otherwise noted. The voltammograms were recorded with either a CH Instruments 1230A or 660C potentiostat using a 0.25 mm Pt disk working electrode, Ag wire quasi-reference electrode, and a Pt wire auxiliary electrode. All voltammograms shown were measured with a scan rate of 0.1 V/s. Reported potentials are referenced to the ferrocenium/ferrocene (Fc⁺⁰) redox couple and were determined by adding ferrocene as an internal standard at the conclusion of each electrochemical experiment.

6.4 Results and Discussion

6.4.1 Syntheses. In the course of preparing [Cr(4-dmcbpy)₃]³⁺ for photophysical studies as discussed in Chapter 3, we found that the trivalent species could be easily accessed through synthesis of the divalent species, followed by in situ oxidation using a chemical oxidant. We also found that the [Cr(4-dmcbpy)₃]²⁺ complex is isolable as the tetrafluoroborate salt (**6.1**) when [Cr(CH₃CN)₄(BF₄)₂] was added to three equivalents of the ligand. The forest-green solid is isolated in high yield by diethyl ether precipitation from the reaction mixture and can be crystallized by diethyl ether diffusion into acetonitrile.

Initially we attempted to access the more reduced forms of the tris 4-dmcbpy complex, namely [Cr(4-dmcbpy)₃]⁺ and [Cr(4-dmcbpy)₃]⁰ in multiple ways. We attempted chemical reductions using cobaltocene in dichloromethane (DCM) and sodium diphenylketyl radical in tetrahydrofuran (THF). We attempted disproportionation of [Cr(4-dmcbpy)₃]²⁺ to [Cr(4-dmcbpy)₃]³⁺ and [Cr(4-dmcbpy)₃]⁺ in methanol as disproportionation of [Cr(phen)₃]²⁺ had been reported previously in protic solvents.⁸ None of these methods produced the monovalent or neutral tris complexes, so we then turned to bulk electrolysis. We attempted bulk electrolysis of [Cr(4-dmcbpy)₃]²⁺ in acetonitrile solution; however, this also did not yield the desired complexes.

Serendipitously, when reattempting the bulk electrolysis in an alternate solvent, N,N-dimethylformamide (DMF), upon dissolution of [Cr(4-dmcbpy)₃](BF₄)₂ there was a near instantaneous color change from the deep-green color of the initial complex to an intense blue-purple color. From this

mixture, a blue-purple powder can be isolated by diethyl ether precipitation. Electrochemical, mass spectroscopic and electronic absorption characterization of the isolated power indicates that it is $[\text{Cr}(4\text{-dmcbpy})_3](\text{BF}_4)$ (**6.2**). The UV-Visible spectrum of $[\text{Cr}(4\text{-dmcbpy})_3](\text{BF}_4)$ (**6.2**) includes multiple bands in the visible range which diminish over time if the sample is exposed to air. Aerobic oxidation yields a violet to green color change and a spectrum which is nearly identical to freshly prepared samples of $[\text{Cr}(4\text{-dmcbpy})_3](\text{BF}_4)_2$ (**6.1**) as shown in Figure 6.1 and A5.3. Additionally, the main ion found in positive-ion mode mass spectrometry is 868.07 m/z with an isotopic pattern that matches $[\text{Cr}(4\text{-dmcbpy})_3]^+$ (Figure A5.4-6). Crystals of this complex can be grown by diethyl ether diffusion into concentrated methanol solution; however, the crystals obtained do not diffract well enough to be suitable for structure determination.

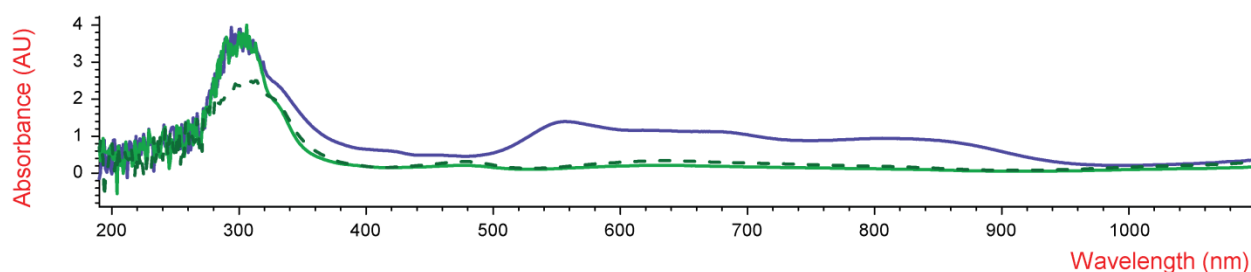


Figure 6.1. Comparison of electronic absorption spectra of $[\text{Cr}(4\text{-dmcbpy})_3]^{n+}$ complexes in CH_3CN . Violet trace is **6.2**, $n = 1$. Green trace is **6.2** after aerobic oxidation. Dashed dark green trace is **6.1**, $n = 2$.

There have been reports of DMF's use as a reducing agent for metal species previously in the literature; however, it is generally used to make nanoparticles of electropositive metals like Ag^+ ,⁹ Au^{3+} ,¹⁰ and Pd^{2+} ,¹¹ and for Pt/Ni alloys.¹² There are several potential byproducts to DMF oxidation,¹³ but most pathways for DMF oxidation generate gases (CO or CO_2 , and H_2). Since no obvious effervescence or gas or pressure generation was observed accompanying the green to indigo color change, it is likely that another pathway is active. One route which does not necessitate gas generation includes the production of carbamic acid and protons.^{9a} It is worth noting that all of the routes to DMF oxidation discussed above

require water. While the exact reduction potential for DMF has not been reported, the solvent has a working range of approximately 1.0 to -3.2 V vs $\text{Fc}^{+/0}$,¹⁴ and it is used extensively as a medium for electrochemical experiments. It was unexpected that it would be sufficiently reducing to convert the $[\text{Cr}(4\text{-dmcbpy})_3]^{2+}$ to $[\text{Cr}(4\text{-dmcbpy})_3]^+$, especially given that it is electrochemically stable over the potential range that encompasses the $[\text{Cr}(4\text{-dmcbpy})_3]^{2+/+}$ couple.

Similar to the preparation of $[\text{Cr}(4\text{-dmcbpy})_3](\text{BF}_4)_2$, $[\text{Cr}(\text{tren}(\text{impy})_3)](\text{BF}_4)_2$ (**6.3**) can be isolated by diethyl ether precipitation of the reaction mixture. This complex can be crystallized by slow diffusion of diethyl ether into concentrated acetonitrile solution.

6.4.2 Solid-State Structural Characterization. Compounds **6.1** and **6.3** can be obtained as diffraction quality crystals. Both complexes crystallize in the space group $P2_1/c$. For each complex, there is minimal disorder in the complex cation, but significant disorder with the BF_4 anions. The complex cations for both **6.1** and **6.3** are shown in Figure 6.1 below. As discussed in Chapters 2 and 5, the iminopyridine complexes synthesized with Cr(II) starting materials are best described as a Cr(III) metal center ligated to an anionic ligand radical. This is true for the iminopyridine complex **6.3** as well and can be directly seen through the comparison of iminopyridine bond lengths both within the complex and by comparison to the Cr(III) analogue.¹⁵

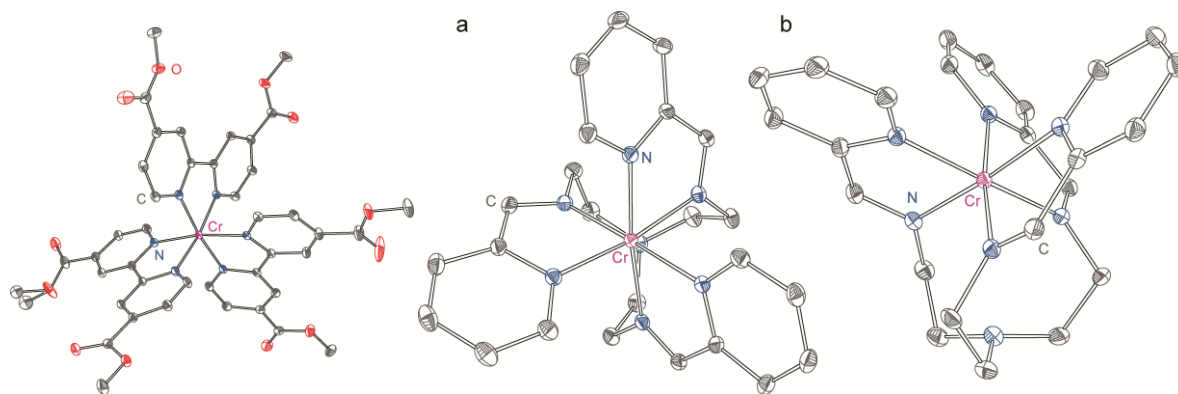


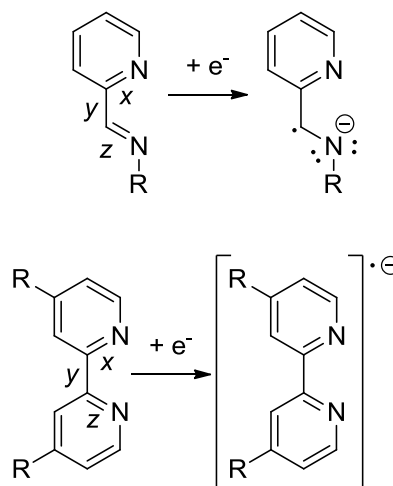
Figure 6.2. The complex cation for **6.1** (left) and two views of the complex cation for **6.3** (center and right) shown at 40% probability. Hydrogen atoms have been omitted for clarity.

One arm of the tripodal ligand $\text{tren}(\text{impy})_3$ has longer C–N bonds and a shorter C–C bridge bond than the other two arms in **6.3** and all of the arms in $[\text{Cr}(\text{tren}(\text{impy})_3)](\text{ClO}_4)_3$, as shown in Table 6.2. The case of the bipyridine complex $[\text{Cr}(4\text{-dmcbpy})_3](\text{BF}_4)_2$ is more difficult to parse. There is no obvious lengthening or shortening of any of the imine C–N or bridge C–C bonds, respectively, when comparing all three 4-dmcbpy ligands in **6.1** or in comparison to the single 4-dmcbpy in $[(\text{phen})_2\text{Cr}(4\text{-dmcbpy})](\text{OTf})_3$ (**3.1**).¹⁶ This is likely due to the larger conjugated system present on the bipyridine type ligands; delocalization of the reducing equivalent is more favorable and so large impacts on the length of a few bonds is much more difficult to observe.

Table 6.2. Selected ligand diimine ligand bond lengths.

Complex	x (Å)	y (Å)	z (Å)
$[\text{Cr}(\text{tren}(\text{impy})_3)](\text{BF}_4)_2$	1.358(2)	1.468(2)	1.277(2)
	1.363(2)	1.454(2)	1.284(2)
	1.378(2)	1.422(2)	1.318(2)
$[\text{Cr}(\text{tren}(\text{impy})_3)](\text{BF}_4)_3^a$	1.365(9)	1.445(8)	1.266(9)
	1.365(6)	1.455(9)	1.264(7)
	1.353(8)	1.435(9)	1.274(8)
$[\text{Cr}(4\text{-dmcbpy})_3](\text{BF}_4)_2$	1.365(2)	1.460(2)	1.369(2)
	1.360(2)	1.458(2)	1.370(2)
	1.364(2)	1.479(2)	1.365(2)
$[(\text{phen})_2\text{Cr}(4\text{-dmcbpy})](\text{OTf})_3^b$	1.364(4)	1.480(3)	1.360(4)

^a From Ref. 15 ^b From Chapter 4.



6.4.3 Electrochemical Characterization and Bulk Electrolysis. The $[\text{Cr}(4\text{-dmcbpy})_3]^{n+}$ complex cation displays six reversible redox waves regardless of the starting oxidation state, as shown in Figure 6.3. For the $\text{tren}(\text{impy})_3$ complexes, three reversible redox waves and one irreversible redox wave is accessible. There is very little change in the position of each of the redox events as the overall charge of the complex cation changes for $[\text{Cr}(4\text{-dmcbpy})_3]$ and $[\text{Cr}(\text{tren}(\text{impy})_3)]$, as can be seen in Table 6.3.

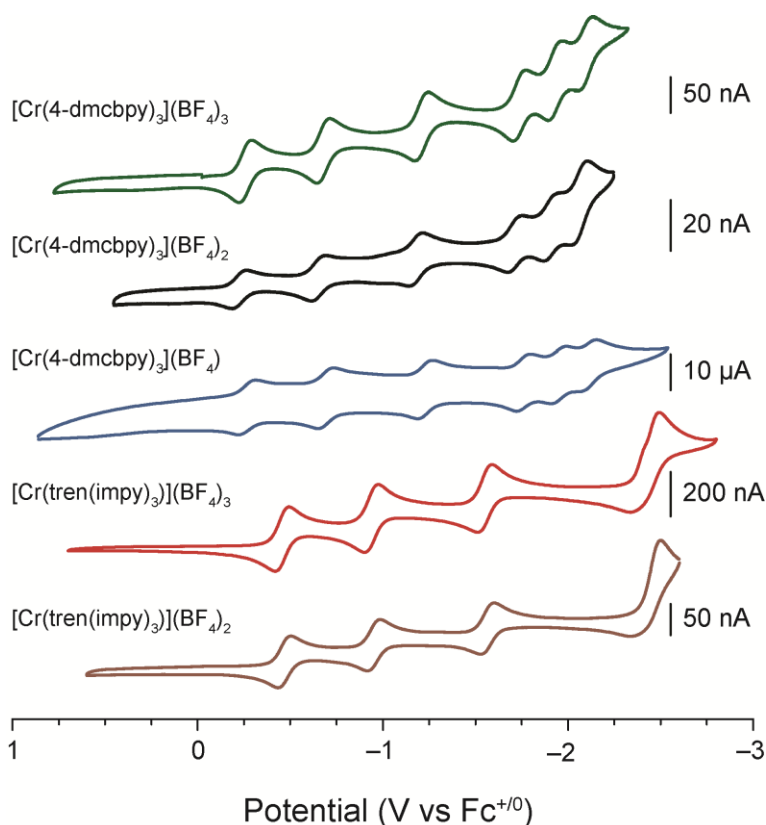


Figure 6.3. Comparison of cyclic voltammograms for 4-dmcbpy and tren(imp)₃ Cr complexes in 0.1 M TBAPF₆ acetonitrile solution.

Table 6.3. Reduction potentials for 4-dmcbpy and (tren(imp)₃ Cr complexes.

	$(E_{1/2}$ vs $Fc^{+/0}$, V) ^a					
	3+/2+	2+/1+	1+/0	0/1-	1-/2-	2-/3-
[Cr(4-dmcbpy) ₃](BF ₄) ₃	-0.26	-0.68	-1.21	-1.74	-1.93	-2.10
[Cr(4-dmcbpy) ₃](BF ₄) ₂	-0.25	-0.69	-1.21	-1.75	-1.94	-2.09
[Cr(4-dmcbpy) ₃](BF ₄)	-0.26	-0.69	-1.22	-1.76	-1.94	-2.10
[Cr(tren(imp) ₃)](BF ₄) ₃	-0.45	-0.93	-1.55	-2.44		
[Cr(tren(imp) ₃)](BF ₄) ₂	-0.46	-0.94	-1.56	-2.42		

^a Conditions for cyclic voltammetry of Cr complexes: Electrolyte, 0.1 M TBAPF₆ in CH₃CN; WE, Pt; CE, Pt Wire; Scan Rate, 100 mV/s.

The only real difference in the cyclic voltammograms is the nature of each of the redox events. As discussed in Chapter 3, for [Cr(4-dmcbpy)₃](BF₄)₃, each of the reversible redox waves is actually a reduction. In the two reduced analogues [Cr(4-dmcbpy)₃](BF₄)₂ and [Cr(4-dmcbpy)₃](BF₄), the nature of

some of the redox events change. In $[\text{Cr}(4\text{-dmcbpy})_3](\text{BF}_4)_2$, the wave at the most positive potential ($-0.256 \text{ V vs Fc}^{+/0}$) occurs as an oxidation and in $[\text{Cr}(4\text{-dmcbpy})_3](\text{BF}_4)$ both waves at -0.250 and $-0.686 \text{ V vs Fc}^{+/0}$ are oxidations. The nature of the waves (oxidative or reductive) can be verified by performing a cyclic voltammogram under stirring conditions. This type of experiment can also show the rest potential and the true oxidation state of the species in bulk solution. For example, a stirring experiment on $[\text{Cr}(4\text{-dmcbpy})_3](\text{BF}_4)$ is shown in Figure 6.4. As potential progresses from positive potentials at the left to negative potentials at the right, the magnitude of the anodic current decreases in two noisy steps at approximately 0.50 V and 0.05 V (vs Ag wire). This is followed by a plateau of nearly constant current between 0 and -0.4 V (vs Ag wire) which has positive sign as potential sweeps negative and negative sign as potential sweeps positive. Lastly, a region of highly variable but increasing cathodic current follows another noisy current step at -0.6 V .

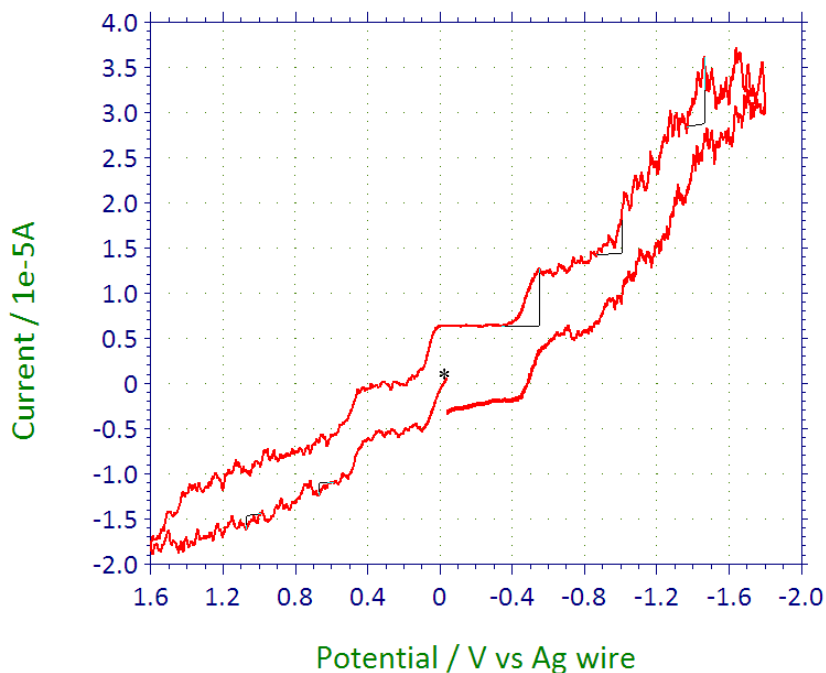


Figure 6.4. Stirring experiment cyclic voltammogram of $[\text{Cr}(4\text{-dmcbpy})_3](\text{BF}_4)$ done to determine oxidation state in bulk solution. The cyclic voltammogram was carried out in 0.1 M TBAPF_6 acetonitrile solution. In this figure, the rest potential is denoted by *, the potential was initially swept positive, then negative, and back to the starting point, and the potential is referenced directly to the Ag wire and not to the $\text{Fc}^{+/0}$ couple.

The areas of noisiness and high current variability indicate potentials at which electron transfer occurs between the electrode and the bulk solution, while the region of constant (small) current just negative of 0 V indicates minimal electron transfer processes between the electrode and the bulk solution and is indicative of the rest potential of the solution and of the oxidation state of the major Cr species. In this potential region, $[\text{Cr}(4\text{-dmcbpy})_3]^+$ is the major component of the solution and we can clearly see two oxidation waves as the potential becomes more positive. Attempts to achieve spontaneous reduction of $[\text{Cr}(\text{tren}(\text{impy})_3)](\text{BF}_4)_2$ in DMF yielded no color changes and no apparent reaction.

From the cyclic voltammograms of each complex, we hypothesized that under the right conditions we would be able to access the formally zero-valent Cr species. We first turned to chemical reducing agents; the $[\text{Cr}(4\text{-dmcbpy})_3]$ complex would require a reducing agent with a formal potential between -1.3 and -1.6 V vs $\text{Fc}^{+/0}$ and the $[\text{Cr}(\text{tren}(\text{impy})_3)]$ complex would require a reductant with a formal potential between -1.6 and -2.5 V vs $\text{Fc}^{+/0}$ to access the overall neutral Cr analogue. Considering the reductant for $[\text{Cr}(4\text{-dmcbpy})_3]$, there are remarkably few common chemical reducing agents that can access the potential window for the zero-valent Cr complex, and the only potentially compatible reducing agent was cobaltocene (CoCp_2).^{14a}

Attempts to use two equivalents of CoCp_2 in DCM to reduce $[\text{Cr}(4\text{-dmcbpy})_3](\text{BF}_4)_2$ to $[\text{Cr}(4\text{-dmcbpy})_3]$ did not appear successful. Although there was an immediate green to intense purple color change upon addition of the CoCp_2 to the $[\text{Cr}(4\text{-dmcbpy})_3](\text{BF}_4)_2$ solution, there was no evidence of the reaction proceeding to the neutral species. After this, a stronger reducing agent, sodium diphenylketyl radical in THF (-2.30 V vs $\text{Fc}^{+/0}$),^{14a} was employed. Slow addition of a solution of two equivalents of sodium diphenylketyl radical in THF to a stirring solution of $[\text{Cr}(4\text{-dmcbpy})_3](\text{BF}_4)_2$ did not yield any product with properties consistent with the desired $[\text{Cr}(4\text{-dmcbpy})_3]$. A cyclic voltammogram (Figure A5.7) of the reaction product from the reduction has a rest potential just negative of the $2+/1+$ couple, indicating an oxidation state of $+1$ at the lowest for the bulk material.

As an alternative to chemical reduction, we attempted to use bulk electrolysis to synthesize $[\text{Cr}(4\text{-dmcbpy})_3]$ from $[\text{Cr}(4\text{-dmcbpy})_3](\text{BF}_4)_2$. Over the course of the experiment the potential was held at the

potential midway between the 1+/0 and 0/1– couples (–1.0 V vs Ag wire), and the working compartment solution changes from green to purple. The solution from the working compartment is isolated and the solvent removed to yield a solid purple product mixed with residual supporting electrolyte. An IR spectrum of this mixture shows complete loss of the ester carbonyl stretch at 1727 cm⁻¹ (Figure A5.8), indicating that the process of bulk electrolysis is incompatible with this particular ligand type.

With this in mind, we turned to applying bulk electrolysis to the complex [Cr(tren(imp_y)₃)](BF₄)₂ which has no ester functionality. Similar to the experiment on [Cr(4-dmcbpy)₃](BF₄)₂, the potential was held between the 1+/0 and 0/1– couples (–1.8 V vs Ag/Ag⁺ reference electrode). Again the working compartment solution undergoes a color change to purple, however in this instance a dark colored solid also adheres to the working electrode. The solubility of the solid is much different than the precursor [Cr(tren(imp_y)₃)] salts and appears to be soluble only in DCM. A cyclic voltammogram of the solid reaction product in 0.1 M TBAClO₄ DCM solution no longer shows any reversible electrochemical processes (Figure A5.9). It is possible that the iminopyridine ligand also makes [Cr(tren(imp_y)₃)] unsuitable for reduction of past the 2+ oxidation state. While a neutral Cr iminopyridine complex has been reported previously,³ it is important to note that the ligands used contain bulky groups adjacent to the imine which can sterically protect the radicals that form upon reduction.

6.5 Conclusions and Outlook

We explored the chemistry of reduced analogues of [Cr(4-dmcbpy)₃](BF₄)₃ and [Cr(tren(imp_y)₃)](BF₄)₃. While the divalent complex cations of both Cr species were easily obtained, accessing more reduced versions proved to be more difficult. The monovalent [Cr(4-dmcbpy)₃](BF₄) was obtained by spontaneous reduction of [Cr(4-dmcbpy)₃](BF₄)₂ in DMF; however, similar reactivity was not seen for [Cr(tren(imp_y)₃)](BF₄)₂. Attempts to synthesize and isolate the zero-valent analogues of both complexes were made via use of chemical reducing agents and by bulk electrolysis, but were unsuccessful. Since neutral Cr complexes of bipyridine without functional groups¹⁷ or with saturated

functional groups¹ have been reported in the literature, we speculate that the ester functionalities and the iminopyridine ligands may make the desired complexes less isolable.

6.7 References

1. Scarborough, C. C.; Sproules, S.; Weyhermüller, T.; DeBeer, S.; Wieghardt, K. *Inorg. Chem.* **2011**, *50*, 12446-12462.
2. Scarborough, C. C.; Lancaster, K. M.; DeBeer, S.; Weyhermüller, T.; Sproules, S.; Wieghardt, K. *Inorg. Chem.* **2012**, *51*, 3718-3732.
3. Lu, C. C.; Bill, E.; Weyhermüller, T.; Bothe, E.; Wieghardt, K. *J. Am. Chem. Soc.* **2008**, *130*, 3181-3197.
4. Garelli, N.; Vierling, P. *J. Org. Chem.* **1992**, *16*, 3046-3051.
5. Jäntti, A.; Wagner, M.; Suontamo, R.; Kolehmainen, E.; Rissanen, K. *Eur. J. Inorg. Chem.* **1998**, *1998*, 1555-1562.
6. *APEX 2*, Bruker Analytical X-Ray Systems, Inc.: Madison, WI, 2008.
7. Sheldrick, G. M. *SHELXTL*, Version 6.14; Bruker Analytical X-Ray Systems, Inc.: Madison, WI, 1999.
8. (a) Herzog, S.; Aul, H. *Z. Naturforsch.* **1960**, *15b*, 617; (b) Herzog, S.; Renner, K. *Chem. Ber.* **1959**, *92*, 872-876.
9. (a) Pastoriza-Santos, I.; Liz-Marzán, L. M. *Langmuir* **1999**, *15*, 948-951; (b) Tsuji, M.; Hashimoto, M.; Nishizawa, Y.; Kubokawa, M.; Tsuji, T. *Chem. – Eur. J.* **2005**, *11*, 440-452.
10. Jeong, G. H.; Kim, M.; Lee, Y. W.; Choi, W.; Oh, W. T.; Park, Q. H.; Han, S. W. *J. Am. Chem. Soc.* **2009**, *131*, 1672-1673.
11. Choo, H. P.; Liew, K. Y.; Liu, H. *J. Mater. Chem.* **2002**, *12*, 934-937.
12. Carpenter, M. K.; Moylan, T. E.; Kukreja, R. S.; Atwan, M. H.; Tessema, M. M. *J. Am. Chem. Soc.* **2012**, *134*, 8535-8542.
13. Yu, J. Y.; Schreiner, S.; Vaska, L. *Inorg. Chim. Acta* **1990**, *170*, 145-147.
14. (a) Connelly, N. G.; Geiger, W. E. *Chem. Rev.* **1996**, *96*, 877-910; (b) Bard, A. J.; Faulkner, L. R. *Electrochemical Methods: Fundamentals and Applications*; John Wiley & Sons, 2000.
15. McLachlan, G. A.; Fallon, G. D.; Spiccia, L. *Acta Crystallogr., Sect. C: Cryst. Struct. Commun.* **1996**, *52*, 309-312.
16. McDaniel, A. M.; Tseng, H.-W.; Damrauer, N. H.; Shores, M. P. *Inorg. Chem.* **2010**, *49*, 7981-7991.
17. Bloom, C. J.; Elliott, C. M.; Schroeder, P. G.; France, C. B.; Parkinson, B. A. *J. Phys. Chem. B* **2003**, *107*, 2933-2938.

Chapter 7. Final Remarks and Future Work

The work in the previous five chapters focused on the synthesis and characterization of transition metal complexes featuring multidentate iminopyridine or polypyridine ligands. The primary applications of the synthesized complexes are in the areas of spin-crossover and solar energy photo-conversion. Although the work on spin-crossover focuses primarily on ground state properties and the work on solar energy photo-conversion deals heavily with excited state properties, these two disparate areas are linked by the fact that small changes in the ligand architecture can give rise to large changes in complex behavior. The goal of this work has been to understand metal-ligand interactions and to develop new ligands and complexes which display desired properties.

Chapter 2 looks at divalent transition-metal (Cr-Zn) complexes of the tripodal iminopyridine ligand $L^{5\text{-OOMe}}$, and considers how metal-ligand interactions affect observation of spin-crossover. The $L^{5\text{-OOMe}}$ ligand provides a fairly strong ligand field, although the addition of ester groups at the 5-position should weaken the field compared to the unfunctionalized parent ligand. It is interesting to note that coordination to the $L^{5\text{-OOMe}}$ ligand leads to an exclusively LS Fe(II) complex, even though the ligand field parameter (D_q) is in the range expected for spin-crossover. The probable reason for this apparent discrepancy is that the ligand field parameter D_q is not as reliable for tripodal complexes, or that the range for expected spin-crossover is shifted to lower energies for this type of geometry. Both the $L^{5\text{-OOMe}}$ and parent $\text{tren}(\text{py})_3$ ligands give Fe(II) complexes that are strictly LS, but both ligands yield Ni(II) D_q values that should make Fe(II) spin-crossover possible.

Also in Chapter 2, in the case of $[\text{Cr}(L^{5\text{-OOMe}})]^{2+}$, the nature of the metal-ligand interaction gives rise to a complex with qualitatively different behavior than the rest of the divalent species. From the X-ray structural, spectroscopic, and electrochemical experimental data, $[\text{Cr}(L^{5\text{-OOMe}})]^{2+}$ is best described as a Cr(III)-anionic ligand radical complex, unlike the other divalent species which are M(II)-neutral ligand complexes. Computational studies performed by Prof. Anthony Rappé, including TD-DFT calculated visible absorption spectra, give good qualitative agreement with the experimentally collected absorption

spectra. Additionally, NTO analyses provide insight into the orbitals involved in the transitions that give rise to visible light absorption. A direct benefit from the comparison of the theory based and experimentally based spectroscopic data and their good agreement is that it validates the computational approach used for these complexes; conclusions may be drawn about theory derived data where spectroscopic handles are not accessible. Understanding the nature of the transitions and the orbitals involved will allow theory to help direct alterations in the ligand in order to improve visible properties for solar photo-conversion applications.

The main focus in Chapter 3 is studying how installation of hydrogen-bonding functional groups at different positions on tripodal iminopyridine ligands affect Fe(II) complex spin-crossover and anion-binding behavior in solution. Addition of amide- or hydroxy-based functional groups at either the 5-position or the 6-position appears to have no large impact on spin-state behavior in solution; in this work, all complexes studied with 6-position functionalization remain high-spin in solution while all complexes without 6-position functionalization remain low-spin. However, the complexes with 5-position amide and hydroxy functionalizations show dramatic anion-dependent ^1H NMR spectra that indicate strong anion binding in solution. In addition to the anion-binding behavior, Cl^- titrations of $[\text{Fe}(\text{L}^{5\text{-ONHtBu}})](\text{BF}_4)_2$ also display a small but significant increase in splitting between the bulk and capillary TMS peaks, and the solution magnetic susceptibility, as up to 1 equivalent of Cl^- is added. The current experimental evidence points to an anion-dependent increase in the high-spin fraction of $[\text{Fe}(\text{L}^{5\text{-ONHtBu}})]^{2+}$ as being responsible for the increase in solution magnetic susceptibility. While installation of hydrogen-bonding functional groups in either the 5-position or the 6-position does not engender anion-dependent spin-state switching in solution, the 5-position functionalized ligands do show strong solution- and solid-state anion binding. Moving to mixed-arm ligands that include both 5-position and 6-position functionalization may allow spin-crossover access in solution. However, these mixed ligands will likely require more complex synthesis and purification than the previously studied exclusively 5- or 6-position substituted ligands. Some technique for protecting all of the primary amines on tren and then deprotecting them individually for reaction without generating a statistical mixture of products would be a desirable way to generate pure

mixed arm ligands. If this is not feasible, purification of the statistical ligand mixtures may be another viable way to recover the desired ligands without contamination. For this route, the amide-based ligands would be better candidates because of their relative ease of handling; the ligand and its precursors are solids with bulky groups adjacent to the hydrogen-bond donor, while the alcohol-based ligand precursors tend to be oils which prevent crystallization, and the sterically unhindered alcohol tends to streak on columns, leading to poorer separations.

Chapters 4 and 5 focus on the ground-state and photophysical properties of Cr(III) complexes. In Chapter 4, hetero- and homoleptic Cr(III) polypyridyl complexes featuring the ester-functionalized 4-dmcbpy ligand are discussed. Ground state characterization shows that inclusion of 4-dmcbpy only slightly perturbs the electronic absorption spectra, giving rise to small red-shifts and increases in molar absorptivity. However, the electron withdrawing nature of the 4-dmcbpy ligand makes each $[(\text{NN})_2\text{Cr}(4\text{-dmcbpy})]^{3+}$ easier to reduce than its homoleptic $[(\text{NN})_3\text{Cr}]^{3+}$ counterpart by at least 200 mV. In contrast to small changes in ground state spectra, excited state photophysical characterization provided by Huan-Wei Tseng and Prof. Niels Damrauer shows inclusion of the 4-dmcbpy ligand greatly reduces both the excited state lifetime and the quantum yield of $[(\text{NN})_2\text{Cr}(4\text{-dmcbpy})]^{3+}$ complexes compared to the homoleptic $[(\text{NN})_3\text{Cr}]^{3+}$ versions. Despite the reduction in excited state lifetime, all 4-dmcbpy complexes store ~ 1.7 eV in the excited state and have lifetimes of multiple μs . These lifetimes would be sufficient for hole-injection into NiO, the most commonly used semiconductor for p-type dye-sensitized solar cells. Additionally, the excited-state reduction potentials are all ≥ 1.9 V vs NHE, which would be strongly photo-oxidizing and sufficient to achieve hole-injection. From this work, the most promising ligand combinations for a heteroleptic Cr(III) dye would include an ester functionalized ligand such as 4-dmcbpy or methyl-1,10-phenanthroline-5-carboxylate, that would provide a way to attach to a surface, enhance (photo)oxidizing power and give rise to small red shifts in the visible absorption spectrum with the caveat that the quantum yield and excited-state lifetime would decrease with incorporation of the ester based ligand. Ancillary ligands, such as 4,7-di(anthracen-1-yl)-1,10-phenanthroline or phenanthro-

[3,4,5,6-*defgh*][1,10]phenanthroline, would have a large conjugated π -system to improve molar absorptivities and to improve excited-state lifetimes and quantum yields.

Preliminary work fabricating NiO porous films on transparent conductive oxide (FTO) on glass and subsequent sensitization ran into many problems. Polymer templated Ni²⁺,¹ NiO nanopowder slurry² and Ni(OH)₂ colloid³ doctor blade deposition and hydrothermal⁴ deposition methods were tried to produce NiO films. The quality of the films produced by all of these methods is highly variable in my hands. Ni(OH)₂ colloid films adhere well to the glass or FTO substrates, but generally turn out darkly colored (brown to black) and have varying uniformity over the film surface and between batches. NiO nanopowder and hydrothermally deposited NiO tend to produce uniform looking films that have problems with adhesion to the FTO or bare glass substrates. Polymer templated NiO produces the most transparent films, but film uniformity and transparency often varies dramatically over the surface of the film and between batches.

In addition to the variability of the NiO films, achieving sensitization with the Cr(III) species is problematic. One major drawback of homo- and heteroleptic polypyridyl complexes is their poor absorption of visible light at $\lambda \geq 500$ nm, which makes it difficult to detect their presence on darkly colored NiO films by visible absorption spectroscopy. Additionally, the ester based complexes must be hydrolyzed in order for adhesion to take place. Attempts to use an acidic/basic pretreatment method described by Qu and Meyer⁵ for ester sensitizer adsorption to TiO₂ were made; however, our dyes and substrates appear to have incompatible stabilities. NiO is unstable toward acid, making acidic pretreatment for ester hydrolysis incompatible and the Cr(III) complexes are unstable toward base, making basic pretreatment for ester hydrolysis also incompatible. Pretreatment with acid for TiO₂ substrates followed by soaking in Cr(III) ester dye solutions does produce sensitization, so ultimately if a route could be found to separately hydrolyze the Cr(III) dyes, sensitization to NiO would become possible.

The poor visible absorption of the polypyridyl Cr(III) complexes prompted the investigation of the ground state and photophysical properties of a family of Cr(III) multidentate iminopyridine complexes

described in Chapter 5. Alteration of the ligand set from bidentate polypyridines (Chapter 4) or bidentate iminopyridines, to tripodal hexadentate iminopyridines moderately improves visible light absorption and leaves ground state electrochemical behavior virtually untouched. However use of the multidentate ligand causes dramatic changes in complex excited state behavior. Photophysical characterization performed by Huan-Wei Tseng and Prof. Niels Damrauer show that addition of the tether to the iminopyridine ligands effectively turns off Cr(III) complex 2E emission. Building on the previous work in Chapter 2, TD-DFT calculations and NTO analyses provided by Prof. Anthony Rappé give insight into the nature of the excited state transitions of the Cr(III) complexes. Here, lower energy quartet states that are only present for the tripodal species $[\text{Cr}(\text{L}2)]^{3+}$ allow a path for non-radiative decay. Additionally, the orbitals involved in both the lowest energy doublet and quartet transitions are ligand based, involve the tether N atom, and are very similar, which can allow facile back intersystem crossing from any doublet states formed. In future work, the understanding gained through the work describe in Chapter 5 will inform ligand alterations that preserve access to long lived excited states. A prime candidate for achieving this would be to move from the nitrogen based tether tren, to another tether such as 2-(aminomethyl)-2-methylpropane-1,3-diamine or cyclohexane-1,3,5-triamine (tach), which do not have amine-based tethering groups. However, the lower energy quartet states may be responsible for both the detrimental non-radiative decay pathway and for the beneficial increase in visible absorption, so changing the tether away from nitrogen could have unintended consequences.

In Chapter 6, reduced analogues of Cr(III) polypyridine and iminopyridine complexes are studied. In these divalent and monovalent complexes, crystallographic, spectroscopic and electrochemical characterization point to reducing equivalents residing on the ligands, and not on the Cr center. Understanding this non-innocent ligand behavior and learning how to control electron localization would be useful for designing new complexes for multi-electron redox transformations. Scarce and expensive transition metals such as ruthenium and platinum are currently used for these types of reactions, but it would be advantageous to use 3d metals, such as chromium, that are more abundant and cost effective.

Although 3d metals typically undergo one electron processes, non-innocent ligands could act as electron reservoirs to accept or provide additional electrons for multi-electron processes.

One of the overall the goals of the work contained in this dissertation has been to understand how changes to the ligand affect ground state and excited state complex properties. The compounds studied in this work have shown that small changes in the ligand set, such as going from an untethered to a tethered system, can lead to dramatic and unexpected changes in complex behavior. Understanding metal-ligand interactions and how they change as the ligand is altered will be crucial for tailoring complexes with specific properties in the areas of spin-crossover and solar photo-conversion.

7.1 References

1. Gibson, E. A.; Smeigh, A. L.; Le Pleux, L.; Fortage, J.; Boschloo, G.; Blart, E.; Pellegrin, Y.; Odobel, F.; Hagfeldt, A.; Hammarström, L. *Angew. Chem., Int. Ed.* **2009**, *48*, 4402-4405.
2. Nattestad, A.; Ferguson, M.; Kerr, R.; Cheng, Y.-B.; Bach, U. *Nanotechnology* **2008**, *19*, 295304.
3. Boschloo, G.; Hagfeldt, A. *J. Phys. Chem. B* **2001**, *105*, 3039-3044.
4. Le Pleux, L.; Chavillon, B.; Pellegrin, Y.; Blart, E.; Cario, L.; Jobic, S.; Odobel, F. *Inorg. Chem.* **2009**, *48*, 8245-8250.
5. Qu, P.; Meyer, G. J. *Langmuir* **2001**, 6720-6728.

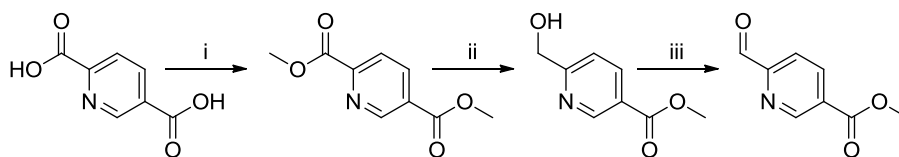
APPENDIX

Appendix A1. Supporting Information for Chapter 2

The work presented in Chapter 2 has been submitted to *Inorganic Chemistry* as: McDaniel, A. M.; Rappé, A. K.; Shores, M. P., *Structural and Electronic Comparison of 1st Row Transition Metal Complexes of a Tripodal Iminopyridine Ligand*. X-ray structural data for $[M(L^{5-00Me})]X_2$ complexes (**2.1-3**, **2.4a**, **2.5**, and **2.7**) will be available as a crystallographic information file (CIF) and detailed DFT calculation and NTO analysis data will be available in pdf form on the Internet upon publication. In addition, these data will be archived electronically along with an electronic version of this dissertation and available through the Shores Group.

A1.1 Full Reference 25 from Chapter 2:

Frisch, M. J.; Trucks, G. W.; Schlegel, H. B.; Scuseria, G. E.; Robb, M. A.; Cheeseman, J. R.; Scalmani, G.; Barone, V.; Mennucci, B.; Petersson, G. A.; Nakatsuji, H.; Caricato, M.; Li, X.; Hratchian, H. P.; Izmaylov, A. F.; Bloino, J.; Zheng, G.; Sonnenberg, J. L.; Hada, M.; Ehara, M.; Toyota, K.; Fukuda, R.; Hasegawa, J.; Ishida, M.; Nakajima, T.; Honda, Y.; Kitao, O.; Nakai, H.; Vreven, T.; J. A. Montgomery, J.; Peralta, J. E.; Ogliaro, F.; Bearpark, M.; Heyd, J. J.; Brothers, E.; Kudin, K. N.; Staroverov, V. N.; Kobayashi, R.; Normand, J.; Raghavachari, K.; Rendell, A.; Burant, J. C.; Iyengar, S. S.; Tomasi, J.; Cossi, M.; Rega, N.; Millam, J. M.; Klene, M.; Knox, J. E.; Cross, J. B.; Bakken, V.; Adamo, C.; Jaramillo, J.; Gomperts, R.; Stratmann, R. E.; Yazyev, O.; Austin, A. J.; Cammi, R.; Pomelli, C.; Ochterski, J. W.; Martin, R. L.; Morokuma, K.; Zakrzewski, V. G.; Voth, G. A.; Salvador, P.; Dannenberg, J. J.; Dapprich, S.; Daniels, A. D.; Farkas, Ö.; Foresman, J. B.; Ortiz, J. V.; Cioslowski, J.; Fox, D. J. *Gaussian 09, Revision B.1*, Gaussian, Inc.: Wallingford CT, 2009.



Scheme A1.1. Synthesis of the ligand aldehyde precursor; i: MeOH, catalytic H₂SO₄, reflux 17 h; ii: NaBH₄, CaCl₂, 1:2 THF: MeOH, 0°C, 45 min; iii: SeO₂, dioxane, 65°C, 48 h.

Table A1.1. Selected geometric data for complexes **2.1-2.5** and **2.7**.

Complex (Metal)	M-N _{imine} (Å)	M-N _{pyridine}	M-N _{tether} (Å)	φ (deg)
2.1 (Cr)	2.0327[28] ^a	2.0598[27] ^a	3.0867(1)	51.7
2.2 (Mn)	2.2064[20] ^a	2.4371[19] ^a	2.5463(2)	39.9
2.3 (Fe)	1.9471[19] ^a	1.9764[19] ^a	3.4271(3)	54.5
2.4a (Co)	2.0790(11) ^b	2.2283(10) ^b	2.6262(2)	50.4
2.5 (Ni)	2.0856[12] ^a	2.1161[12] ^a	3.3030(2)	50.9
2.7 (Zn)	2.095(3) ^b	2.348(3) ^b	2.694(3)	46.0

^a The errors for these bond distances were calculated by averaging the bond distances for each type of bond and taking the square root of the sum of the squares of the bond esds.

^b There is only one crystallographically independent bond of this type, so there are no average bond distances.

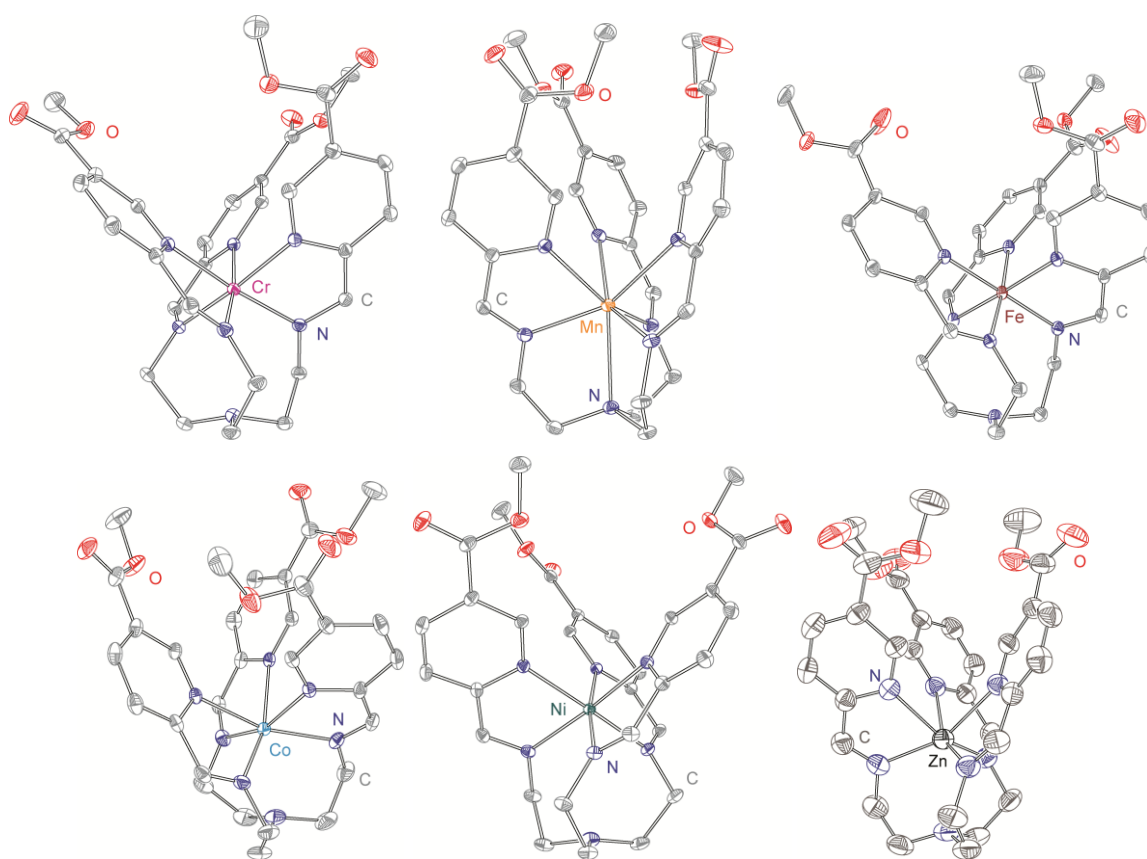


Figure A1.1. Side-on views of the $[ML^{5-00Me}]^{2+}$ complex cations in the structures of **2.1-2.5** and **2.7**, rendered with 40% probability ellipsoids. Red, dark blue and gray ellipsoids represent O, N and C atoms, respectively. All hydrogen atoms are omitted for clarity.

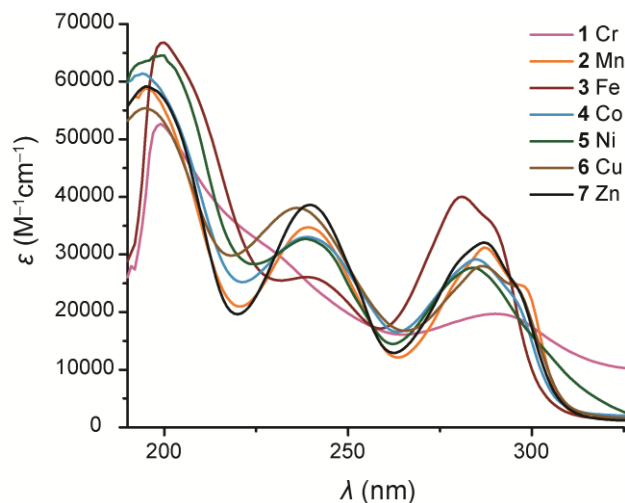


Figure A1.2. UV absorption spectra of complexes **2.1-2.7** in CH_3CN at room temperature.

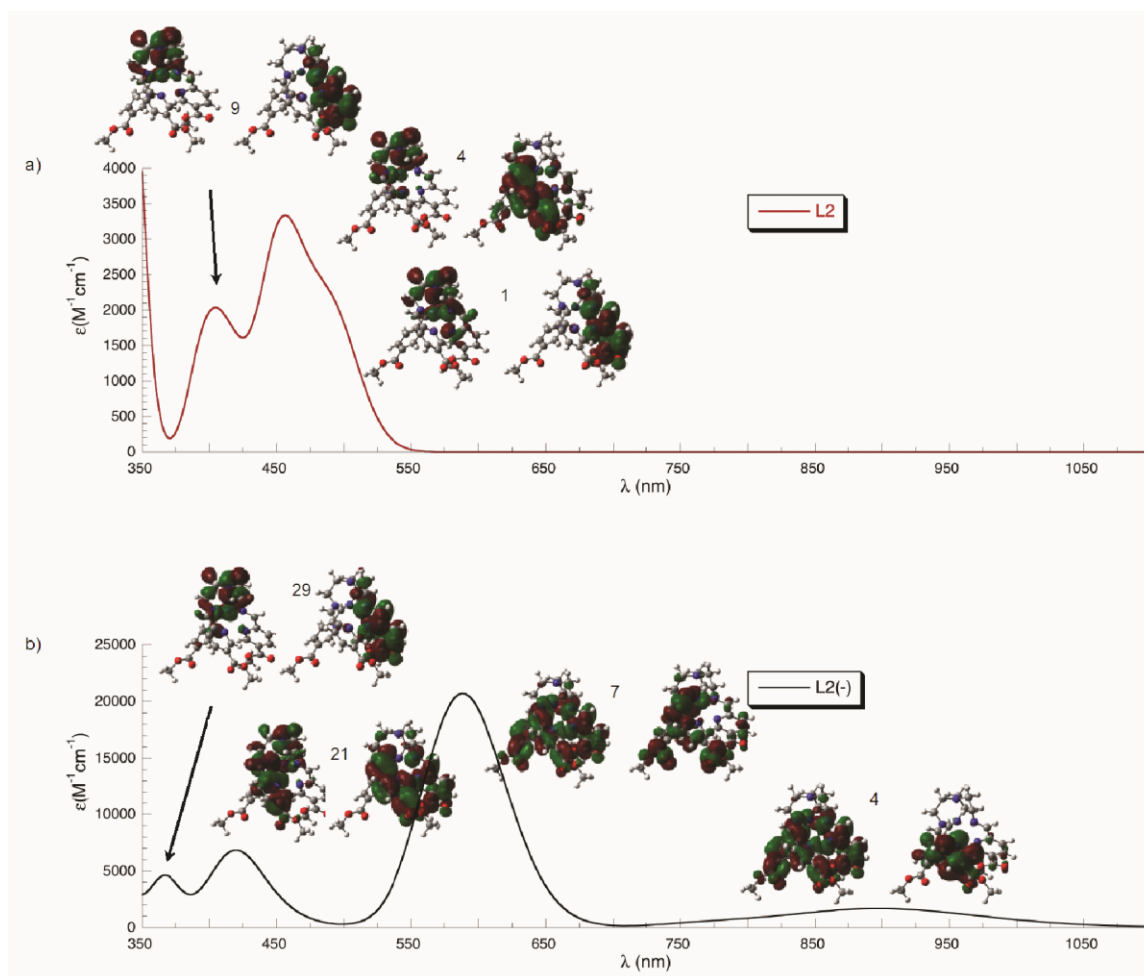
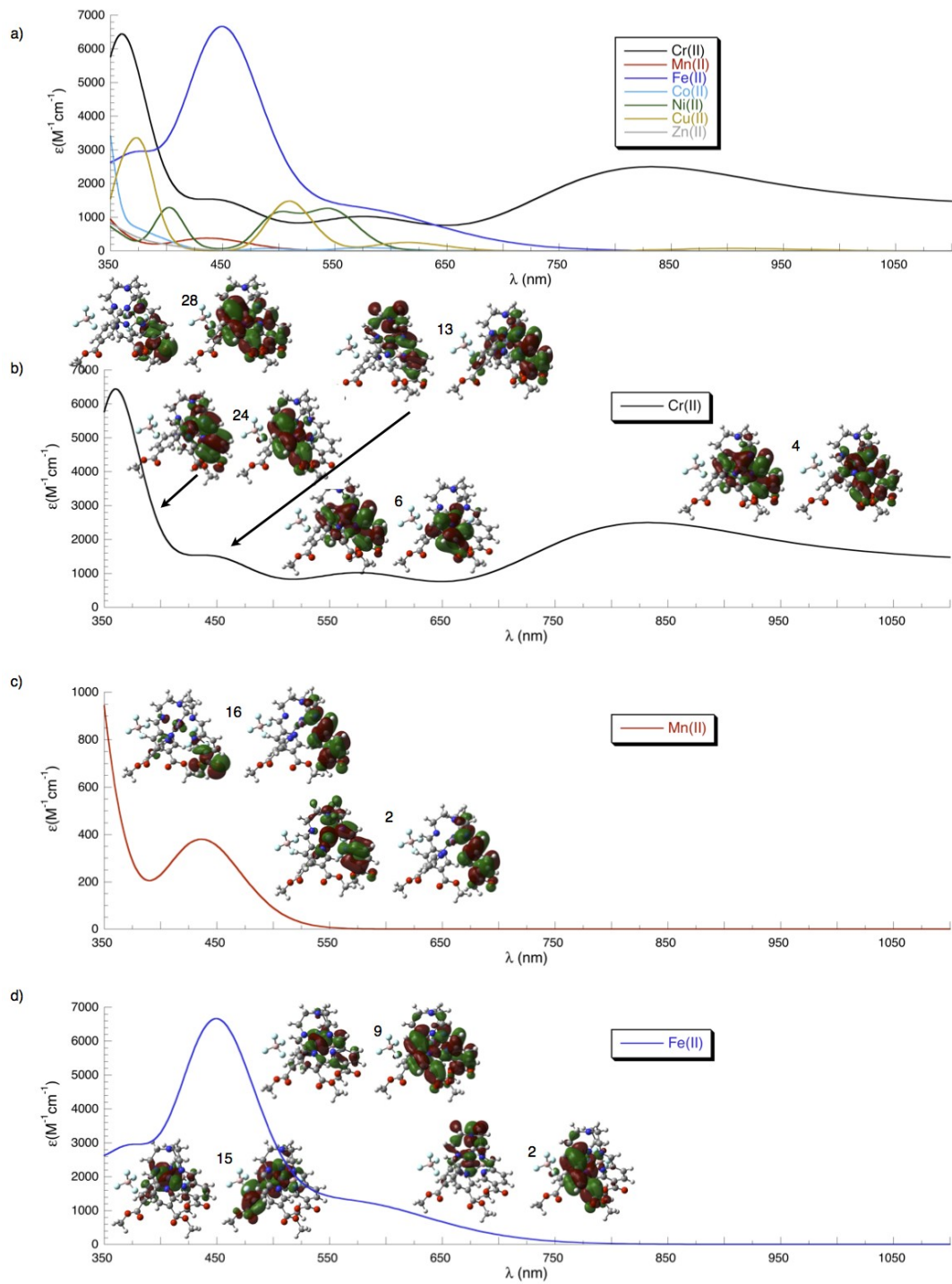


Figure A1.3. Simulated electronic absorption spectra and select natural transition orbital (NTO) pairs for (a) $\text{L}^{5\text{-OOMe}}$ and (b) its anion, $(\text{L}^{5\text{-OOMe}})^-$. For each NTO pair, the electron is transferred from the left structure to the right structure. NTO pairs are numbered in order of increasing energy of transition.



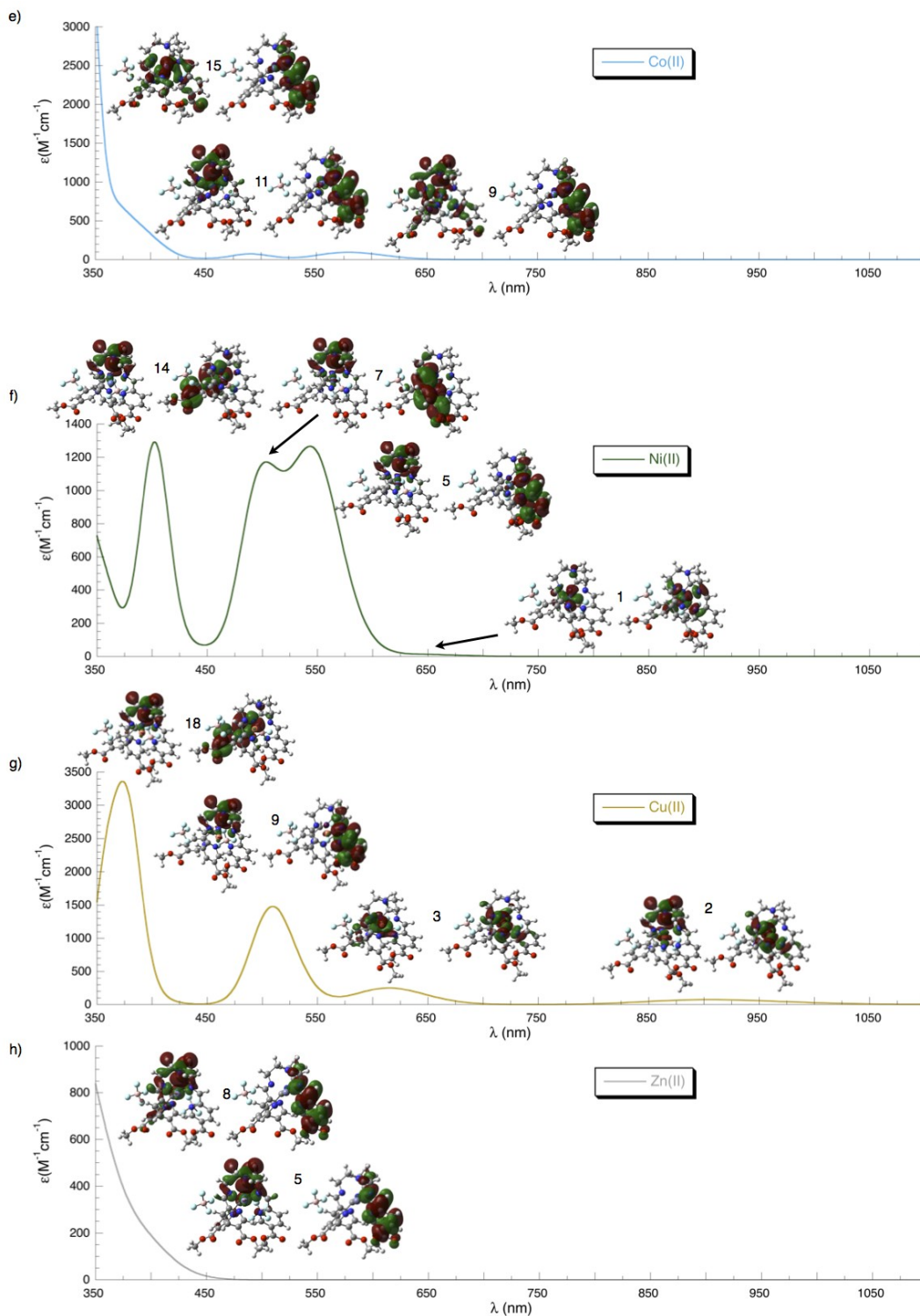


Figure A1.4. Simulated electronic absorption spectra and select natural transition orbitals (NTOs) for compounds **2.1-2.7'** (pages 163-164); for each NTO pair, the electron is transferred from the left structure to the right structure; NTO pairs are numbered in order of increasing energy of transition: (a) overlay of the computed spectra; (b) Cr **2.1**; (c) Mn **2.2'**; (d) Fe **2.3'**; (e) Co **2.4'**; (f) Ni **2.5'**; (g) Cu **2.6'**; (h) Zn **2.7'**.

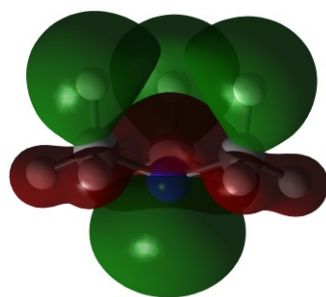


Figure A1.5. Orbital amplitude surface for the HOMO of trimethylamine.

Appendix A2. Supporting Information for Chapter 3

Part of the work presented in Chapter 3 has been submitted to *European Journal of Inorganic Chemistry* as: McDaniel, A. M.; Shores, M. P., *Synthesis of Functionalized Hexadentate Fe(II) Complexes: Toward Anion-Dependent Spin Switching in Polar Media*. X-ray structural data for complexes **3.3** and **3.11** will be available as a crystallographic information file (CIF) and on the Internet upon publication. In addition, these data, and data for **3.8** will be archived electronically along with an electronic version of this dissertation and available through the Shores Group.

A2.1 Additional Information on Calculating Binding Constants Using ^1H NMR Data

The preliminary work described in Chapter 3 suggests that strong binding of Cl^- is achieved in solution by $[\text{Fe}(\text{L}^{5\text{-ONHtBu}})]^{2+}$ and by $[\text{Fe}(\text{L}^{5\text{-OH}})]^{2+}$. Quantification of the association constants for these species would be useful and could potentially be done using ^1H NMR titration data. In addition to the 1stOpt program (<http://www.7d-soft.com/>) previously used by our group to calculate association constants for Fe(II) anion binding complexes from electronic absorption spectroscopic data,¹ two programs have been used in the literature to calculate anion association constants using ^1H NMR titration data.

The program HypNMR is available for purchase from Dr. Peter Gans at Protonic Software (<http://www.hyperquad.co.uk/hypnrmr.htm>). This program processes NMR chemical shift data (shifts averaged by virtue of fast exchange) to get equilibrium constants and has been used to calculate association constants for the trisimidazolium cage organized around Fe(II) by Fabbrizzi and coworkers.² The original publication on HypNMR applied NMR spectroscopy as a method for determining protonation constants for polyprotic bases.³

A second program, WinEQNMR2, is freely available for download (<http://www.nuigalway.ie/chem/Mike/wineqnmr.htm>). After obtaining the program files, users must contact Dr. Michael J. Hynes to obtain the password for file extraction. This program and its predecessors

WinEQNMR and EQNMR have been used in ~550 publications to calculate anion association constants in organic and transition metal-based compounds, including the amide functionalized bipyridine Ru(II) complexes reported by Beer and coworkers.⁴ The original publication in Dalton Transactions must be referenced for each publication reporting binding constants determined using WinEQNMR2.⁵

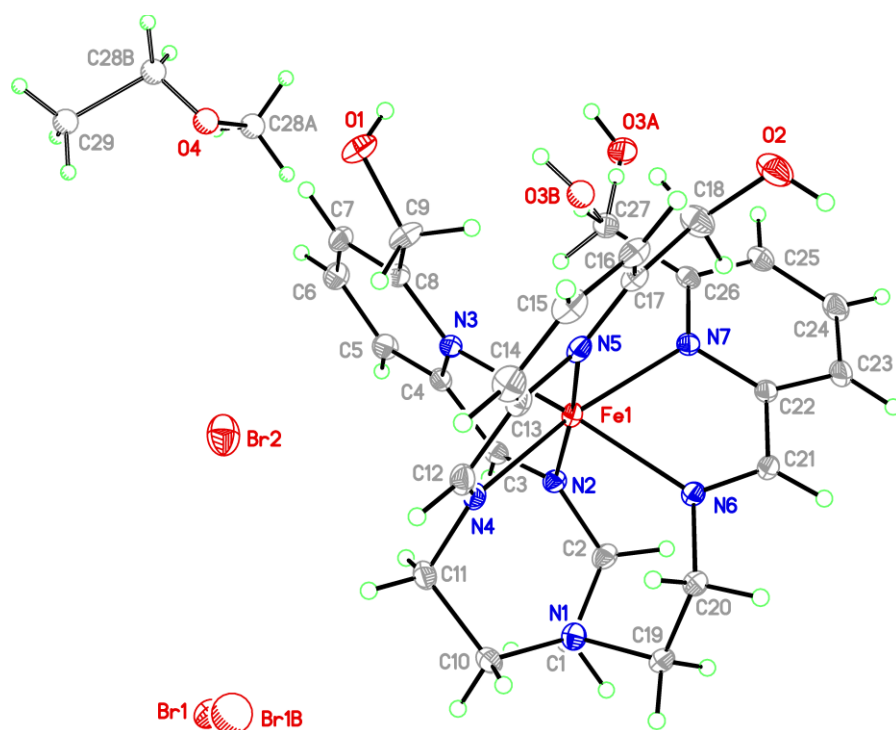


Figure A2.1. Full crystal structure for **3.8**, rendered at 40% ellipsoids. Disordered bromide, hydroxyl group and solvent molecules are rendered as shaded circles.

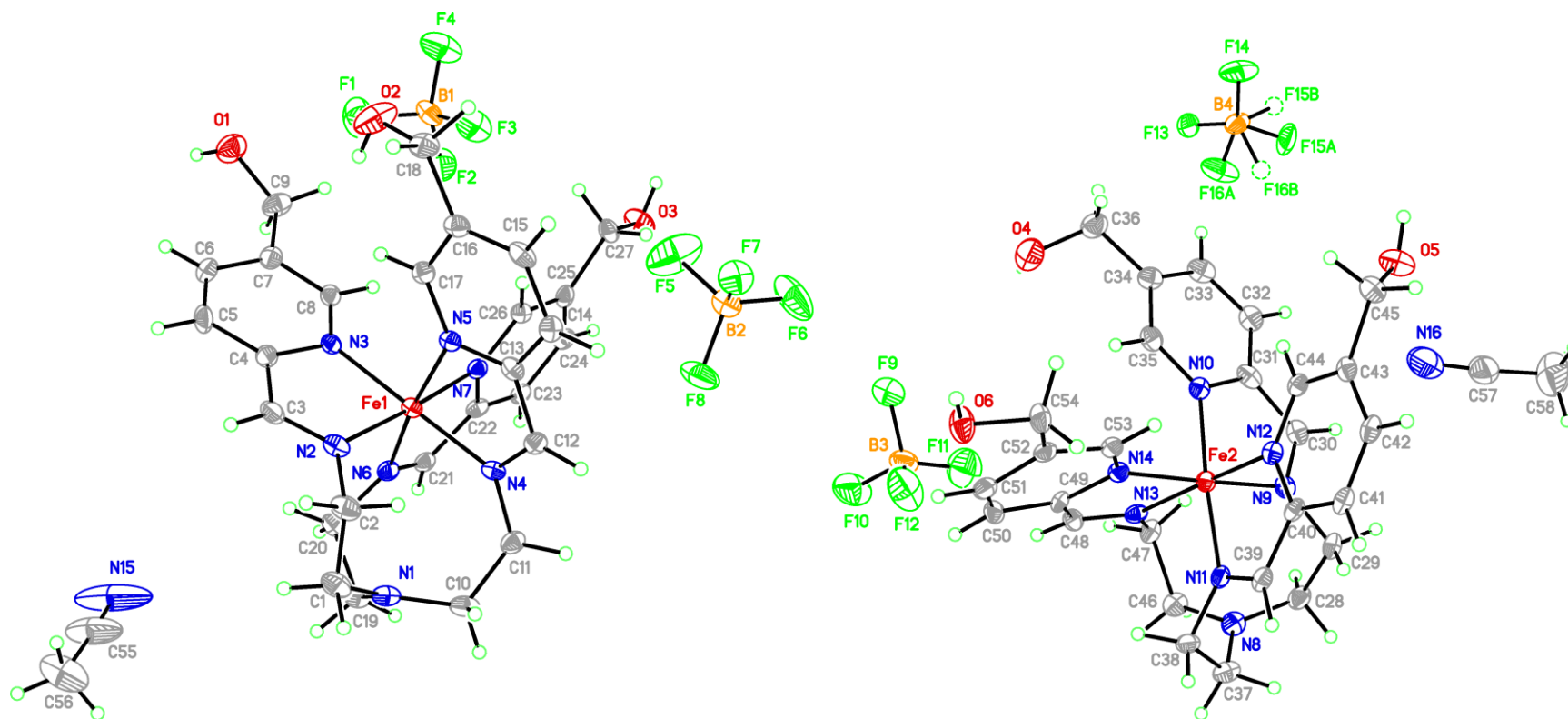


Figure A2.2. Full crystal structure for 3.3·CH₃CN, shown as two halves (right, left) of the asymmetric unit cell and rendered at 40% ellipsoids. Minor disordered components are included as dotted circles.

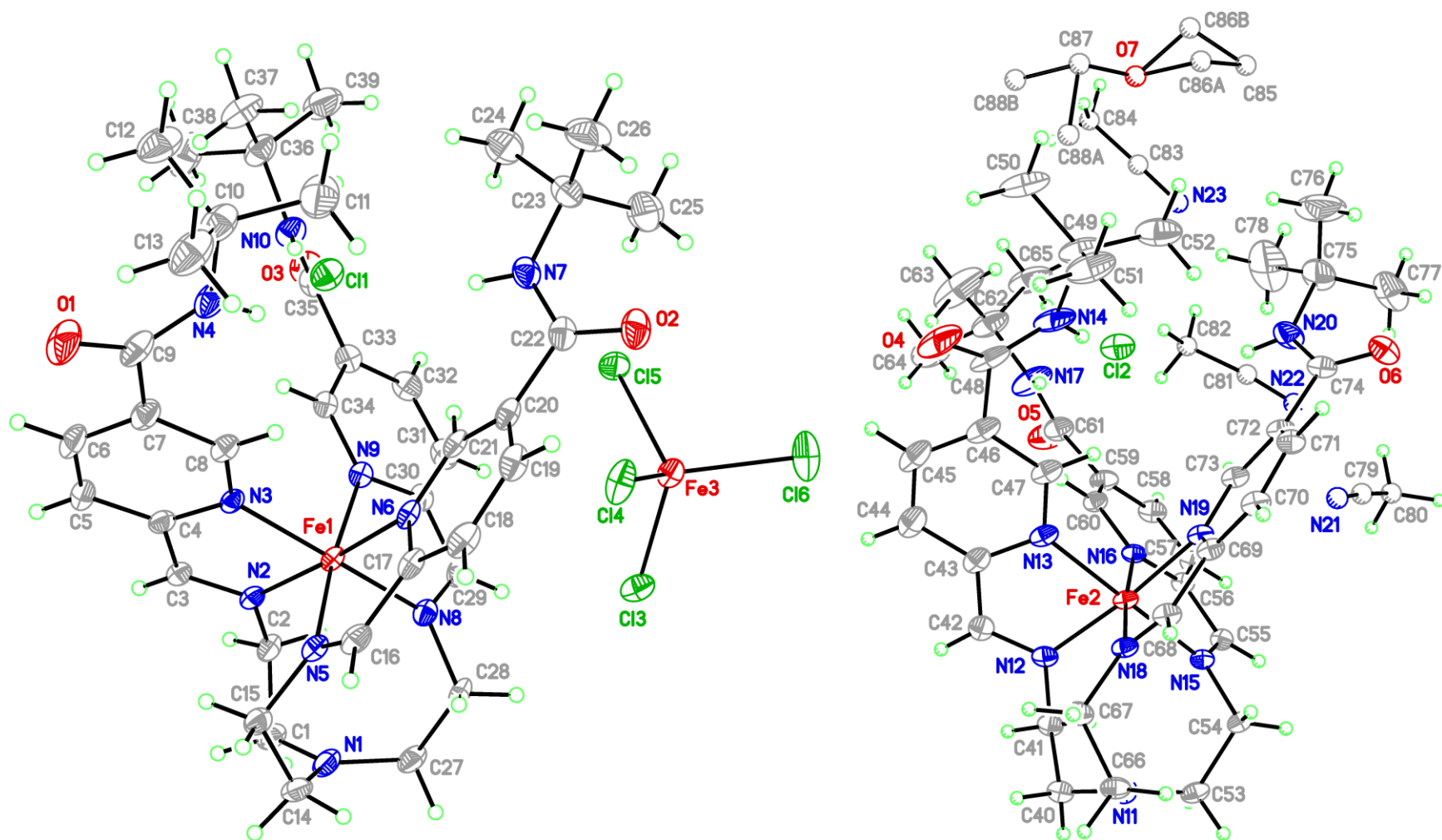


Figure A2.3. Full crystal structure for **3.11**, shown as two halves (right, left) of the asymmetric unit cell and rendered at 40% ellipsoids. Disordered solvent molecules are rendered as shaded circles.

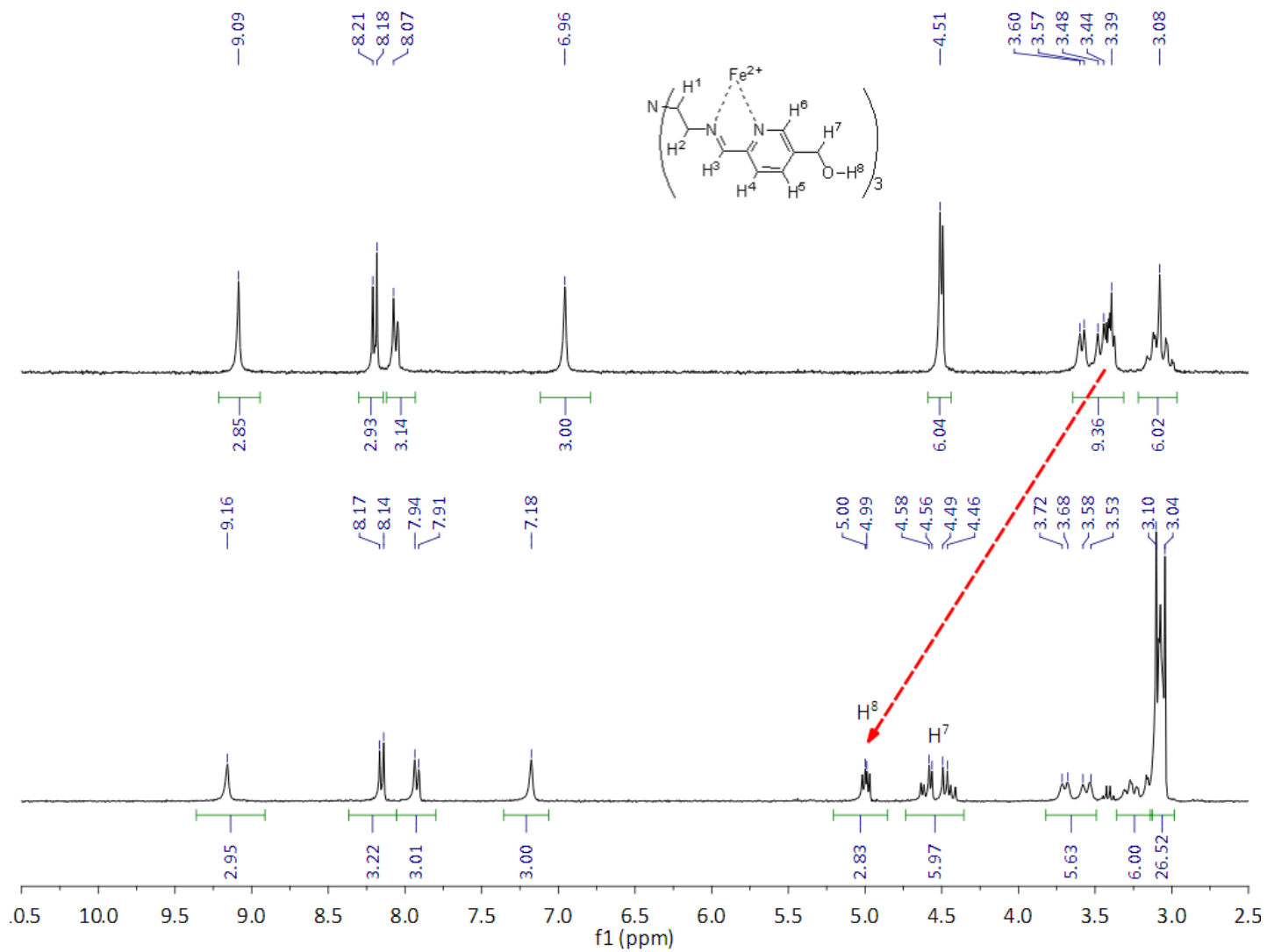


Figure A2.4. ^1H NMR spectra of **3.3** in CD_3CN before (top) and after addition of 2 equivalents TBACl (bottom). Data were obtained at 300 MHz and 24.9 $^\circ\text{C}$.

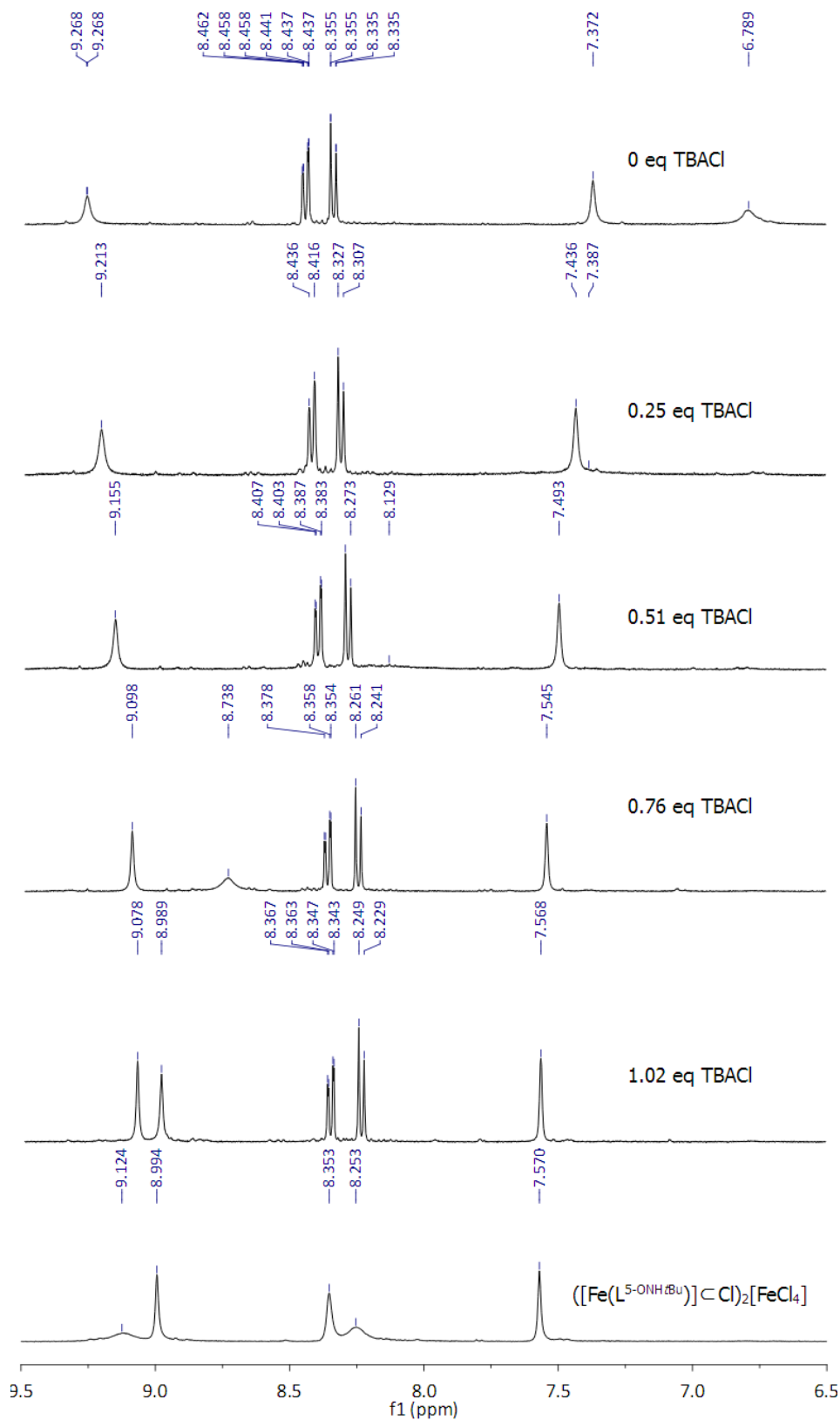


Figure A2.5. Aromatic region in ^1H NMR-monitored chloride titration of **3.12**. The top and bottom spectra give the aromatic regions of **3.12** and **3.11**, respectively, for comparison.

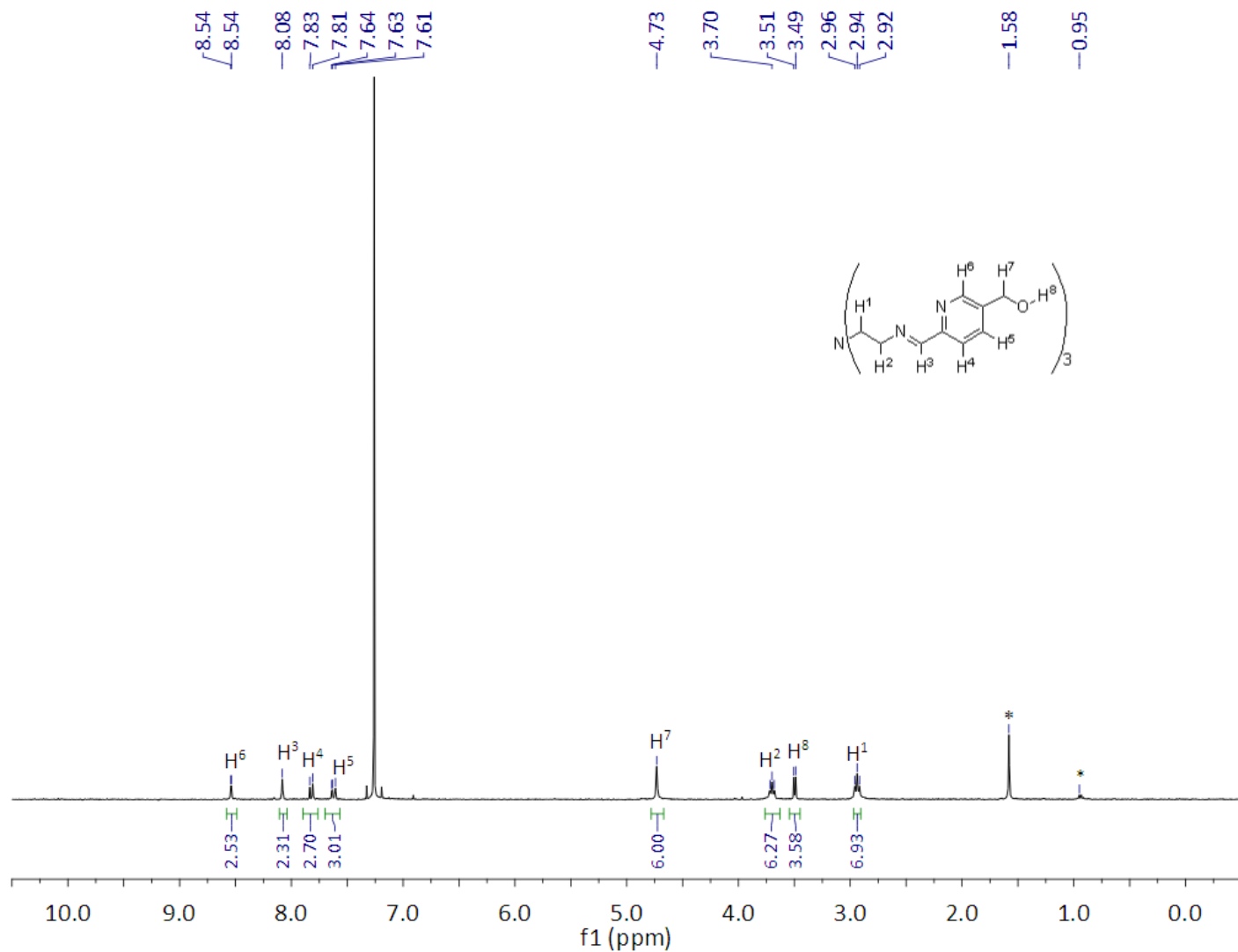


Figure A2.6. Room temperature 1H NMR spectrum of L^{5-OH} in $CDCl_3$; data obtained at 300 MHz. Resonances labeled with * are H_2O (1.58 ppm) and silicone grease (0.95 ppm).

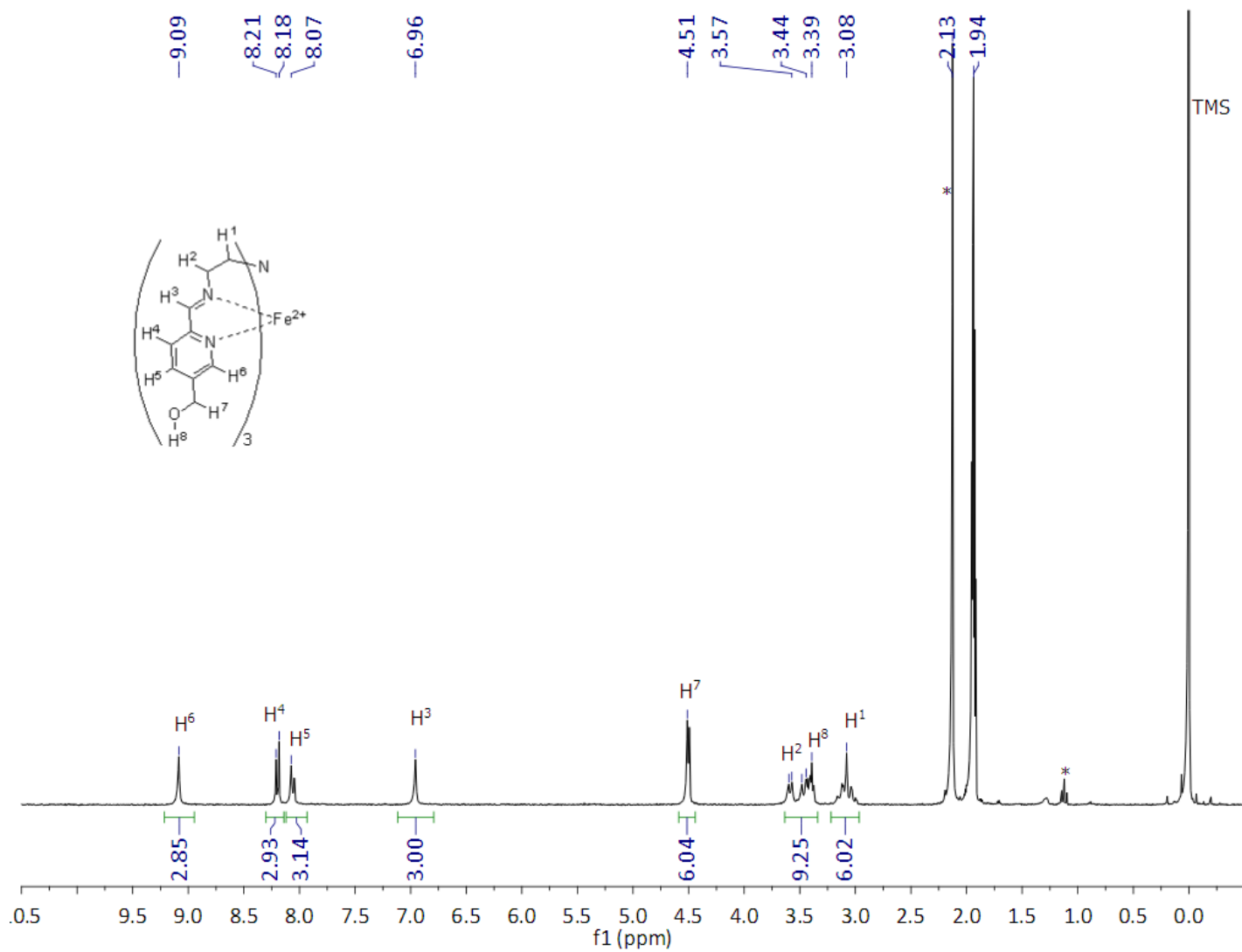


Figure A2.7. Room temperature ^1H NMR spectrum of **3.3** in CD_3CN ; data obtained at 300 MHz and 24.9°C. Resonances labeled with * are water (2.13 ppm) and diethyl ether (1.12 ppm).

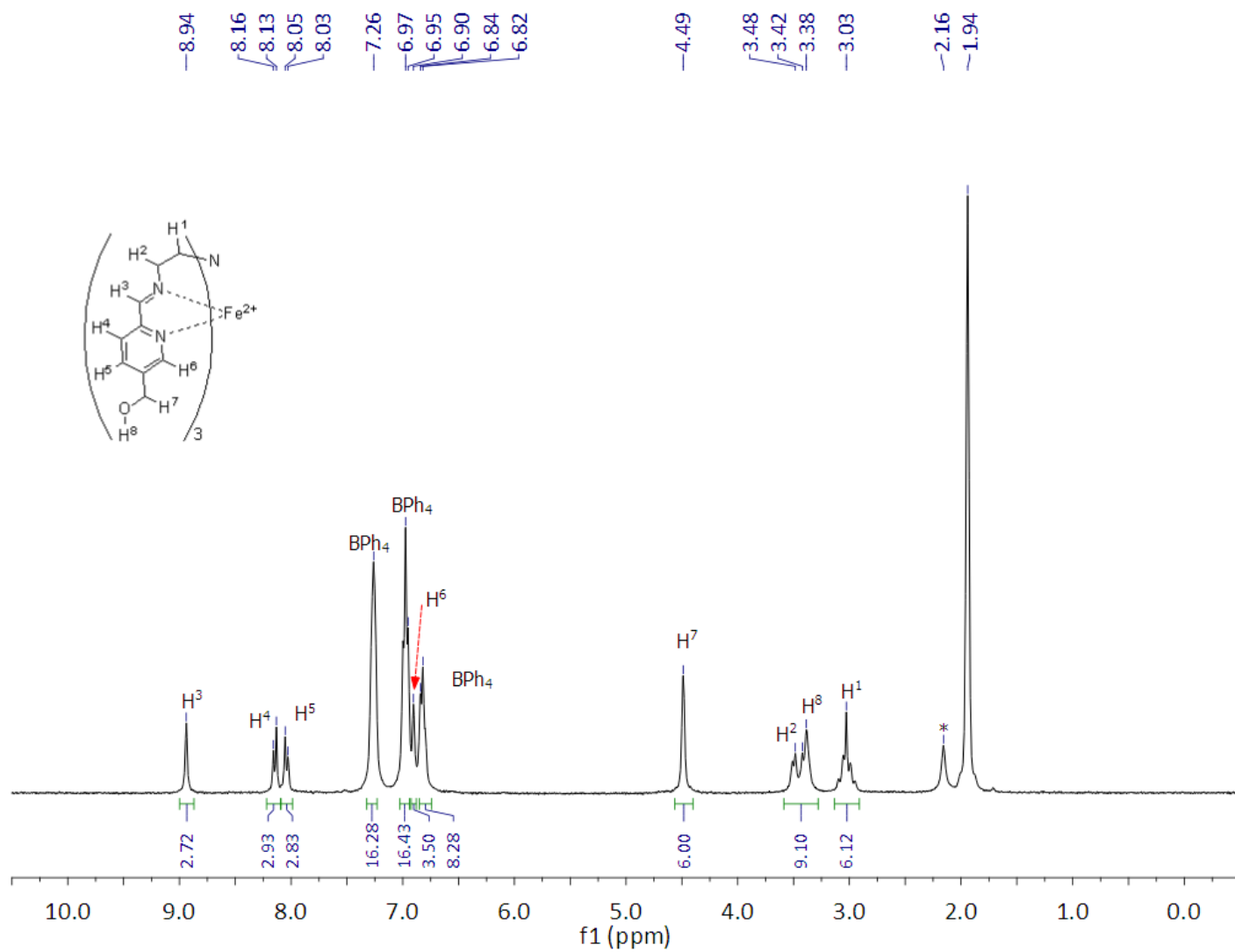


Figure A2.8. Room temperature ^1H NMR spectrum of **3.4** in CD_3CN ; data obtained at 300 MHz. Resonance labeled with * is water (2.16 ppm).

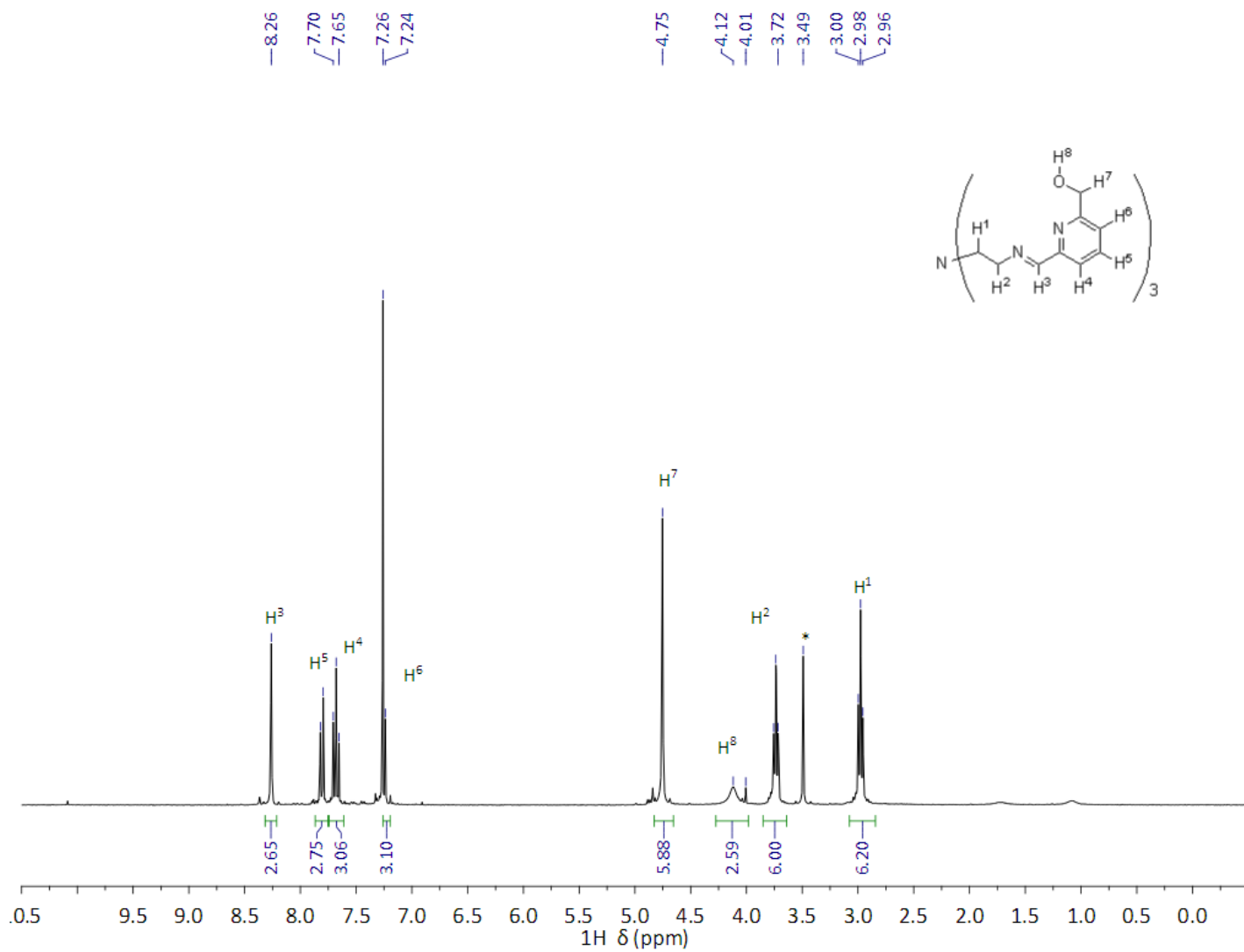


Figure A2.9. Room temperature 1H NMR spectrum of L^{6-OH} in $CDCl_3$; data obtained at 300 MHz. Resonance labeled with * is methanol (3.49 ppm).

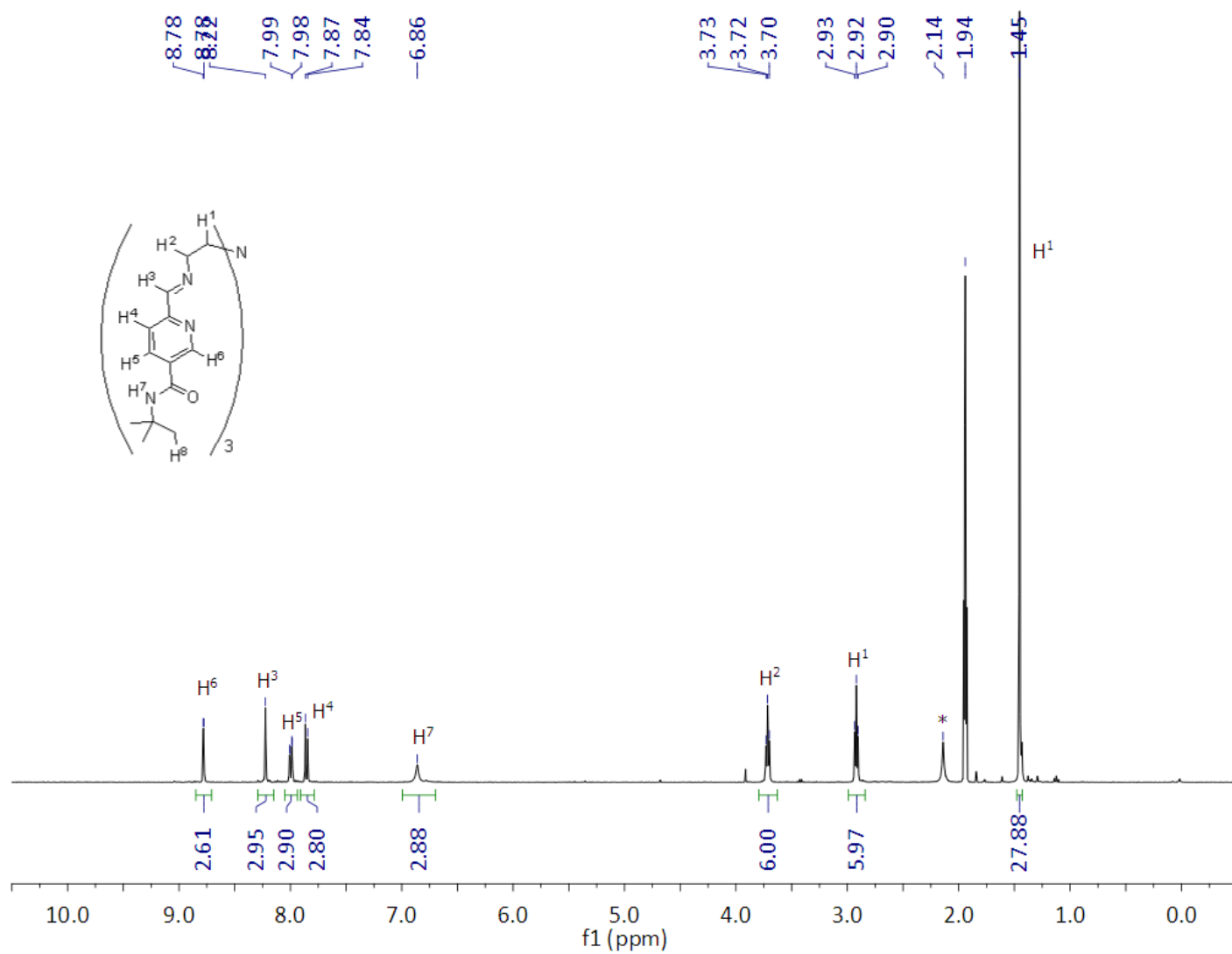


Figure A2.10. Room temperature ^1H NMR spectrum of $\text{L}^{5\text{-OHtBu}}$ in CD_3CN ; data obtained at 400 MHz. Resonance labeled with * is water (2.14 ppm).

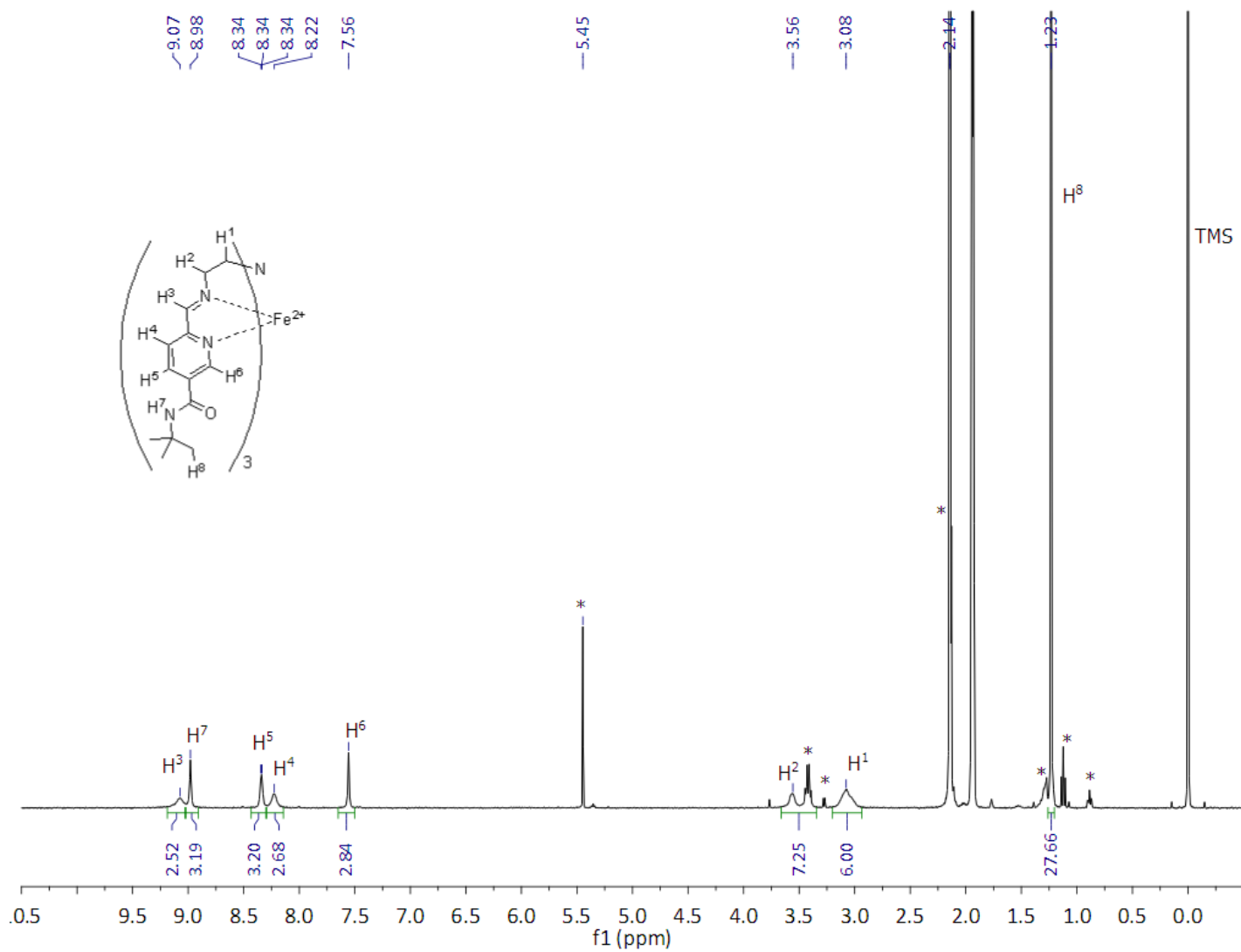


Figure A2.11. Room temperature ¹H NMR spectrum of **3.11** in CD₃CN; data obtained at 400 MHz and 24.2°C. Resonances labeled with * are dichloromethane (5.45 ppm), diethyl ether (3.42 and 1.12 ppm), methanol (3.28 ppm), water (2.14 ppm), and pentane (1.28 and 0.89 ppm).

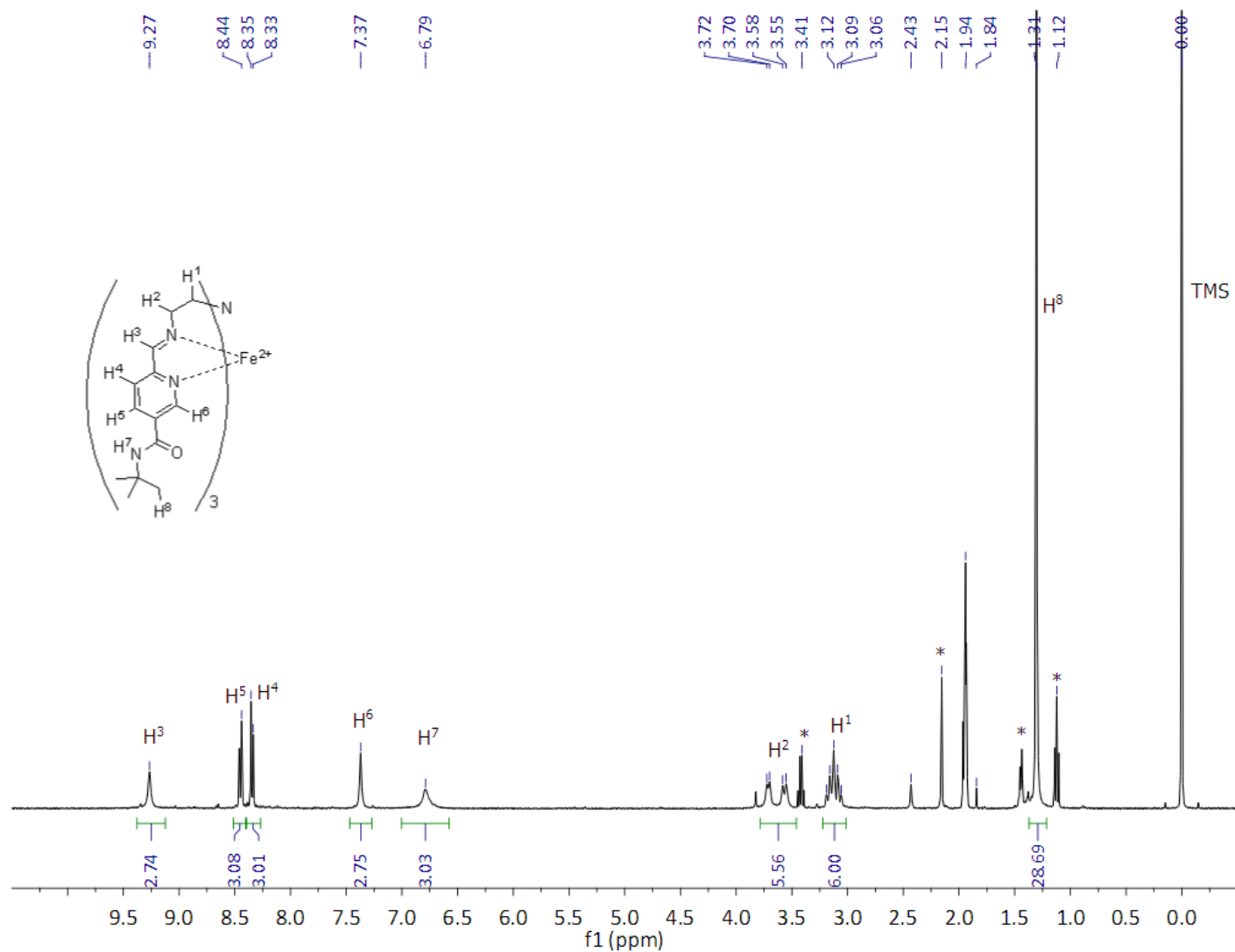


Figure A2.12. Room temperature ^1H NMR spectrum of **3.12** in CD_3CN ; data obtained at 400 MHz and 23.4°C. Resonances labeled with * are diethyl ether (3.41 and 1.12 ppm), water (2.15 ppm) and cyclohexane (1.44 ppm).

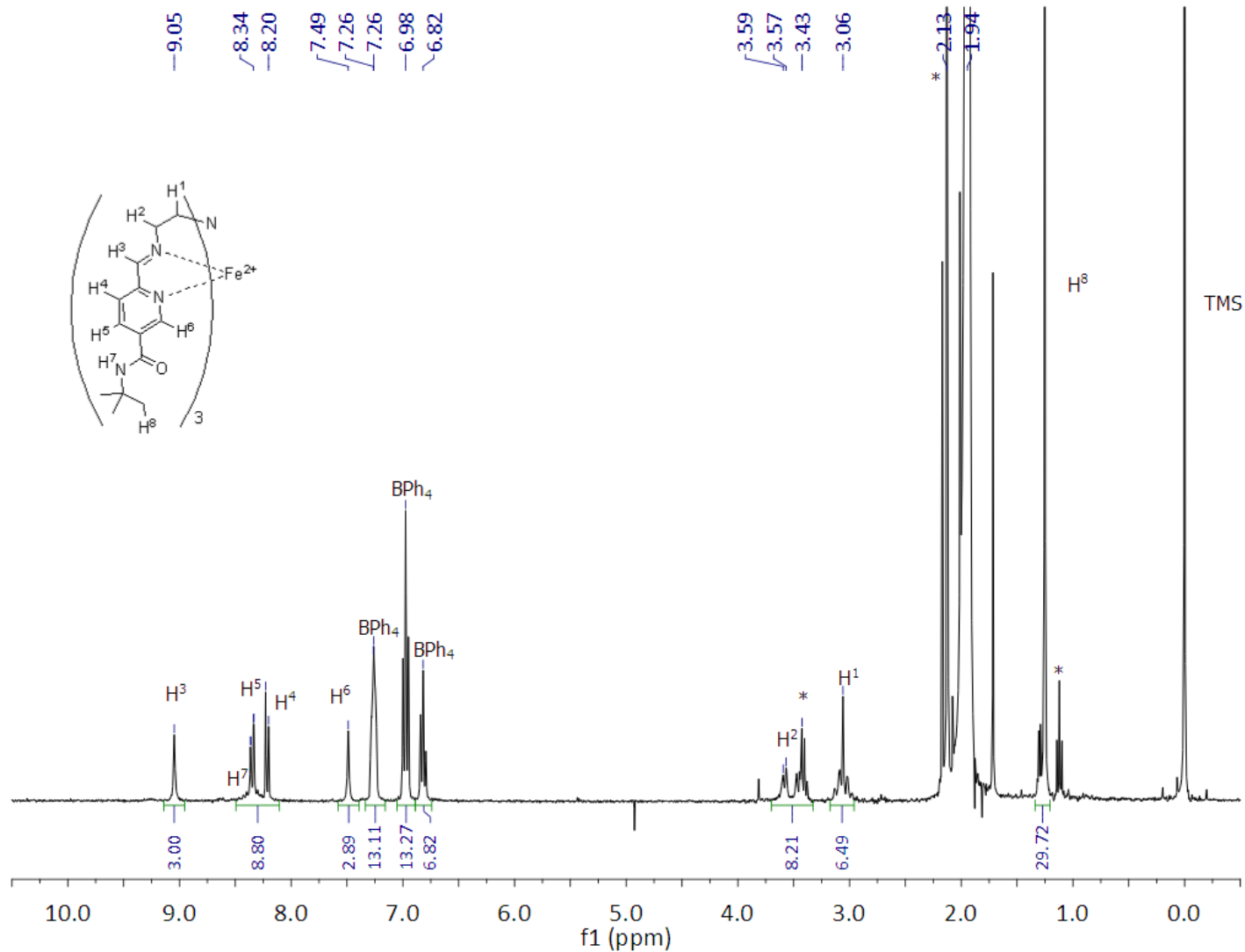


Figure A2.13. Room temperature ¹H NMR spectrum of **3.13** in CD₃CN; data obtained at 300 MHz and 24.8°C. Resonances labeled with * are diethyl ether (3.43 and 1.12 ppm) and water (2.13 ppm).

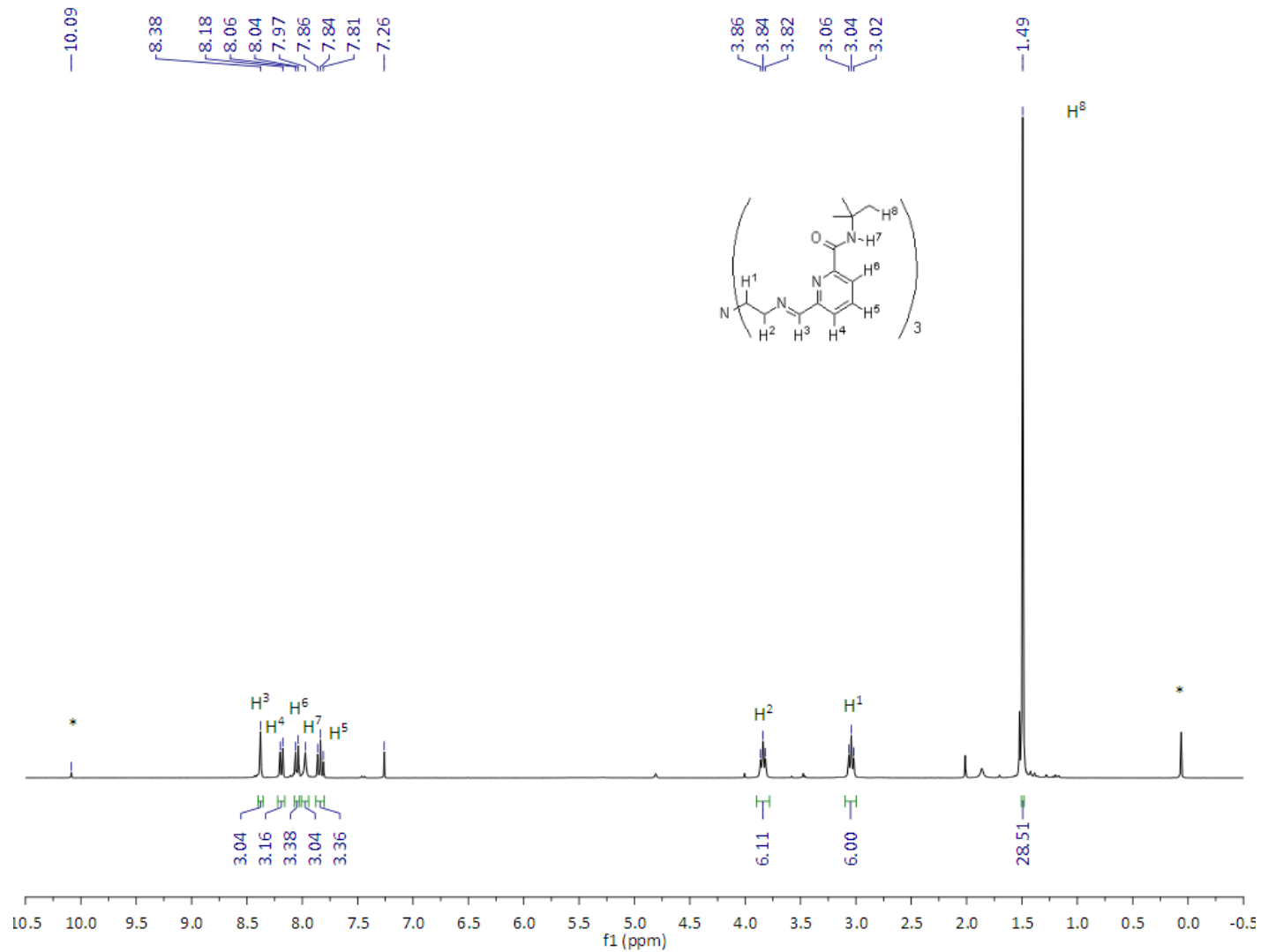


Figure A2.14. Room temperature ^1H NMR spectrum of $L^{6-OHtBu}$ in CDCl_3 ; data obtained at 300 MHz. Resonances labeled with * are residual aldehyde starting material (10.09 ppm) and silicone grease (0.06 ppm).

A2.2 References

1. Ni, Z.; Shores, M. P. *J. Am. Chem. Soc.* **2008**, *131*, 32-33.
2. Amendola, V.; Boiocchi, M.; Colasson, B.; Fabbrizzi, L.; Douton, M.-J. R.; Ugozzoli, F. *Angew. Chem., Int. Ed.* **2006**, *45*, 6920-6924.
3. Frassinetti, C.; Ghelli, S.; Gans, P.; Sabatini, A.; Moruzzi, M. S.; Vacca, A. *Anal. Biochem.* **1995**, *231*, 374-382.
4. Beer, P. D.; Dent, S. W.; Wear, T. J. *J. Chem. Soc., Dalton Trans.* **1996**, 2341-2346.
5. Hynes, M. J. *J. Chem. Soc., Dalton Trans.* **1993**, 311-312.

Appendix A3. Supporting Information for Chapter 4

The work presented in Chapter 3 has been published in: McDaniel, A. M.; Tseng, H.-W.; Damrauer, N. H.; Shores, M. P. *Inorg. Chem.* **2010**, *49*, 7981-7991. X-ray structural data for [(phen)₂Cr(4-dmcbpy)](OTf)₃·1.3CH₃CN (**4.1**·1.3CH₃CN) are available on the Internet as a crystallographic information file (CIF) at:

http://pubs.acs.org/doi/suppl/10.1021/ic1009972/suppl_file/ic1009972_si_002.cif

A3.1 Experimental Section

A3.1.1 X-Ray Structure Determination Details. A suitable crystal of **4.1**·1.3CH₃CN was coated with Paratone-N oil and supported on a Cryoloop before being mounted on a Bruker Kappa Apex II CCD diffractometer under a stream of dinitrogen. Data collection was performed at 110 K with Mo K α radiation and a graphite monochromator, affording complete coverage and 4-fold redundancy. Initial lattice parameters were determined from 320 reflections harvested from 36 frames; these parameters were later refined against all data. Crystallographic data and metric parameters are presented in Table 1. Data were integrated and corrected for Lorentz and polarization effects using SAINT, and semiempirical absorption corrections were applied using SADABS.¹ The structure was solved by direct methods and refined against F² with the SHELXTL 6.14 software package.² Unless otherwise noted, thermal parameters for all non-hydrogen atoms were refined anisotropically. Hydrogen atoms were added at the ideal positions and were refined using a riding model where the thermal parameters were set at 1.2 times those of the attached carbon atom (1.5 for methyl protons).

In the structure of **4.1**·1.3CH₃CN, two of the triflate anions show positional disorder and one solvent molecule is only partially occupied. In one anion, atoms O58, O59, S60, C61, F63 and F64 are split over two positions, with atoms O57 and F62 common between the two triflate positions. The split atoms were tied to a free variable which refined to a 70:30 ratio for the A and B positions, respectively. The second triflate was handled similarly, with atoms O66, O67, S68, C69, F70, F71 and F72 split over two

disordered positions in an 89:11 ratio, and both components having O65 in common. In both cases, the disordered triflate portions were restrained to match the bond angles and distances found in the non disordered triflate within the structure and the atoms in the less-occupied B sites were refined with isotropic displacement parameters. In addition, one of the two acetonitrile solvent molecules present in the structure (containing N76, C77 and C78) has only partial occupation (30%). The displacement parameters for these atoms were refined isotropically. The bond distances and angles for the partially occupied solvate atoms were also restrained to match those found for the fully occupied acetonitrile molecule.

A3.1.2 Detailed Instrumentation and Methods for Photophysical Measurements

A3.1.2a. Emission Spectra and Quantum Yields. The complex solutions were prepared with an absorbance of ~ 0.1 at 320 nm. Emission spectra were recorded at 23-24 °C using Photon Technology International Fluorometer System with an Ushio UXL-75XE Xenon Short Arc Lamp and PTI-814 Photomultiplier Detection System with a Hamamatsu R928P photomultiplier tube operating at -1000 V dc. The measurements were carried out at a single excitation wavelength of 320 nm, and the emission at 90° relative to the excitation light was recorded from 650 to 850 nm. Emission spectra reported here were corrected for instrument response using a tungsten lamp provided by the manufacturer, which has been calibrated against a NIST tungsten lamp.

A3.1.2b Emission Lifetimes. Sample solutions were prepared and deoxygenated in exactly the same manner as described above for emission spectra and quantum yields measurements. The measurements were done at 23-24 °C. Each sample was excited with 355 nm laser pulses (10 Hz; ~ 0.3 $\mu\text{J/pulse}$) generated by a Continuum Minilite II Q-Switched Nd:YAG Laser. Two dielectric mirrors and one bandpass filter (300-360 nm) in front of the sample were used to eliminate residual 532 nm and 1064 nm laser radiation. The emitted light was detected at 90° with respect to the excitation laser using a Hamamatsu H9305-02 photomultiplier tube (PMT) operating at -900 Vdc. A notch filter (725 ± 5 nm) was placed within a lens-tube assembly (two back-to-back plano-convex lenses, $f_0 = 25.4$ mm/diameter =

25.4 mm) in front of the detector and the emission intensity was monitored. The PMT signal was terminated with a 50 Ω resistor into a LeCroy 9384L Oscilloscope. Maximum signal levels were kept well below the measured linearity of the PMT response. Each emission transient was acquired by averaging 3000 scans with a time window of 180 to 4000 μ s depending on the lifetimes of the complexes. The data from the oscilloscope was transferred to a personal computer and fit with a single exponential decay model using Labview code of local origin to obtain the lifetimes. For any single lifetime measurement (3000 scans), no sample degradation is observed in UV-Vis comparisons (after vs before).

In longer experiments such as the temperature dependent studies, samples that include bipyridine and/or bipyridine derivatives (as opposed to phenanthroline species), except for $[\text{Cr}(4\text{-dmcbpy})_3]^{3+}$ (**4.8**), show minor degradation (less than ~ 10 % based on absorbance change at the excitation wavelength) provided care has been taken to keep the excitation power low. Complex **4.8** shows a ~ 13 % decrease in the absorbance at 355 nm and ~ 60 % increase at 325 nm. This is possibly the solvento species due to ligand replacement of 4-dmcbpy by H_2O . A similar phenomenon has been observed for $[\text{Cr}(\text{bpy})_3]^{3+}$.³ We have measured the emission spectrum for **4.8** before and after heating to 80 $^\circ\text{C}$. While the intensity decreases, no other bands are observed in the window of 650 – 850 nm.

A3.1.2c. Transient Absorption Spectra. Transient absorption kinetics were measured every 10 nm from 350 to 650 nm. The excitation laser pulses at 355 nm (2 Hz; 1.5 mJ/pulse) are derived from the Continuum Minilite II Q-Switched Nd:YAG Laser described above. In this transient absorption spectrometer setup, the laser beam is cylindrically focused onto the sample housed in a 1 cm \times 1 cm quartz cuvette at 90 $^\circ$ to the probe beam. A Newport/Oriel lamp system with a 75 W Xenon arc lamp (ozone-free, part number 6263) is used to provide the broad-band probe source. A 1 in. diameter beam of this light is focused into the sample using a plano-convex $f_0 = 100$ mm lens achieving a spot size of ~ 1 mm diameter (approximately collimated in the 1 cm path length cuvette) and a probe volume that overlaps with the cylindrically focused pump light. Prior to the sample, the white light is passed through a cylindrical cell filled with water to remove IR radiation. Following the sample, the probe beam is re-collimated and then focused via two plano-convex lenses ($f_0 = 50$ mm) into a monochromator. Based on

entrance and exit slit widths that were used (1 mm), the wavelengths probed span ± 2 nm. Probe intensity as a function of wavelength is monitored with a negatively-biased Hamamatsu R-928 PMT operating at -1000 Vdc. The standard PMT circuit has been modified to use only the first 4 dynode stages to accommodate the probe flux (a non-zero background) with good dynamic range.⁴ In the experiments reported herein, the signal from the PMT was through an external 460Ω resistor into a LeCroy 9384L Oscilloscope. Transient absorption or bleach kinetics at each wavelength were obtained by averaging 30 oscilloscope time-traces of probe intensity with the pump laser on followed immediately by averaging 30 time-traces of probe intensity with the pump off. The time window on the oscilloscope always accommodated at least 10 multiples of the measured lifetime. These pump-on and pump-off time traces were transferred to a personal computer and processed with Labview programs of local origin to determine a ΔA signal as a function of time (at a given wavelength of data collection). The whole collection process was repeated three times and an average $\Delta A(t)$ (at each wavelength of interest) was determined. Each $\Delta A(t)$ signal at each wavelength of interest was fit with a single exponential decay model. Transient absorption spectra reported herein consist of a plot of the pre-exponential of these $\Delta A(t)$ kinetics fits as a function of wavelength.

In order to minimize the effect of photochemistry on transient spectra, four sample solutions were used to obtain each spectrum (each sample accounts for 7-8 data points in the final ΔA spectrum). A bulk solution (15 mL) of complex was pre-prepared with an absorbance of ~ 0.4 at 355 nm. An aliquot of 3.5 mL solution was transferred into a quartz cuvette for each set of 7-8 $\Delta A(t)$ measurements used to build the $\Delta A(\lambda)$ spectrum. No major degradation (less than $\sim 10\%$ based on absorbance change at the excitation wavelength) was observed. The $\Delta A(t)$ kinetics show single exponential decay and for the spectra reported herein, samples were not deoxygenated.

Table A3.1. Selected bond lengths and angles for [(phen)₂Cr(4-dmcbpy)](OTf)₃·1.3CH₃CN (4.1·1.3CH₃CN).

<i>Bond Lengths (Å)</i>					
Cr1-N1	2.048(2)	Cr1-N12	2.063(2)	Cr1-N15	2.051(2)
Cr1-N26	2.047(2)	Cr1-N36	2.032(2)	Cr1-N41	2.044(2)
<i>Bond Angles (deg)</i>					
N1-Cr1-N12	80.58(8)	N1-Cr1-N15	91.21(8)	N15-Cr1-N12	88.11(8)
N26-Cr1-N1	168.65(9)	N26-Cr1-N12	90.73(8)	N26-Cr1-N15	81.16(9)
N36-Cr1-N1	93.77(8)	N36-Cr1-N12	97.96(8)	N36-Cr1-N15	172.70(9)
N36-Cr1-N26	94.66(8)	N36-Cr1-N41	79.31(8)	N41-Cr1-N1	94.89(8)
N41-Cr1-N12	174.60(9)	N41-Cr1-N15	94.96(8)	N41-Cr1-N26	94.13(8)
<i>Torsion Angles (deg)</i>					
N1-C14-C13-N12	0.2(3)	N15-C28-C27-N26	-2.7(3)		
N36-C38-C39-N41	1.6(3)	C37-C38-C39-C40	2.5(4)		

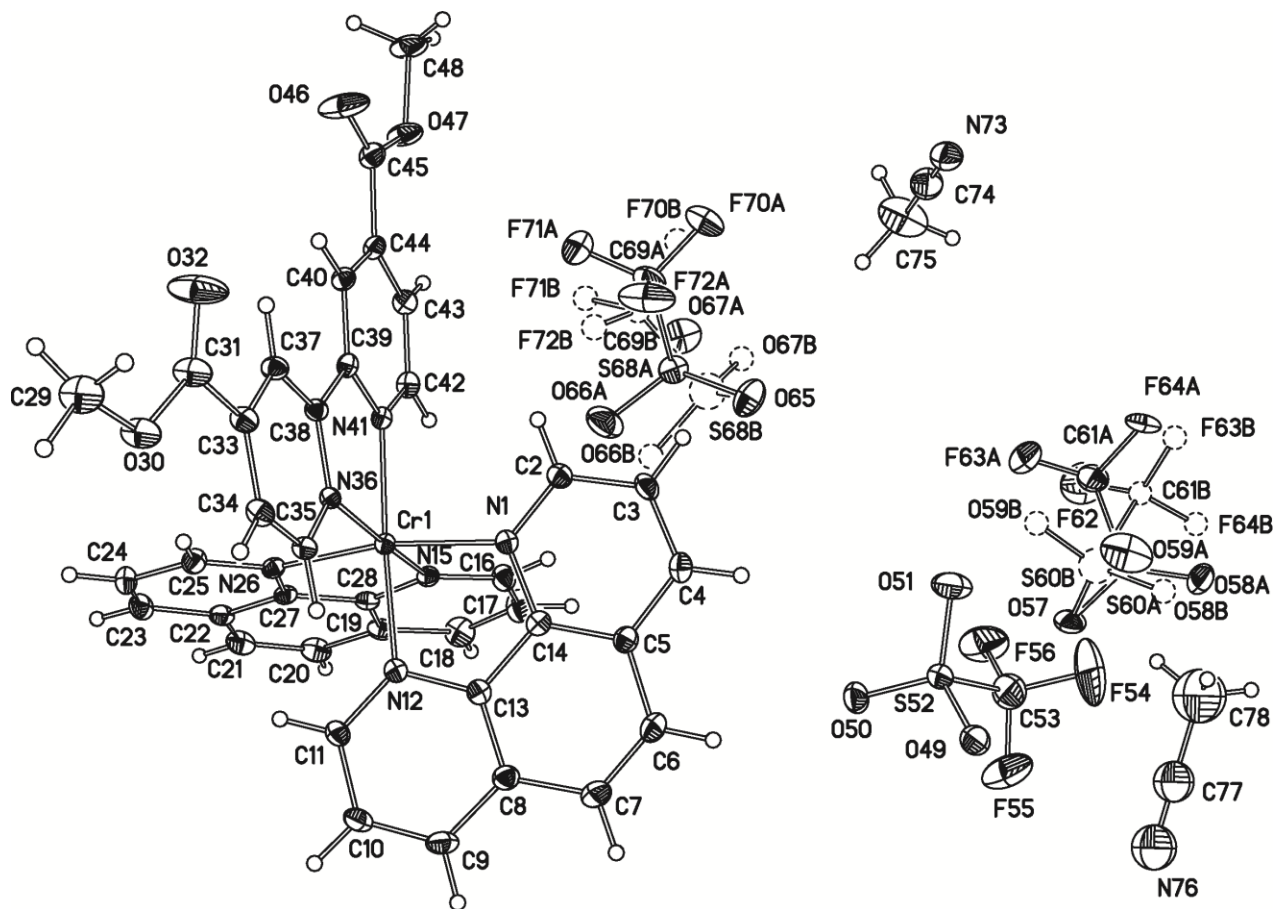


Figure A3.1. Full crystal structure for complex 4.1·1.3CH₃CN, rendered at 40% thermal ellipsoids. H atoms are not numbered in the figure. Minor components of disordered sites are shown in dashed circles.

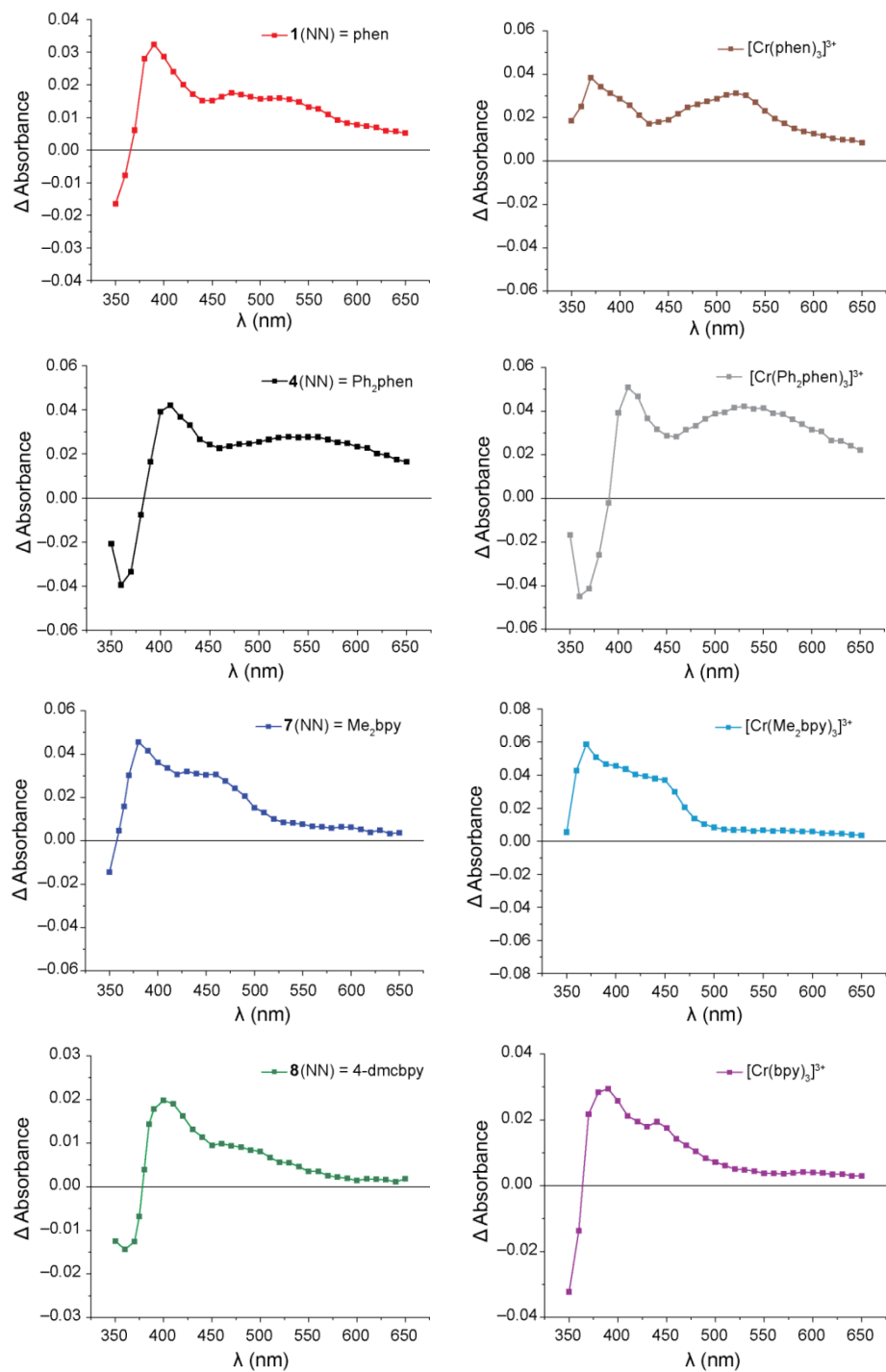


Figure A3.2. Transient absorption spectra on a μs timescale for Cr(III) polypyridyl complexes in 1 M $\text{HCl}_{(\text{aq})}$. The spectra were determined from a single exponential fit to transient absorption (or bleach) kinetics collected at each of the wavelengths for which there is a dot. The lines are included as guides to the eye.

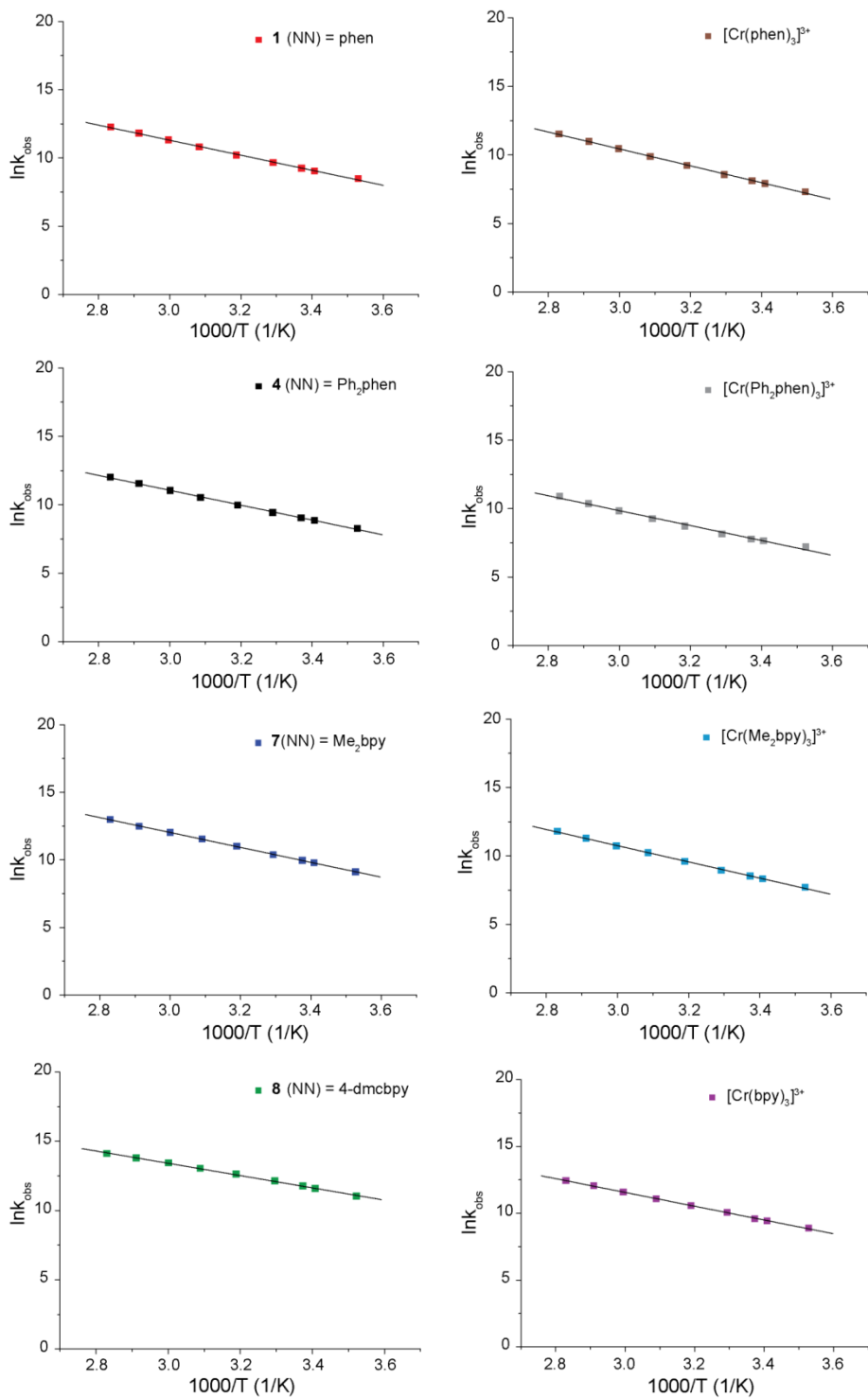


Figure A3.3. Temperature dependence of the observed rate constant ($k_{obs} = 1/\tau_{obs}$) for Cr(III) polypyridyl complexes in degassed 1 M $\text{HCl}_{(aq)}$.

Table A3.2. Ground state reduction potentials and peak separations for Cr(III) polypyridyl complexes. Values are assigned according to formal changes in Cr oxidation states for comparison to previous literature reports.

	$E_{1/2}$, V vs Fc^+/Fc^a					
	$3+/2+$	$2+/1+$	$1+/0$	$0/1-$	$1-/2-$	$2-/3-$
[Cr(phen) ₃]	-0.65 (70)	-1.17 (72)	-1.71 (75)	-2.21 (77)		
[Cr(Ph ₂ phen) ₃]	-0.67 (74)	-1.11 (71)	-1.63 (69)	-2.05 (66)		
[Cr(bpy) ₃]	-0.63 (72)	-1.15 (71)	-1.72 (69)	-2.34 (74)		
[Cr(Me ₂ bpy) ₃]	-0.79 (70)	-1.29 (75)	-1.82 (75)			
[(phen) ₂ Cr(4-dmcbpy)](4.1)	-0.42 (70)	-1.01 (74)	-1.61 (73)	-1.90 (72)		
[(Ph ₂ phen) ₂ Cr(4-dmcbpy)](4.4)	-0.45 (76)	-0.99 (66)	-1.54 (63)	-1.87 (73)		
[(Me ₂ bpy) ₂ Cr(4-dmcbpy)](4.7)	-0.47 (67)	-1.11 (67)	-1.71 (64)	-1.92 (64)		
[Cr(4-dmcbpy) ₃](4.8)	-0.26 (66)	-0.68 (71)	-1.21 (72)	-1.74 (71)	-1.93 (66)	-2.10 (67)

^a Conditions for cyclic voltammetry of Cr complexes: Electrolyte, 0.1 M TBAPF₆ in CH₃CN; WE, Pt; CE, Pt Wire; Scan Rate, 100 mV/s.

A3.2 References

1. *APEX 2*, Bruker Analytical X-Ray Systems, Inc.: Madison, WI, 2008.
2. Sheldrick, G. M. *SHELXTL*, Version 6.14; Bruker Analytical X-Ray Systems, Inc.: Madison, WI, 1999.
3. (a) Lilie, J.; Waltz, W. L. *Inorg. Chem.* **1983**, *22*, 1473-1478; (b) Jamieson, M. A.; Serpone, N.; Henry, M. S.; Hoffman, M. Z. *Inorg. Chem.* **1979**, *18*, 214-216; (c) Kane-Maguire, N. A. P.; Conway, J.; Langford, C. H. *J. Chem. Soc., Chem. Commun.* **1974**, 801 - 802; (d) Maestri, M.; Bolletta, F.; Serpone, N.; Moggi, L.; Balzani, V. *Inorg. Chem.* **1976**, *15*, 2048-2051; (e) Jamieson, M. A.; Serpone, N.; Hoffman, M. Z. *J. Am. Chem. Soc.* **1983**, *105*, 2933-2937.
4. Damrauer, N. H.; Boussie, T. R.; Devenney, M.; McCusker, J. K. *J. Am. Chem. Soc.* **1997**, *119*, 8253-8268.

Appendix A4. Supporting Information for Chapter 5

The work presented in Chapter 4 has been submitted to *Inorganic Chemistry* as: McDaniel, A. M.; Tseng, H.-W.; Hill, E. A.; Damrauer, N. H.; Rappé, A. K.; Shores, M. P., *Syntheses and Photophysical Investigations of Cr(III) Hexadentate Iminopyridine Complexes and Their Tris(Bidentate) Analogues*. X-ray structural data for $[\text{Cr}(\mathbf{L2})](\text{BF}_4)_3 \cdot \text{CH}_3\text{CN}$ (**5.2**·CH₃CN) and $[\text{Cr}(\mathbf{L4})_3](\text{BF}_4)_3$ (**5.4**) will be available as a crystallographic information file (CIF) and detailed DFT calculation and NTO analysis data will be available in pdf form on the Internet upon publication. In addition, these data will be archived electronically along with an electronic version of this dissertation and available through the Shores Group.

A4.1 Full Reference 21 from Chapter 5:

Frisch, M. J.; Trucks, G. W.; Schlegel, H. B.; Scuseria, G. E.; Robb, M. A.; Cheeseman, J. R.; Scalmani, G.; Barone, V.; Mennucci, B.; Petersson, G. A.; Nakatsuji, H.; Caricato, M.; Li, X.; Hratchian, H. P.; Izmaylov, A. F.; Bloino, J.; Zheng, G.; Sonnenberg, J. L.; Hada, M.; Ehara, M.; Toyota, K.; Fukuda, R.; Hasegawa, J.; Ishida, M.; Nakajima, T.; Honda, Y.; Kitao, O.; Nakai, H.; Vreven, T.; J. A. Montgomery, J.; Peralta, J. E.; Ogliaro, F.; Bearpark, M.; Heyd, J. J.; Brothers, E.; Kudin, K. N.; Staroverov, V. N.; Kobayashi, R.; Normand, J.; Raghavachari, K.; Rendell, A.; Burant, J. C.; Iyengar, S. S.; Tomasi, J.; Cossi, M.; Rega, N.; Millam, J. M.; Klene, M.; Knox, J. E.; Cross, J. B.; Bakken, V.; Adamo, C.; Jaramillo, J.; Gomperts, R.; Stratmann, R. E.; Yazyev, O.; Austin, A. J.; Cammi, R.; Pomelli, C.; Ochterski, J. W.; Martin, R. L.; Morokuma, K.; Zakrzewski, V. G.; Voth, G. A.; Salvador, P.; Dannenberg, J. J.; Dapprich, S.; Daniels, A. D.; Farkas, Ö.; Foresman, J. B.; Ortiz, J. V.; Cioslowski, J.; Fox, D. J. *Gaussian 09, Revision B.1*, Gaussian, Inc.: Wallingford CT, 2009.

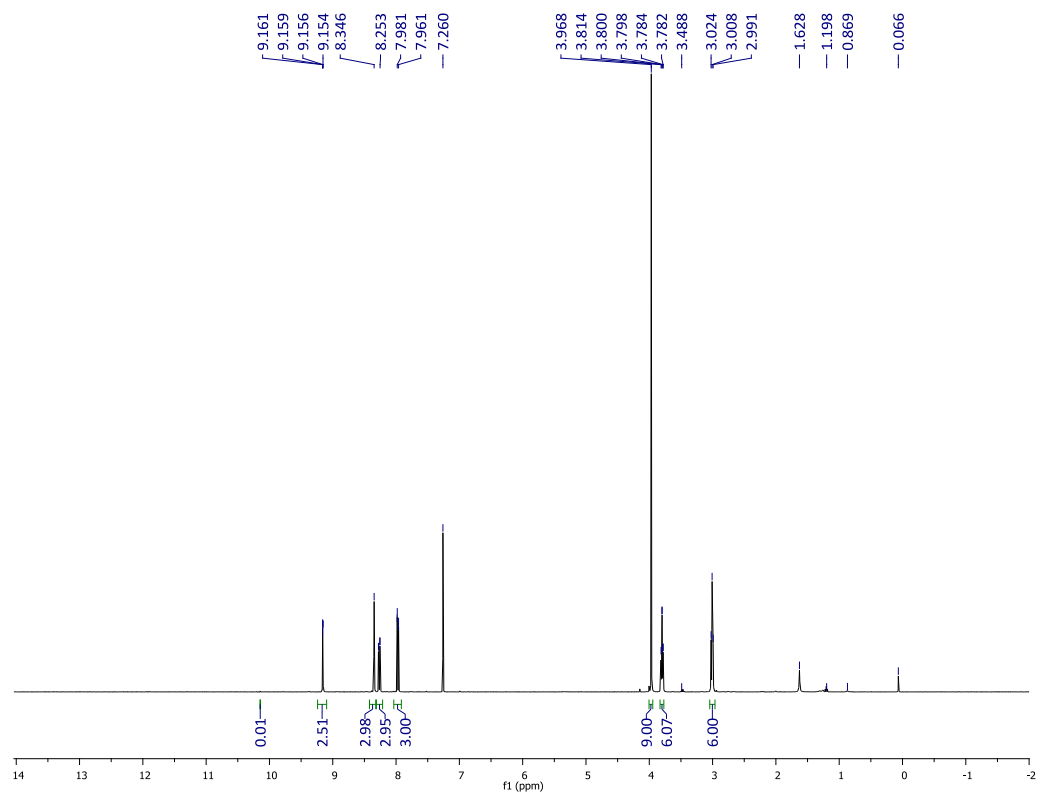


Figure A4.1. ^1H NMR of L2 in CDCl_3 at 26 °C and 400 MHz.

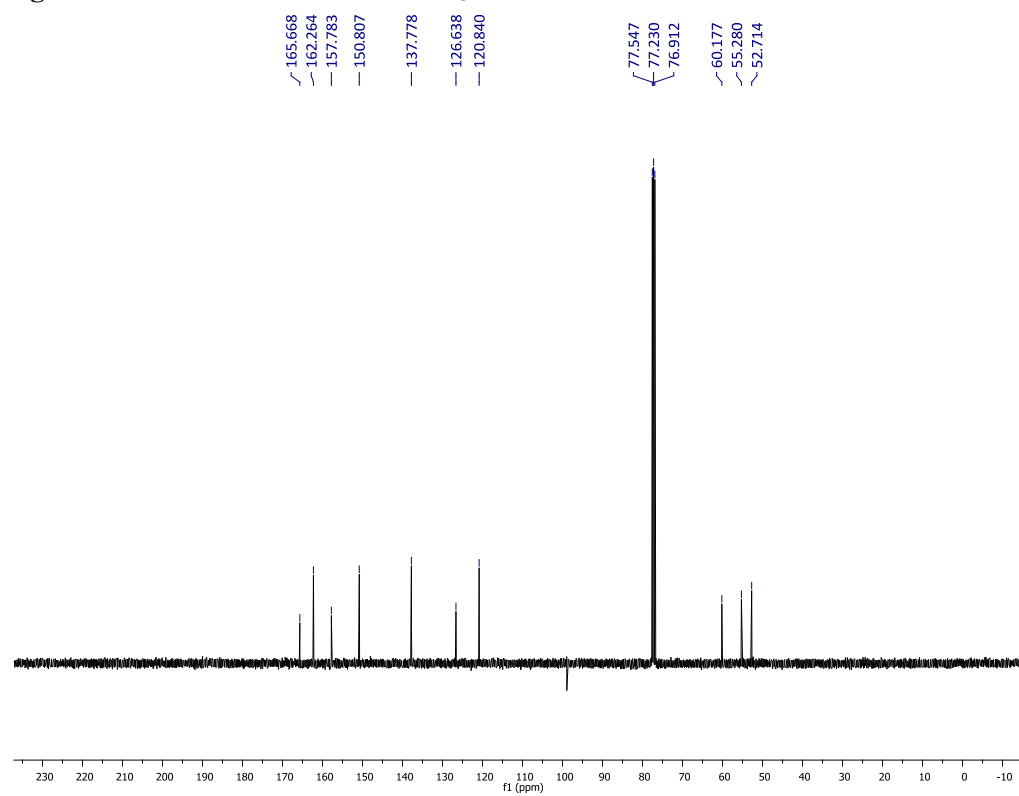


Figure A4.2. ^{13}C NMR of L2 in CDCl_3 at 26 °C and 400 MHz.

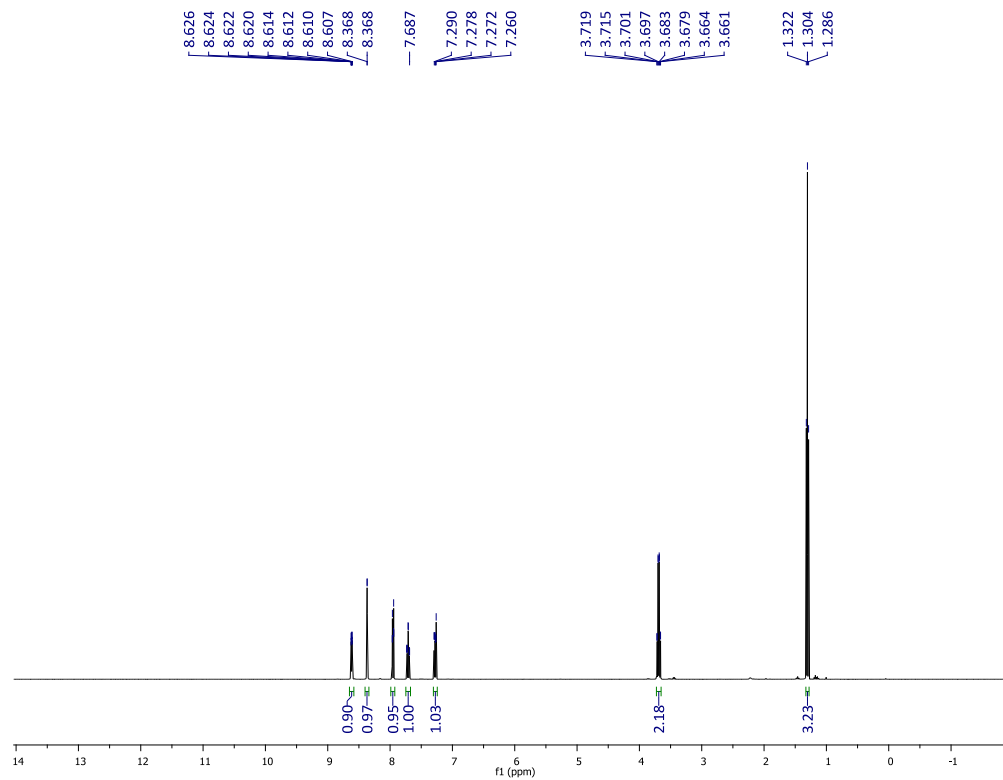


Figure A4.3. ^1H NMR of L3 in CDCl_3 at 26 °C and 400 MHz.

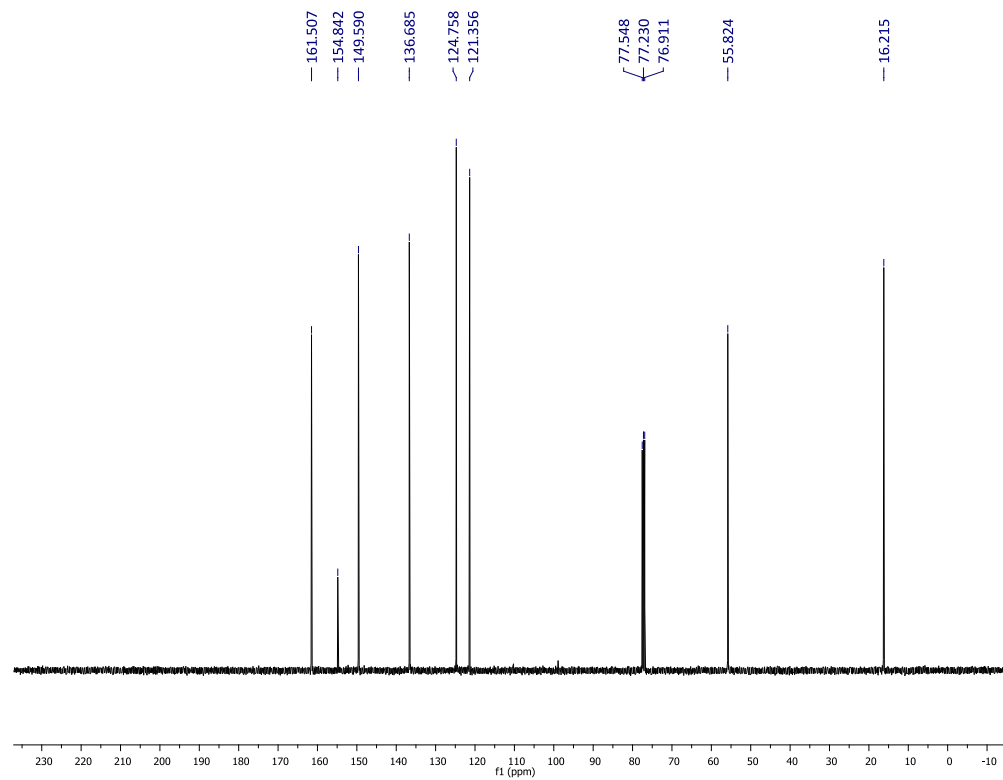


Figure A4.4. ^{13}C NMR of L3 in CDCl_3 at 26 °C and 400 MHz.

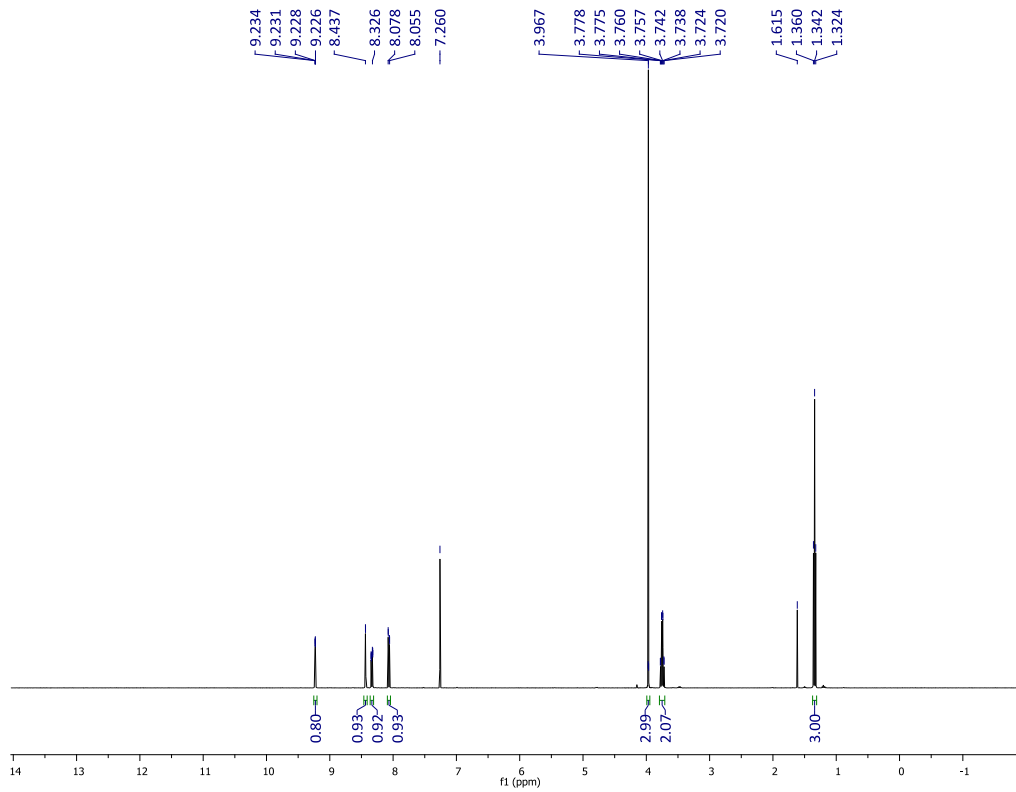


Figure A4.5. ^1H NMR of L4 in CDCl_3 at 26 °C and 400 MHz.

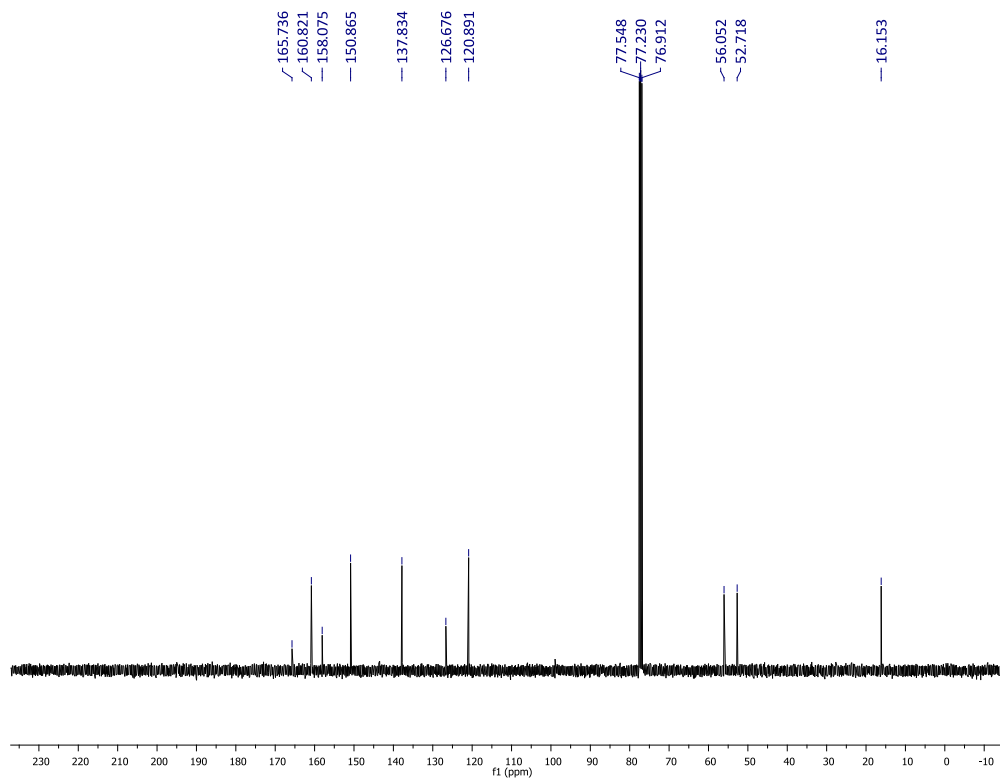


Figure A4.6. ^{13}C NMR of L4 in CDCl_3 at 26 °C and 400 MHz.

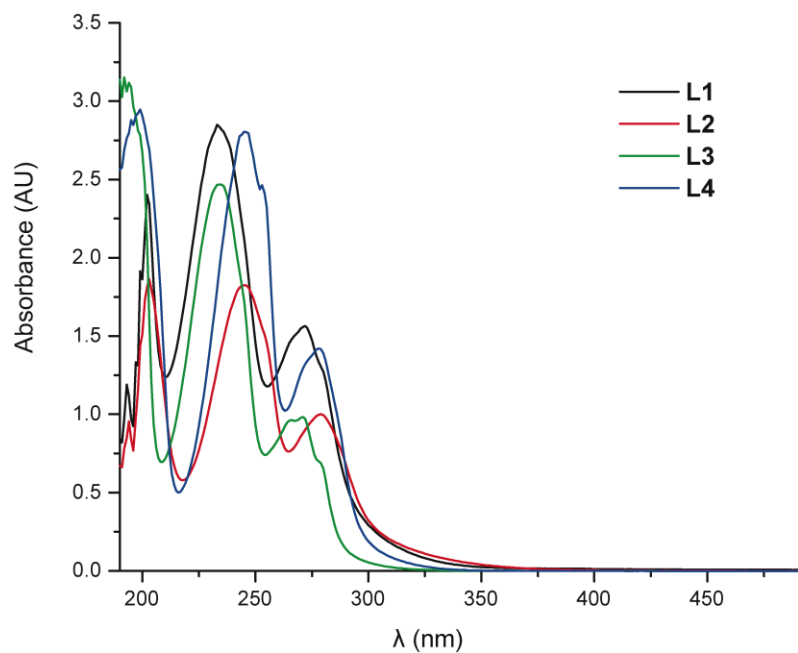


Figure A4.7. Absorption spectra of L1 and L2 in acetonitrile and L3 and L4 in pentane ($\sim 10\mu\text{M}$ - 1mM).

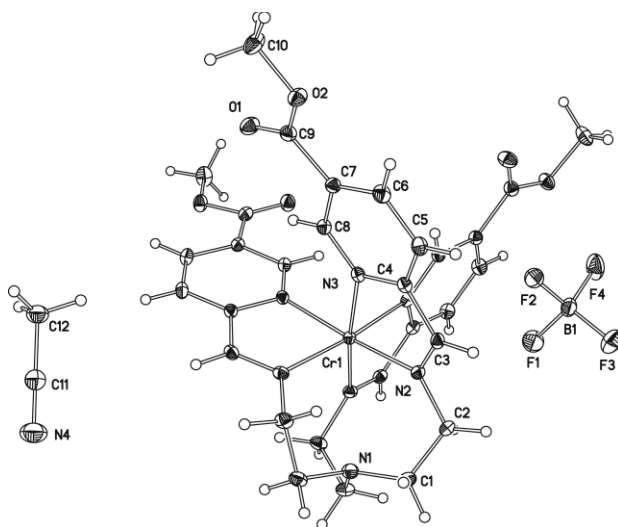


Figure A4.8. The full complex cation, and crystallographically independent anion and solvent molecules in the structure of $5.2 \cdot \text{CH}_3\text{CN}$, shown at 40% ellipsoids. The cation and acetonitrile each sit on a special position of three-fold rotational symmetry, and only the crystallographically independent atoms are labeled.

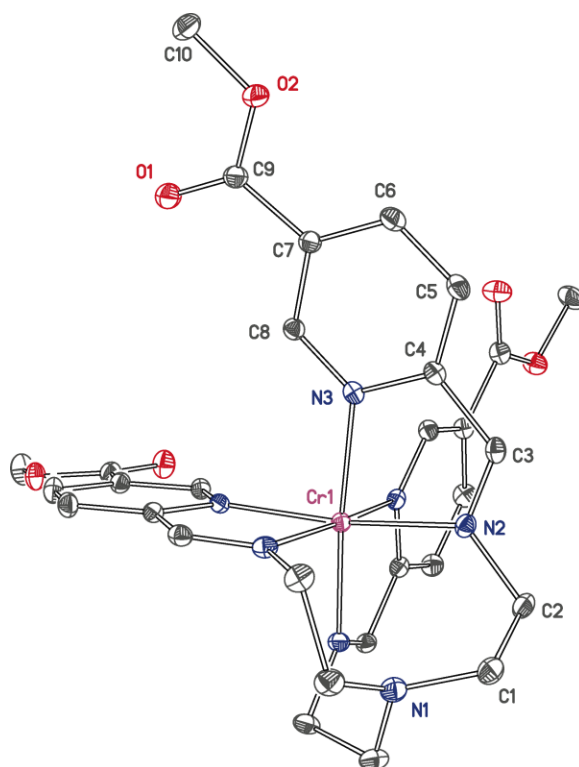


Figure A4.9. Alternate view of Cr(III) complex cation in the structure of **5.2**·CH₃CN, highlighting the octahedral coordination of the Cr center. Hydrogen atoms are omitted for clarity and structure is shown at 40% ellipsoids.

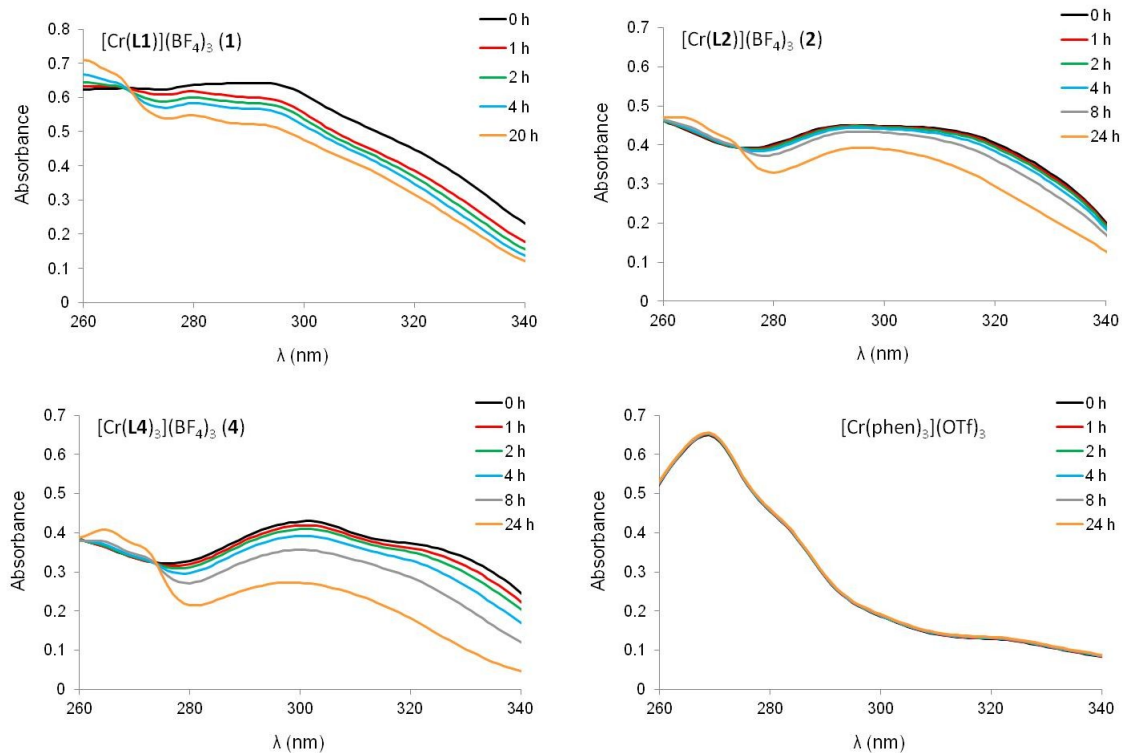


Figure A4.10. Absorption spectra for complexes **5.1**, **5.2**, **5.4**, and $[\text{Cr}(\text{phen})_3](\text{OTf})_3$ in $1\text{M HCl}_{(\text{aq})}$ over 24 hours.

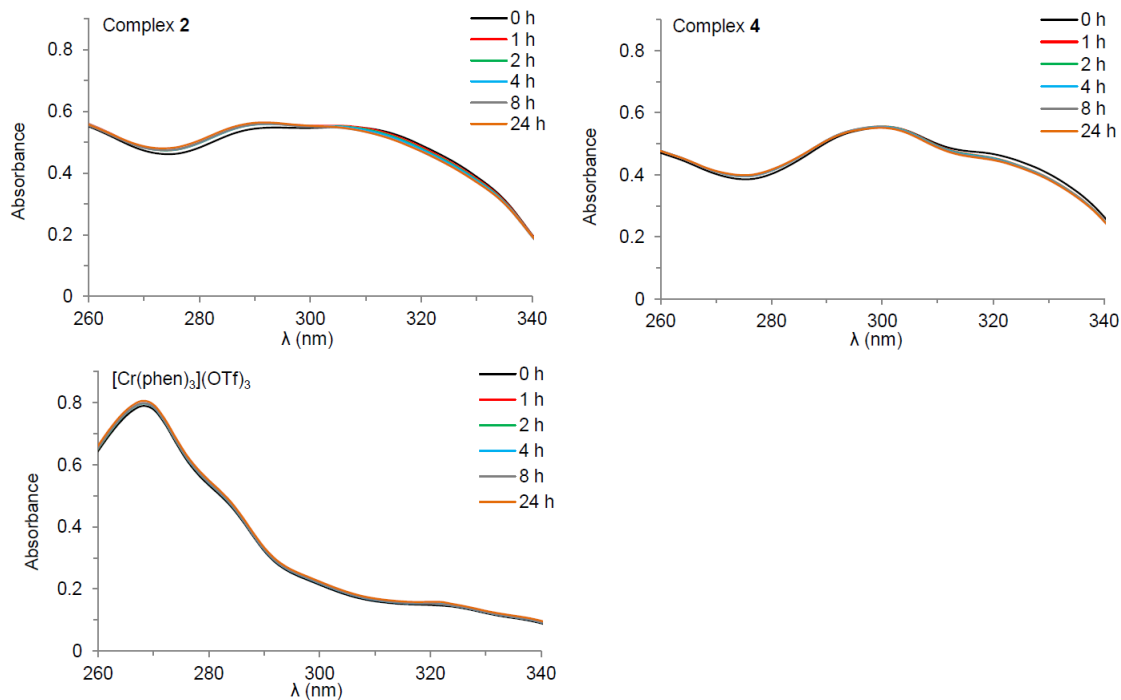


Figure A4.11. Absorption spectra for complexes **5.2**, **5.4**, and $[\text{Cr}(\text{phen})_3](\text{OTf})_3$ in acetonitrile over 24 hours.

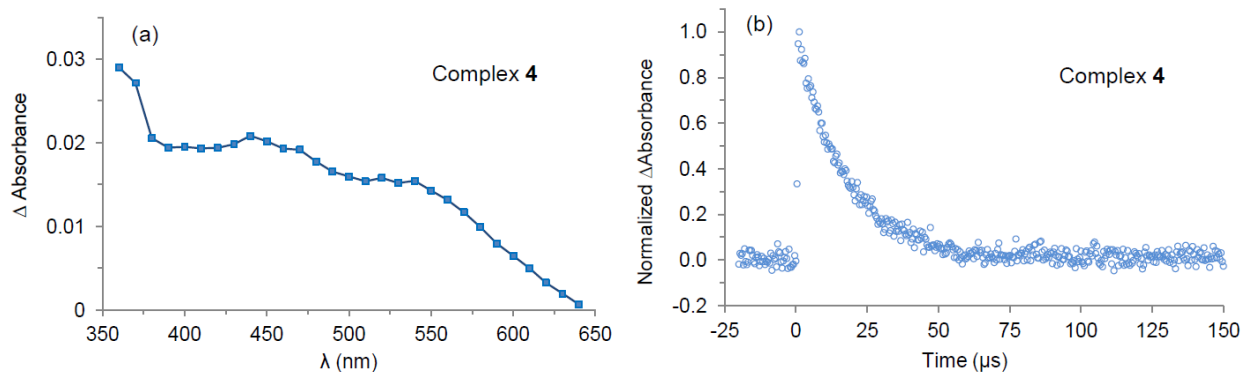


Figure A4.12. (a) Transient absorption spectrum for complex **5.4** recorded in deoxygenated acetonitrile at room temperature. (b) A typical transient absorption kinetic trace at 420 nm.

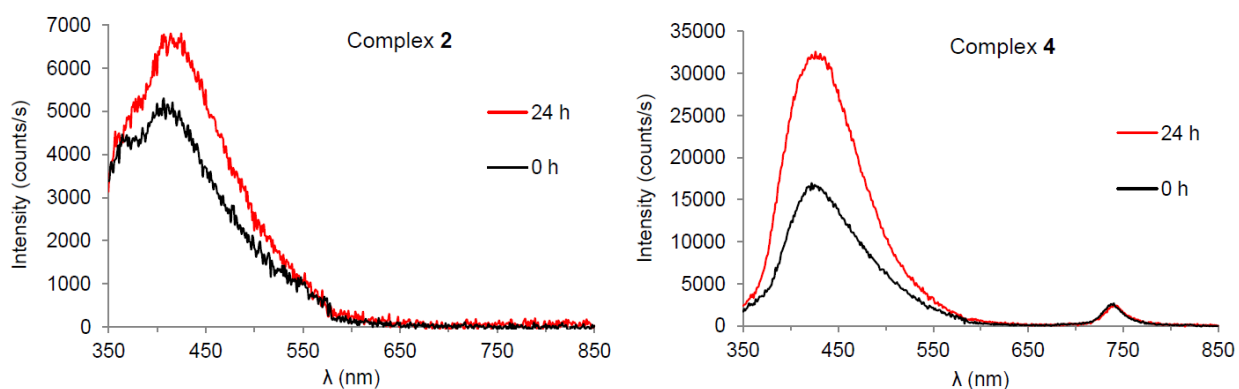


Figure A4.13. Emission spectra for complexes **5.2** and **5.4** in acetonitrile right after dissolution and at 24 hours featuring unknown emissions at 350 nm to 550 nm. The samples were excited at 300 nm.

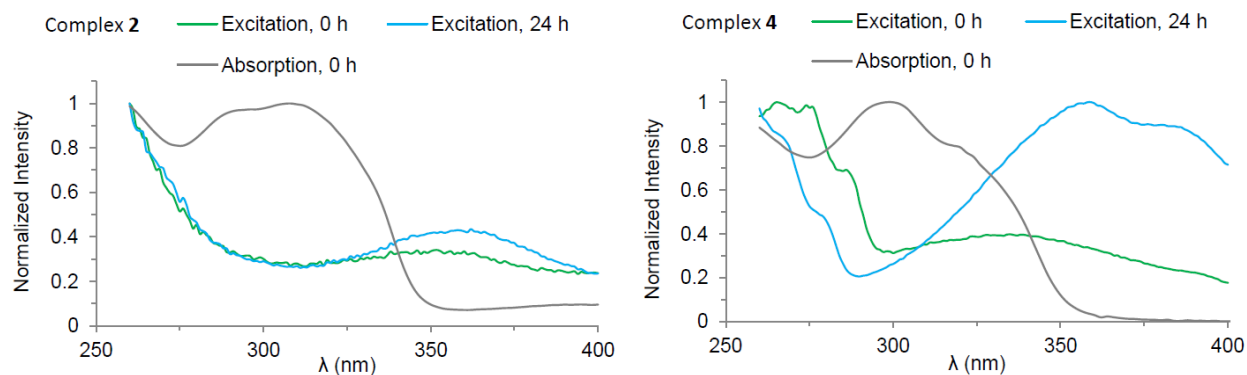


Figure A4.14. Excitation spectra for complexes **5.2** and **5.4** in acetonitrile at 0 and 24 hours after dissolution. The excitation spectra were obtained by monitoring emission intensity at 470 nm and the spectra were corrected for excitation intensity. Absorption spectra were also included for comparison.

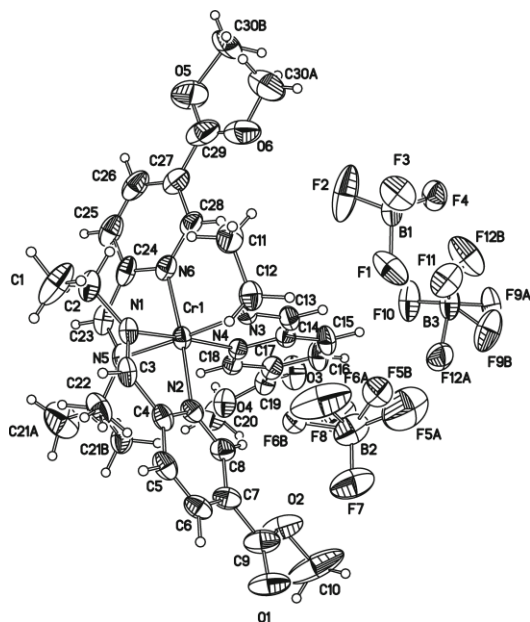


Figure A4.15. The full structure of **5.4** including disordered components (labeled A and B) at 40% ellipsoids.

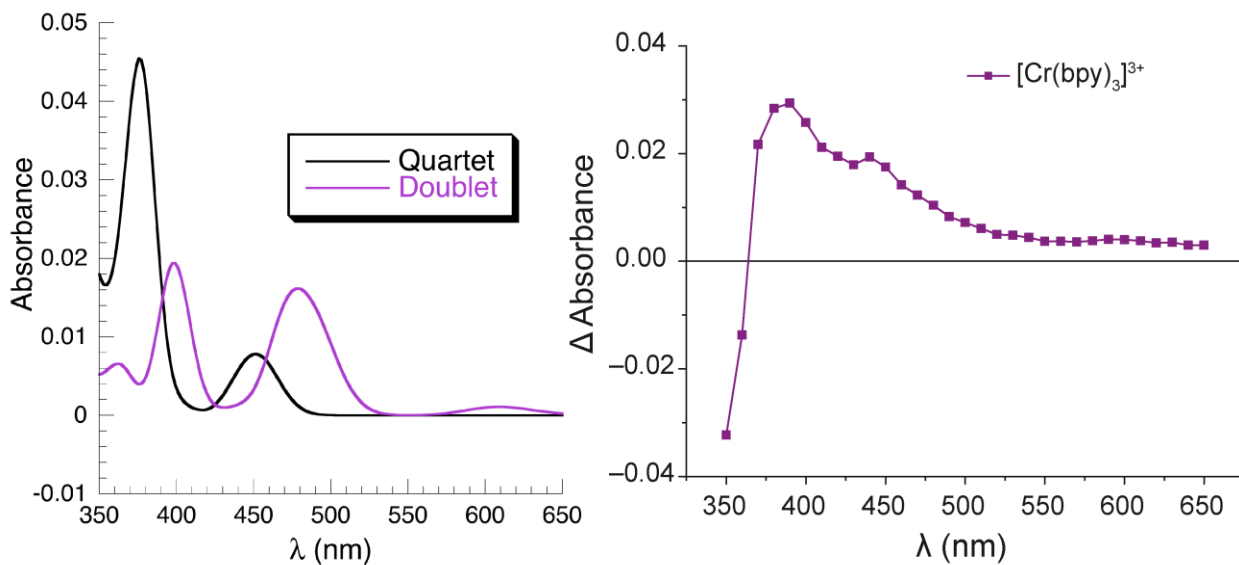


Figure A4.16. Calculated doublet and quartet excited state absorption spectra of $[\text{Cr}(\text{bpy})_3]^{3+}$ (left) and transient absorption spectrum of $[\text{Cr}(\text{bpy})_3]^{3+}$ (right). Transient absorption spectrum is from Chapter 4 and published in *Inorg. Chem.* **2010**, *49*, 7981-7991.

A4.2 Details of Computational Analyses. In order to understand why **5.1** and **5.2** do not display doublet emission while $[\text{Cr}(\text{bpy})_3]^{3+}$, $[\text{Cr}(4\text{-dmcby})_3]^{3+}$, and **5.4** do, multi-determinantal (MD) UB3LYP-DFT and TD-DFT computational studies were performed. The excitation energy diagram (Figure 5.7 in Chapter 5), has been annotated here (Figure A4.17) to highlight alternative hypotheses for the unique behavior of **5.2** relative to $[\text{Cr}(4\text{-dmcby})_3]^{3+}$ and **5.4**. Several potential non-radiative deactivation pathways are discussed.

1) Intersystem crossing to sextet states *a*, competing with intersystem crossing to the doublet state manifold *b*, or internal conversion in the quartet manifold, *c*, highlighted in blue in Figure A4.17. Note, the doublet manifold for **5.2** is depleted relative to $[\text{Cr}(4\text{-dmcby})_3]^{3+}$ and **5.4**. Competitive intersystem crossing to the sextet manifold followed by internal conversion to the lowest sextet could mediate access to the depleted doublet manifold.

2) Reverse intersystem crossing from intermediate states in the doublet manifold, *d*, could compete with internal conversion within the doublet manifold, *e*, highlighted in green in Figure A4.17.

3) The low lying quartet states highlighted in red in Figure A4.17, a feature unique to **5.2**, could lead to the excitation being trapped due to a lack of an intersystem crossing pathway to the doublet manifold of comparable energy and orbital character, *f*. This third alternative is also available for the other molecules shown in Figure A4.17. However, in **5.2** the lowest quartet state is more than 0.5 eV lower in energy (relative to the other complexes) and is expected to provide a facile non-radiative pathway to the ground state due to large Franck-Condon factors. In fact, this pathway would also serve in deactivating phosphorescence from any low energy doublets that do form.

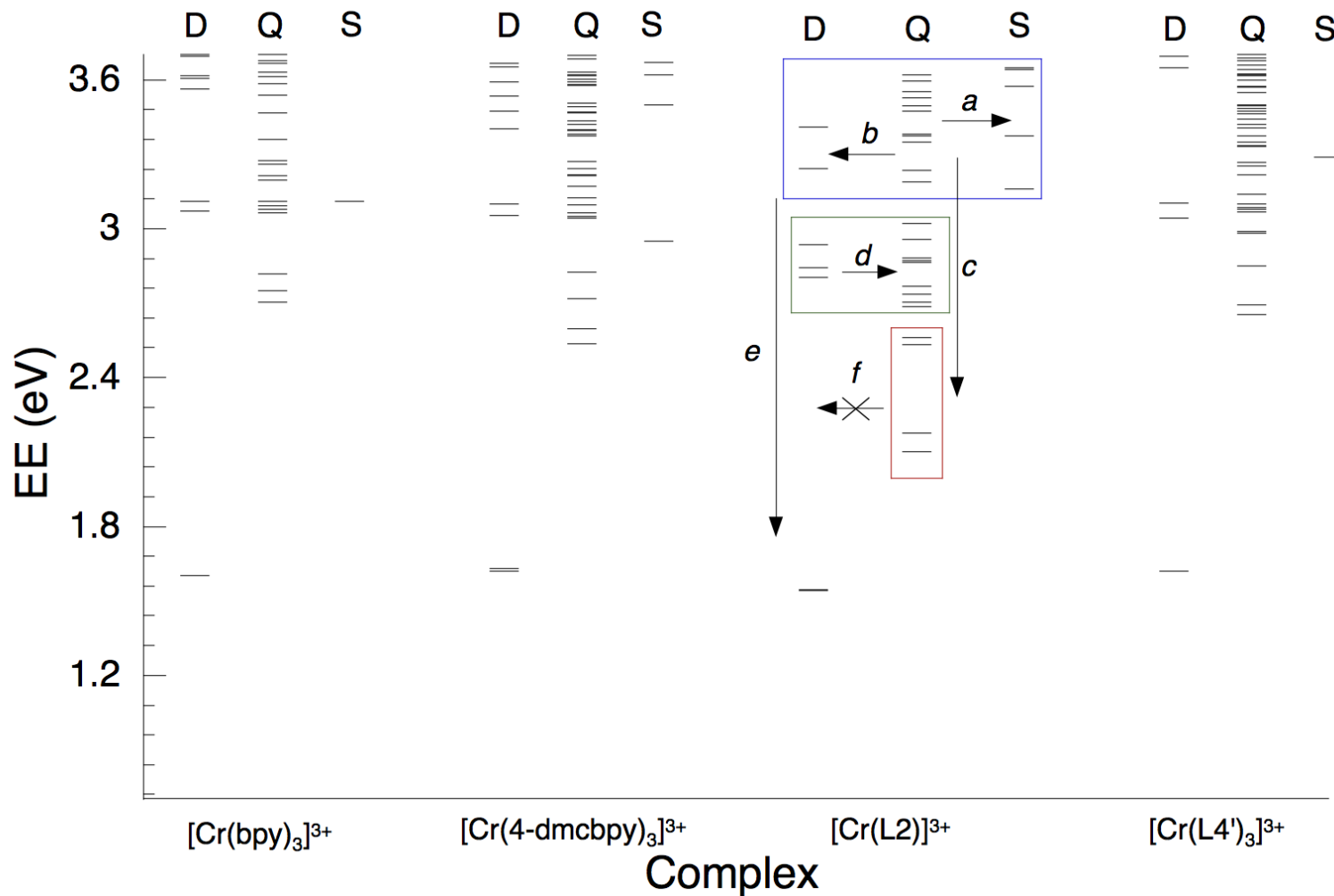


Figure A4.17. Computed excitation energies for selected Cr(III) complexes, where the ground state quartet energy for each complex is set at zero. For each species, the left column is the doublet manifold (D), the middle column is the quartet manifold (Q), and the right column is the sextet manifold (S). Unique features of $[\text{Cr}(\text{L2})]^{3+}$ are highlighted with red, green, and blue boxes; arrows refer to potential intersystem crossing (a,b,d,f) or relaxation (c,e) events.

NTO analyses of the high (3.1-3.5 eV), middle (2.6-3.1 eV), and low (2.1-2.6 eV) energy regions of the electronic spectrum of **5.2** differentiate the three deactivation hypotheses outlined above (Figure A4.18-20). Comparison of the higher energy excited state NTOs (Figure A4.18) suggests significant spatial congruence (orbitals of similar shape in the same region of space) between some of the quartet states and the sextet states in the 3.1-3.5 eV window. This spatial congruence suggests significant spin-orbit coupling between the states and the potential for rapid intersystem crossing into the sextet manifold, *a*. There is also significant spatial congruence between the states in the doublet and quartet manifolds in this energy window, consistent with intersystem crossing to the doublet manifold, *b*.

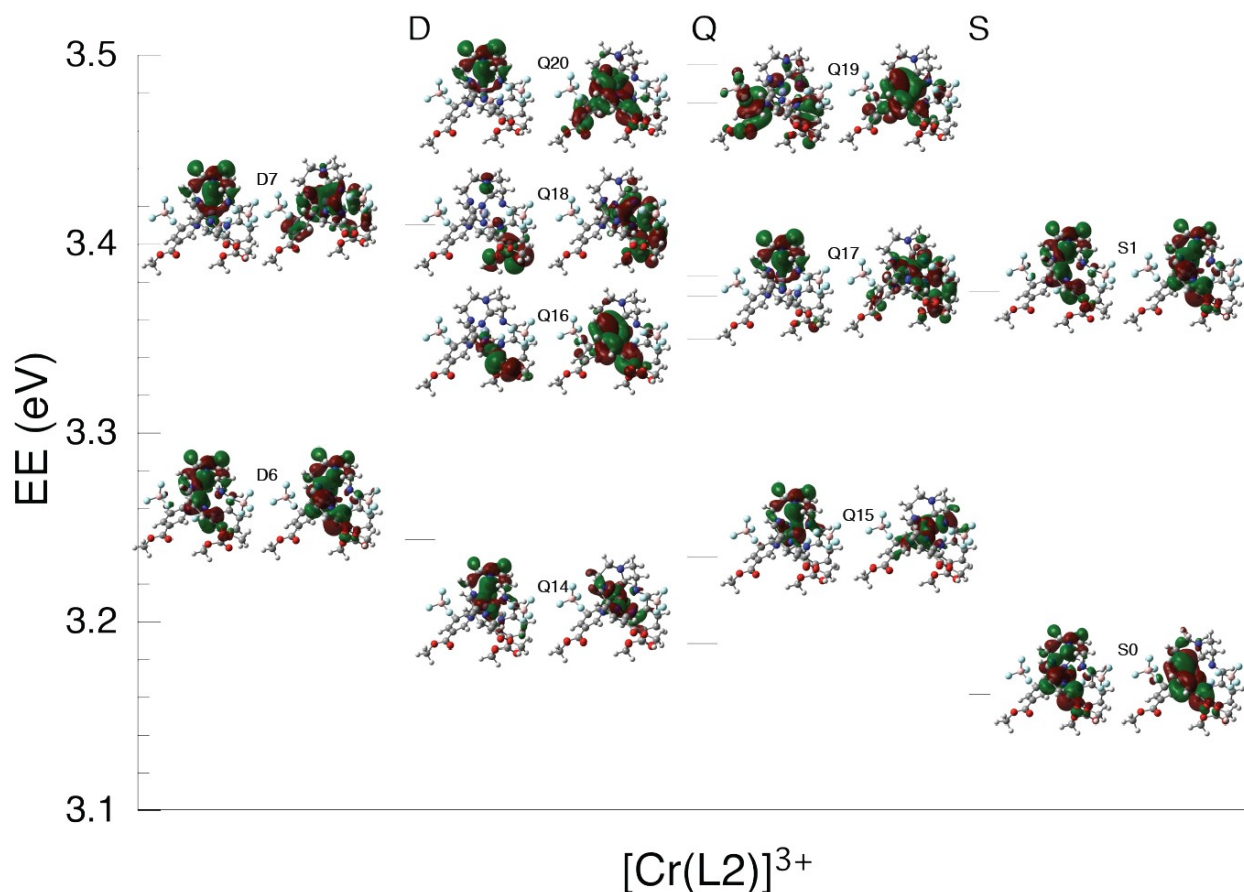


Figure A4.18. Natural transition orbital (NTO) analyses for the 3.1-3.5 eV range for **5.2**. For each orbital pair, an electron is removed from the left orbital and deposited into the right orbital. NTO pair labels are denoted by the spin manifold (Doublet or Quartet or Sextet) and are numbered by increasing energy of transition.

The rapid back intersystem crossing hypothesis, *d*, finds support from the NTOs in Figure A4.19 for states within the 2.6-3.1 eV window. In particular, the 2.92 eV doublet, D5, ($N_{\text{amine}} \rightarrow \text{Cr } t_{2g}$ transition) matches the 2.93 eV quartet with $N_{\text{amine}} \rightarrow \text{Cr } e_g^*$ character, Q12.

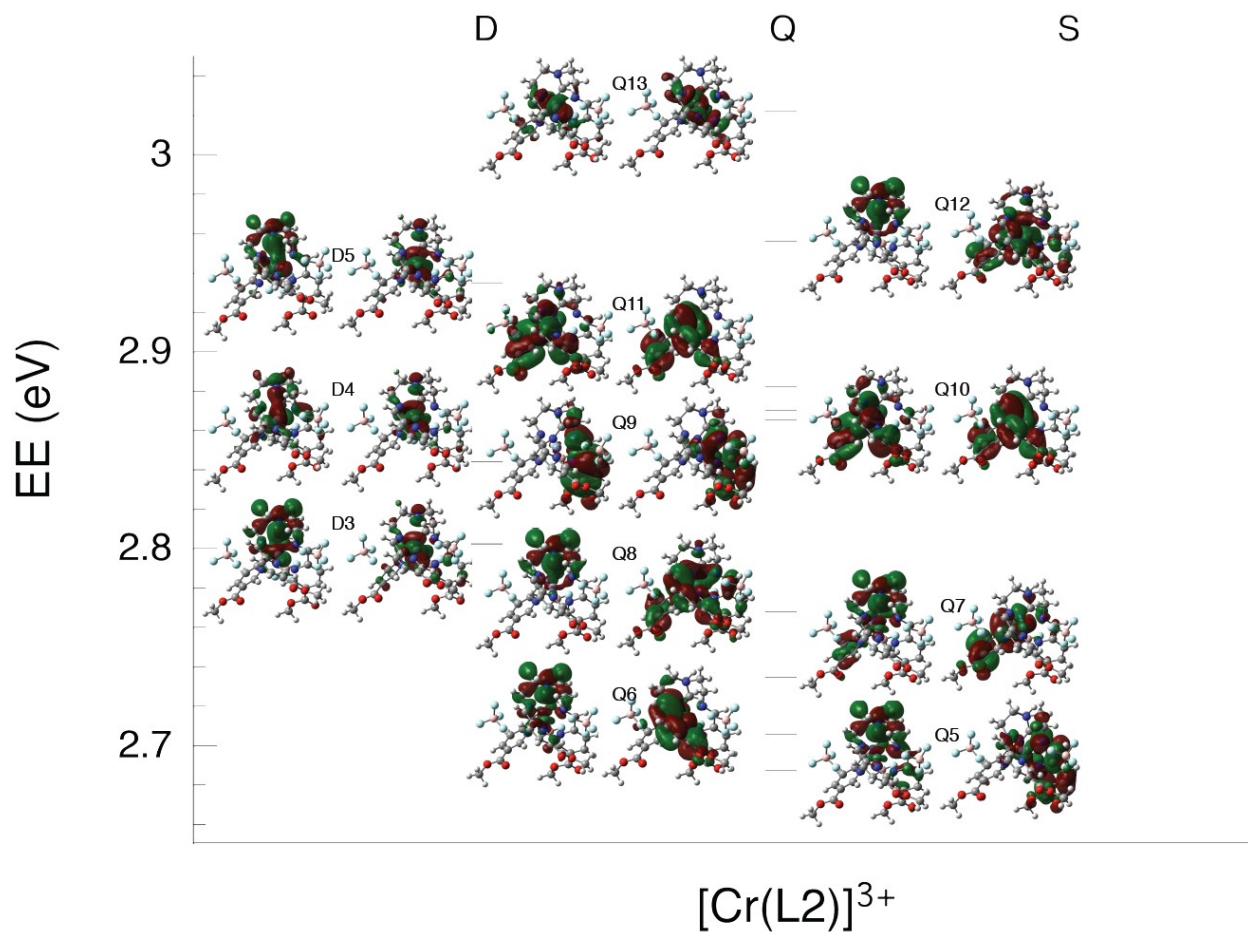


Figure A4.19. Natural transition orbital (NTO) analyses for the 2.6-3.1 eV range for **5.2**. For each orbital pair, an electron is removed from the left orbital and deposited into the right orbital. NTO pair labels are denoted by the spin manifold (Doublet or Quartet or Sextet) and are numbered by increasing energy of transition.

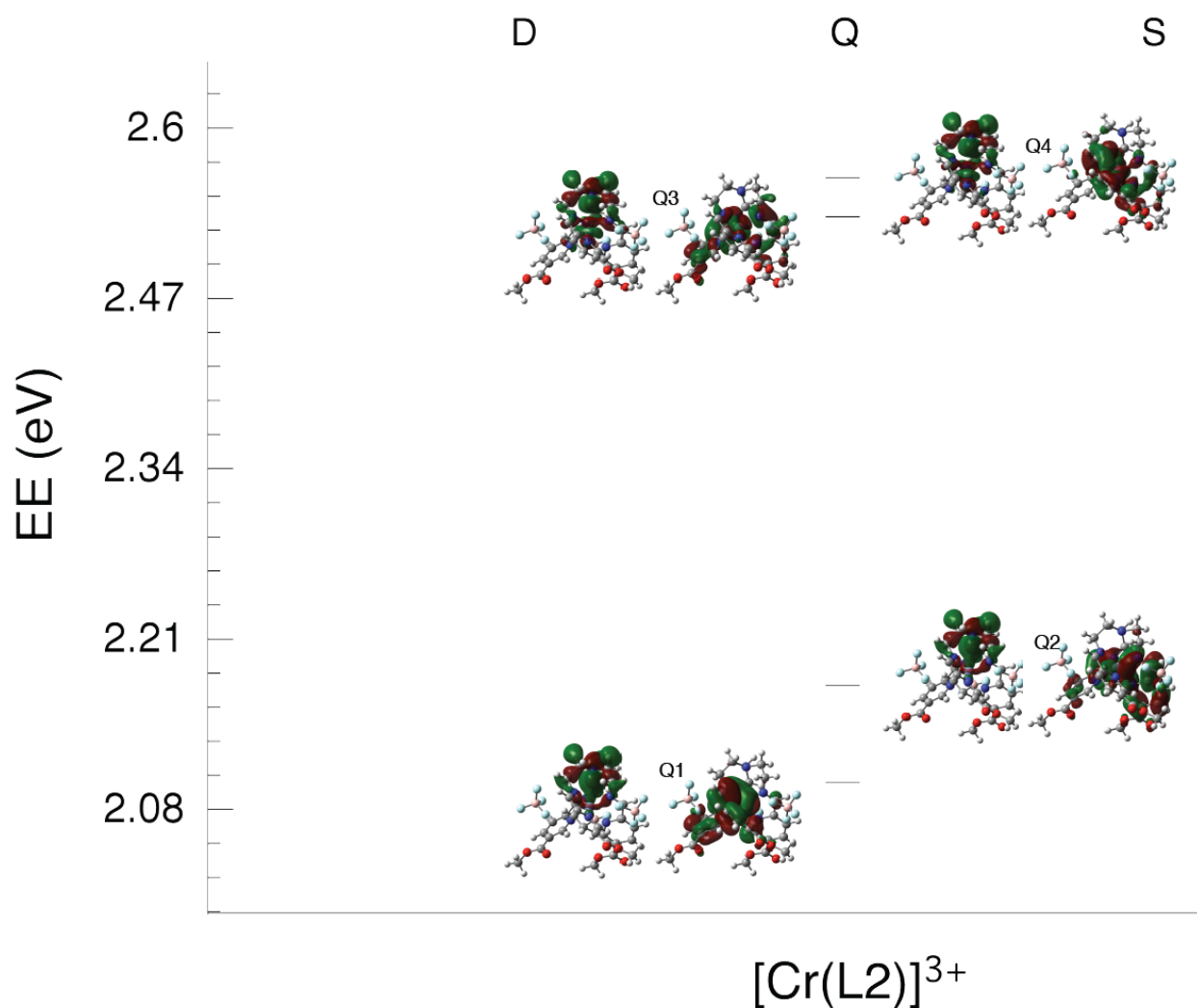


Figure A4.20. Natural transition orbital (NTO) analyses for the 2.1-2.6 eV range for **5.2**. For each orbital pair, an electron is removed from the left orbital and deposited into the right orbital. NTO pair labels are denoted by the spin manifold (Doublet or Quartet or Sextet) and are numbered by increasing energy of transition.

The NTOs for the lowest energy quartet states (Figure A4.20, $N_{\text{amine}} \rightarrow \text{Cr } t_{2g}$) do not display significant congruence with the lowest energy doublets that are low spin t_{2g}^3 configurations. The generality of the orbital character of the lowest doublet and quartet states was probed by generating the NTOs for the lowest doublets and quartets for $[\text{Cr}(4\text{-dmcbpy})_3]^{3+}$, and **5.4'** as well, see Figure A4.21.

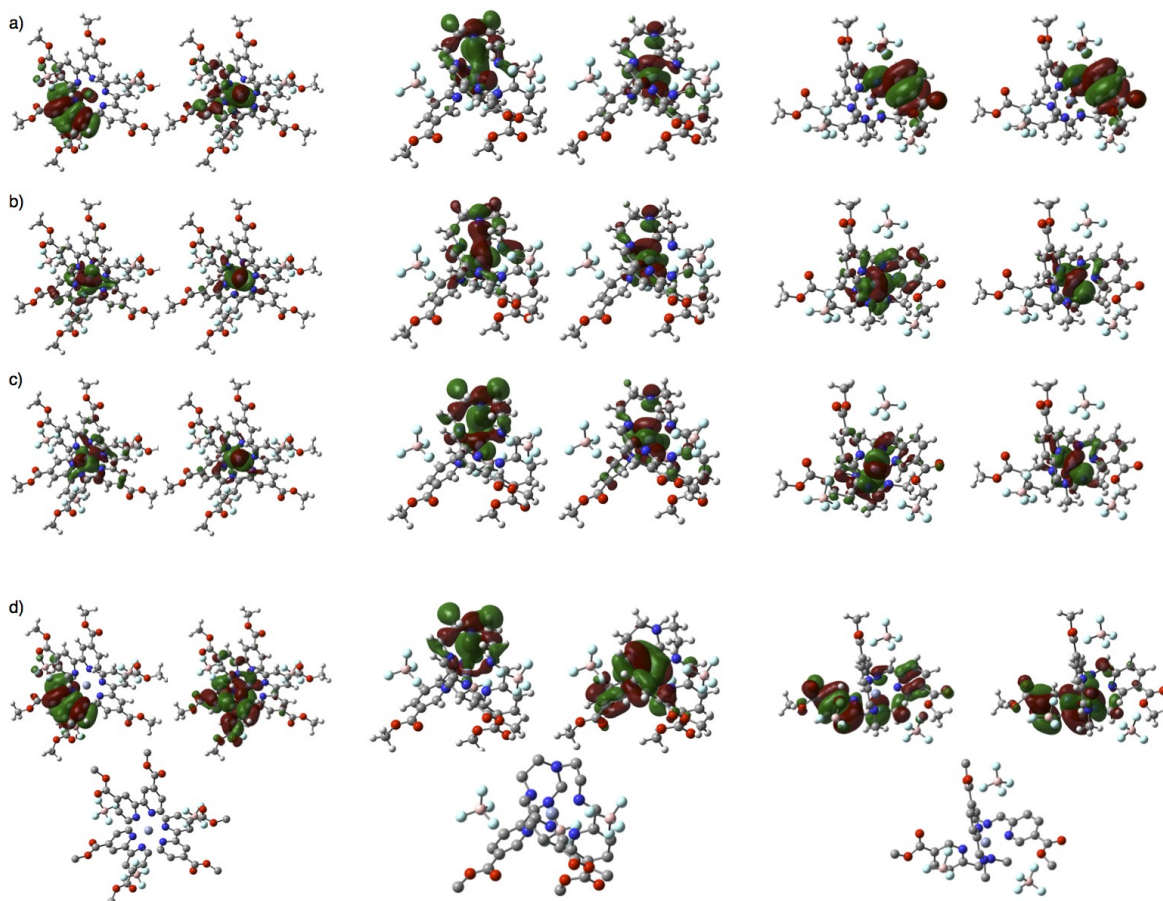


Figure A4.21. Natural transition orbitals (NTOs) for $[\text{Cr}(4\text{-dmcbpy})_3]^{3+}$ (left), **5.2** (middle) and **5.4'** (right): (a-c) the lowest three doublet transitions; (d) the lowest quartet transitions. In each pair, the left NTO corresponds to where the excitation is from while the right NTO is where the excitation is to. Hydrogen atoms have been removed for clarity.

For **5.2**, $[\text{Cr}(4\text{-dmcbpy})_3]^{3+}$, and **5.4'** the lowest quartet excited states all involve excitation from a ligand (ligand π or N_{amine}) orbital to an orbital that is an admixture of ligand π^* and Cr t_{2g} character. In contrast, while for **5.2** the lowest doublet is a $N_{\text{amine}} \rightarrow \text{Cr } t_{2g}$ transition, for $[\text{Cr}(4\text{-dmcbpy})_3]^{3+}$ and **5.4'** the second set of doublet states (lowest doublet transitions) arise from transitions that are dominantly $\text{Cr } t_{2g} \rightarrow \text{Cr } t_{2g}$ in character (equation 5.3 in the Chapter 5). For both $[\text{Cr}(4\text{-dmcbpy})_3]^{3+}$ and **5.4'** there is a small admixture of ligand character in the donating orbital, larger admixture for iminopyridine than bpy. For **5.2**, the admixture of ligand character dominates; the transition for **5.2** is from a N_{amine} ligand orbital to a Cr t_{2g} orbital ($N_{\text{amine}} \rightarrow \text{Cr } t_{2g}$ transition). For both $[\text{Cr}(4\text{-dmcbpy})_3]^{3+}$ and **5.4'** the higher energy low spin

t_{2g}^3 doublet states can readily undergo internal conversion to the lower t_{2g}^3 doublet states via the large congruence of orbital character, electronic coupling, and ligand geometry. For **5.2**, due to a disparity of orbital character (and ligand geometry), internal conversion from higher doublets competes with intersystem crossing to a set of quartet states with congruent orbital character (and ligand geometry) that share little orbital character with the lowest doublet states.

Table A4.1. Selected bond lengths [Å] and angles [°] for **5.2**-CH₃CN; some symmetry equivalent atoms and all H atoms are omitted (data for all atoms available in the CIF file)

Cr(1)-N(2)	2.0506(13)	O(2)-C(10)	1.448(2)	C(7)-C(9)	1.496(2)
Cr(1)-N(3)	2.0680(13)	C(3)-C(4)	1.463(2)	B(1)-F(4)	1.385(2)
N(1)-C(1)	1.4529(17)	N(3)-C(8)	1.3301(19)	B(1)-F(3)	1.388(2)
C(1)-C(2)	1.531(2)	N(3)-C(4)	1.3636(18)	B(1)-F(1)	1.393(2)
O(1)-C(9)	1.202(2)	C(4)-C(5)	1.379(2)	B(1)-F(2)	1.401(2)
C(2)-N(2)	1.4741(19)	C(5)-C(6)	1.396(2)	N(4)-C(11)	1.148(5)
N(2)-C(3)	1.274(2)	C(6)-C(7)	1.386(2)	C(11)-C(12)	1.446(5)
O(2)-C(9)	1.3310(18)	C(7)-C(8)	1.398(2)		
N(2)-Cr(1)-N(2)#1	99.10(4)	N(2)-C(3)-C(4)	118.02(13)		
N(2)-Cr(1)-N(2)#2	99.10(4)	C(8)-N(3)-C(4)	118.53(13)		
N(2)#1-Cr(1)-N(2)#2	99.10(4)	C(8)-N(3)-Cr(1)	128.32(10)		
N(2)-Cr(1)-N(3)	79.30(5)	C(4)-N(3)-Cr(1)	113.08(10)		
N(2)#1-Cr(1)-N(3)	88.31(5)	N(3)-C(4)-C(5)	122.78(14)		
N(2)#2-Cr(1)-N(3)	172.59(5)	N(3)-C(4)-C(3)	114.39(12)		
N(2)-Cr(1)-N(3)#1	172.59(5)	C(5)-C(4)-C(3)	122.78(13)		
N(2)#1-Cr(1)-N(3)#1	79.30(5)	C(4)-C(5)-C(6)	118.52(14)		
N(2)#2-Cr(1)-N(3)#1	88.31(5)	C(7)-C(6)-C(5)	118.72(13)		
N(3)-Cr(1)-N(3)#1	93.40(5)	C(6)-C(7)-C(8)	119.50(13)		
N(2)-Cr(1)-N(3)#2	88.31(5)	C(6)-C(7)-C(9)	123.14(13)		
N(2)#1-Cr(1)-N(3)#2	172.59(5)	C(8)-C(7)-C(9)	117.30(12)		
N(2)#2-Cr(1)-N(3)#2	79.30(5)	N(3)-C(8)-C(7)	121.92(13)		
N(3)-Cr(1)-N(3)#2	93.40(5)	O(1)-C(9)-O(2)	125.76(14)		
N(3)#1-Cr(1)-N(3)#2	93.40(5)	O(1)-C(9)-C(7)	123.25(14)		
C(1)#1-N(1)-C(1)	116.69(6)	O(2)-C(9)-C(7)	110.98(13)		
C(1)#1-N(1)-C(1)#2	116.69(6)	F(4)-B(1)-F(3)	109.67(15)		
C(1)-N(1)-C(1)#2	116.69(6)	F(4)-B(1)-F(1)	110.04(16)		
N(1)-C(1)-C(2)	109.96(14)	F(3)-B(1)-F(1)	110.28(16)		
N(2)-C(2)-C(1)	108.66(12)	F(4)-B(1)-F(2)	108.62(16)		
C(3)-N(2)-C(2)	119.16(13)	F(3)-B(1)-F(2)	109.70(15)		
C(3)-N(2)-Cr(1)	115.09(10)	F(1)-B(1)-F(2)	108.49(14)		
C(2)-N(2)-Cr(1)	125.75(10)	N(4)-C(11)-C(12)	180.000(1)		
C(9)-O(2)-C(10)	115.83(13)				

Symmetry transformations used to generate equivalent atoms:

#1 -y+1,x-y+1,z #2 -x+y,-x+1,z

Table A4.2. Selected bond lengths [Å] and angles [°] for **5.4**; all H atoms are omitted (data for all atoms available in the cif file)

Cr(1)-N(5)	2.041(3)	C(4)-C(5)	1.374(5)	C(23)-C(24)	1.430(7)
Cr(1)-N(1)	2.042(3)	C(5)-C(6)	1.374(6)	C(24)-C(25)	1.375(6)
Cr(1)-N(3)	2.048(3)	N(5)-C(23)	1.295(5)	C(25)-C(26)	1.383(8)
Cr(1)-N(2)	2.057(3)	N(5)-C(22)	1.469(6)	C(26)-C(27)	1.378(7)
Cr(1)-N(4)	2.063(3)	O(5)-C(29)	1.220(7)	C(27)-C(28)	1.393(6)
Cr(1)-N(6)	2.068(3)	O(5)-C(30B)	1.68(2)	C(27)-C(29)	1.464(8)
N(1)-C(3)	1.280(5)	C(6)-C(7)	1.378(6)	F(1)-B(1)	1.413(6)
N(1)-C(2)	1.484(5)	N(6)-C(28)	1.338(5)	B(1)-F(2)	1.350(5)
O(1)-C(9)	1.208(5)	N(6)-C(24)	1.362(5)	B(1)-F(4)	1.366(5)
C(1)-C(2)	1.487(6)	O(6)-C(29)	1.302(8)	B(1)-F(3)	1.373(5)
N(2)-C(8)	1.321(5)	O(6)-C(30A)	1.358(8)	B(3)-F(9B)	1.284(9)
N(2)-C(4)	1.375(4)	C(7)-C(8)	1.389(5)	B(3)-F(9A)	1.324(7)
O(2)-C(9)	1.310(5)	C(7)-C(9)	1.502(6)	B(3)-F(10)	1.341(5)
O(2)-C(10)	1.471(6)	C(11)-C(12)	1.507(6)	B(3)-F(11)	1.353(5)
N(3)-C(13)	1.287(5)	C(13)-C(14)	1.451(5)	B(3)-F(12A)	1.530(8)
N(3)-C(12)	1.479(5)	C(14)-C(15)	1.368(5)	B(3)-F(12B)	1.570(10)
O(3)-C(19)	1.198(5)	C(15)-C(16)	1.376(6)	B(2)-F(5B)	1.282(12)
C(3)-C(4)	1.451(6)	C(16)-C(17)	1.370(6)	B(2)-F(7)	1.333(7)
O(4)-C(19)	1.309(5)	C(17)-C(18)	1.390(5)	B(2)-F(6A)	1.353(7)
O(4)-C(20)	1.466(5)	C(17)-C(19)	1.502(5)	B(2)-F(8)	1.360(6)
N(4)-C(18)	1.335(4)	C(21A)-C(22)		B(2)-F(5A)	1.438(9)
N(4)-C(14)	1.368(4)	C(21B)-C(22)		B(2)-F(6B)	1.499(12)
N(5)-Cr(1)-N(1)	87.69(12)	C(13)-N(3)-Cr(1)	113.9(2)		
N(5)-Cr(1)-N(3)	175.12(12)	C(12)-N(3)-Cr(1)	128.2(2)		
N(1)-Cr(1)-N(3)	95.66(11)	N(1)-C(3)-C(4)	118.8(3)		
N(5)-Cr(1)-N(2)	96.85(13)	C(19)-O(4)-C(20)	116.6(3)		
N(1)-Cr(1)-N(2)	80.62(12)	C(18)-N(4)-C(14)	118.9(3)		
N(3)-Cr(1)-N(2)	87.22(12)	C(18)-N(4)-Cr(1)	128.7(2)		
N(5)-Cr(1)-N(4)	96.85(12)	C(14)-N(4)-Cr(1)	112.4(2)		
N(1)-Cr(1)-N(4)	173.54(11)	C(5)-C(4)-N(2)	121.1(4)		
N(3)-Cr(1)-N(4)	80.11(12)	C(5)-C(4)-C(3)	123.8(3)		
N(2)-Cr(1)-N(4)	94.24(11)	N(2)-C(4)-C(3)	115.0(3)		
N(5)-Cr(1)-N(6)	79.81(14)	C(6)-C(5)-C(4)	119.7(3)		
N(1)-Cr(1)-N(6)	96.28(12)	C(23)-N(5)-C(22)	121.3(4)		
N(3)-Cr(1)-N(6)	96.25(12)	C(23)-N(5)-Cr(1)	113.7(3)		
N(2)-Cr(1)-N(6)	175.58(12)	C(22)-N(5)-Cr(1)	124.7(3)		
N(4)-Cr(1)-N(6)	89.07(11)	C(29)-O(5)-C(30B)	111.1(9)		
C(3)-N(1)-C(2)	120.8(3)	C(5)-C(6)-C(7)	119.0(4)		
C(3)-N(1)-Cr(1)	113.8(2)	C(28)-N(6)-C(24)	119.6(3)		
C(2)-N(1)-Cr(1)	125.3(3)	C(28)-N(6)-Cr(1)	128.0(3)		
C(8)-N(2)-C(4)	119.0(3)	C(24)-N(6)-Cr(1)	112.3(3)		
C(8)-N(2)-Cr(1)	129.4(2)	C(29)-O(6)-C(30A)	115.0(6)		
C(4)-N(2)-Cr(1)	111.5(2)	C(6)-C(7)-C(8)	119.4(4)		
C(9)-O(2)-C(10)	114.7(4)	C(6)-C(7)-C(9)	119.1(4)		
N(1)-C(2)-C(1)	115.8(4)	C(8)-C(7)-C(9)	121.5(4)		
C(13)-N(3)-C(12)	117.4(3)	N(2)-C(8)-C(7)	121.9(3)		

O(1)-C(9)-O(2)	125.5(5)	O(6)-C(29)-C(27)	115.2(5)
O(1)-C(9)-C(7)	123.0(4)	F(2)-B(1)-F(4)	111.5(4)
O(2)-C(9)-C(7)	111.5(4)	F(2)-B(1)-F(3)	111.2(4)
N(3)-C(12)-C(11)	111.8(3)	F(4)-B(1)-F(3)	110.3(3)
N(3)-C(13)-C(14)	118.6(3)	F(2)-B(1)-F(1)	109.8(4)
C(15)-C(14)-N(4)	122.1(4)	F(4)-B(1)-F(1)	109.3(4)
C(15)-C(14)-C(13)	123.1(3)	F(3)-B(1)-F(1)	104.5(4)
N(4)-C(14)-C(13)	114.9(3)	F(9B)-B(3)-F(10)	131.7(6)
C(14)-C(15)-C(16)	118.6(4)	F(9A)-B(3)-F(10)	115.1(5)
C(17)-C(16)-C(15)	119.9(4)	F(9B)-B(3)-F(11)	111.6(5)
C(16)-C(17)-C(18)	119.5(4)	F(9A)-B(3)-F(11)	122.1(5)
C(16)-C(17)-C(19)	119.1(3)	F(10)-B(3)-F(11)	115.1(4)
C(18)-C(17)-C(19)	121.4(4)	F(9A)-B(3)-F(12A)	104.5(6)
N(4)-C(18)-C(17)	121.0(3)	F(10)-B(3)-F(12A)	93.0(4)
O(3)-C(19)-O(4)	125.1(4)	F(11)-B(3)-F(12A)	99.8(4)
O(3)-C(19)-C(17)	122.2(4)	F(9B)-B(3)-F(12B)	102.4(9)
O(4)-C(19)-C(17)	112.7(3)	F(10)-B(3)-F(12B)	86.3(5)
C(21A)-C(22)-N(5)	123.1(7)	F(11)-B(3)-F(12B)	94.2(5)
N(5)-C(22)-C(21B)	113.4(5)	F(12A)-B(3)-F(12B)	164.9(6)
N(5)-C(23)-C(24)	118.9(4)	F(5B)-B(2)-F(7)	129.2(10)
N(6)-C(24)-C(25)	121.3(5)	F(7)-B(2)-F(6A)	114.1(6)
N(6)-C(24)-C(23)	115.1(4)	F(5B)-B(2)-F(8)	112.1(10)
C(25)-C(24)-C(23)	123.5(4)	F(7)-B(2)-F(8)	114.2(5)
C(24)-C(25)-C(26)	119.2(5)	F(6A)-B(2)-F(8)	111.0(5)
C(27)-C(26)-C(25)	119.5(4)	F(7)-B(2)-F(5A)	108.3(5)
C(26)-C(27)-C(28)	119.2(5)	F(6A)-B(2)-F(5A)	101.8(6)
C(26)-C(27)-C(29)	120.5(5)	F(8)-B(2)-F(5A)	106.4(5)
C(28)-C(27)-C(29)	120.3(5)	F(5B)-B(2)-F(6B)	101.6(10)
N(6)-C(28)-C(27)	121.2(4)	F(7)-B(2)-F(6B)	95.1(7)
O(5)-C(29)-O(6)	121.3(7)	F(8)-B(2)-F(6B)	94.0(7)
O(5)-C(29)-C(27)	123.4(7)	F(5A)-B(2)-F(6B)	138.1(7)

Appendix A5. Supporting Information for Chapter 6

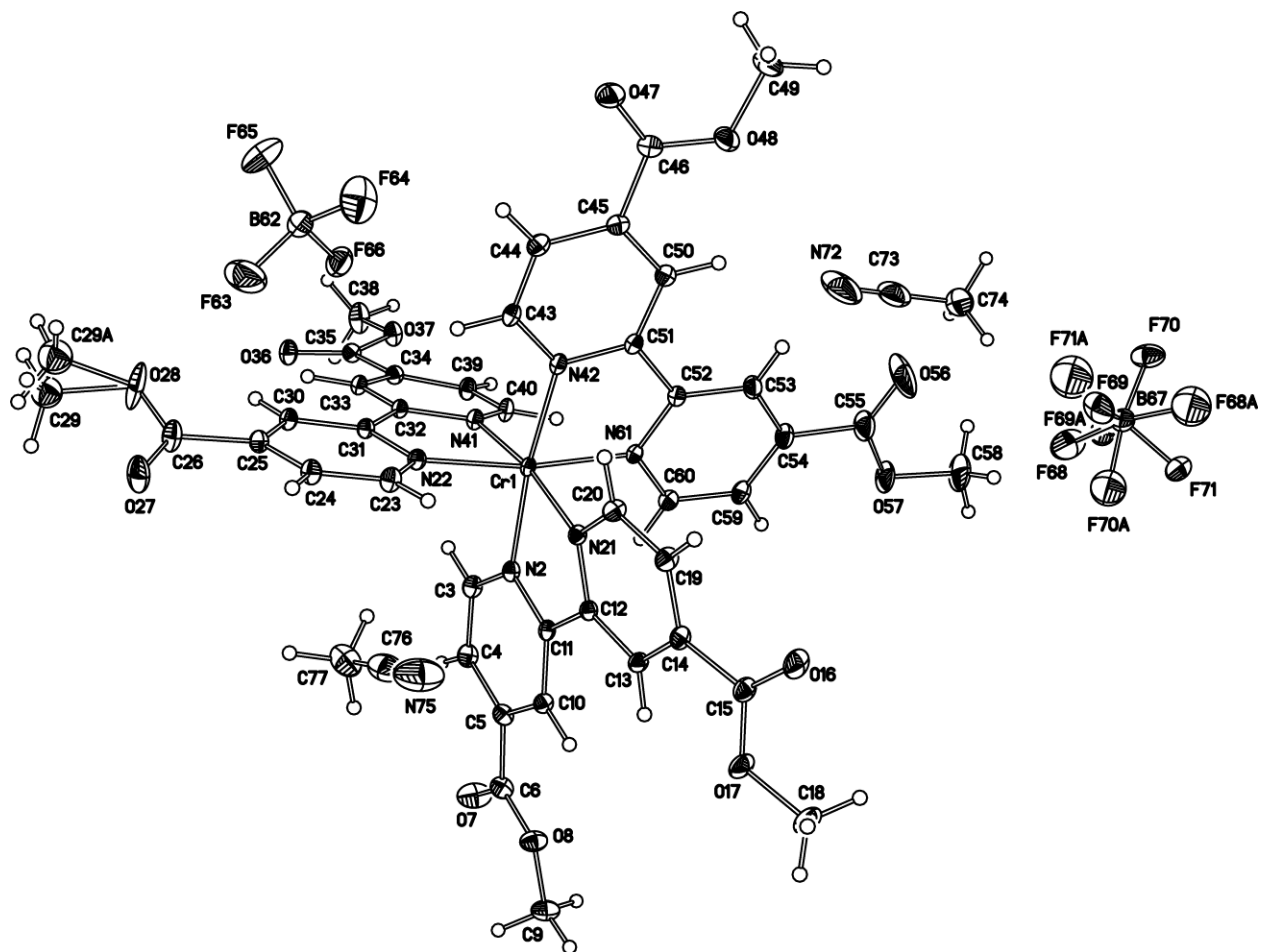


Figure A5.1. Full structure of $6.1 \cdot 2\text{CH}_3\text{CN}$, rendered at 40% ellipsoids.

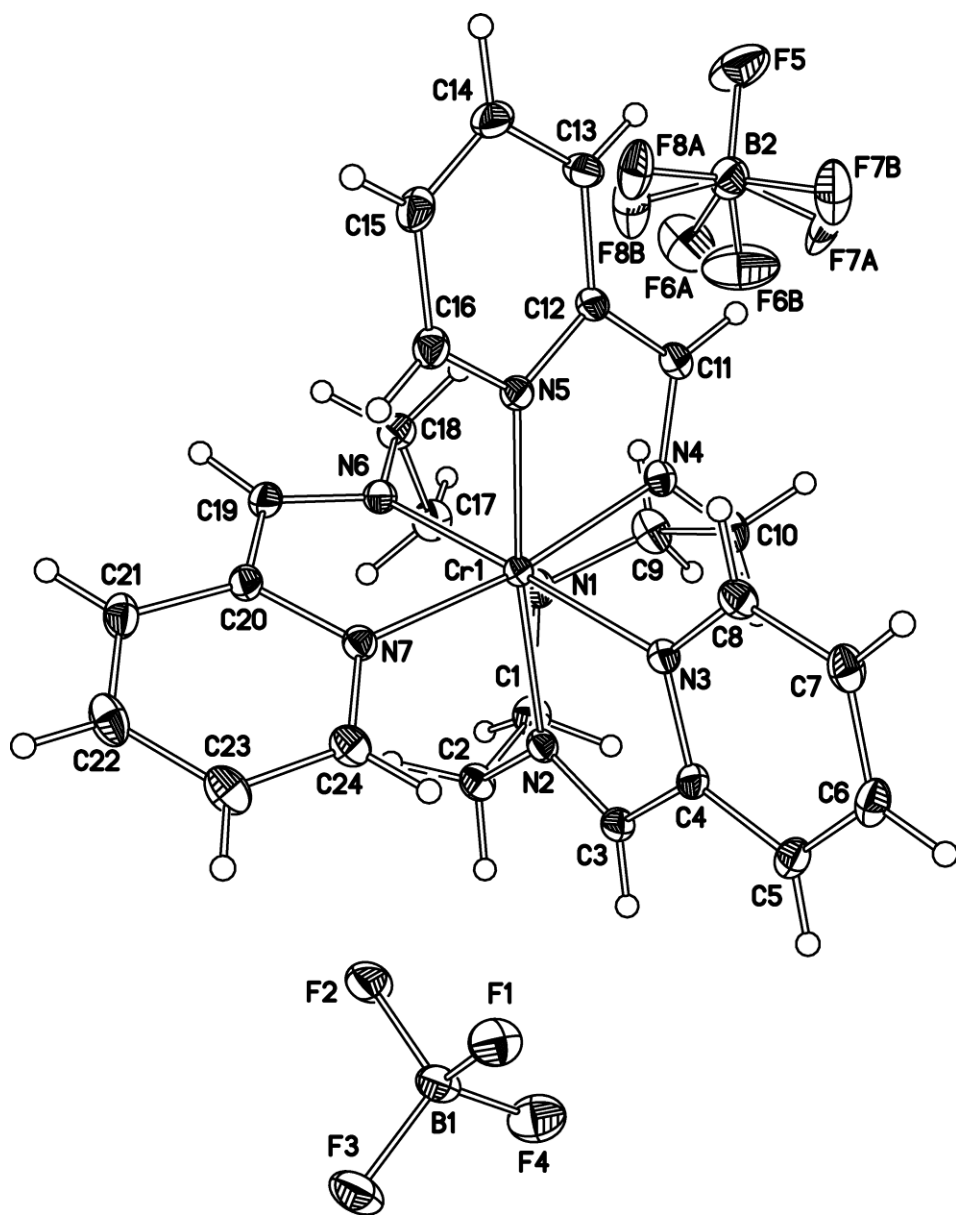


Figure A5.2. Full structure of 6.3, rendered at 40% ellipsoids.

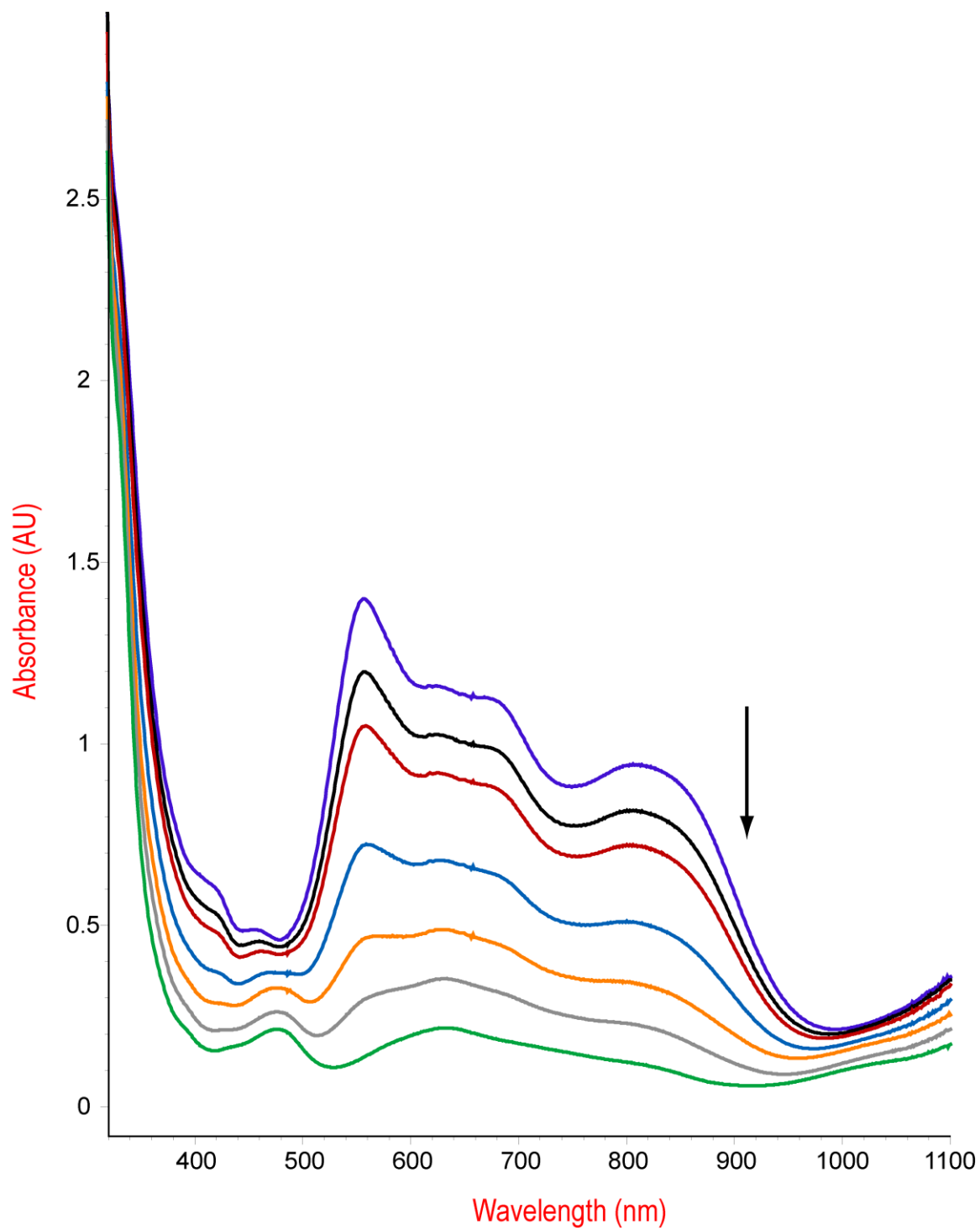


Figure A5.3. Electronic absorption spectra showing aerobic oxidation of **6.2**, $[\text{Cr}(4\text{-dmcbpy})_3](\text{BF}_4)$ in CH_3CN , monitored over 35 minutes.

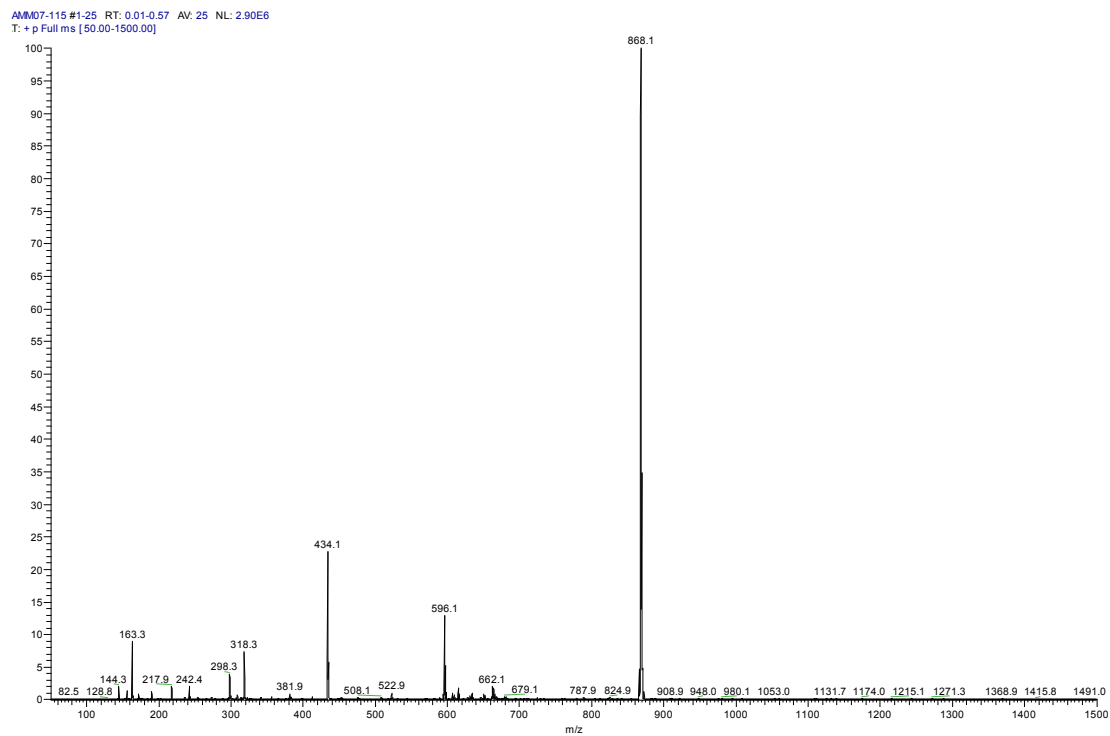


Figure A5.4. Positive ion mass spectrum of $[\text{Cr}(4\text{-dmcbpy})_3](\text{BF}_4)$ **6.2** in CH_3CN .

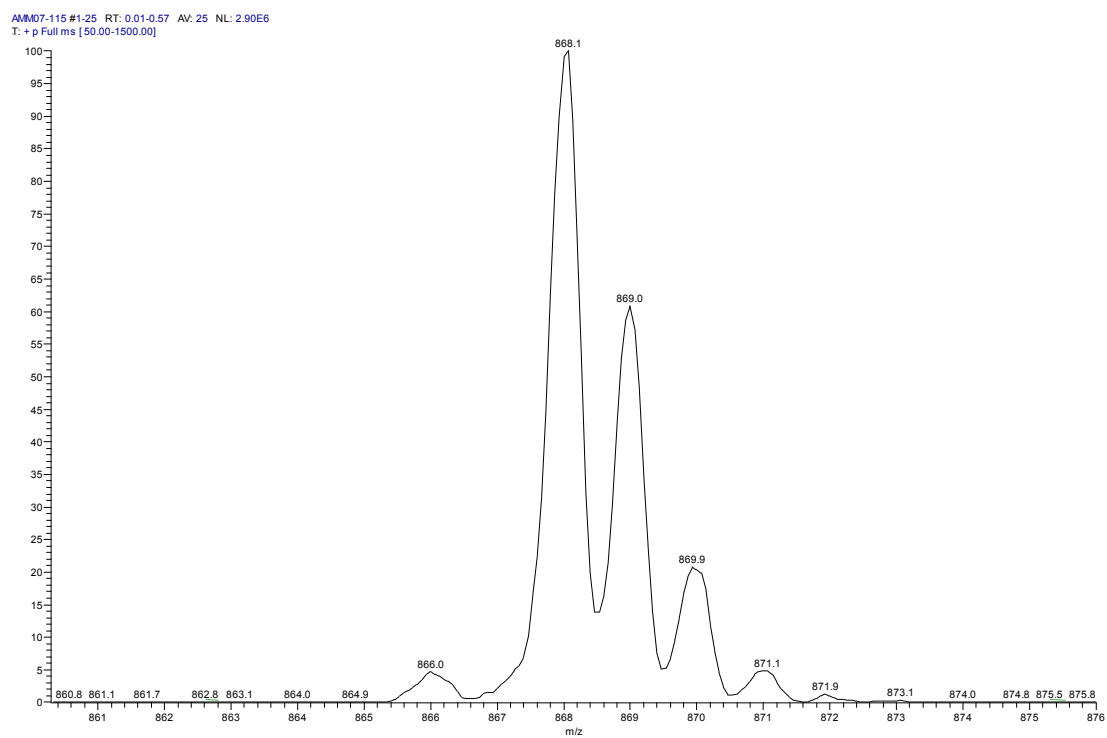


Figure A5.5. Experimental isotopic pattern of the 868.07 m/z peak ($[\text{Cr}(4\text{-dmcbpy})_3]^+$) of **6.2** in CH_3CN .

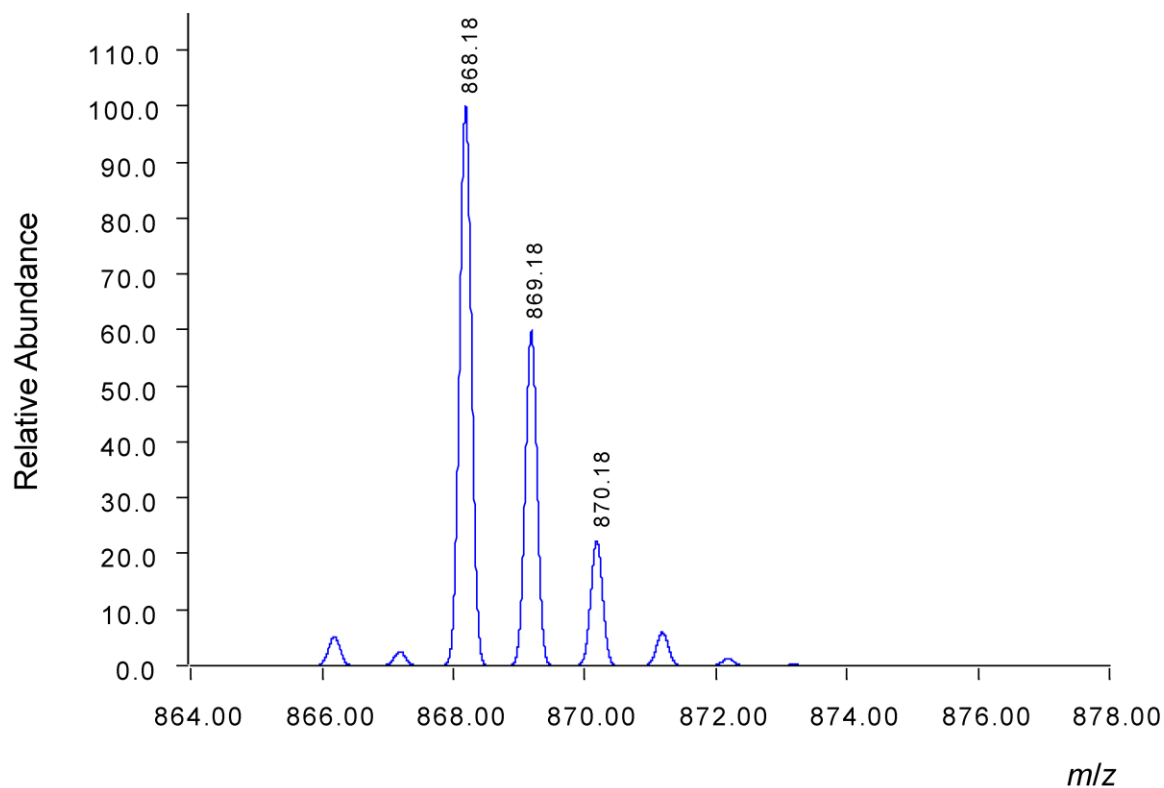


Figure A5.6. Simulated isotopic pattern of the 868.07 m/z peak ($[\text{Cr}(4\text{-dmcbpy})_3]^+$) of **6.2** in CH_3CN .

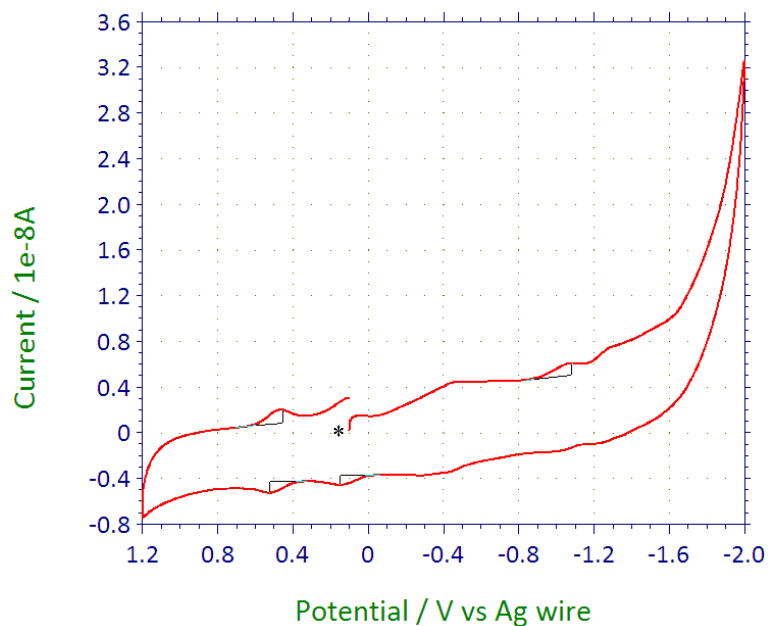


Figure A5.7. Cyclic voltammogram of reaction product from reduction of $[\text{Cr}(4\text{-dmcbpy})_3](\text{BF}_4)_2$ with sodium diphenylketyl radical, collected in 0.1 M TBAPF_6 THF solution. In this figure, the rest potential is denoted by * and the potential is referenced directly to the Ag wire and not to the $\text{Fc}^{+/0}$ couple.

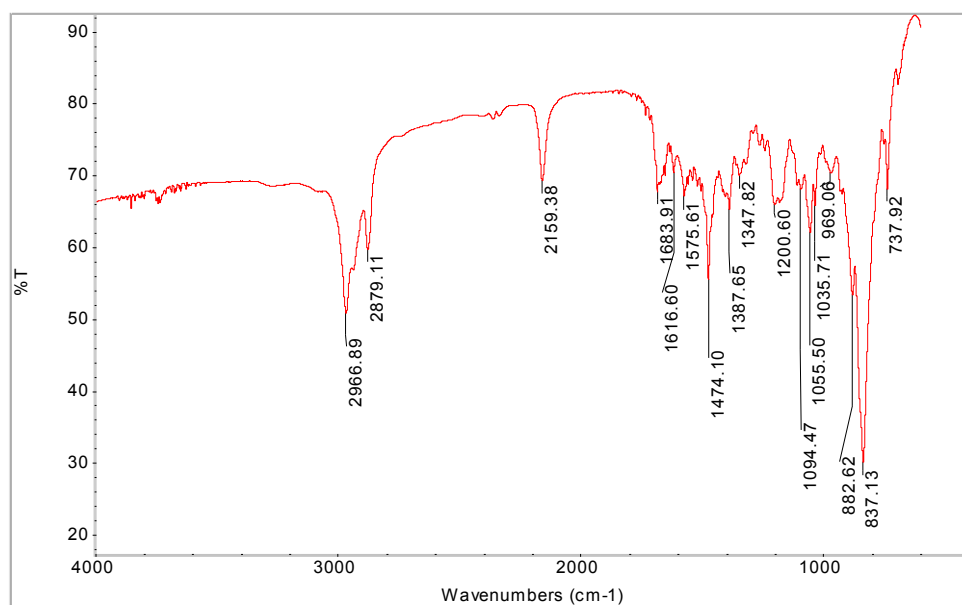


Figure A5.8. KBr pellet IR spectrum of working compartment product from reduction of $[\text{Cr}(4\text{-dmcby})_3](\text{BF}_4)_2$ by bulk electrolysis in 0.1 M TBAPF_6 CH_3CN .

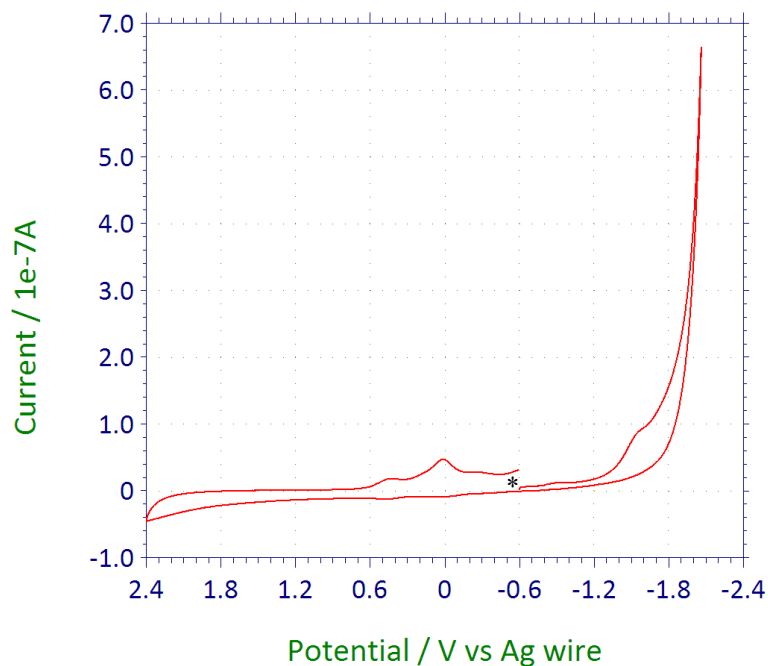


Figure A5.9. Cyclic voltammogram of solid reaction product from reduction of $[\text{Cr}(\text{tren}(\text{impy})_3)](\text{BF}_4)_2$ by bulk electrolysis, collected in 0.1 M TBAClO_4 DCM solution. In this figure, the rest potential is denoted by * and the potential is referenced directly to the Ag wire and not to the $\text{Fc}^{+/0}$ couple.

Appendix A6. Notebook Cross-references for Iminopyridine, Polypyridine and Related Compounds

L^{5-OH}	AMM02-39
$[Fe(L^{5-OH})](BF_4)_2$	AMM02-69
$[Fe(L^{5-OH})](SO_4)_2$	AMM02-40
$[Fe(L^{5-OH})](BPh_4)_2$	AMM02-55
L^{6-OH}	AMM03-13
$L^{5-ONHtBu}$	AMM02-142
$[Fe(L^{5-ONHtBu})](BF_4)_2$	AMM09-81
$([FeL^{5-ONHtBu}]Cl)_2[FeCl_4]$	AMM09-81
$L^{6-ONHtBu}$	AMM02-154
$[(phen)_2Cr(4-dmcbpy)](OTf)_3$	AMM03-71
$[(Me_2bpy)_2Cr(4-dmcbpy)](OTf)_3$	AMM04-71
$[(Ph_2phen)_2Cr(4-dmcbpy)](OTf)_3$	AMM05-128
$[Cr(4-dmcbpy)_3](BF_4)_3$	AMM04-147
$[Cr(4-dmcbpy)_3](BF_4)_2$	AMM04-69
$[Cr(4-dmcbpy)_3](BF_4)$	AMM06-154
L^{5-OMe} (aka L2)	AMM08-109
$[Cr(L^{5-OMe})](BF_4)_2$	AMM08-143
$[Mn(L^{5-OMe})](OTf)_2$	AMM08-21
$[Fe(L^{5-OMe})](OTf)_2$	AMM08-64
$[Co(L^{5-OMe})](ClO_4)_2$	AMM08-153
$[Ni(L^{5-OMe})](ClO_4)_2$	AMM08-63
$[Cu(L^{5-OMe})](OTf)_2$	AMM09-59
$[Zn(L^{5-OMe})](OTf)_2$	AMM09-12
tren(py) ₃ (aka L1)	AMM08-23
py-im-et (aka L3)	AMM06-134 (recommend using excess ethylamine)
E-py-im-et (aka L4)	AMM08-46
$[Cr(L1)](BF_4)_2$	AMM08-11
$[Cr(L1)](BF_4)_3$	AMM08-13 and -39
$[Cr(L2)](BF_4)_3$	AMM06-97 (Ag oxidation) AMM06-105 (thianthrene oxidation)
$[Cr(L3)](BF_4)_2$	AMM06-131
$[Cr(L3)](BF_4)_3$	AMM07-49
$[Cr(L4)](BF_4)_2$	AMM07-128
$[Cr(L4)](BF_4)_3$	AMM07-130
$[Zn(L4)](OTf)_2$ (colorless)	AMM09-19 and -26
$[Zn(L4)](OTf)_2$ (blue)	AMM09-26, -43, -50 and -53
$[Ga(L4)](NO_3)_3$ (blue)	AMM08-83 and -89
$[Ga(L2)](NO_3)_3$	AMM08-87 and 9-14
NaBAr ^F	AMM08-139
4,4',5,5'-tetrahydro-2,2'-bioxazole	AMM04-85
$[Cr(OAc)_2(H_2O)]_2$	AMM07-132
$[Cr(CH_3CN)_4](BF_4)_2$	AMM04-141